ASME
SETTING THE STANDARD

Transactions of the ASME, Journal of Fluids Engineering
(ISSN 0098-2202) is published monthly by
The American Society of Mechanical Engineers,
Three Park Avenue, New York, NY 10016.
Periodicals postage paid at New York, NY
and additional mailing offices.
POSTMASTER: Send address changes to Transactions of the
ASME, Journal of Fluids Engineering, c/o THE AMERICAN
SOCIETY OF MECHANICAL ENGINEERS,
22 Law Drive, Box 2300, Fairfield, NJ 07007-2300.
CHANGES OF ADDRESS must be received at Society
headquarters seven weeks before they are to be effective.
Please send old label and new address.

Journal of Fluids Engineering

Published Monthly by ASME

VOLUME 131 • NUMBER 4 • APRIL 2009

RESEARCH PAPERS

Flows in Complex Systems

Fundamental Issues and Canonical Flows

Multiphase Flows

Techniques and Procedures

This journal is printed on acid-free paper, which exceeds the ANSI Z39.48-1992 specification for permanence of paper and library materials. ♾™
♻ 85% recycled content, including 10% post-consumer fibers.

(**Contents continued**)

Journal of Fluids Engineering **Volume 131, Number 4** **APRIL 2009**

TECHNICAL BRIEFS

The ASME Journal of Fluids Engineering is abstracted and indexed in the following:

Applied Science & Technology Index, Chemical Abstracts, Chemical Engineering and Biotechnology Abstracts (Electronic equivalent of Process and Chemical Engineering), Civil Engineering Abstracts, Computer & Information Systems Abstracts, Corrosion Abstracts, Current Contents, Ei EncompassLit, Electronics & Communications Abstracts, Engineered Materials Abstracts, Engineering Index, Environmental Engineering Abstracts, Environmental Science and Pollution Management, Excerpta Medica, Fluidex, Index to Scientific Reviews, INSPEC, International Building Services Abstracts, Mechanical & Transportation Engineering Abstracts, Mechanical Engineering Abstracts, METADEX (The electronic equivalent of Metals Abstracts and Alloys Index), Petroleum Abstracts, Process and Chemical Engineering, Referativnyi Zhurnal, Science Citation Index, SciSearch (The electronic equivalent of Science Citation Index), Shock and Vibration Digest, Solid State and Superconductivity Abstracts, Theoretical Chemical Engineering

M. Brian Thomas
Department of Industrial and Manufacturing Engineering,
Cleveland State University,
2121 Euclid Avenue, SH 221
Cleveland, OH 44115-2214
e-mail: m.thomas.84@csuohio.edu

Gary P. Maul
Department of Industrial, Welding, and Systems Engineering,
The Ohio State University,
210 Baker Systems,
1971 Neil Avenue,
Columbus, OH 43210
e-mail: maul.1@osu.edu

Considerations on a Mass-Based System Representation of a Pneumatic Cylinder

Pneumatic actuators can be advantageous over electromagnetic and hydraulic actuators in many servo motion applications. The difficulty in their practical use comes from the highly nonlinear dynamics of the actuator and control valve. Previous works have used the cylinder's position, velocity, and internal pressure as state variables in system models. This paper replaces pressure in the state model with the mass of gas in each chamber of the cylinder, giving a better representation of the system dynamics. Under certain circumstances, the total mass of gas in the cylinder may be assumed to be constant. This allows development of a reduced-order system model. [DOI: 10.1115/1.3089533]

Keywords: pneumatics, servo motion, control

1 Introduction and Review

Pneumatic actuators present an alternative to the use of electromagnetic and hydraulic actuators in servo motion applications. Like electromagnetic actuators (i.e., motors), pneumatic actuators are generally clean and reliable in operation. Like hydraulic actuators, pneumatic actuators may be directly coupled to a payload without the need for a transmission. Servopneumatics offer high power-to-weight ratios and can provide a cost benefit as high as 10:1 over competing technologies [1,2]. In certain niche applications, pneumatic actuators provide unique advantages over competitive technologies. Unlike electromagnetic actuators, pneumatic actuators are naturally compliant due to the compressibility of air but are well adapted to wash-down environments. The natural compliance of a pneumatic actuator also makes it advantageous when personnel must be inside the work envelope of the machine [3].

The principal barrier to the more widespread application of servopneumatic technology in industry has been the problem of control. The dynamics of a pneumatic actuator are highly nonlinear due to the effects of friction, air compressibility, and time delays and are compounded by the nonlinear flow characteristics of flow control valves [3]. Linear control methods such as proportional-integral-derivative (PID), while well understood by both engineers and technicians, perform poorly when coupled to such highly nonlinear systems. With the recent availability of low-cost powerful microprocessors, computationally expensive nonlinear control strategies may now be performed in real time. Advanced control strategies applied to servopneumatics include fuzzy control [4], sliding mode control [5], model-based adaptive control [1,6], neural networks [7], and pulse-width modulation schemes for solenoid valves [8,9].

The principal contributions of this paper are as follows:

(1) Presentation of a mass-based state representation for a pneumatic cylinder. Previous works use position, velocity, and the pressure in two chambers of a cylinder as state variables, as these quantities are readily measured. A mass-based representation more closely links the state variables with the process dynamics.
(2) Formal development and verification of the constant mass assumption. This assumption states that under certain conditions, the total mass of gas within a pneumatic actuator is constant. In other words, the instantaneous rate of mass flow going into one chamber of a pneumatic cylinder under servo control is equal to the mass flow rate, leaving the other chamber. This assumption can remain valid even when the underlying preconditions are not met.
(3) A reduced-order system model, based on the constant mass assumption, for advanced control algorithms. This model uses three state variables—position, velocity, and equilibrium position—instead of four.

The first significant works dealing with the modeling of servopneumatics are two papers by Shearer [10,11], in which he developed a linear model for small motions of a double-rod cylinder about its midstroke position. While his model is quite restricted in its practical application, most subsequent researchers have used Shearer's methodology toward model development. Other examples of linear models for pneumatic actuators include Liu and Bobrow [12], Kunt and Singh [13], and Hamiti et al. [14]. Shearer's methodology may also be used in developing nonlinear models of pneumatic actuators. A thorough nonlinear model was developed by Richer and Hurmuzlu [15], incorporating not only the nonlinear dynamics of the cylinder itself but also propagation delays and losses in the air lines connecting valve and cylinder and the dynamics of the valve. Kawakami et al. [16] compared the results of linearized and nonlinear models for a pneumatic positioning axis with experimental data, finding that the linearized model differs significantly from experimental results. More recent works have focused on the problem of observability for the nonlinear system [8,17].

Servopneumatic systems find applications in both the laboratory and the plant floor. Caldwell et al. [18] discussed the use of pneumatic actuators in a humanoid robot. The properties of pneumatic muscle actuators make them well suited for this application: a high power-to-weight ratio, flexibility, and mechanical behavior similar to those of human muscle tissue. A light-weight internal combustion engine can power the robot, giving it mobility without needing an umbilical cord nor heavy banks of batteries. Pneumatics have been considered for a number of more conventional robot designs. Torque control of individual actuators allows a robot to have force control at its end effector [19]. A survey by Harrison et al. [20] indicates an industry interest in modular pneumatic robots for flexible automation applications, particularly assembly, part handling, and quality control. Finally, this research supported an effort to incorporate servopneumatic actuators in a food process-

Contributed by the Fluids Engineering Division of ASME for publication in the JOURNAL OF FLUIDS ENGINEERING. Manuscript received July 25, 2007; final manuscript received December 22, 2008; published online March 6, 2009. Review conducted by Joseph Katz.

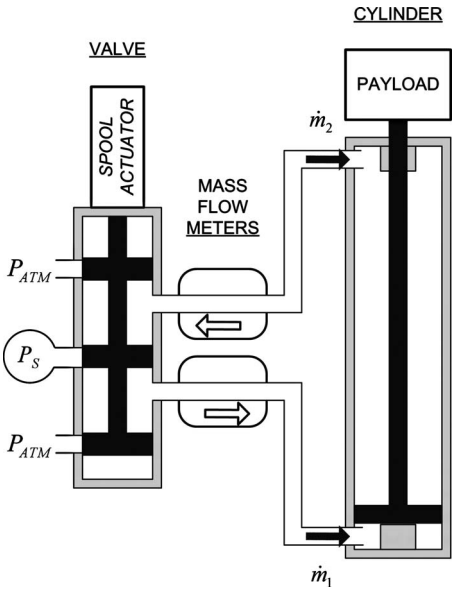

Fig. 1 Servopneumatic system

ing environment. Pneumatic actuators were chosen over other technologies due to their clean operation and compatibility with equipment wash-down procedures.

2 System Models

A typical servopneumatic system consists of a pneumatic actuator, one or more control valves to regulate flow, a position sensor, and a controller. The components may be selected from an extensive list of models and vendors, depending on the particular requirements of the application. This work considers a system consisting of a single-rod, double-acting pneumatic cylinder with a proportional spool valve controlling the flow of air to and from the cylinder (Fig. 1). Mass flow meters measure flow in and out of the cylinder. Table 1 details the configuration of the system. Previous work by the authors contains a simulation of a similar system [21]; its configuration is detailed in Table 2.

2.1 Conventional Representation. The conventional mathematical representation of a pneumatic actuator uses four state variables (x, $\dot{x}$, P_1, and P_2) and three nonlinear differential equations to describe the dynamics of the system. Though previous works deriving these equations differ on their underlying assumptions, they all use the general approach presented by Shearer in Ref. [10]. This approach begins with the internal energy of volume of gas,

Table 1 Experimental system properties

Cylinder	Parker 02.00 HMAU 34A
Servovalve	Festo MPYE-5
Position feedback	Linear potentiometer
Flow measurement	TSI 40241 mass flowmeter
Cylinder stroke, L	304.8 mm (12.0 in.)[a]
Cylinder diameter, d	50.8 mm (2.0 in.)
Rod diameter, d_{rod}	25.4 mm (1.0 in.)
Payload mass, M	1.6 kg (3.5 lb)[b]
	170 kPa (25 psi (gauge))
	340 kPa (50 psi (gauge))
Supply pressure, P_S	520 kPa (75 psi (gauge))
Orientation	Vertical; rod end up or down
Control	Proportional; implemented through LABVIEW

[a]Stroke shortened to accommodate 300 mm length of potentiometer.
[b]Includes estimated mass of piston and rod.

Table 2 Simulation system properties, from Ref. [21]

Cylinder	Festo DNG-50–200-P-A
Servovalve	Festo MPYE-5[a]
Position feedback	Gemco Blue Ox 952QD
Flow measurement	None
Cylinder stroke, L	175 mm[b]
Cylinder diameter, d	50.0 mm
Rod diameter, d_{rod}	25 mm
Payload mass, M	11.0 kg[c]
Static friction, F_{stat}	21.8 N (4.90 lb)
Dynamic friction, F_{dyn}	6.9 N (1.55 lb)
Viscous friction, b	2.19 N s/m(0.125 lbs/in.)
Orientation	Vertical; rod end down
Control	PI with velocity feed-forward; implemented through Allen-Bradley M02AE motor control module

[a]Factory modified to accept a ±10 V command signal.
[b]Effective length shortened from 200 mm by an internal position-sensing magnet.
[c]Includes estimated mass of piston and rod.

$$E = c_V \rho V T \tag{1}$$

The derivative of the internal energy with respect to time, when applied to the chambers of a pneumatic cylinder, yields two state equations,

$$\dot{P}_1 = \frac{\gamma R T}{A_1 x + V_{X,1}} \dot{m}_1 - \frac{\gamma P_1 A_1}{A_1 x + V_{X,1}} \dot{x} \tag{2}$$

$$\dot{P}_2 = \frac{\gamma R T}{A_2 (L - x) + V_{X,2}} \dot{m}_2 + \frac{\gamma P_2 A_2}{A_2 (L - x) + V_{X,2}} \dot{x} \tag{3}$$

where $V_{X,1}$ and $V_{X,2}$ are the excess volumes of gas in either end of the cylinder and in the plumbing between the cylinder and the valve. Derivation of Eqs. (2) and (3) is provided in Appendix A. The third governing equation for the pneumatic actuator addresses the mechanical dynamics of the system,

$$\ddot{x} = (Mg + P_1 A_1 - P_2 A_2 - P_{\text{atm}} A_{\text{rod}} - b\dot{x} - F_{\text{fric}})/M \tag{4}$$

The derivation of Eqs. (2) and (3) assumes that the gas undergoes adiabatic processes in the cylinder. Shearer [10] demonstrated that for an assumption of isothermal processes, the equation for pressure dynamics is similar, differing only by the factor γ, the ratio of specific heats. For dry air at 20 °C, this ratio γ is 1.40. Equation (5) presents the general form for the pressure dynamics of an isothermal process, which may be compared with the general form for an adiabatic process, which is presented in Eq. (6),

$$\dot{P} = \frac{RT}{V} \dot{m} - \frac{P}{V} \dot{V} \tag{5}$$

$$\dot{P} = \frac{\gamma R T}{V} \dot{m} - \frac{\gamma P}{V} \dot{V} \tag{6}$$

There has been considerable discussion in previous works as to the "best" method for modeling a pneumatic cylinder. Shearer assumed an adiabatic process in Ref. [11]; many subsequent researchers have assumed the same, as the heat transfer process is thought to be significantly slower than the pressure, flow, and mechanical processes. Exceptions include Pu and Weston [22], who assumed an isothermal model to aid in their analysis. Richer and Hurmuzlu [15] used an intermediate term, α, which is bounded by 1.0 and γ. Based on previous works, these authors suggest a value of α closer to γ for charging processes and closer to 1.0 for discharging processes. Using a three-parameter model, Backé and Ohligschläger [23] found a pneumatic cylinder in motion initially behaves adiabatically, but heat flow works to restore isothermal conditions. Kawakami et al. [16] found that the differ-

ences between an isothermal and an adiabatic model are not significant in their simulation and recommended using the mathematically less-complicated isothermal model.

The state equations—Eqs. (2)–(4)—do not address the computation of the mass flow rates into each chamber of the cylinder, $\dot{m}_1$ and $\dot{m}_2$. These flow rates are dependent on the design, construction, and operation of the valve (or valves), the upstream and downstream pressures, and the length and sizing of the plumbing used in the system. Reference [15] presents a thorough discussion on the propagation losses and delays that do occur but are often ignored in systems with short lengths of air line. For the actual flow through a valve, the literature presents at least three models. Most researchers use the theoretical model of compressible flow through an orifice [24], expressed as,

$$\dot{m} = \begin{Bmatrix} C_D A \dfrac{P_{up}}{\sqrt{RT_1}} \sqrt{\dfrac{2\gamma}{\gamma-1}\left[\left(\dfrac{P_{dn}}{P_{up}}\right)^{2/\gamma} - \left(\dfrac{P_{dn}}{P_{up}}\right)^{(\gamma+1)/\gamma}\right]} & : \left(\dfrac{P_{dn}}{P_{up}}\right) > \left(\dfrac{P_{dn}}{P_{up}}\right)_{crit} \\ C_D A \dfrac{P_{up}}{\sqrt{RT_1}} \times 0.6847 & : \left(\dfrac{P_{dn}}{P_{up}}\right) \le \left(\dfrac{P_{dn}}{P_{up}}\right)_{crit} \end{Bmatrix} \tag{7}$$

where the critical pressure ratio

$$\left(\frac{P_{dn}}{P_{up}}\right)_{crit} = \left(\frac{2}{\gamma+1}\right)^{\gamma/\gamma-1} \tag{8}$$

separates the choked and unchoked regimes of flow through the orifice. For air, the critical pressure ratio is 0.528. The National Fluid Power Association (NFPA) presents a less-complicated model that produces similar results using the same critical pressure ratio as the orifice flow equation [25]. Equation (9) uses English units of measurement, as is the convention in the literature,

$$Q_{SCFM} = \begin{Bmatrix} 22.48 \times C_V \sqrt{\dfrac{(P_{up}-P_{dn})P_{dn}}{T}} & : \left(\dfrac{P_{dn}}{P_{up}}\right) > \left(\dfrac{P_{dn}}{P_{up}}\right)_{crit} \\ 11.22 \times C_V \dfrac{P_{up}}{\sqrt{T}} & : \left(\dfrac{P_{dn}}{P_{up}}\right) \le \left(\dfrac{P_{dn}}{P_{up}}\right)_{crit} \end{Bmatrix} \tag{9}$$

Less familiar through the literature is the Instrument Society of America (ISA) model for compressible flow through a valve. This model was developed to account for the observation that two valves with the same flow coefficient C_v can exhibit different flow characteristics. In addition to the flow coefficient, the ISA model contains a critical pressure drop ratio, X_T. The critical pressure drop ratio is a reflection of the complexity of the flow path geometry through the valve and changes the point at which choked flow occurs [26],

$$Q_{SCFM} = \begin{Bmatrix} 22.67 \times C_V P_{up}\left(1 - \dfrac{X}{3X_T}\right)\sqrt{\dfrac{X}{T}} & : X < X_T \\ 15.11 \times C_V P_{up}\sqrt{\dfrac{X_T}{T}} & : X \ge X_T \end{Bmatrix} \tag{10}$$

where

$$X = \frac{P_{up}-P_{dn}}{P_{up}} = 1 - \left(\frac{P_{dn}}{P_{up}}\right) \tag{11}$$

Equation (10) uses English units of measure, as is the convention in the literature. Equations (9) and (10) may be converted to mass flow rates by multiplying the volumetric flow rate by standard density.

Figure 2 compares the orifice flow model, the NFPA flow model, and the ISA flow model using three values of X_T. Experimental data collected in the course of this research support the use of the ISA model over the orifice flow model—note that the ISA model in Fig. 2 lacks the choked-flow behavior predicted by Eq. (7). If one considers a valve as a series of orifice-type obstructions to the flow of gas rather than as a single orifice, the ISA model becomes more attractive than single-orifice models. Using Eq. (7), one can show that flow through two orifice plates in series as a function of the total pressure drop is different from that through a single orifice plate. It is not difficult to find flow conditions in which one orifice experiences choked flow while the other is unchoked.

2.2 Mass-Based System Representation. Equations (2)–(4) describe the conventional state representation of a pneumatic cylinder. An alternate representation for the pneumatic cylinder uses the mass of gas in each chamber of the cylinder, the cylinder position, and the cylinder velocity (m_1, m_2, x, and $\dot{x}$) as state variables. The derivatives for the mass of gas in either chamber are found through application of the appropriate flow model of Eq. (7), Eq. (9), or Eq. (10). The mechanical dynamics of Eq. (4) must be expressed in terms of mass rather than pressure. From the ideal gas law, pressure in a closed chamber is a function of the mass of gas in the chamber. Applied to the cylinder,

$$P_1 = \frac{m_1 RT}{A_1 x + V_{X,1}} \tag{12}$$

$$P_2 = \frac{m_2 RT}{A_2 (L-x) + V_{X,2}} \tag{13}$$

The mechanical dynamics of the cylinder may be expressed as

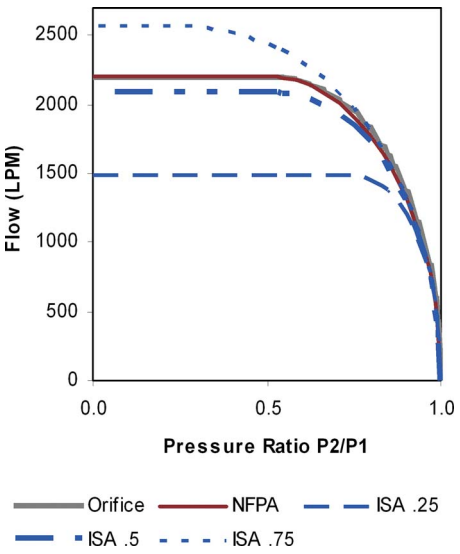

Fig. 2 Valve flow models

Table 3 Comparative energy rates

	System studied	System from Ref. [21]
Orientation	Rod end up	Rod end down
Incoming flow	Blind end	Rod end
Payload direction of travel	Up	Up
Supply pressure	340 kPa (50 psi (gauge))	550 kPa (80 psi (gauge))
Representative test velocity	200 mm/s	254 mm/s
Velocities tested	20–1200 mm/s	6.1–889 mm/s
Acceleration	20 m/s^2	1.27 m/s^2
Coulomb friction force	N/A	6.9 N
Flow rate (source)	75 SLPM (data)	136 SLPM (simulation)
Potential energy rate, $\dot{E}_P = Mg\dot{x}$	3.1 J/s	27.4 J/s
Kinetic energy rate, $\dot{E}_K = M\ddot{x}\cdot\dot{x}$	6.4 J/s	3.5 J/s
Energy rate from Coulomb friction, $\dot{E}_F = F_{\text{fric}}\dot{x}$	N/A	1.8 J/s
Energy rate from viscous friction, $\dot{E}_F = b\dot{x}^2$	N/A	0.14 J/s
Incoming gas (air) energy rate, $\dot{E}_{\text{air}} = \frac{d}{dt}(c_V \rho V T) = \dot{m} c_P T - PA\dot{x}$	338 J/s	588 J/s

$$\ddot{x} = \frac{1}{M}\left(Mg + \frac{m_1 RT}{x + x_{T,1}} - \frac{m_2 RT}{(L-x) + x_{T,2}} - P_{\text{atm}} A_{\text{rod}} - b\dot{x} - F_{\text{fric}}\right) \tag{14}$$

where $x_{T,1}$ and $x_{T,2}$ represent the equivalent cylinder lengths of the excess volumes in the cylinder and hose,

$$x_{T,1} = \frac{V_{X,1}}{A_1} \tag{15}$$

$$x_{T,2} = \frac{V_{X,2}}{A_2} \tag{16}$$

The principal benefit of a mass-based system representation is that it provides a direct link between the dynamics of the control valve and those of the pneumatic cylinder, as pneumatic servo valves regulate mass flow rather than pressure. The principal disadvantage of a mass-based representation is that pressure is more readily measured than flow or mass.

2.3 Constant Mass Assumption. If the sum of the mass of gas in both chambers of the cylinder is constant, a reduced-order system model may be derived. Consider a frictionless pneumatic cylinder moving at a constant velocity, $\dot{x}$. Assume that no external forces act on the cylinder and that constant pressures and temperatures exist in both chambers of the cylinder. While temperature will change in an adiabatic process, it is assumed here that the temperature change is not significant [16]. Further, assume that the cylinder does not reach its limits of travel. With these assumptions, the time derivative of the ideal gas law for the blind end of the cylinder, Eq. (12), becomes

$$P_1 A_1 \dot{x} = \dot{m}_1 RT \tag{17}$$

For the rod end,

$$-P_2 A_2 \dot{x} = \dot{m}_2 RT \tag{18}$$

The forces acting on the cylinder piston are balanced,

$$P_1 A_1 = P_2 A_2 + P_{\text{atm}} A_{\text{rod}} \tag{19}$$

Combining Eqs. (17)–(19),

$$\dot{m}_1 = -\dot{m}_2 + e \tag{20}$$

where the error term from atmospheric pressure acting over the area of the rod, e, is defined as

$$e = \frac{P_{\text{atm}} A_{\text{rod}} \dot{x}}{RT} \tag{21}$$

Using the representative values found in Table 3, the error term e is found to be 7.6% of the measured mass flow rate. Note that the error is proportional to velocity. Also note that the cylinder used in this study has a relatively thick rod, which magnifies the error in Eq. (21). Supposing that the rod diameter is reduced to 12.7 mm, the error reduces to 1.9% of the mass flow rate. It is therefore argued that for many applications, the error term can be ignored, so that

$$\dot{m}_1 = -\dot{m}_2 \tag{22}$$

Because the mass flow rates are equal in magnitude and opposing in direction, the sum $m_1 + m_2$ must be constant,

$$m_1 + m_2 = m \tag{23}$$

This demonstrates that an assumption of a constant mass of gas in a pneumatic cylinder is valid when the cylinder travels at a constant velocity for many common valve-cylinder configurations. An energy analysis evaluates the strength of the underlying conditions for the constant mass assumption. In considering a pneumatic cylinder moving vertically, the rate of energy entering the cylinder as pressurized gas must equal the rate of energy stored within the cylinder, plus the energy extracted from the gas through various means, plus the energy leaving with the air displaced from the other chamber of the cylinder. For the cylinder under consideration, energy extracted from the gas may (a) increase the gravitational potential energy of the payload, (b) increase the kinetic energy of the payload through acceleration, and (c) be converted to heat by overcoming friction in the cylinder.

Table 3 shows the calculated values of these energy rates for typical experiments conducted in the course of this study. Table 3 also includes values from the earlier study [21], in which the magnitude of the Coulomb friction was measured. The significance of Table 3 is that the energy rate supplied by the incoming flow of gas is at least one order of magnitude larger than the energy rates due to changes in kinetic energy, potential energy, and overcoming friction. This suggests the constant mass assumption can be a valid system approximation even when the prerequisite conditions are not present.

Numeric simulation, incorporating the effects of friction, pressure losses in the hoses, and external loading on the cylinder, supports the constant mass assumption. The simulation modeled the system response to a number of command trajectories, having

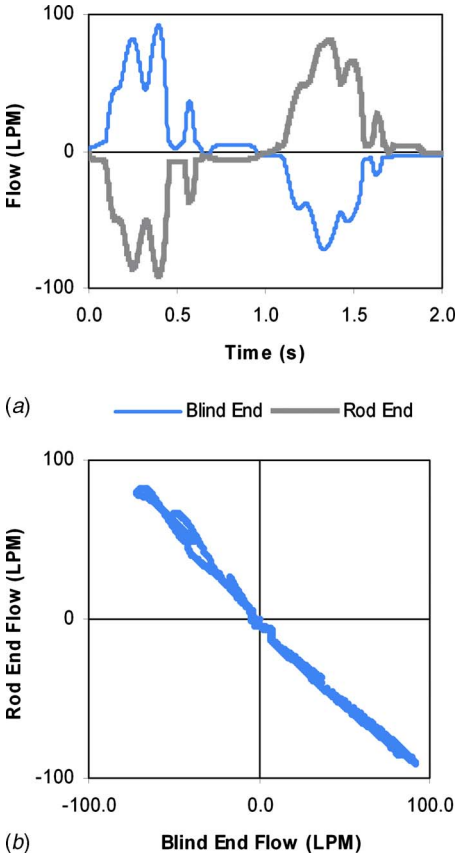

Fig. 3 Simulated mass flow rates, from Ref. [21], 254 mm/s command velocity, and 655 kPa supply. (*a*) Flow versus time and (*b*) flow versus flow.

velocities from 6 mm/s to 890 mm/s and accelerations to 8.89 m/s^2. Figure 3(*a*) shows a typical mass flow rate graph from the simulation as a function of time; Fig. 3(*b*) shows the same data, plotting rod end flow as a function of blind end flow. Regression in Fig. 3(*b*) shows that the best-fit line has a slope of −1.103, with an R^2 value of 0.987. Similar results were obtained for all simulations in which the cylinder did not reach either limit of its stroke.

Experimental verification of the constant mass assumption was accomplished using two TSI 40241 mass flow sensors (Shoreview, MN) capable of measuring air flow to 300 SLPM (standard liters per minute). The configuration of Fig. 1 provided simultaneous flow measurements for both chambers of the cylinder. Because the mass flow sensors are unidirectional, they were configured so that one measured incoming flow to one chamber, while the other measured outgoing flow from the other. A complete flow history was obtained by interweaving two data records in which the direction of measurement was reversed. A proportional controller, implemented through LABVIEW, tracked a repeating trapezoidal position command signal. Details concerning the trajectories tested and measurements are given in Table 4.

Figure 4(*a*) shows the measured mass flow rates for the cylinder in the upright position, moving at 200 mm/s and having a nominal supply pressure of 340 kPa (50 psi (gauge)). The relationship between the flow rates is apparent. The constant mass assumption predicts that the flow rate data will fall on a line having a slope of −1. The best-fit line for these data, forced to pass through the origin, has a slope of −0.9359 and an R^2 value of 0.9546, validating the constant mass assumption. While the loops at either end of Fig. 4(*b*) are a visually salient deviation from the constant mass assumption, they do not represent a significant portion of the data.

Table 4 Experimental trajectory properties

Trajectory	Trapezoidal command position, repeating
Stroke	25–275 mm (250 mm total)
Command velocity	Variable, from 20 mm/s to 1200 mm/s
Command acceleration	Infinite ($d^2x/dt^2=\infty$)
Dwell time	0.5 s
Sampling frequency	~100 Hz
Number of samples	5 complete cycles, including dwell

Rather, they are associated with the transient spike in the air flow at the beginning of each cycle, occurring concurrently with the acceleration of the cylinder.

Table 5 lists the slope of the best-fit lines for the experiments conducted, and Table 6 lists the R^2 values. Figures 5 and 6 chart these data. While agreement with the constant mass assumption is good, the general trend is that the error increases as a function of velocity. Equation (21) predicts this trend, as it contains an error term proportional to velocity. Also contributing to the error is the acceleration of the cylinder. As the command velocity increases, a larger fraction of the duty cycle occurs with the cylinder under acceleration, violating the preconditions set for the constant mass assumption.

The constant mass assumption can remain valid even when the cylinder undergoes stick-slip motion, characterized by short periods of rapid motion with longer periods in which friction prevents motion. Stick-slip is a common phenomenon in compliant systems with friction at low command velocities. In Fig. 7(*a*) the experimental system is observed to undergo stick-slip behavior on retraction; Fig. 7(*b*) shows the constant mass assumption remaining

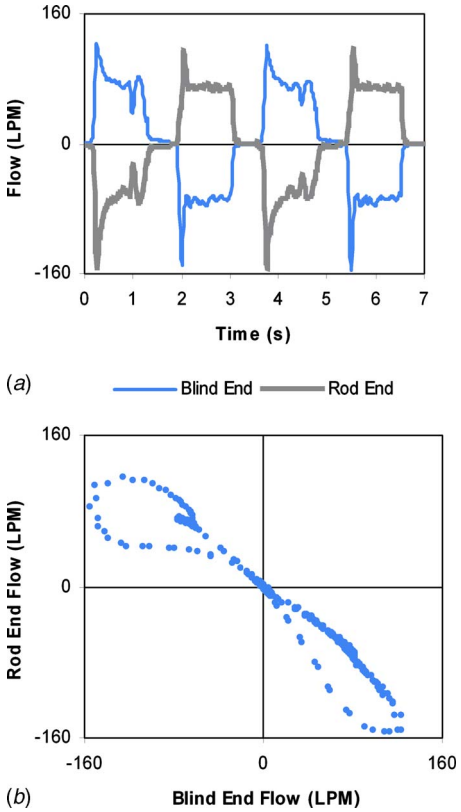

Fig. 4 Typical measured mass flow rates, 200 mm/s command velocity, 340 kPa, and rod end up. (*a*) Flow versus time and (*b*) flow versus flow.

Table 5 Slope of best-fit line, flow from rod end versus flow from blind end of cylinder

Commandvelocity (mm/s)	170 kPa, rod end up	170 kPa, rod end down	340 kPa, rod end up	340 kPa, rod end down	520 kPa, rod end up	520 kPa, rod end down
20	−0.8857	−0.8992	−0.9686	−0.9996	−0.9452	−1.0178
50	−0.9312	−0.9506	−0.9976	−1.0117	−1.0082	−1.0172
100	−0.9397	−0.9431	−0.9791	−0.9880	−0.9942	−1.0063
200	−0.9013	−0.9108	−0.9359	−0.9501	−0.9572	−0.9795
300	N/A[a]	N/A[a]	−0.9076	−0.9233	−0.9338	−0.9443
400	−0.8733	−0.8824	−0.8928	−0.8976	−0.9164	−0.9081
800	−0.8564	−0.8770	N/A[b]	N/A[b]	N/A[b]	N/A[b]
1200	−0.8561	−0.8764	N/A[b]	N/A[b]	N/A[b]	N/A[b]

[a]No data collected.
[b]Flow sensors saturated at this combination of pressure and velocity.

valid. The validity of the constant mass assumption with stick-slip was verified repeatedly in simulation [21], as exemplified in Fig. 8.

2.4 Reduced-Order System Model. The constant mass assumption permits a reduced-order model of the pneumatic cylinder to be developed using position, x, velocity, $\dot{x}$, and the cylinder's equilibrium position, x_{eq}, as state variables. In a pneumatic cylinder, equilibrium is established when forces on opposite sides of the piston face are balanced, $P_1A_1=P_2A_2$. Following the discussion concerning Eq. (21), error from ignoring the effects of atmospheric pressure acting over the piston rod has been ignored. In a mass-based system representation of a closed cylinder with no leakage and no stiction, static equilibrium is established at

$$x_{eq} = \frac{m_1(L + x_{T,2}) - m_2 x_{T,1}}{m_1 + m_2} \tag{24}$$

The time derivative of Eq. (24) yields

$$\dot{x}_{eq} = (L + x_{T,1} + x_{T,2})\left(\frac{\dot{m}_1 m_2 - \dot{m}_2 m_1}{(m_1 + m_2)^2}\right) \tag{25}$$

For a constant-velocity motion of the cylinder in which the limits of travel are not reached, the constant mass assumption, stated in Eqs. (22) and (23), simplifies Eq. (25) to

$$\dot{x}_{eq} = (L + x_{T,1} + x_{T,2})\frac{\dot{m}_1}{m} \tag{26}$$

The mechanical dynamics of Eq. (14) may also be expressed as a function of displacement away from equilibrium,

$$\ddot{x} = \frac{1}{M}(Mg - \tilde{k}_{cyl}(x - x_{eq}) - b\dot{x} - P_{atm}A_{rod} - F_{fric}) \tag{27}$$

where $\tilde{k}_{cyl}$ is the nonlinear spring stiffness of the gas in both chambers of the cylinder. This stiffness may be expressed in terms of the equilibrium position and is derived in Appendix B. For small displacements about equilibria not near the limits of travel,

$$\tilde{k}_{cyl} \cong \left(\frac{P_1A_1}{x_{eq} + x_{T,1}} + \frac{P_2A_2}{L - x_{eq} + x_{T,2}}\right) \tag{28}$$

Table 7 summarizes the state equations for the three models of a pneumatic cylinder presented in this paper.

For the purposes of simulation, the reduced-order model does not provide a significant advantage in computational speed, and

Table 6 R^2 values, flow from rod end versus flow from blind end of cylinder

Command velocity (mm/s)	170 kPa, rod end up	170 kPa, rod end down	340 kPa, rod end up	340 kPa, rod end down	520 kPa, rod end up	520 kPa, rod end down
20	0.9465	0.9468	0.9710	0.9644	0.9838	0.9776
50	0.9289	0.9224	0.9674	0.9678	0.9808	0.9784
100	0.9374	0.9201	0.9696	0.9635	0.9784	0.9746
200	0.9215	0.9139	0.9546	0.9486	0.9689	0.9679
300	N/A[a]	N/A[a]	0.9409	0.9392	0.9612	0.9473
400	0.9056	0.9013	0.9315	0.9300	0.9412	0.9334
800	0.9088	0.8754	N/A[b]	N/A[b]	N/A[b]	N/A[b]
1200	0.8927	0.8539	N/A[b]	N/A[b]	N/A[b]	N/A[b]

[a]No data collected.
[b]Flow sensors saturated at this combination of pressure and velocity.

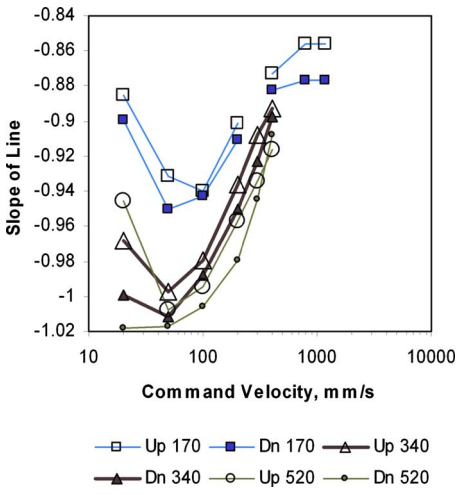

Fig. 5 Slope of best-fit line through flow data

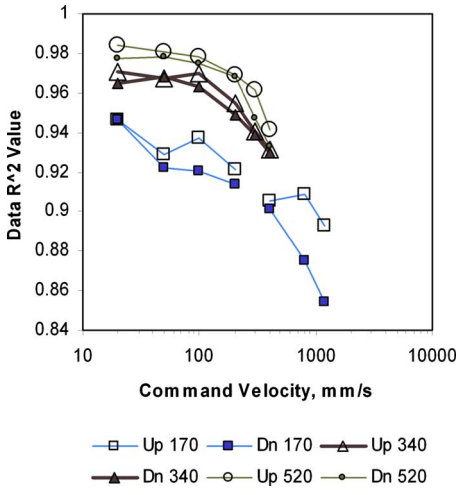

Fig. 6 Goodness of fit (R^2) of best-fit line through flow data

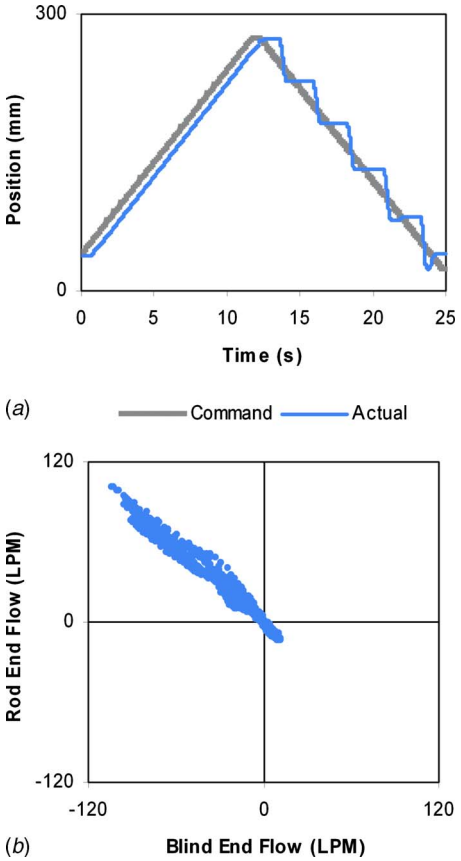

Fig. 7 Mass flow rates under stick-slip, 20 mm/s command velocity, 520 kPa, and rod end up. (*a*) Position versus time and (*b*) flow versus flow.

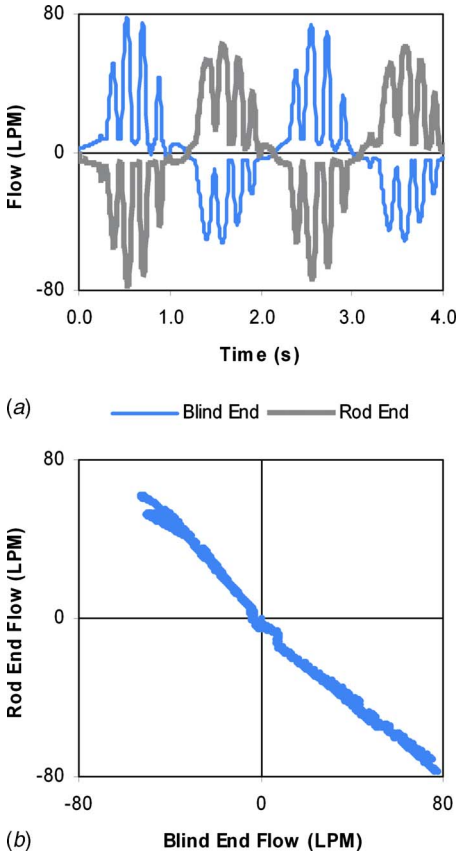

Fig. 8 Simulated mass flow rates under stick-slip, 152 mm/s peak command velocity, and 340 kPa supply. (*a*) Flow versus time and (*b*) flow versus flow.

the simplifying assumptions cause it to lose fidelity. Where the reduced-order model is beneficial is in the control of a servopneumatic system. Adaptive controllers use an internal model of the plant to update controller gains. The lower-order model lowers the computational time needed in the controller loop. Previous works also found that lower-order models can provide better results than higher-order models due to the destabilizing effects of uncertainties in the higher-order models [27]. Similarly, advanced disturbance rejection control (ADRC) can also benefit from a lower-order system model. ADRC does not model the system under control but does require knowledge of the order of the model to be able to effectively treat unmodeled dynamics as disturbances to the system [28]. The lower-order model is less restrictive to the ADRC, as it needs less information from the system during operation.

3 Conclusions

Conventional state representation of a pneumatic cylinder uses four variables—position, velocity, and two pressures—to model the system. A model replacing pressure with the mass of gas in each chamber has been developed. It provides a more direct conceptual link between the command signal to the servovalve and the dynamics of the cylinder. Consideration of mass flow leads to the constant mass assumption, which states that for a pneumatic cylinder under servo control, the instantaneous mass flow rate going into one chamber of the cylinder is equal to that going out of the other. It implies the sum of the masses of gas in both chambers is constant. The underlying assumptions to the constant mass assumption are that the cylinder moves at a constant velocity without external loads or friction and does not reach either limit of travel. The constant mass assumption was verified by both simulation and experimentation.

Table 7 State equations for pneumatic cylinder models

Conventional model $(x,\dot{x},P_1,P_2)$	
$\dot{P}_1=\frac{\gamma RT}{A_1x+V_{X,1}}\dot{m}_1-\frac{\gamma P_1A_1}{A_1x+V_{X,1}}\dot{x}$	(2)
$\dot{P}_2=\frac{\gamma RT}{A_2(L-x)+V_{X,2}}\dot{m}_2+\frac{\gamma P_2A_2}{A_2(L-x)+V_{X,2}}\dot{x}$	(3)
$\ddot{x}=\frac{1}{M}(Mg+P_1A_1-P_2A_2-P_{\text{atm}}A_{\text{rod}}-b\dot{x}-F_{\text{fric}})$	(4)
$(\dot{m}_1,\dot{m}_2)=f(\text{valve})$	(7)–(11)
Mass-based model $(x,\dot{x},m_1,m_2)$	
$\ddot{x}=\frac{1}{M}\left(Mg+\frac{m_1RT}{x+x_{T,1}}-\frac{m_2RT}{(L-x)+x_{T,2}}-P_{\text{atm}}A_{\text{rod}}-b\dot{x}-F_{\text{fric}}\right)$	(14)
$(\dot{m}_1,\dot{m}_2)=f(\text{valve})$	(7)–(11)
Reduced-order model $(x,\dot{x},x_{\text{eq}})$	
$\ddot{x}=\frac{\tilde{k}_{\text{cyl}}(x_{\text{eq}}-x)}{M}+\frac{1}{M}(Mg-b\dot{x}-P_{\text{atm}}A_{\text{rod}}-F_{\text{fric}})$	(29)
$\dot{x}_{\text{eq}}=(L+x_{T,1}+x_{T,2})\frac{\dot{m}_1}{m}$	(26)
$\dot{m}_1=f(\text{valve})$	(7)–(11)

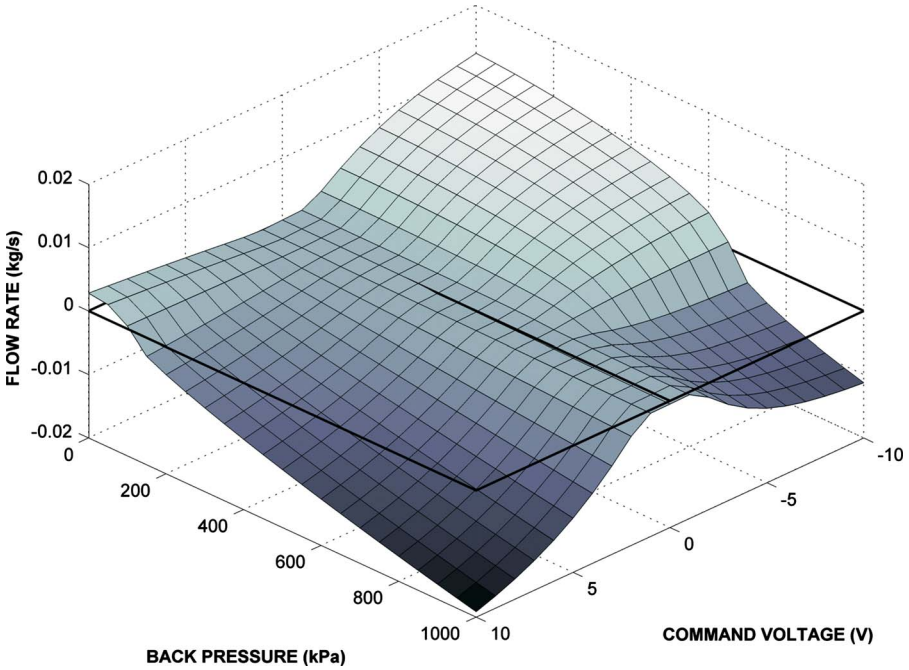

Fig. 9 Mass flow rate $\dot{m}_1$ to the blind end of the cylinder as a function of the command voltage and cylinder pressure, supply pressure=660 kPa

The constant mass assumption permits a reduced-order state model of the system, in which the mass flow rate input acts on the cylinder's equilibrium position, with classical mechanics describing the cylinder's position and velocity. This model is beneficial for control methodologies such as advanced disturbance rejection control which require knowledge of the order of the system being controlled.

A recommended area for future research is in the design of a pneumatic servovalve. The present paradigm seeks a spool valve position as a linear function of the command voltage. The valve used in this study has its own feedback controller to obtain this behavior. The weakness of this paradigm is that it results in nonlinear flow behavior, exemplified in Fig. 9. This shows the flow rate into one chamber of the cylinder as a function of both the static command voltage and the back pressure in the cylinder. An improved design paradigm for a pneumatic servovalve is to have the mass flow rate be proportional to the command voltage, thus removing a significant nonlinearity from the servopneumatic system.

Acknowledgment

The authors wish to acknowledge the Nestlé R&D Center, Inc., in Marysville, OH, for their support of this project.

Nomenclature

A = area
b = coefficient of viscous damping
C_D = discharge coefficient
c_p, c_V = specific heats
C_V = flow coefficient
d = diameter
E = energy
F = force
F_{dyn} = Coulomb friction
F_{stat} = static friction (stiction)
k = stiffness or gain
L = stroke length
M = combined mass of payload, piston, and rod
m = gas mass
P = pressure
Q_{SCFM} = volumetric flow rate, SCFM
R = gas constant
T = temperature
V = volume
X = pressure drop ratio
x = cylinder position
γ = ratio of specific heats
ρ = density

Subscripts

1 = cylinder blind end
2 = cylinder rod end
air = air
atm = atmosphere
crit = critical
cyl = cylinder
dn = downstream
eq = equilibrium
fric = friction
rod = cylinder rod
S = supply
spring = spring
T = equivalent with tubing
up = upstream
valve = valve
X = excess

Appendix A

The state equation for a gas, also known as the ideal gas law,

$$P = \rho RT \tag{A1}$$

The internal energy contained in a homogenous volume of gas,

$$E = c_V \rho VT \tag{A2}$$

In an adiabatic process, the time rate of change in the internal energy is equal to the rate of energy added to the control volume by the incoming gas flow, less the rate of work the control volume performs on the cylinder piston,

$$\frac{d}{dt}(c_V \rho V T) = \dot{m} c_P T - P\dot{V} \tag{A3}$$

Applying Eq. (A1) to Eq. (A3),

$$\frac{d}{dt}\left(\frac{c_V}{R} PV\right) + P\dot{V} = \dot{m} c_P T \tag{A4}$$

The universal gas constant R, the specific heats of a gas, c_P and c_V, and the ratio of specific heats, γ, are related,

$$R \equiv c_P - c_V \tag{A5}$$

$$\gamma \equiv \frac{c_P}{c_V} \tag{A6}$$

For air, $\gamma = 1.4$. Expanding Eq. (A4), with substitution of Eqs. (A5) and (A6),

$$\dot{P} = \frac{\gamma RT}{V}\dot{m} - \frac{\gamma P}{V}\dot{V} \tag{A7}$$

Equation (A7) is the general form of the pressure dynamics of a volume of gas. Applied to either chamber of the pneumatic cylinder,

$$\dot{P}_1 = \frac{\gamma RT}{A_1 x + V_{X,1}}\dot{m}_1 - \frac{\gamma P_1 A_1}{A_1 x + V_{X,1}}\dot{x} \tag{A8}$$

$$\dot{P}_2 = \frac{\gamma RT}{A_2(L-x) + V_{X,2}}\dot{m}_2 + \frac{\gamma P_2 A_2}{A_2(L-x) + V_{X,2}}\dot{x} \tag{A9}$$

where $V_{X,1}$ and $V_{X,2}$ are the excess volumes of gas in either end of the cylinder and in the plumbing between the cylinder and the valve.

Appendix B

Assuming adiabatic compression and expansion of the gas in the cylinder, the initial (equilibrium) energy is equal to the displaced internal energy state of the gas plus the potential energy stored in the compressed gas,

$$E_{eq} = E_{air} + E_{spring} \tag{B1}$$

The initial energy of the gas in the blind end is

$$E_{eq,1} = c_V m_1 T \tag{B2}$$

Applying the relationships between the specific energies of a gas and its gas constant,

$$E_{eq,1} = \frac{P_1(A_1 x_{eq} + V_{X,1})}{\gamma - 1} \tag{B3}$$

When the cylinder is displaced from equilibrium, the energy state of the gas changes,

$$E_{air,1} = \frac{(P_1 + \Delta P_1)(A_1(x_{eq} + \Delta x) + V_{X,1})}{\gamma - 1} \tag{B4}$$

The potential energy stored by the gas in the blind end, acting as a spring, is given by

$$E_{spring,1} = \tfrac{1}{2}\tilde{k}_1 \Delta x^2 \tag{B5}$$

where $\tilde{k}_1$ is the effective nonlinear spring rate for the blind end, defined as the change in force per unit displacement.

$$\tilde{k}_1 = \frac{-\Delta F}{\Delta x} = \frac{-\Delta P_1 A_1}{\Delta x} \tag{B6}$$

Combining Eqs. (B1) and (B3)–(B5),

$$\frac{P_1(A_1 x_{eq} + V_{X,1})}{\gamma - 1} = \frac{(P_1 + \Delta P_1)(A_1(x_{eq} + \Delta x) + V_{X,1})}{\gamma - 1} + \frac{1}{2}\tilde{k}_1 \Delta x^2 \tag{B7}$$

Multiplying by $(\gamma - 1/\Delta x)$ and eliminating like terms,

$$0 = P_1 A_1 + \left(\frac{\Delta P_1 A_1}{\Delta x}\right) x_{eq} + \left(\frac{\Delta P_1 A_1}{\Delta x}\right)\Delta x + \left(\frac{\Delta P_1 A_1}{\Delta x}\right)\frac{V_{X,1}}{A_1} + \frac{\gamma - 1}{2}\tilde{k}_1 \Delta x \tag{B8}$$

After substitution of Eq. (B6),

$$P_1 A_1 = \tilde{k}_1\left(x_{eq} + x_{T,1} - \Delta x\left(\frac{\gamma - 3}{2}\right)\right) \tag{B9}$$

Substituting Eqs. (12) and (15) into Eq. (B9),

$$\tilde{k}_1 = \frac{m_1 RT}{(x_{eq} + x_{T,1})\left(x_{eq} + x_{T,1} - \frac{\gamma - 3}{2}\Delta x\right)} \tag{B10}$$

A similar analysis may be performed on the rod end of the cylinder. In this case, the deflection is $-\Delta x$ as it acts in the opposite direction on chamber 2 than on chamber 1,

$$\tilde{k}_2 = \frac{-\Delta F}{-\Delta x} = \frac{-\Delta P_2 A_2}{-\Delta x} \tag{B11}$$

$$\frac{P_2(A_2(L - x_{eq}) + V_{X,2})}{\gamma - 1} = \frac{(P_2 + \Delta P_2)(A_2(L - x_{eq} - \Delta x) + V_{X,2})}{\gamma - 1} + \frac{1}{2}\tilde{k}_2 \Delta x^2 \tag{B12}$$

$$0 = -P_2 A_2 + \left(\frac{\Delta P_2 A_2}{\Delta x}\right)(L - x_{eq}) - \left(\frac{\Delta P_2 A_2}{\Delta x}\right)\Delta x + \left(\frac{\Delta P_2 A_2}{\Delta x}\right)\frac{V_{X,2}}{A_2} + \frac{\gamma - 1}{2}\tilde{k}_2 \Delta x \tag{B13}$$

$$P_2 A_2 = \tilde{k}_2\left(L - x_{eq} + x_{T,2} + \Delta x\left(\frac{\gamma - 3}{2}\right)\right) \tag{B14}$$

$$\tilde{k}_2 = \frac{m_2 RT}{((L - x_{eq}) + x_{T,2})\left((L - x_{eq}) + x_{T,2} + \frac{\gamma - 3}{2}\Delta x\right)} \tag{B15}$$

The total stiffness of the pneumatic cylinder is the sum of the stiffness of both chambers,

$$\tilde{k}_{cyl} = \tilde{k}_1 + \tilde{k}_2 = RT\left(\frac{m_1}{(x_{eq} + x_{T,1})\left(x_{eq} + x_{T,1} - \frac{\gamma - 3}{2}\Delta x\right)} + \frac{m_2}{\left((L - x_{eq}) + x_{T,2}\right)\left((L - x_{eq}) + x_{T,2} + \frac{\gamma - 3}{2}\Delta x\right)}\right) \tag{B16}$$

Equation (B16) shows that the stiffness of the pneumatic cylinder is highly dependent not only on the position of the cylinder, x, but also on the displacement away from equilibrium Δx. When the cylinder's equilibrium position is not near the limits of travel, small displacements in Eq. (B16) may be neglected,

$$\tilde{k}_{\text{cyl}} \cong RT\left(\frac{m_1}{(x_{\text{eq}}+x_{T,1})^2}+\frac{m_2}{((L-x_{\text{eq}})+x_{T,2})^2}\right) \tag{B17}$$

Equations (12) and (13) may be substituted into Eq. (B17) to express stiffness in terms of cylinder pressures,

$$\tilde{k}_{\text{cyl}} \cong \frac{P_1A_1}{(x_{\text{eq}}+x_{T,1})}+\frac{P_2A_2}{((L-x_{\text{eq}})+x_{T,2})} \tag{B18}$$

References

[1] Bobrow, J. E., and Jabbari, F., 1991, "Adaptive Pneumatic Force Actuation and Position Control," ASME J. Dyn. Syst., Meas., Control, **113**, pp. 267–272.

[2] Richardson, R., Plummer, A. R., and Brown, M. D., 2001, "Self-Tuning Control of a Low-Friction Pneumatic Actuator Under the Influence of Gravity," IEEE Trans. Control Syst. Technol., **9**(2), pp. 330–334.

[3] Moore, P. R., and Pu, J. S., 1996, "Pneumatic Servo Actuator Technology," IEE Colloq. on Actuator Technology: Current Practice and New Developments **110**, pp. 3/1–3/6.

[4] Shih, M., and Ma, M.-A., 1998, "Position Control of a Pneumatic Cylinder Using Fuzzy PWM Control Method," Mechatronics, **8**, pp. 241–253.

[5] Richer, E., and Hurmuzlu, Y., 2000, "A High Performance Pneumatic Force Actuator System: Part II-Nonlinear Controller Design," ASME J. Dyn. Syst., Meas., Control, **122**, pp. 426–434.

[6] McDonell, B. W., and Bobrow, J. E., 1993, "Adaptive Tracking Control of an Air Powered Robot Actuator," ASME J. Dyn. Syst., Meas., Control, **115**, pp. 427–433.

[7] Gross, D. C., and Rattan, K. S., 1998, "An Adaptive Multilayer Neural Network for Trajectory Control of a Pneumatic Cylinder," IEEE International Conference on Systems, Man, and Cybernetics, San Diego, CA, Vol. 2, pp. 1662–1667.

[8] Barth, E. J., Zhang, J., and Goldfarb, M., 2003, "Control Design for Relative Staility in a PWM-Controlled Pneumatic System," ASME J. Dyn. Syst., Meas., Control, **125**(3), pp. 504–508.

[9] Shih, M.-C., and Ma, M.-A., 1998, "Position Control of a Pneumatic Cylinder Using PWM Control Method," Mechatronics, **8**, pp. 241–253.

[10] Shearer, J. L., 1956, "Study of Pneumatic Processes in the Continuous Control of Motion With Compressed Air–I," Trans. ASME, **78**, pp. 233–242.

[11] Shearer, J. L., 1956, "Study of Pneumatic Processes in the Continuous Control of Motion With Compressed Air–II," Trans. ASME, **78**, pp. 243–249.

[12] Liu, S., and Bobrow, J. E., 1988, "An Analysis of a Pneumatic Servo System and Its Application to a Computer-Controlled Robot," ASME J. Dyn. Syst., Meas., Control, **110**, pp. 228–235.

[13] Kunt, C., and Singh, R., 1990, "A Linear Time Varying Model for On-Off Valve Controlled Pneumatic Actuators," ASME J. Dyn. Syst., Meas., Control, **112**, pp. 740–747.

[14] Hamiti, K., Voda-Besançon, A., and Roux-Boisson, H., 1996, "Position Control of a Pneumatic Cylinder Under the Influence of Stiction," Control Eng. Pract., **4**(8), pp. 1079–1088.

[15] Richer, E., and Hurmuzlu, Y., 2000, "A High Performance Pneumatic Force Actuator System: Part I—Nonlinear Mathematical Model," ASME J. Dyn. Syst., Meas., Control, **122**, pp. 416–425.

[16] Kawakami, Y., Akao, J., Kawai, S., and Machiyama, T., 1988, "Some Considerations on the Dynamic Characteristics of Pneumatic Cylinders," J. Fluid Control, **19**(2), pp. 22–36.

[17] Bigras, P., 2005, "Sliding-Mode Observer as a Time-Variant Estimator for Control of Pneumatic Systems," ASME J. Dyn. Syst., Meas., Control, **127**, pp. 499–502.

[18] Caldwell, D. G., Badihi, T. D., and Medrano-Cerda, G. A., 1998, "Pneumatic Muscle Actuator Technology a Light Weight Power System for a Humanoid Robot," IEEE International Conference on Robotics and Automation," Leuven, Belgium, Vol. 4, pp. 3053–3058.

[19] McDonell, B. W., and Bobrow, J. E., 1998, "Modeling, Identification, and Control of a Pneumatically Actuated Robot," IEEE Trans. Rob. Autom., **14**(5), pp. 124–129.

[20] Harrison, R., Weston, R. H., Moore, P. R., and Thatcher, T. W., 1987, "A Study of Application Areas for Modular Robots," Robotica, **5**, pp. 217–221.

[21] Thomas, M. B., 2003, "Advanced Servo Control of a Pneumatic Actuator," Ph.D. thesis, Ohio State University, Columbus, OH.

[22] Pu, J. S., and Weston, R. H., 1990, "Steady State Analysis of Pneumatic Servo Drives," Proc. Inst. Mech. Eng., Part C: J. Mech. Eng. Sci., **204**, pp. 377–387.

[23] Backé, W., and Ohligschläger, O., 1989, "A Model of Heat Transfer in Pneumatic Chambers," J. Fluid Control, **20**, pp. 61–78.

[24] Andersen, B. W., 1976, *The Analysis and Design of Pneumatic Systems*, Robert E. Kreiger, New York.

[25] Hong, I. T., and Tessmann, R. K., 1996, "The Dynamic Analysis of Pneumatic Systems Using HyPneu," International Fluid Power Exposition and Technical Conference, Chicago, IL.

[26] Thomas, J. H., 2000, "Proper Valve Size Helps Determine Flow," Control Engineering Online, http://www.manufacturing.net/ctl/article/CA188679

[27] Bobrow, J. E., and Jabbari, F., 1991, "Adaptive Pneumatic Force Actuation and Position Control," ASME J. Dyn. Syst., Meas., Control, **113**, pp. 267–272.

[28] Gao, Z., 2006, "Active Disturbance Rejection Control: A Paradigm Shift in Feedback Control Design," *Proceedings of the American Control Conference*, Minneapolis, MN, pp. 2399–2405.

Dynamic Model and Numerical Simulation for Synchronal Rotary Compressor

Hui Zhou
e-mail: zhouhui1125@gmail.com

Zongchang Qu

Hua Yang

Bingfeng Yu

Institute of Compressor,
Xi'an Jiaotong University,
Xi'an 710049, China

The synchronal rotary compressor (SRC) has been developed to resolve high friction and severe wear that usually occur in conventional rotary compressors due to the high relative velocity between the key tribo-pairs. In this study, the working principle and structural characteristics of the SRC are presented first. Then, the kinematic and force models are established for the key components—cylinder, sliding vane, and rotor. The velocity, acceleration, and force equations with shaft rotation angle are derived for each component. Based on the established models, numerical simulations are performed for a SRC prototype. Moreover, experiments are conducted to verify the established models. The simulated results show that the average relative velocity between the rotor and the cylinder of the present compressor decreases by 80–82% compared with that of the conventional rotary compressors with the same size and operating parameters. Moreover, the average relative velocity between the sliding contact tribo-pairs of the SRC decreases by 93–94.3% compared with that of the conventional rotary compressors. In addition, the simulated results show that the stresses on the sliding vane are greater than those on the other components. The experimental results indicate that the wear of the side surface of the sliding vane is more severe than that of the other components. Therefore, special treatments are needed for the sliding vane in order to improve its reliability. These findings confirm that the new SRC has lower frictional losses and higher mechanical efficiency for its advanced structure and working principle. [DOI: 10.1115/1.3089534]

Keywords: synchronal rotary compressor, dynamic model, motion, forces

1 Introduction

Rotary type compressors are used more widely than reciprocating compressors in refrigeration and air-conditioning systems because they have advantages such as less components, simpler structure, better dynamic equilibrium characteristics, and higher reliability. However, owing to the high relative velocity between the rotor, the cylinder, and the sliding vane of the conventional rotary compressors, the frictional loss is high and then limits their performances. Much work has been devoted to reducing the friction and wear of the conventional rotary compressors.

Jeon and Lee [1] discussed the tribological characteristics of sliding surfaces between the vane and the flange in the rotary compressor and conducted experiments to evaluate the effects of different hard coatings on the compressor performance. Suh et al. [2] and Demas and Polycarpou [3] conducted compressor tribological experiments by using a high tribometer to explore the contact conditions. Oh et al. [4] and Oh and Kim [5] investigated the friction and wear characteristics of sliding surfaces with various coatings for a rotary compressor. They conducted experiments with different working media and pressures in order to find out the best surface treatment method to improve the tribological properties. Huang and Shiau [6] described a method to improve the rotary vane compressor performance by employing extended rods on both edges of each vane and guide slots on both cover plates. In addition, Huang and Li [7] also established an optimum model and found the optimal tolerance allocation for a vane rotary compressor. Cai et al. [8] proposed a perfect profile of the vane tip for a rotary vane compressor to reduce the friction and wear of the vane. Ooi [9] predicted that a 50% reduction in mechanical loss can be achieved by employing a multivariable, direct search, constrained optimization technique. Lee and Oh [10] conducted tribological experiments under various operation conditions and proposed an optimum initial surface roughness to prolong the wear life of sliding surfaces.

The research mentioned above on reducing the friction and wear is mostly focused on surface treatment and structural optimization for rotary compressors. However, the research cannot reduce the friction and wear caused by high relative velocity between the key moving parts in the conventional rotary compressors radically. This paper develops an innovative synchronal rotary mechanism, in which the high friction and severe wear caused by high relative velocity in the conventional rotary compressors are effectively reduced by the method of the cylinder and the rotor rotating around their own axis synchronously.

Recently, we have performed the research on kinematics characteristics of the vane [11] and leakage model [12] of the SRC. However, no studies have been published on the whole system dynamic model of the SRC. The purpose of this study is to investigate the performance of the SRC by establishing the dynamic model and testing the dynamic performance.

2 Working Principle and Structural Characteristics

Figure 1 shows the working principle and structural characteristics of the proposed SRC. It can be seen from Fig. 1 that the machine's main components consist of a rotor, a cylinder, a sliding vane, a shaft, and two end covers.

The outside wall of the rotor and the inside wall of the cylinder are tangent to each other, and they form the working chamber together. The rotor is driven by the shaft, and it rotates around its center O_R at the angular velocity ω. The cylinder is driven by the connecting sliding vane, and it rotates around its own center O_C at the angular velocity ω_C. The sliding vane serves as a connector of

Contributed by the Fluids Engineering Division of ASME for publication in the JOURNAL OF FLUIDS ENGINEERING. Manuscript received October 24, 2007; final manuscript received January 9, 2009; published online March 6, 2009. Assoc. Editor: Chunill Hah.

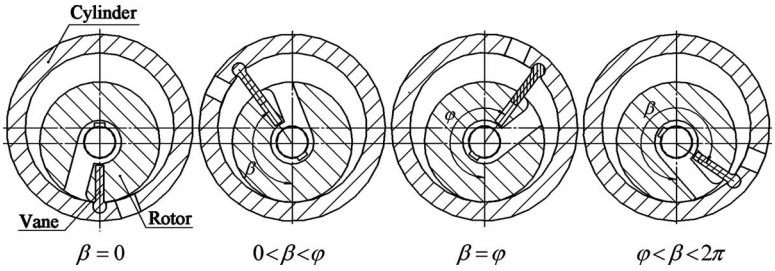

Fig. 1 Cross-section diagram of a synchronal rotary compressor

the rotor and the cylinder, and it separates the working chamber into a suction chamber and a compression chamber.

We define the starting point as the tangent point, β as the shaft rotation angle, and φ as the discharge angle. The typical stages of the working process are shown in Fig. 1. It can be seen in Fig. 1 that when $\beta=0$, the discharge stage is finished. When $0<\beta<\varphi$, the compression chamber volume decreases with the increase in β, and the gas is compressed; meanwhile, the suction chamber volume increases and the gas is sucked in. During this stage, the suction chamber volume equals the compression chamber volume when $\beta=\pi$. When $\beta=\varphi$, the discharge process starts and the gas is expelled from the compression chamber. When $\beta=2\pi$, the discharge is completed; the compression chamber closes and the suction chamber is full of fresh gas again. Thus, one operating cycle is completed.

Because the relative velocity between the sliding contact tribopairs of the SRC is much smaller than that of the conventional rotary compressors, the SRC has many advantages such as lower friction and wear, easier to achieve seals, and lower vibration and noise level.

3 Kinematic Model for the Sliding Vane and the Cylinder

3.1 Velocity and Acceleration of the Sliding Vane. The sliding vane driven by the rotor exhibits a composite planar motion. It rotates with the rotor at a uniform speed, and it reciprocates along the vane slot simultaneously. In order to analyze the kinematics characteristics of the sliding vane, a rotational coordinate system O_RXY, which rotates synchronously with the rotor, is established.

The velocity triangle of the sliding vane is shown in Fig. 2. According to the theorem of velocity composition, the absolute velocity $\boldsymbol{v}_{SG}$ of the barycenter G equals the vector sum of the convected velocity $\boldsymbol{v}_{SGe}$ and the relative velocity $\boldsymbol{v}_{SGr}$,

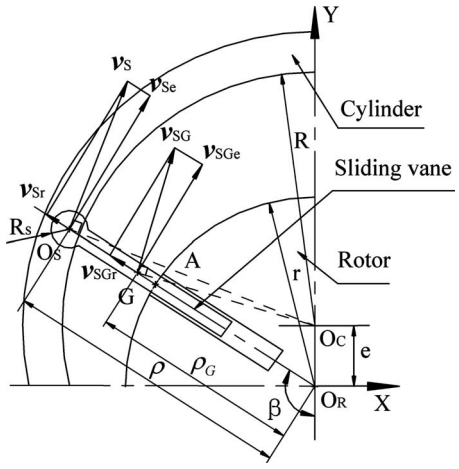

Fig. 2 Velocity triangle of the sliding vane

$$\boldsymbol{v}_{SG}=\boldsymbol{v}_{SGe}+\boldsymbol{v}_{SGr} \tag{1}$$

The displacement of the barycenter G relative to the rotor center O_R is given as

$$x=\rho-r-R_S=-e\cos\beta+\sqrt{(R+R_S)^2-e^2\sin^2\beta}-r-R_S \tag{2}$$

Therefore, the relative velocity of the barycenter G to the rotor center O_R can be expressed as

$$v_{SGr}=\dot{x}=\frac{dx}{dt}=\omega\left(e\sin\beta-\frac{e^2\sin\beta\cos\beta}{(R+R_S)^2-e^2\sin^2\beta}\right) \tag{3}$$

The convected velocity of the barycenter G is given by

$$v_{SGe}=\omega\rho_G=\omega(-e\cos\beta+\sqrt{(R+R_S)^2-e^2\sin^2\beta}-R_S-L/2) \tag{4}$$

According to the theorem of acceleration composition, the absolute acceleration $\boldsymbol{a}_{SG}$ of point G equals the vector sum of the convected acceleration $\boldsymbol{a}_{SGe}$, the relative acceleration $\boldsymbol{a}_{SGr}$, and the Coriolis acceleration $\boldsymbol{a}_{SGk}$,

$$\boldsymbol{a}_{SG}=\boldsymbol{a}_{SGe}+\boldsymbol{a}_{SGr}+\boldsymbol{a}_{SGk} \tag{5}$$

where

$$a_{SGe}=\omega^2\rho_G=\omega^2(-e\cos\beta+\sqrt{(R+R_S)^2-e^2\sin^2\beta}+R_S-L/2)$$

$$\begin{aligned}a_{SGr}&=\ddot{x}=d^2x/dt^2\\&=\omega^2e\cos\beta-\omega^2e^2\{\cos 2\beta[(R+R_S)^2-e^2\sin^2\beta]^{-0.5}\\&\quad+1/4e^2\sin^2(2\beta)[(R+R_S)^2-e^2\sin^2\beta]^{-1.5}\}\end{aligned} \tag{6}$$

$$\boldsymbol{a}_{SGk}=2\boldsymbol{\omega}\times\boldsymbol{v}_{SGr}$$

3.2 Velocity and Acceleration of the Cylinder. Unlike the conventional rotary compressors, the cylinder of the SRC is not fixed but driven by the sliding vane and rotates synchronously with the rotor around its own center. In order to analyze the kinematics characteristics of the cylinder, a rotational coordinate system O_CXY, which rotates synchronously with the cylinder, is established.

Figure 3 shows the velocity triangle of the cylinder. Because the hinge joint hole center of the cylinder coincides with the head center O_S of the sliding vane, the absolute velocity $\boldsymbol{v}_C$ for the hinge joint hole center of the cylinder equals the absolute velocity $\boldsymbol{v}_S$ for the point O_S on the sliding vane. On the basis of the above motion model of the sliding vane, the absolute velocity $\boldsymbol{v}_C$ at shaft rotation angle β can be expressed as

$$\boldsymbol{v}_C=\boldsymbol{v}_S=\boldsymbol{v}_{Se}+\boldsymbol{v}_{Sr} \tag{7}$$

where

$$v_{Se}=\omega\rho=\omega(-e\cos\beta+\sqrt{(R+R_S)^2-e^2\sin^2\beta})$$

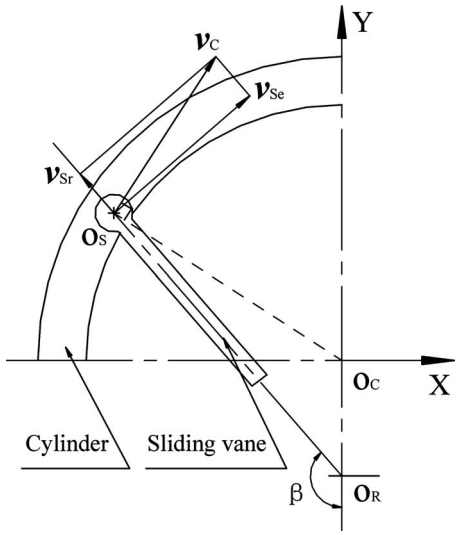

Fig. 3 Velocity triangle of the cylinder

$$v_{Sr} = \dot{x} = \frac{dx}{dt} = \omega\left(e \sin \beta - \frac{e^2 \sin \beta \cos \beta}{(R + R_S)^2 - e^2 \sin^2 \beta}\right) \tag{8}$$

Accordingly, the cylinder angular velocity ω_C and angular acceleration ε_C can be expressed as

$$\omega_C = v_C/R = \sqrt{{v_{Se}}^2 + {v_{Sr}}^2}/R$$
$$\varepsilon_C = \dot{\omega}_C = d\omega_C/dt \tag{9}$$

3.3 Kinematic Simulation and Analysis. Based on the kinematic models established above, simulations of the relative velocity between the key moving components can be performed. Figure 4 shows the comparison of average relative velocity between the rotor and the cylinder of the SRC and the conventional rotary compressors with the same design and operating parameters. In Fig. 4, it can be seen that the average relative velocity between the rotor and the cylinder of the SRC decreases by approximately 80–82% compared with that of the conventional rotary compressors. As a result, the disadvantages caused by high relative velocity between the rotor and the cylinder such as severe wear, difficulty to control the meshing clearance between the rotor and the cylinder, and difficulty to achieve seals can be overcome.

For a SRC and a rolling piston compressor (RPC), the vane and the rotor are in sliding contact and the large frictional loss exists between them. For a rotary vane compressor (RVC), the vane tips and the cylinder are in sliding contact and the large frictional loss exists between the vane tips and the cylinder. The frictional loss would decrease if the relative velocity between these sliding contact tribo-pairs could decrease effectively. Figure 5 shows the comparison of average relative velocity between the sliding contact tribo-pairs of the SRC and the conventional rotary compressors with the same design and operating parameters. It can be seen in Fig. 5 that the average relative velocity between the sliding contact tribo-pairs is 0.8 m/s for the SRC, 11.3 m/s for the RPC, and 13.6 m/s for the RVC. Thus, the average relative velocity between the sliding contact tribo-pairs of the SRC decreases by 92.8–94.1% compared with that of the conventional rotary compressors. Therefore, the disadvantages caused by high relative velocity between the sliding contact tribo-pairs such as large frictional loss and severe wear could be overcome completely.

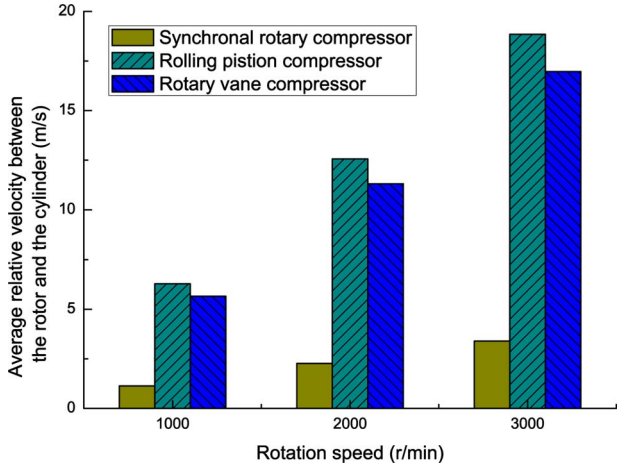

Fig. 4 Comparison of average relative velocity between the rotor and the cylinder

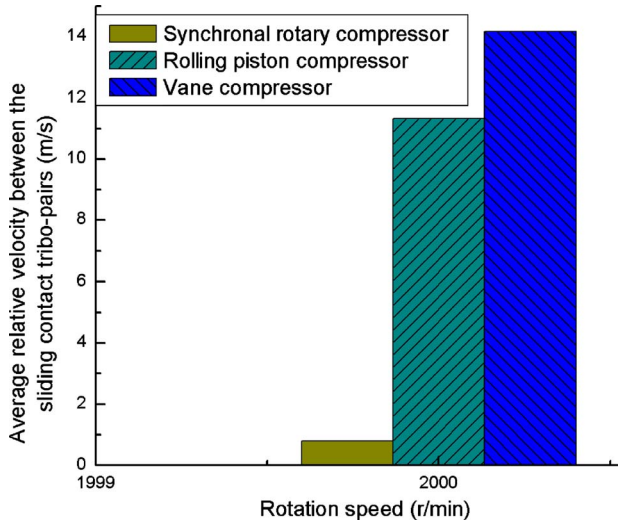

Fig. 5 Comparison of average relative velocity between the sliding contact tribo-pairs

4 Force Model for the Key Components

The force models established in this research include not only the principal forces but also the often neglected component weight and the frictional forces from the oil film. In the models, we assume the following:

(1) The pressure pulsation of the intake and discharge processes is ignored, which means that the intake and discharge pressures are regarded as constants.
(2) The effect of oil film thickness change on friction coefficient is neglected; i.e., the friction coefficient is considered constant.
(3) Gas leakage and energy loss in gas flow are ignored.

4.1 Force Model for the Cylinder.

4.1.1 Forces Acting on the Cylinder. Figure 6 shows the forces acting on the cylinder. The forces are defined to be positive when their direction is the same as the positive direction of the X or Y axis of the rotational coordinate system O_CXY. The moments are defined to be positive when they drive the cylinder to rotate in the same direction with ω.

4.1.1.1 Gas force F_{Cg} and moment M_{Cg}. The working chamber is separated into a suction chamber and a compression chamber by the sliding vane, and the gas force F_{Cg} acting on the cyl-

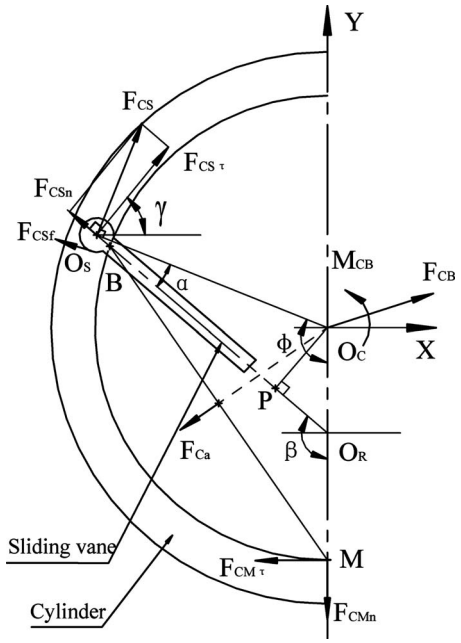

Fig. 6 Forces acting on the cylinder

inder is caused by the pressure difference in the suction chamber and the compression chamber. As shown in Fig. 3, $\angle O_R B O_C = \alpha$. The gas force is given by

$$F_{Cg} = 2HR \sin\left(\frac{\beta - \alpha}{2}\right)[P_d(\beta) - P_s(\beta)] \tag{10}$$

where $P_s(\beta)$ is the suction chamber pressure at the shaft rotation angle β, which equals the constant suction pressure P_s, and $P_d(\beta)$ is the corresponding compression chamber pressure that may be calculated by

$$P_d(\beta) = P_s \times [V/V_d(\beta)]^n \tag{11}$$

In Eq. (11), V is the total volume of the working chamber and $V_d(\beta)$ is the compression chamber volume at shaft rotation angle β.

The gas force components in X and Y directions can be given by

$$F_{Cgx} = F_{Cg} \sin(\phi/2)$$
$$F_{Cgy} = F_{Cg} \cos(\phi/2) \tag{12}$$

According to the geometrical relationship shown in Fig. 3, $O_R B = \rho'$, ϕ can be expressed as

$$\phi = \arccos\{[e - e\cos(2\beta) + 2\cos\beta(R^2 - e^2\sin^2\beta)^{1/2}]/2eR\} \tag{13}$$

The gas force crosses the center O_C of the cylinder, and thus the moment caused by gas at the center O_C is zero.

4.1.1.2 Driving force F_{CS} and moment M_{CS} from the sliding vane. The driving force on the cylinder by the sliding vane can be divided into two components, namely, the normal component F_{CSn} and the tangential component $F_{CS\tau}$, which is normal and tangential to the cylinder surface, respectively. The arms of F_{CSn} and $F_{CS\tau}$ at the cylinder center O_C are given as

$$L_{CSn} = O_C P = \pm e \sin\beta$$
$$L_{CS\tau} = O_S P = -e\cos\beta + \sqrt{(R + R_S)^2 - e^2\sin^2\beta} + e\cos\beta \tag{14}$$

When $0 \le \beta < \pi$, the sign of L_{CSn} in Eq. (14) is "+;" when $\pi \le \beta < 2\pi$, the sign of L_{CSn} is "−."

The driving moment M_{CS} to the cylinder by the sliding vane is given by

$$M_{CS} = F_{CSn} \times L_{CSn} + F_{CS\tau} \times L_{CS\tau} \tag{15}$$

F_{CSn} and $F_{CS\tau}$ can be decomposed along the X and Y directions, respectively, and the included angle of the force $F_{CS\tau}$ and the X axis is γ. The components can be obtained by

$$F_{CSnx} = F_{CSn} \times |\sin\gamma| = F_{CSn} \times \sqrt{1 - \cos^2\gamma}$$
$$F_{CSny} = F_{CSn} \times |\cos\gamma|$$
$$F_{CS\tau x} = F_{CS\tau} \times |\cos\gamma| \tag{16}$$
$$F_{CS\tau y} = F_{CS\tau} \times |\sin\gamma| = F_{CS\tau} \times \sqrt{1 - \cos^2\gamma}$$

where γ is defined as

$$\gamma = \arccos([e^2 + \rho^2 - (R + R_S)^2]/2e[-e\cos\beta + \sqrt{(R + R_S)^2 - e^2\sin^2\beta}]) \tag{17}$$

4.1.1.3 Forces from lubricating oil at the meshing point. Lubricating oil exists in the meshing clearance of the rotor and the cylinder. Because of the relative motion between the rotor and the cylinder, there are normal fluid hydrodynamic forces F_{CMn} and tangential frictional forces $F_{CM\tau}$ from the lubricating oil acting on the cylinder. F_{CMn} is transmitted to the shaft and causes moment of flexion, which can be ignored because it is much smaller than that of the other moments on the shaft.

According to the lubrication theory, the tangential frictional force $F_{CM\tau}$ and frictional moment $M_{CM\tau}$ at the meshing point can be obtained by

$$F_{CM\tau} = \frac{\mu\alpha_o r^2 H(\omega - \omega_C)}{\delta_o}$$
$$M_{CM\tau} = \frac{\mu\alpha_o r^2 RH(\omega - \omega_C)}{\delta_o} \tag{18}$$

4.1.1.4 Frictional force from the head of the sliding vane. The sliding vane rotates in the hinge joint hole of the cylinder and causes the sliding frictional force F_{CSf}, which is given by

$$F_{CSf} = f_{CS} \cdot F_{CS} = f_{CS} \cdot \sqrt{F_{CSn}^2 + F_{CS\tau}^2} \tag{19}$$

4.1.1.5 Weight G_C. The weight of the cylinder due to gravity is given as

$$G_C = m_C g \tag{20}$$

4.1.1.6 Bearing housing opposing force F_{CB}, frictional force F_{CBf}, and frictional resistance moment M_{CBf}. The gas force, the driving force by the sliding vane, the frictional forces, and the weight of the cylinder will be transferred to the cylinder bearing ultimately. Therefore, the bearing housing opposing force components in X and Y directions can be written as

$$F_{CBx} = F_{Cgx} + F_{CS\tau x} + F_{CSnx}$$
$$F_{CBy} = F_{Cgy} + F_{CS\tau y} + F_{CSny} + G_C \tag{21}$$

Thus the resultant force F_{CB} is given by

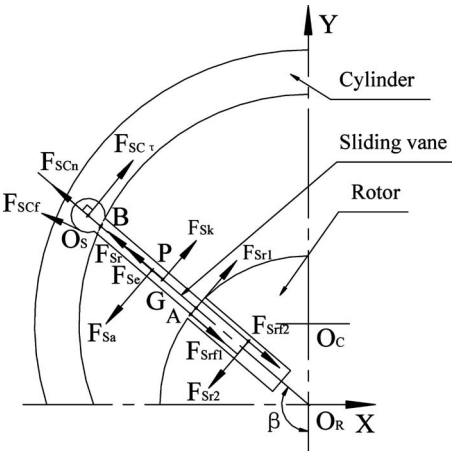

Fig. 7 Forces acting on the sliding vane

$$F_{CB} = (F_{CBx}{}^2 + F_{CBy}{}^2)^{1/2} \tag{22}$$

Accordingly, the frictional force and moment acting on the cylinder are given by

$$\begin{aligned} F_{CBf} &= f_{CB} F_{CB} \\ M_{CBf} &= F_{CBf} R_B \end{aligned} \tag{23}$$

4.1.2 Differential Equation of Rotation of the Cylinder. According to the differential equations of rotation of a rigid body with a fixed axis, the differential equation of rotation of the cylinder can be expressed as

$$J_C \varepsilon_C = \sum M_i(F) = M_{CS} + M_{CM\tau} + M_{CBf} \tag{24}$$

where J_C is the rotary inertia of the cylinder.

4.2 Force Model for the Sliding Vane. The forces acting on the sliding vane are the gas force, the contact forces and frictional forces from the vane slot, the constrained forces from the cylinder, and the inertia forces due to the vane motion, etc. Figure 7 shows all the forces acting on the sliding vane. The forces are assumed to be positive when they deviate from the rotor, and the moments are assumed to be positive when they inhibit the sliding vane rotation.

4.2.1.1 Gas force F_{Sg} . The pressure difference between the suction chamber and the compression chamber exerts gas force to the sliding vane. The gas force is given by

$$\begin{aligned} F_{Sg} &= -[P_d(\beta) - P_s(\beta)] \times l(\beta) \times H \\ &= -[P_d(\beta) - P_s(\beta)] \times (-e \cos\beta + \sqrt{R^2 - e^2 \sin^2\beta} - r) \times H \end{aligned} \tag{25}$$

Thus, the moment M_{Sg} at the head center O_S of the sliding vane by the gas force can be given as

$$M_{Sg} = F_{Sg} \cdot L_{Sg} = F_{Sg} \cdot [(\sqrt{R^2 - e^2 \sin^2\beta} - r)/2 + R_S] \tag{26}$$

4.2.1.2 Constrained force F_{SC} by the cylinder. The constrained force F_{SC} on the sliding vane by the cylinder can be divided into the normal component F_{SCn} and the tangential component $F_{SC\tau}$. F_{SCn} and $F_{SC\tau}$ are equal and opposite to the driving forces $F_{CS\tau}$ and F_{CSn} on the cylinder by the sliding vane, respectively.

4.2.1.3 Contact forces F_{SR1}, F_{SR2} and frictional forces F_{SRf1}, F_{SRf2} from the rotor. As shown in Fig. 7, F_{SR1} is the contact force caused by the vane slot up margin, and F_{SRf1} is the corresponding frictional force. F_{SR2} is the contact force acting on the sliding vane end part by the vane slot, and F_{SRf2} is the corresponding frictional force.

Both F_{SR1} and F_{SR2} are normal to the vane side surface. The moments at the head center O_S of the sliding vane caused by F_{SR1} and F_{SR2} are given by

$$\begin{aligned} M_{SR1} &= F_{SR1} \cdot L_{SR1} = F_{SR1} \cdot [-e \cos\beta + \sqrt{(R+R_S)^2 - e^2 \sin^2\beta} - r] \\ M_{SR2} &= F_{SR2} \cdot L_{SR2} = F_{SR2} \cdot (L - R_S) \end{aligned} \tag{27}$$

F_{SRf1} and F_{SRf2} act along the contact surface of the sliding vane and the vane slot, and their directions are opposite to the velocity $\boldsymbol{v}_{Sr}$. F_{SRf1} and F_{SRf2} are given by

$$\begin{aligned} F_{SRf1} &= \mp f_{SR} \cdot F_{SR1} \\ F_{SRf2} &= \mp f_{SR} \cdot F_{SR2} \end{aligned} \tag{28}$$

In Eq. (28), when $0 \le \beta < \pi$, the signs of F_{SRf1} and F_{SRf2} are "−." When $\pi \le \beta < 2\pi$ the signs are "+."

The moments at the point O_S by F_{SRf1} and F_{SRf2} can be obtained by

$$\begin{aligned} M_{SRf1} &= -F_{SRf1} \cdot b/2 \\ M_{SRf2} &= F_{SRf2} \cdot b/2 \end{aligned} \tag{29}$$

4.2.1.4 Frictional force F_{SCf} on the sliding vane head by the cylinder. This force is equal and opposite to the F_{CSf} on the cylinder.

4.2.1.5 Inertia forces and moments. The inertia forces caused by the vane motion include the convected inertial force F_{Se}, the relative inertia force F_{Sr}, and the Coriolis inertial force F_{Sk}. These inertia forces cross the barycenter of the sliding vane and can be written as

$$\begin{aligned} F_{Se} &= m_C \cdot a_{SGe} \\ F_{Sk} &= -m_C \cdot a_{SGk} \\ F_{Sr} &= -m_C \cdot a_{SGr} \end{aligned} \tag{30}$$

The corresponding moments caused by the inertia forces may be expressed as

$$\begin{aligned} M_{Se} &= 0 \\ M_{Sk} &= F_{Sk} \cdot L_{Sk} = F_{Sk} \cdot (L/2 - R_S) \\ M_{Sr} &= 0 \end{aligned} \tag{31}$$

A set of simultaneous equations including the normal and tangential force balance equations of the sliding vane, the moment balance equation for the head of the sliding vane, and the differential equation of the cylinder rotation are obtained as

$$\begin{aligned} &-F_{CSn} + F_{Se} + F_{Sr} - F_{SR1} \cdot f_{SR} - F_{SR2} \cdot f_{SR} = 0 \\ &-F_{CS\tau} + F_{Sa} + F_{Sk} + F_{SR1} - F_{SR2} = 0 \\ &F_{Sg} L_{Sg} + F_{Sk} L_{Sk} + F_{SR1} \cdot L_{SR1} \\ &\quad - F_{SR2} \cdot L_{SR2} \pm F_{SR1} \cdot f_{SR} \cdot \frac{b}{2} \mp F_{SR2} \cdot f_{SR} \cdot \frac{b}{2} = 0 \\ &F_{CSn} \times L_{CSn} + F_{CS\tau} \times L_{CS\tau} = J_C \varepsilon_C \end{aligned} \tag{32}$$

This equation set can be expressed in the following form of matrix:

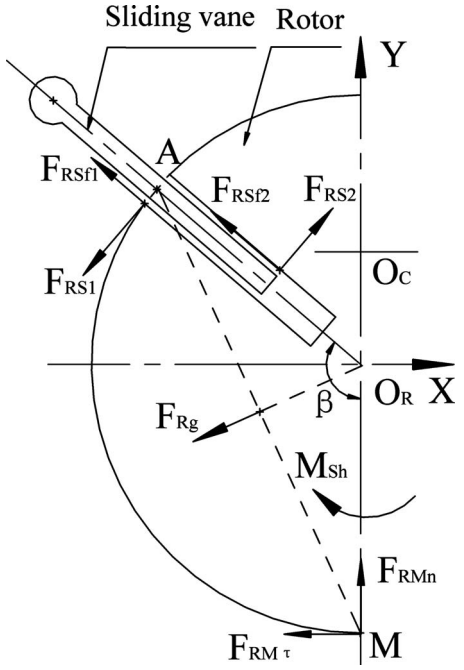

Fig. 8 Forces acting on the rotor

$$\begin{pmatrix} -1 & 0 & 1 & -1 \\ 0 & -1 & -f_{SR} & -f_{SR} \\ L_{CS\tau} & L_{CSn} & 0 & 0 \\ 0 & 0 & L_{SR1} \pm f_{SR} \cdot b/2 & -L_{SR1} \mp f_{SR} \cdot b/2 \end{pmatrix} \cdot \begin{pmatrix} F_{CS\tau} \\ F_{CSn} \\ F_{SR1} \\ F_{SR2} \end{pmatrix} = \begin{pmatrix} -F_{Sg} - F_{Sk} \\ -F_{Se} - F_{Sr} \\ J_C \varepsilon_C \\ -F_{Sg} L_{Sg} - F_{Sk} L_{Sk} \end{pmatrix} \tag{33}$$

All the four unknown forces can be obtained by solving the above matrix. Based on these four forces, all the other unknown forces acting on the cylinder and the sliding vane could be obtained.

4.3 Force Model for the Rotor. In the SRC, the rotor rotates at a uniform angular velocity ω. The forces and moments acting on the rotor are shown in Fig. 8, including the gas force, the reaction forces and frictional forces on the vane slot from the sliding vane, the frictional forces from the two end covers, the normal dynamic flow force and the tangential frictional force created by the lubricating oil at the meshing point M of the rotor and the cylinder, and the driving moment from the shaft.

4.3.1.1 Gas force F_{Rg}. The gas force acting on the rotor is caused by the pressure difference between the suction chamber and the compression chamber. The gas force F_{Rg} crosses the rotor center O_R and is given by

$$F_{Rg} = 2Hr \sin\frac{\beta}{2}[P_d(\beta) - P_s(\beta)] \tag{34}$$

The moment M_{Rg} created by the gas force is zero because the gas force crosses the center of the rotor.

4.3.1.2 Reaction forces F_{RS1}, F_{RS2} and frictional forces F_{RSf1}, F_{RSf2} from the sliding vane. These four forces acting on the rotor from the sliding vane are force couples with the corresponding F_{SR1}, F_{SR2}, F_{SRf1}, and F_{SRf2} described previously in the force model for the sliding vane.

The moments at the rotor center O_R caused by these four forces are given by

$$\begin{aligned} M_{RS1} &= F_{RS1} \cdot L_{RS1} = F_{RS1} \cdot r \\ M_{RS2} &= F_{RS2} \cdot L_{RS2} \\ &= F_{RS2} \cdot [-e \cos\beta + \sqrt{(R+R_S)^2 - e^2 \sin^2\beta} - L + R_S] \\ M_{RSf1} &= F_{RSf1} \cdot b/2 \\ M_{RSf2} &= -F_{RSf2} \cdot b/2 \end{aligned} \tag{35}$$

4.3.1.3 Frictional forces from the end covers and forces from the lubricating oil at the meshing point. There is lubricating oil in the gap between the rotor and the two cylinder end covers and in the meshing clearance of the rotor and the cylinder. The relative motion between the rotor and the cylinder causes viscous frictional forces and moments. Based on the lubrication theory, the viscous frictional force and frictional moment acting on the rotor by the oil between the rotor and the two cylinder end covers can be obtained as

$$\begin{aligned} F_{RCf} &= \frac{2\pi\mu(\omega_C - \omega)(r^4 - {r_{\text{in}}}^4)}{\delta_O(r - r_{\text{in}})} \\ M_{RCf} &= \frac{\pi\mu(\omega_C - \omega)(r^4 - {r_{\text{in}}}^4)}{\delta_O} \end{aligned} \tag{36}$$

Likely, the frictional force and moment acting on the rotor by the oil at the meshing point can be calculated by

$$\begin{aligned} F_{RM\tau} &= \frac{\mu\alpha_o r^2 H(\omega_C - \omega)}{\delta_O} \\ M_{RM\tau} &= \frac{\mu\alpha_o r^3 H(\omega_C - \omega)}{\delta_O} \end{aligned} \tag{37}$$

4.3.1.4 Resistance moment M_z. The resistance moment is composed of all the force moments acting on the rotor and is given by

$$M_z = M_{RS1} + M_{RS2} + M_{RSf1} + M_{RSf2} + M_{RCf} + M_{RM\tau} \tag{38}$$

5 Simulation Results and Discussion

Based on the established models, forces on the cylinder, the sliding vane, and the rotor can be simulated for a SRC prototype used in the experiment. We choose 1000 rpm as the rotational speed. The friction coefficient of each frictional surface depends on the material, the contact surface roughness, the lubrication, the relative velocity, etc. In this study, the friction coefficients f_{SR}, f_{CS}, and f_{CB} are set to be 0.11, 0.12, and 0.008, respectively, according to the empirical values by Oh et al. [4], Oh and Kim [5], Solzak and Polycarpou [13], and Xu et al. [14] in their tribological experiments.

5.1 Simulation Results for Forces on the Cylinder. Figure 9 shows the simulation results of the forces acting on the cylinder. From Fig. 9, it can be noted that the gas force and the bearing force are the principal forces acting on the cylinder and are much greater than the other forces. They both reach their maximum values at the shaft rotation angle of 220 deg, where the discharge process starts. In addition, the bearing loads are composed mainly of the gas force, and the other forces such as the driving force and frictional force from the sliding vane can be neglected because they are much smaller. The simulation results of the cylinder forces may be helpful to choose proper bearings for the compressor to improve the life and reliability.

5.2 Simulation Results for Forces on the Sliding Vane. Figure 10 shows the simulation results of all the forces acting on the sliding vane. The forces on the sliding vane are more complex than those on the other components, for the sliding vane serves as

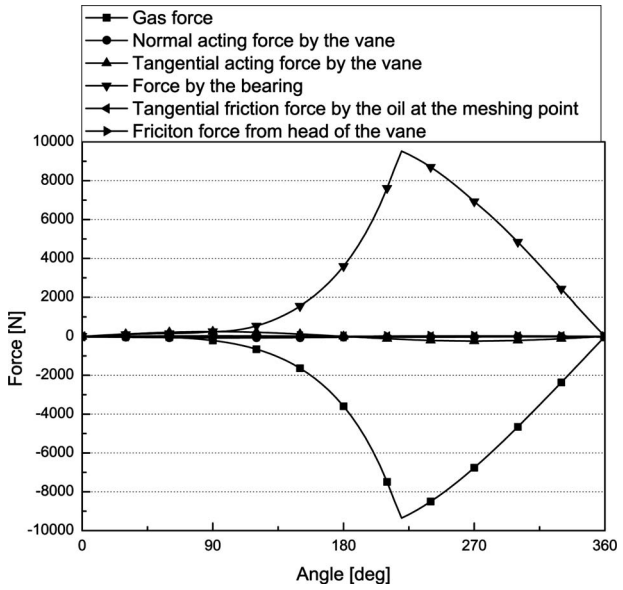

Fig. 9 Results of forces on the cylinder

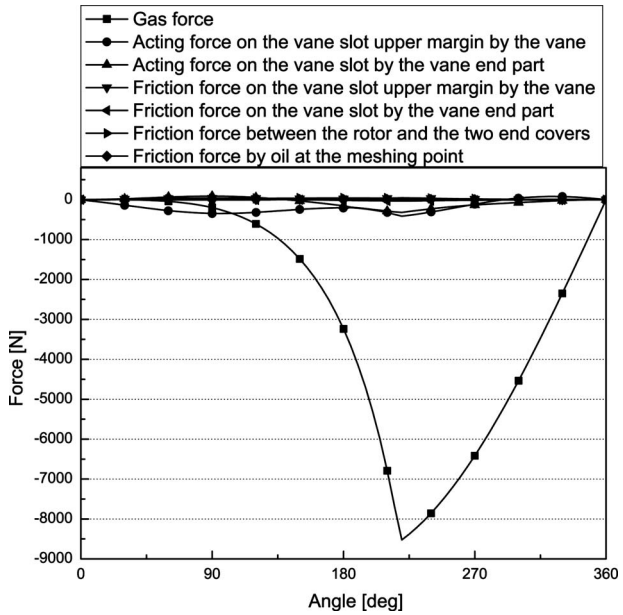

Fig. 11 Results of forces on the rotor

a connector that drives the cylinder to rotate and at the same time is driven by the rotor. In Fig. 10, it can be seen that the principal forces acting on the sliding vane are the contact forces by the vane slot, the tangential constrained forces by the cylinder, and the gas force. The other forces are relatively much smaller, varying over a range from −38 N to 79 N. Moreover, in Fig. 10, the tangential constrained force by the cylinder fluctuates from −247.9 N to 237.9 N and changes from negative to positive at the rotation angle π, which not only increases the machine vibration but also aggravates the fatigue damage of the sliding vane. It is suggested that the inertia of the cylinder should be reduced in order to mitigate the negative impacts on the sliding vane.

5.3 Simulation Results for Forces on the Rotor. Figure 11 shows the simulation results of the forces acting on the rotor. From Fig. 11, it can be noted that the gas force is the greatest in all forces, and its maximum value occurs at the shaft rotation angle of 220 deg, where the discharge process just starts. All the other forces are less than 346 N. In addition, it can be seen that the resistant moment consists mainly of the acting forces by the sliding vane, and the frictional moments are relatively smaller.

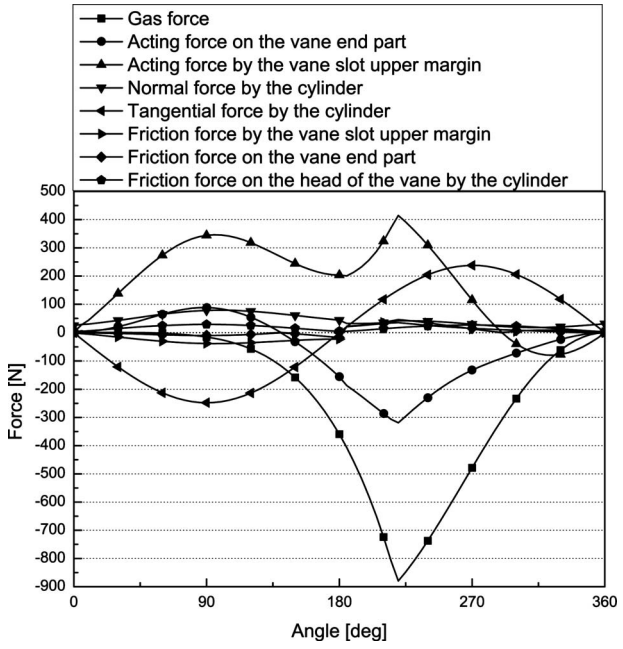

Fig. 10 Results of forces on the vane

6 Model Verification

6.1 Test Bench. In order to verify the established models and investigate the general performances of the SRC, a compressor test bench was set up. On the test bench, the general performances and the input torque of the SRC were measured. Furthermore, the investigation of sliding vane wear conditions was carried out.

Figure 12 shows the schematic of the test bench. The test bench consists of the main parts, such as a second refrigerant calorimeter, a compressor, a condenser, an electronic expansion valve (EEV), a torque meter, and a motor. The structural parameters and the operating parameters of the prototype used in the experiment are listed in Table 1.

6.2 Model Verification.

6.2.1 Indirect Verification of the Forces on the Sliding Vane. The sliding vane is one of the critical components that affect the compressor leakage and reliability directly. Because of the very

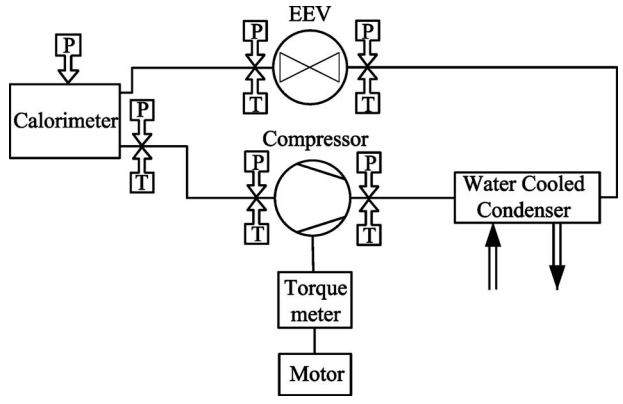

Fig. 12 Test bench

Table 1 Parameters for the SRC prototype

Structural parameters		Operating parameters	
Diameter of the cylinder (m)	0.120	Evaporating temperature (k)	273
Diameter of the rotor (m)	0.108	Suction pressure (MPa)	0.3
Height of the cylinder (m)	0.070	Discharge pressure (MPa)	1.5
Thickness of the sliding vane (m)	0.008	Subcooling (K)	7
Radial length of the sliding vane (m)	0.029	Superheat (K)	10
Eccentricity (m)	0.006	Refrigerant	R134a

complex forces on the sliding vane, a high speed composite plane motion of the sliding vane, and little space for the sensor to fit in, it is very difficult to measure the forces on the sliding vane directly. Thus, the forces on the sliding vane can be verified indirectly by investigating the friction and wear of the sliding vane used in the experiment.

Figure 13 shows the worn sliding vane after running 72 h in the compressor test bench. It can be seen that the middle part and the end part of the side face were severely worn. The simulated results of the forces on the sliding vane show that the forces on the vane side surface caused by the vane slot up margin within the rotation angle range of 90–290 deg are greater than that within the other rotation angle range. Moreover, the end part of the sliding vane is continuously under heavy stress. Therefore, it appears that the simulated results might agree well with the experimental wear results of the sliding vane.

6.2.2 Moment Verification. The established models of the SRC may be verified through measuring the torque input of the SRC. The comparison between simulated and measured results of the resistant moment is shown in Fig. 14. It can be seen from Fig. 14 that the simulated result is consistent with the measured result, which might confirm the correctness of the established models. The deviation of the average resistant moment between the experimental data and the simulated results is less than 5%. The measured torque input is smaller than the simulated resistant moment within the rotation angle range of 190–270 deg, and the former is greater than the latter within the other rotation angle range. The error between the measured torque input and the simulated resistant moment reaches the maximum value (11 N.m) at the shaft rotation angle of 220 deg, which may be caused by the buffering of the rotor and the shaft coupling.

Fig. 13 Wear of the sliding vane

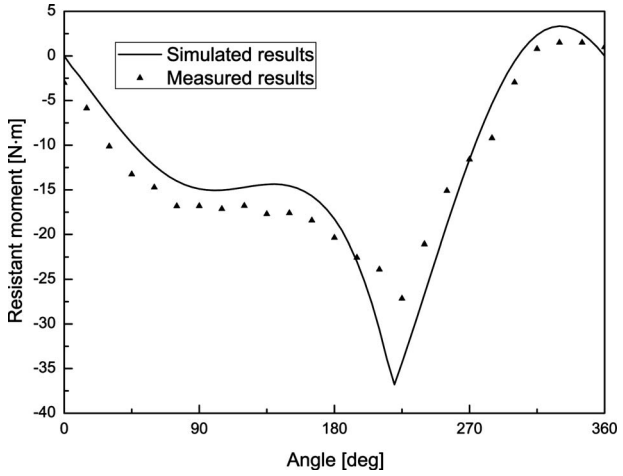

Fig. 14 Comparison between simulated and measured results

7 Conclusions

The dynamic model has been established, and numerical simulations have been conducted for a novel SRC in order to study its dynamic characteristics. Motion and stress for its components have been discussed in detail. From the research, the following conclusions could be drawn:

(a) The average relative velocity between the rotor and the cylinder of the SRC is only 18–20% of that of the conventional rotary compressors, and the average relative velocity between the sliding contact tribo-pairs of the SRC is only 5.9–7.1% of that of the conventional rotary compressors. Thus, the much lower relative velocity will contribute to resolve those problems caused by high relative velocity between the rotor and the cylinder, such as severe wear, difficulty to control the mating clearance between the rotor and the cylinder, and difficulty to achieve seals.

(b) The cylinder has an angular acceleration, which causes the output torque to fluctuate seriously. The fluctuation will increase when the shaft rotational speed rises. When the rotational speed exceeds 3000 rpm, the machine is found to operate roughly. Therefore, in order to improve the operation smoothness of the machine at a high rotational speed, the inertia moment of the cylinder is needed to decrease. Moreover, a flywheel may be useful for the SRC.

(c) The sliding vane is a key component of the SRC. The forces on the sliding vane are very complex because the sliding vane serves as a connector that drives the cylinder to rotate and at the same time is driven by the rotor. Therefore, further research should be performed to investigate the fatigue strength and structure optimization of the sliding vane based on this study. The simulated and experimental results show that there is severe wear on the vane surfaces, and then special treatments have to be applied to the sliding vane surfaces to improve the reliability of the SRC.

Acknowledgment

The authors acknowledge the National Natural Science Foundation of China (NSFC) for funding this research project as part of the Design for Fluid Mechanism Program (Grant No. 50476053).

Nomenclature

$\boldsymbol{a}_{SG}$ = absolute acceleration for point G of the sliding vane

$\boldsymbol{a}_{SGe}, \boldsymbol{a}_{SGr}, \boldsymbol{a}_{SGk}$ = convected, relative, and Coriolis acceleration for point G of the sliding vane

b = thickness of the sliding vane
e = eccentricity
f_{CB} = friction coefficient of the cylinder bearing
f_{SR} = friction coefficient between the vane and the vane slot
f_{CS} = friction coefficient between the vane and the cylinder
F_{CB}, F_{CBx}, F_{CBy} = bearing opposing force and its components
F_{CBf} = bearing frictional force
F_{Cg}, F_{Cgx}, F_{Cgy} = gas force on the cylinder and its components
F_{CMn}, $F_{CM\tau}$ = normal and tangential forces by oil at the meshing point
F_{CS}, F_{CSn}, $F_{CS\tau}$ = driving force on the cylinder by the sliding vane and the corresponding normal and tangential components
F_{CSnx}, F_{CSny} = components in X and Y directions of F_{CSn}
F_{CSf} = frictional force on the cylinder by head of the vane
$F_{CS\tau x}$, $F_{CS\tau y}$ = components in X and Y directions of $F_{CS\tau}$
F_{Sg} = gas force on the sliding vane
$F_{SC\tau}$, F_{SCn} = normal and tangential constrained force on vane by the cylinder
F_{SR1}, F_{SRf1} = contact force on the vane from the vane slot up margin and the corresponding frictional force
F_{SR2}, F_{SRf2} = contact force on the vane end part from the vane slot and the corresponding frictional force
F_{Se}, F_{Sr}, F_{Sk} = convected, relative, and Coriolis inertial force of the vane
F_{RCf} = frictional force by oil among the rotor and the cylinder end covers
$F_{RM\tau}$ = frictional force on the rotor from oil at the meshing point
F_{Rg} = gas force on the rotor
F_{RS1}, F_{RS2} = reaction forces on rotor from the sliding vane
F_{RSf1}, F_{RSf2} = frictional forces on rotor from the sliding vane
G_C = weight of the cylinder
H = height of the cylinder
J_C = cylinder rotary inertia
$l(\beta)$ = length, $l(\beta)=\rho'-R_R$
L = radial length of the vane
L_{CSn}, $L_{CS\tau}$, L_{RS1}, L_{RS2}, L_{Sg}, L_{Sk}, L_{SR1}, L_{SR2} = arms of the corresponding forces
m_C = mass of the cylinder
M_{Cg}, $M_{CM\tau}$, M_{CS}, M_{CBf} = moments on the cylinder by the corresponding forces
M_{RCf}, $M_{RM\tau}$, M_{RS1}, M_{RS2}, M_{RSf1}, M_{RSf2}, M_{Rg} = moments on the rotor created by the corresponding forces
M_{Se}, M_{Sg}, M_{Sk}, M_{Sr}, M_{SR1}, M_{SR2}, M_{SRf1}, M_{SRf2} = moments on the sliding vane created by the corresponding forces
M_z = total resistance moment
$P_s(\beta)$ = suction chamber pressure at shaft rotation angle β
$P_d(\beta)$ = compression chamber pressure at rotation angle β
r = rotor radius
r_{in} = rotor inside radius
R = cylinder radius
R_B = cylinder bearing radius
R_S = sliding vane radius
t = time
$\boldsymbol{v}_C$ = absolute velocity of the cylinder
$\boldsymbol{v}_S$, $\boldsymbol{v}_{Se}$, $\boldsymbol{v}_{Sr}$, = absolute, convected, and relative velocity for point O_S of the vane
$\boldsymbol{v}_{SG}$, $\boldsymbol{v}_{SGe}$, $\boldsymbol{v}_{SGr}$ = absolute, convected, and relative velocity for point G of the vane
V = total volume of the working chamber
$V_d(\beta)$ = compression chamber volume at rotation angle β
x = displacement
α = angle, $\alpha=\angle O_R B O_C$
α_O = bow angle of the oil film
β = shaft rotation angle
γ = included angle between of the $F_{CS\tau}$ with axis X
ϕ = angle, $\phi=\angle M O_C B$
ρ = length of $O_S O_R$
ρ' = length of $O_R B$
ρ_G = length of $O_R G$
ω = rotor angular velocity
ω_C = cylinder angular velocity
ε_C = cylinder angular acceleration
μ = kinematic viscosity of the lubricating oil
δ_O = oil film thickness

References

[1] Jeon, H-.G., and Lee, K-.S., 2007, "Friction and Wear of Lubricated Sliding Surfaces of Coated Vane and Flange in Rotary Compressor With Carbon Dioxide as a Refrigerant," Asian Pacific Conference for Fracture and Strength, pp. 1785–1788.
[2] Suh, A. Y., Patel, J. J., and Polycarpou, A. A., 2006, "Scuffing of Cast Iron and Al390-T6 Materials Used in Compressor Applications," Wear, **260**, pp. 735–744.
[3] Demas, N. G., and Polycarpou, A. A., 2006, "Tribological Investigation of Cast Iron Air-Conditioning Compressor Surfaces in CO_2 Refrigerant," Tribol. Lett., **22**, pp. 271–278.
[4] Oh, S.-D., Lee, K.-S., and Kim, J.-S., 2006, "Experimental Investigation on Friction and Wear of Coated Vane Under the Environments of Lubricants and CO_2 as a Refrigerant," Key Eng. Mater., **326–328**(II), pp. 1185–1188.
[5] Oh, S. D., and Kim, J. W., 2004, "Friction and Wear Characteristics of TiN Coated Vane for the Rotary Compressor in a R410a Refrigerant," Tribol. Trans., **48**(1), pp. 29–33.
[6] Huang, Y. M., and Shiau, C.-S., 2006, "Optimal Tolerance Allocation for a Sliding Vane Compressor," ASME J. Mech. Des., **128**, pp. 98–107.
[7] Huang, Y. M., and Li, C. L., 2005, "The Stress of Sliding Vanes in a Rotary Compressor," 2005 World Tribology Congress III, pp. 99–100.
[8] Cai, H., Li, L., and Guo, B., 2005, "Research on Tip Profile of Vane for Rotary Vane Compressor," Fluid Machinery Group-International Conference on Compressors and Their Systems, pp. 215–222.
[9] Ooi, K. T., 2005, "Design Optimization of a Rolling Piston Compressor for Refrigerators," Appl. Therm. Eng., **25**, pp. 813–829.
[10] Lee, Y.-Ze., and Oh, S.-D., 2003, "Friction and Wear of the Rotary Compressor Vane–Roller Surfaces for Several Sliding Conditions," Wear, **255**, pp. 1168–1173.
[11] Zhou, H., Qu, Z., and Feng, J., 2005, "Sliding Vane Kinetic Characteristics Analysis for a SRC," J. Shanghai Jiaotong Univ., **39**(9), pp. 982–984.
[12] Zhou, H., Qu, Z., and Yu, B., 2007, "Leakage Research in Synchronal Rotary Gas Compressor," China J. Mech. Eng., **18**(2), pp. 205–208.
[13] Solzak, T. A., and Polycarpou, A. A., 2006, "Tribology of WC/C Coatings for Use in Oil-Less Piston-Type Compressors," Surf. Coat. Technol., **201**, pp. 4260–4265.
[14] Xu, H., Cai, C., Yan, J., Wang, K., and Zhou, S., 2000, "*Machine Design Handbook 2*," China Machine Press, Beijing, China, Chap. 16, pp. 16–23.

Angelo Cervone
Postdoctoral Fellow
e-mail: angcervone@mbox.me.es.osaka-u.ac.jp

Yoshinobu Tsujimoto
Professor
e-mail: tujimoto@me.es.osaka-u.ac.jp

Engineering Science,
Osaka University,
1-3 Machikaneyama, Toyonaka,
Osaka 560-8531, Japan

Yutaka Kawata
Professor
Osaka Institute of Technology,
5-6-1 Omiya, Asahi-Ku,
Osaka 535-8505, Japan
e-mail: kawata@med.oit.ac.jp

Evaluation of the Dynamic Transfer Matrix of Cavitating Inducers by Means of a Simplified "Lumped-Parameter" Model

The paper will present an analytical model for the evaluation of the pressure and flow rate oscillations in a given axial inducer test facility. The proposed reduced order model is based on several simplifying assumptions and takes into account the facility design and the dynamic properties of the tested inducer. The model has been used for evaluating the dynamic performance of a prototype of the LE-7 engine liquid oxygen (LOX) inducer, in tests carried out under given external flow rate excitations. The main results of these calculations will be shown, including the expected oscillations under a wide range of operational conditions and the influence of facility design. Calculations showed that the only way to obtain the two linearly independent test conditions, necessary for evaluating the inducer transfer matrix, is by changing the facility suction line: Any other changes in the facility design would result ineffective. Some other important design indications provided by the analytical model will be presented in the paper. [DOI: 10.1115/1.3089535]

1 Introduction

Space rocket turbopumps are one of the most crucial components of all primary propulsion concepts powered by liquid propellant engines. Generally these pumps include an axial inducer, upstream of the centrifugal stages, in order to improve the suction performance and reduce the propellant tank pressure and weight. Severe limitations are associated with the design of high power density, dynamically stable machines capable of meeting the extremely demanding suction, pumping, and reliability requirements of space transportation systems [1].

It is well known that many of the flow instabilities acting on axial inducers are significantly influenced by the so-called "dynamic matrix," which relates the pressure and flow oscillations at the pump inlet with those at the pump outlet [2–4]. The first steps in the analytical and experimental characterizations of the dynamic matrix date back to the work of Brennen and co-worker in the 1970s [5,6]. However, more recent works have given important contributions by evaluating the previously obtained results through a careful analysis of the successive experimental and numerical data (see, for example, Refs. [7,8]).

Conventionally, the dynamics of hydraulic systems is treated in terms of "lumped-parameter models," which assume that the distributed physical effects between two measuring stations can be represented by lumped constants. This assumption is usually considered valid when the geometrical dimensions of the system are significantly shorter than the acoustic wavelength at the considered frequency. As a direct consequence of this assumption, the dynamic matrix of a generic system like an axial inducer can be written as

$$\begin{bmatrix} \hat{p}_d \\ \hat{Q}_d \end{bmatrix} = \begin{bmatrix} H_{11} & H_{12} \\ H_{21} & H_{22} \end{bmatrix} \begin{bmatrix} \hat{p}_u \\ \hat{Q}_u \end{bmatrix}$$

where $\hat{p}$ and $\hat{Q}$ are, respectively, the pressure and flow rate oscillating components, and the subscripts u and d denote, respectively, the flow conditions upstream and downstream of the considered system. As a consequence of the well known electrical analogy, the negative of the real part of H_{12} is usually denoted as the system "resistance," the negative of the imaginary part of H_{12} is referred as the system "inertance," and the negative of the imaginary part of H_{21} is the system "compliance" [9,2].

It is known that the pump resistance plays a decisive role in its unstable behavior [2]. Considering that at a frequency of 0 Hz it has the same meaning of the slope of the pump performance curve, it is easy to understand that a positive value of the resistance is directly connected to surge-mode instabilities. Furthermore, it has been shown that other flow instabilities, such as rotating cavitation, are promoted by particular combinations of values of the elements of the transfer matrix [3]. By this point of view, cavitation compliance and mass flow gain factor play a decisive role, as clearly shown by a number of analytical and experimental analyses [10,11].

Various experimental activities have also shown that, imposing a flow oscillation to the system, its behavior can turn from stable to unstable depending on the value of the frequency of imposed oscillations [9,2].

The above observations confirm the importance of obtaining a sufficiently accurate prediction of the dynamic matrix of a cavitating inducer, by both analytical and experimental means. To this purpose, the present paper will describe a simplified analytical model for the evaluation of the dynamic transfer matrix of not just the axial inducer, but the entire test facility in which it is installed. The model is based on simple preliminary assumptions (one-dimensional flow, small oscillations, incompressible fluid, and quasisteady response of the components) and can be used for predicting the expected pressure and flow rate oscillations in the facility under a given fluctuation externally imposed to the system. As a consequence, useful indications can be obtained on how to design the facility for obtaining the best experimental performance. The inducer transfer matrix, not being the main point on which the present analytical calculations are focused, is evaluated by means of a simplified theoretical-empirical model.

In the paper, the proposed model will be applied to the cavitation test facility of the Engineering Science Department at Osaka University. The test inducer used for the calculations is a model of the liquid oxygen inducer of the Japanese LE-7 rocket engine. Previous experimental activities carried out on this inducer [12]

Contributed by the Fluids Engineering Division of ASME for publication in the JOURNAL OF FLUIDS ENGINEERING. Manuscript received February 6, 2008; final manuscript received January 19, 2009; published online March 9, 2009. Assoc. Editor: Steven Ceccio.

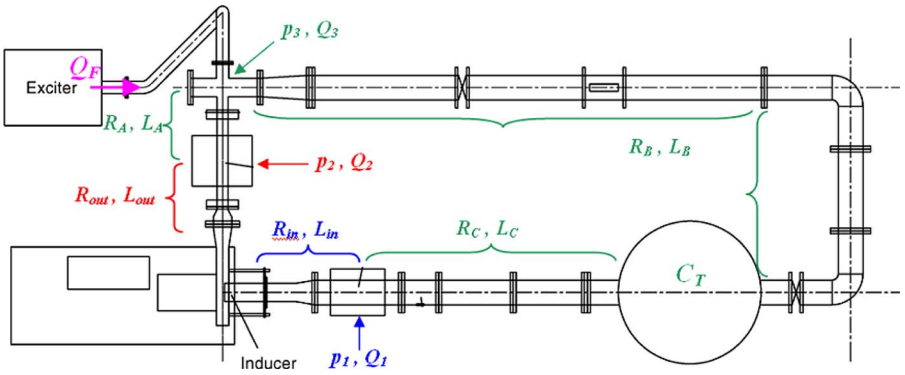

Fig. 1 Schematic of the experimental facility

have shown that several flow instabilities are promoted by the cavitating pattern on the pump. The experiments, mainly focused on the characterization of the different flow instabilities acting on the inducer and their field of existence, lead to the detection of instabilities including rotating cavitation, asymmetric blade cavitation, and higher order modes. It has also been shown that some of these instabilities can be reduced or suppressed by changing the casing geometry: Rotating cavitation and asymmetric cavitation, as an example, are strongly reduced by means of a *J*-groove on the casing.

2 Experimental Apparatus

A sketch of the cavitation facility of the Engineering Science Department at Osaka University is shown in Fig. 1. The figure also shows the main notations, which will be used in the present paper.

The actual sections where the pressure and flow rate oscillations are measured are denoted by subscripts 1 (upstream of the inducer) and 2 (downstream of the inducer). The sector of the facility included between these two points will be referred in the following as "measurement section." A given external flow rate oscillation (denoted by Q_F) is imposed just downstream of the measurement point 2, by means of a dedicated apparatus. The suction line (between tank and upstream measurement point) is denoted by subscript *C*, while the discharge line (between the fluctuator and the main tank entrance) is denoted by subscript *B*. The internal pipe diameter is 203.5 mm in the suction and discharge lines and 155.2 mm inside the measurement section. A conical expansion is installed downstream the fluctuator, while a conical contraction is present just after the measurement point 1. Two valves for the regulation of the flow rate are mounted in the discharge section.

The test inducer used for the present calculations (Fig. 2) is a model of the liquid oxygen inducer of the Japanese LE-7 rocket engine. It is a three-bladed axial inducer, with a tip radius r_T =74.9 mm and a profiled, variable-radius hub (the hub/tip radii ratio is 0.25 at the inlet and 0.51 at the outlet). The inlet tip blade angle is 7.5 deg and the tip solidity is 1.91.

3 Model Description

The proposed model is based on the following initial assumptions.

(1) The flow is assumed unsteady, quasi-one-dimensional.
(2) All oscillations are assumed to be small (only first order terms are taken into account in the equations).
(3) The working fluid is assumed incompressible and compliance is therefore considered negligible, except for regions where cavitation or air volumes are present.
(4) The response of all components of the system is assumed quasisteady. Even if it has been widely shown that this assumption is not valid in real pumps under cavitating conditions [7,8,11], it could represent a good starting point for the simplified reduced order analysis presented in this paper. As it will be shown in the following, the results and the main conclusions drawn by the analyses are not significantly affected by this assumption, especially for what concerns the design of the experiment.

Under the above assumptions, pressure and flow rate can be written in a complex form, as functions of time, as follows:

$$p(t) = \bar{p} + \hat{p} \cdot e^{i\omega t}$$

$$Q(t) = \bar{Q} + \hat{Q} \cdot e^{i\omega t}$$

where $\bar{p}$ and $\bar{Q}$ (usually real) are the pressure and flow rate steady values, $\hat{p}$ and $\hat{Q}$ (usually complex) are the pressure and flow rate oscillating components, and ω is the frequency of the oscillations.

The relevant components for the evaluation of the dynamic matrix are the oscillating ones. Under the above assumptions, the matrices of all the components of the facility can be easily evaluated as follows.

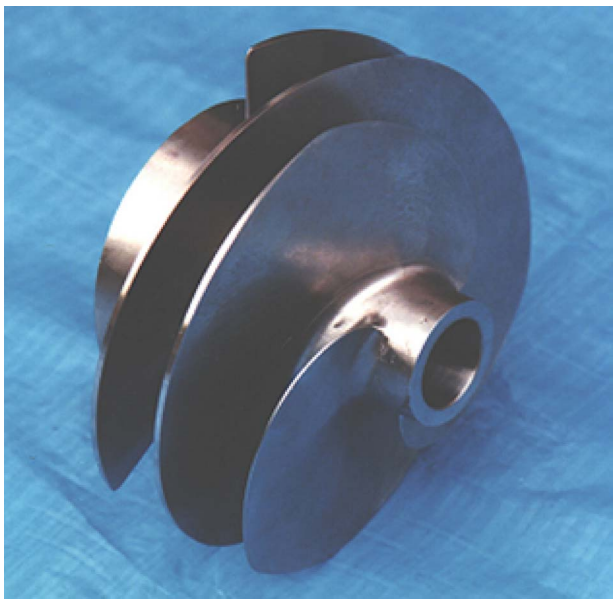

Fig. 2 The test inducer

3.1 Pipes. With a suitable manipulation of the generic continuity and momentum equations, the dynamic matrix can be written as follows:

$$H = \begin{bmatrix} 1 & -R - i\omega L \\ 0 & 1 \end{bmatrix}$$

where the resistance R and the inertance L are given by

$$R = k\rho \frac{\bar{Q}_u}{A_u^2} + \rho\left(\frac{1}{A_d^2} - \frac{1}{A_u^2}\right)\bar{Q}_u$$

$$L = \rho\frac{1}{\lambda}$$

in which ρ is the density of the working fluid, A is the pipe section, λ is the "inertial length" of the pipe (defined as the mean pipe section divided to pipe length), and k is the loss coefficient inside the pipe.

3.2 Main Tank. In this case, the dynamic matrix is given by

$$H = \begin{bmatrix} 1 & 0 \\ -i\omega C & 1 \end{bmatrix}$$

where the compliance C is

$$C = \frac{\bar{V}}{\gamma \bar{p}}$$

in which $\bar{p}$ and $\bar{V}$ are the mean pressure and volume of the air at the top of the tank, and γ is the specific heat ratio of air.

3.3 Inducer. In the noncavitating case, it can be shown that the inducer dynamic matrix is very simple, with a similar structure to that of pipe sections. In this case the inertance L is simply given by the inertial length of blade passages, while the resistance R can be evaluated using the momentum equation as follows:

$$R = -\frac{\rho\Omega r_T}{A_u}\frac{d\psi}{d\phi} + \rho\bar{Q}_u\left(\frac{1}{A_d^2} - \frac{1}{A_u^2}\right)$$

in which Ω is the inducer rotating speed, r_T is the inducer tip radius, and $d\psi/d\phi$ is the slope of the inducer performance curve.

In the cavitating case the equations become more complicated. The driving parameter is the presence of a vapor region on the blades, the oscillations of which generate a shift between the inlet and outlet flow oscillations. The evaluation of the volume of cavity formed inside the pump, as a function of the flow coefficient ϕ and the cavitation number σ, is therefore needed. Elaboration of the continuity and momentum equations shows that the dynamic matrix is

$$H = \begin{bmatrix} 1 - (S + i\omega X) & -R - i\omega L \\ -i\omega C & 1 - i\omega M \end{bmatrix}$$

where $S+i\omega X$ is the pressure gain factor, $R+i\omega L$ is the pump impedance, C is the cavitation compliance, and M is the mass flow gain factor. These parameters are defined as follows:

$$S + i\omega X = -2\left.\frac{\partial\psi}{\partial\sigma}\right|_\phi + CL_{\text{ind}}\omega^2 - i\omega\left(\frac{\rho\bar{Q}_u}{A_d^2}C - \frac{\rho\Omega r_T}{A_d}\left.\frac{\partial\psi}{\partial\phi}\right|_\sigma C\right)$$

$$R + i\omega L = -\frac{\rho\Omega r_T}{A_d}\left.\frac{\partial\psi}{\partial\phi}\right|_\sigma - \rho\bar{Q}_u\left(\frac{1}{A_u^2} - \frac{1}{A_d^2}\right) + ML_{\text{ind}}\omega^2 - i\omega M\left(\frac{\rho\bar{Q}_u}{A_d^2} - \frac{\rho\Omega r_T}{A_d}\left.\frac{\partial\psi}{\partial\phi}\right|_\sigma\right) + i\omega L_{\text{ind}}$$

$$C = -\frac{2}{\rho\Omega^2 r_T^2}\left.\frac{\partial V_C}{\partial\sigma}\right|_\phi$$

$$M = -\frac{1}{A_u\Omega r_T}\left.\frac{\partial V_C}{\partial\phi}\right|_\sigma$$

in which V_C is the cavity volume and L_{ind} is the inertance of inducer blade passages.

After having tried different approaches for the evaluation of the cavity volume V_C, including suitable modifications to the Brennen–Acosta model of partially cavitating cascades [13,14], a simpler empirical-theoretical model will be proposed here. The choice of this model was led by the consideration that the present work is not aimed to an accurate evaluation of the inducer dynamic characteristics, but to a characterization of the entire facility, in order to acquire useful theoretical and design indications for the successive experimental activities.

The cavitation volume has therefore been estimated using a polynomial relationship and taking into account the experimental data provided by Brennen for a 10.2 cm inducer [13]. Considering that these data give an estimation of the cavitation compliance on the inducer at four different values of σ, the following relation was used:

$$V_C(\phi,\sigma) = a_1(\sigma - \sigma_c)^4 + a_2(\sigma - \sigma_c)^3 + a_3(\sigma - \sigma_c)^2 + a_4(\sigma - \sigma_c) + V_C(\sigma_c)$$

where the constants a_1, a_2, a_3, and a_4 can be evaluated using the four experimental values of $C(\sigma)$ provided by Brennen [13]. In the above equation, σ_c is the "choked cavitation number" of the Brennen–Acosta partially cavitating cascade model (i.e., the cavitation number for which the cavity becomes infinitely long [13]), which depends on the inducer geometry and the incidence angle and, as a consequence, the flow coefficient.

The cavity volume at the choked cavitation number, $V_C(\sigma_c)$, is evaluated assuming the following.

(1) At the choked cavitation number σ_c, complete breakdown occurs (i.e., the head rise of the inducer falls to zero).
(2) At σ_c, the blade channels are completely filled by bubbly cavitation, having a void fraction α_0, which can be evaluated using the relationship shown by Brennen [5],

$$\Delta\psi = \frac{\alpha_0(2 - \alpha_0)\phi^2}{2(1 - \alpha_0)^2 \sin^2\beta_b}$$

where β_b is the tip blade angle and $\Delta\psi$ is the amount of breakdown, estimated using assumption (1).
(3) The cavity volume at choked cavitation number is finally estimated by multiplying the void fraction α_0 to the blade channel volume.

Calculations confirmed that the model can reasonably reproduce the experimental transfer matrix as shown in Ref. [13].

3.4 Characterization of the Complete Facility. Four unknowns have to be evaluated for the solution of the problem: the pressure and flow oscillations at the inlet measurement point, $\hat{p}_1$ and $\hat{Q}_1$, and the correspondent oscillations at the outlet measurement point, $\hat{p}_2$ and $\hat{Q}_2$. The first two equations for their evaluation can be obtained by considering the equilibrium inside the measurement section

$$\begin{bmatrix} \hat{p}_2 \\ \hat{Q}_2 \end{bmatrix} = \begin{bmatrix} HM_{11} & HM_{12} \\ HM_{21} & HM_{22} \end{bmatrix}\begin{bmatrix} \hat{p}_1 \\ \hat{Q}_1 \end{bmatrix}$$

where the transfer matrix HM is given by

$$HM = \begin{bmatrix} 1 & -R_{\text{out}} - i\omega L_{\text{out}} \\ 0 & 1 \end{bmatrix}\begin{bmatrix} 1 - (S + i\omega X) & -R_{\text{ind}} - i\omega L_{\text{ind}} \\ -i\omega C_{\text{ind}} & 1 - i\omega M \end{bmatrix} \times \begin{bmatrix} 1 & -R_{\text{in}} - i\omega L_{\text{in}} \\ 0 & 1 \end{bmatrix}$$

Considering the components of the facility between the downstream measurement section and the flow rate fluctuator (see Fig. 1), it is possible to write the oscillations immediately after the fluctuator as

$$\hat{Q}_3 = \hat{Q}_2 + \hat{Q}_F$$

$$\hat{p}_3 = \hat{p}_2 - (R_A + i\omega L_A)\hat{Q}_2$$

The "boundary conditions" of the problem can be written by considering the equilibrium equations in the sector of the facility outside the measurement section

$$\begin{bmatrix} \hat{p}_1 \\ \hat{Q}_1 \end{bmatrix} = \begin{bmatrix} HB_{11} & HB_{12} \\ HB_{21} & HB_{22} \end{bmatrix} \begin{bmatrix} \hat{p}_3 \\ \hat{Q}_3 \end{bmatrix}$$

where the transfer matrix HB is given by

$$HB = \begin{bmatrix} 1 & -R_C - i\omega L_C \\ 0 & 1 \end{bmatrix} \begin{bmatrix} 1 & 0 \\ -i\omega C_T & 1 \end{bmatrix} \begin{bmatrix} 1 & -R_B - i\omega L_B \\ 0 & 1 \end{bmatrix}$$

Combining the above expressions, it is possible to obtain the last two equations needed for the solution of the problem.

The solution of the problem in the noncavitating case is of particular interest. In this case, taking into account the simpler structure of the inducer dynamic matrix, the pressure and flow rate oscillations can be shown to be equal to

$$\hat{Q}_1 = \hat{Q}_2 = \frac{-(R_B + i\omega L_B)\hat{Q}_F}{(R_m + R_A + R_B + R_C) + i\omega(L_m + L_A + L_B + L_C)}$$

$$\hat{p}_1 = \frac{\hat{Q}_F}{i\omega C_T} + \frac{(R_C + i\omega L_C)(R_B + i\omega L_B)\hat{Q}_F}{(R_m + R_A + R_B + R_C) + i\omega(L_m + L_A + L_B + L_C)}$$

$$\hat{p}_2 = \frac{\hat{Q}_F}{i\omega C_T} + \frac{[(\bar{R} + R_C) + i\omega(\bar{L} + L_C)](R_B + i\omega L_B)\hat{Q}_F}{(R_m + R_A + R_B + R_C) + i\omega(L_m + L_A + L_B + L_C)}$$

where

$$R_m = R_{\text{in}} + R_{\text{ind}} + R_{\text{out}}$$

$$L_m = L_{\text{in}} + L_{\text{ind}} + L_{\text{out}}$$

The first term in the expressions of $\hat{p}_1$ and $\hat{p}_2$ is usually very small due to the large value of the tank compliance C_T and can therefore be neglected, at least for sufficiently high values of the exciting frequency ω. As an example, for the Osaka University facility with LE-7 engine LOX inducer under nominal operating conditions (ϕ=0.078, Ω=3000 rpm, mean tank pressure $\bar{p}$ =1 atm, and air volume in the tank $\bar{V}$=625 liters), it is possible to obtain the following values for the ratio of the first term to the second term in the expression of $\hat{p}_1$:

0.255 for $\omega = 1$ Hz

0.057 for $\omega = 2$ Hz

0.023 for $\omega = 3$ Hz

0.007 for $\omega = 5$ Hz

0.002 for $\omega = 10$ Hz

3.5 "Backward" Calculation. Once the pressure and flow rate oscillations are known by means of the above equations, they can be used as input data to simulate the evaluation of the measured transfer matrix HM. In this case, at least two experimental results obtained under linearly independent conditions are needed to find the four unknown elements of the matrix. Indicating by subscripts a and b the two experimental results used for the calculation, it is possible to write

$$\begin{bmatrix} \hat{p}_{2a} \\ \hat{Q}_{2a} \end{bmatrix} = \begin{bmatrix} HM_{11} & HM_{12} \\ HM_{21} & HM_{22} \end{bmatrix} \begin{bmatrix} \hat{p}_{1a} \\ \hat{Q}_{1a} \end{bmatrix}$$

$$\begin{bmatrix} \hat{p}_{2b} \\ \hat{Q}_{2b} \end{bmatrix} = \begin{bmatrix} HM_{11} & HM_{12} \\ HM_{21} & HM_{22} \end{bmatrix} \begin{bmatrix} \hat{p}_{1b} \\ \hat{Q}_{1b} \end{bmatrix}$$

which lead to the following system of four equations in four unknowns:

$$\underbrace{\begin{bmatrix} \hat{p}_{1a} & \hat{Q}_{1a} & 0 & 0 \\ \hat{p}_{1b} & \hat{Q}_{1b} & 0 & 0 \\ 0 & 0 & \hat{p}_{1a} & \hat{Q}_{1a} \\ 0 & 0 & \hat{p}_{1b} & \hat{Q}_{1b} \end{bmatrix}}_{T} \begin{bmatrix} HM_{11} \\ HM_{12} \\ HM_{21} \\ HM_{22} \end{bmatrix} = \begin{bmatrix} \hat{p}_{2a} \\ \hat{p}_{2b} \\ \hat{Q}_{2a} \\ \hat{Q}_{2b} \end{bmatrix}$$

It is clear that, for better accuracy in the evaluation of the elements of HM, the determinant of the matrix T should be as far as possible from zero. This is obtained by taking two experimental results under sufficiently independent conditions. In the noncavitating case, using the equations for the pressure and flow rate oscillations and neglecting the first term in the expression of $\hat{p}_1$, it is possible to obtain the following result for the determinant of matrix T:

$$\det T = \left\{ \frac{(R_{Ba} + i\omega L_{Ba})(R_{Bb} + i\omega L_{Bb})[(R_{Cb} - R_{Ca}) + i\omega(L_{Cb} - L_{Ca})]\hat{Q}_F^{\,2}}{[(R_m + R_{Aa} + R_{Ba} + R_{Ca}) + i\omega(L_m + L_{Aa} + L_{Ba} + L_{Ca})][(R_m + R_{Ab} + R_{Bb} + R_{Cb}) + i\omega(L_m + L_{Ab} + L_{Bb} + L_{Cb})]} \right\}^2$$

It is therefore clear that, if no changes are made to the section C of the facility (i.e., the suction line, between the tank and the upstream measurement point), the determinant of the matrix T will be equal to zero whatever other change is made to the other sections of the facility. It could be shown that this is true also under cavitating conditions. Furthermore, if calculations are carried out in the case when the fluctuator is installed on the suction line instead of the discharge line, the opposite result is obtained: In that case, the only effective changes would be those affecting the section of the facility where there is no fluctuator, i.e., the discharge line.

This result provides a first important design indication for the experiments: The two linearly independent conditions, needed for the evaluation of the dynamic matrix, can be obtained only by changes in the suction line. These changes can involve the resistance R_C, the inertance L_C, or both. All these options will be evaluated in the following.

4 Results and Discussion

Two different sets of calculations will be presented here. The first one allows for the evaluation of the expected oscillations in the facility under its nominal design, in different operational con-

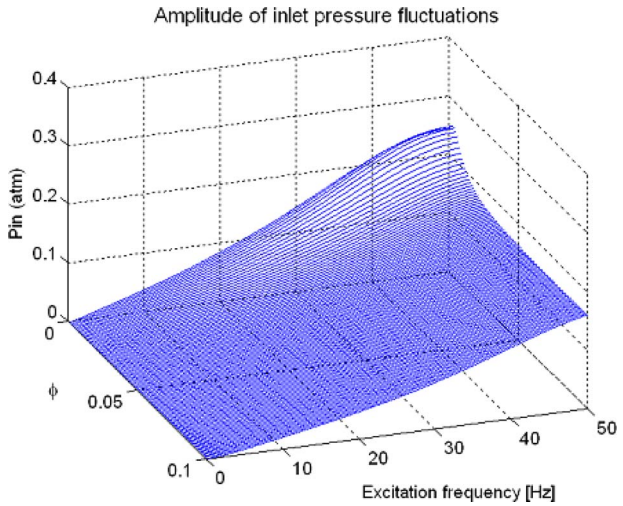

Fig. 3 Amplitude of the upstream pressure oscillations, as a function of the excitation frequency ω and the flow coefficient ϕ (cavitating conditions), for $\Omega=3000$ rpm, $\sigma=0.1$, and amplitude of the flow rate oscillations generated by the fluctuator equal to 1 l/s

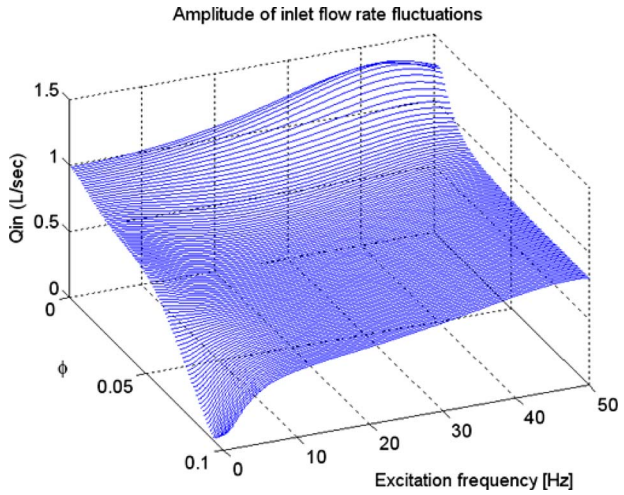

Fig. 5 Amplitude of the upstream flow rate oscillations, as a function of the excitation frequency ω and the flow coefficient ϕ (cavitating conditions), for $\Omega=3000$ rpm, $\sigma=0.1$, and amplitude of the flow rate oscillations generated by the fluctuator equal to 1 l/s

ditions. The second one will be a "backward" calculation, aimed to the estimation of the effectiveness of several alternative designs of the facility for obtaining the second linearly independent experimental condition.

4.1 Nominal Design: Pressure and Flow Rate Oscillations. The 3D plots from Figs. 3–6 show the amplitude of pressure and flow rate fluctuations under cavitating conditions, as functions of the excitation frequency and the flow coefficient, for $\sigma=0.1$, $\Omega=3000$ rpm, and amplitude of the flow rate oscillations generated by the fluctuator equal to 1 l/s. Since there is no phase information in the 3D plots, Figs. 7–10 show the amplitude and phase of pressure and flow rate fluctuations under cavitating conditions, as functions of the excitation frequency, for $\sigma=0.1$, $\Omega=3000$ rpm, $\phi=0.078$ (inducer nominal operating conditions), and amplitude of the flow rate oscillations generated by the fluctuator equal to 1 l/s. The phase delay is calculated with respect to the flow rate oscillations generated by the fluctuator.

4.2 Evaluation of Alternative Facility Designs. The effectiveness of different facility designs has been evaluated by means of the backward calculation. The results provided by the model have therefore been used as a starting point for the evaluation of the dynamic matrix elements, in order to compare this evaluation to the actual nominal values provided by the model. The dynamic matrix elements have been evaluated at different excitation frequencies ω and flow coefficients ϕ.

In order to better simulate the real experimental conditions expected in the facility, three different "artificial" error sources have been intentionally added to the nominal data. The first two error sources are a random "white noise" at all the frequencies included in the spectrum of the measured signal (which simulates the typical white noise usually present in laboratory environments) and a defined sinusoidal noise at 60 Hz (frequency of electrical disturbance in Japan). The third error source consists in taking only a finite number of decimals from the numerical solutions provided by the model, in order to simulate the experimental sensors' accuracy.

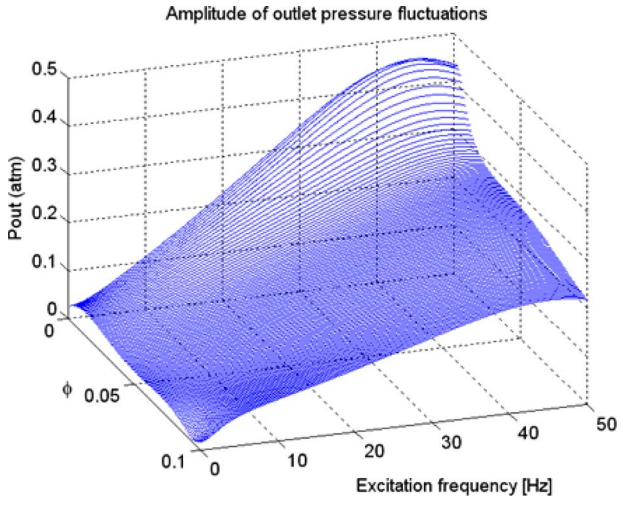

Fig. 4 Amplitude of the downstream pressure oscillations, as a function of the excitation frequency ω and the flow coefficient ϕ (cavitating conditions), for $\Omega=3000$ rpm, $\sigma=0.1$, and amplitude of the flow rate oscillations generated by the fluctuator equal to 1 l/s

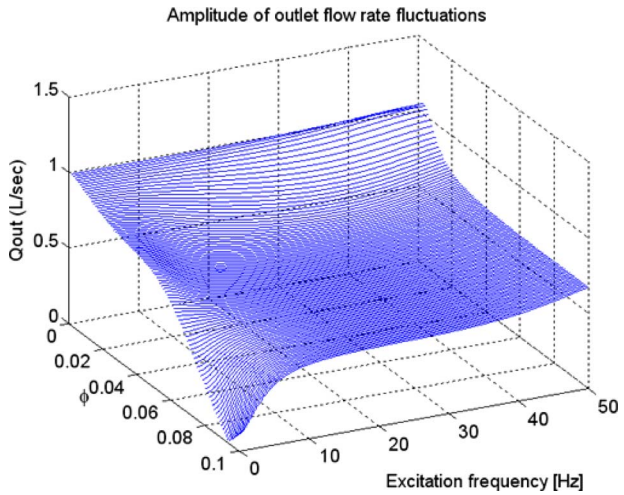

Fig. 6 Amplitude of the downstream flow rate oscillations, as a function of the excitation frequency ω and the flow coefficient ϕ (cavitating conditions), for $\Omega=3000$ rpm, $\sigma=0.1$, and amplitude of the flow rate oscillations generated by the fluctuator equal to 1 l/s

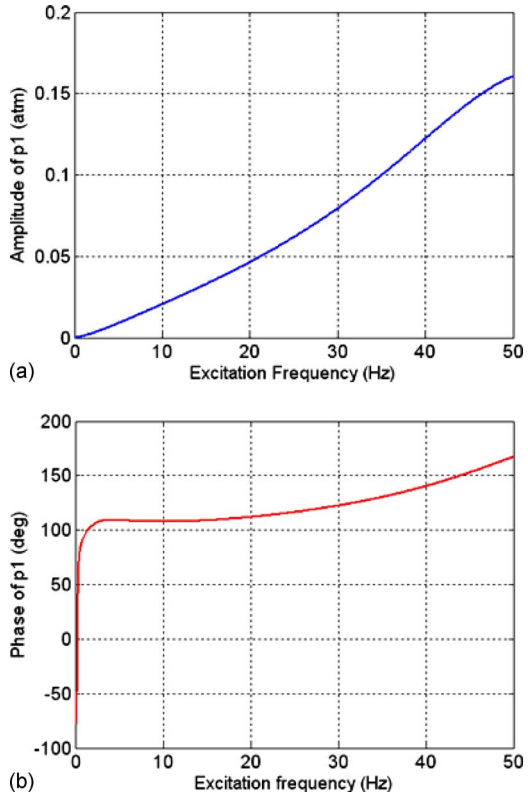

Fig. 7 Amplitude and phase of the upstream pressure oscillations, as a function of the excitation frequency ω (cavitating conditions), for $\Omega=3000$ rpm, $\sigma=0.1$, $\phi=0.078$, and amplitude of the flow rate oscillations generated by the fluctuator equal to 1 l/s

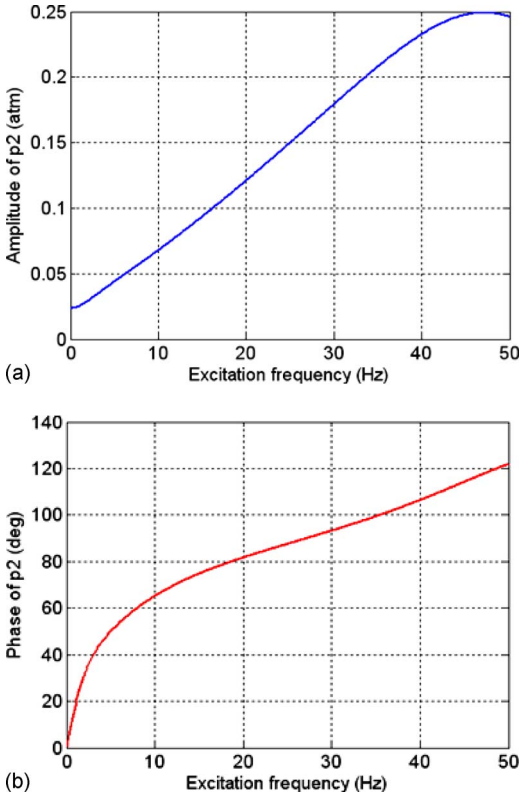

Fig. 8 Amplitude and phase of the downstream pressure oscillations, as a function of the excitation frequency ω (cavitating conditions), for $\Omega=3000$ rpm, $\sigma=0.1$, $\phi=0.078$, and amplitude of the flow rate oscillations generated by the fluctuator equal to 1 l/s

A fourth important source of errors is given by the determinant of the evaluation matrix T, which is usually almost singular in sufficiently realistic design cases.

The simulated experimental signal obtained by this procedure was then elaborated using the Fourier analysis (as it were a real experimental signal), and the information related to the known excitation frequency was extracted in terms of amplitude and phase of the oscillations at that frequency. Finally, these extrapolated data were used for the evaluation of the components of the transfer matrix, which were compared with the expected ones.

In the proposed calculations, three different alternative facility designs have been considered, according to the following nomenclature.

Nominal. The nominal value of the matrix element, as obtained by the analytical model equations.

New design 6 (ND6) single. For obtaining the second linearly independent condition, a resistance is added to the suction line of the facility. The resistance is constituted by a single perforated plate with 69 holes of 12 mm diameter.

New design 6 (ND6) M-stage. The same as above, but in this case the resistance is constituted by a multistage perforated plate. Three plates with holes of 12 mm diameter are considered, having a different number of holes (58 holes for the first plate, 73 for the second, and 91 for the third), in order to provide a better distribution of the resistance loss and avoid cavitation in the plates.

New design 7 (ND7). In this case, the inertance of the suction line of the facility is increased by adding a long pipe section having a length equal to 6.3 m.

The plots in Figs. 11–16 are referred to the case $\sigma=0.1$ (cavitating conditions), $\Omega=3000$ rpm, with amplitude of the flow rate oscillations generated by the fluctuator equal to 1 l/s. The determinant of the evaluation matrix T and a comparison between the nominal and the evaluated elements of the dynamic matrix are shown for the cases "ND6 single," "ND6 M-stage," and "ND7." Only the components HM_{12} and HM_{21} of the dynamic matrix (the most interesting by the point of view of inducer instabilities) are shown. Two cases are considered: fixed flow coefficient ($\phi=0.078$) with variable excitation frequency, and fixed excitation frequency ($\omega=5$ Hz) with variable flow coefficient.

With respect to the flow coefficient, the results are generally good, with acceptably small errors. With respect to the excitation frequency, the results are also good, but there is a loss in accuracy at very low excitation frequencies (less than 1 Hz) and at higher excitation frequencies (more than 20 Hz, except for ND7, which is more effective also at higher frequencies). The lower accuracy of results at low frequencies can be explained considering the very low value of pressure oscillations in that case (see Figs. 7 and 8). As a consequence, the accuracy of the pressure transducers becomes a significant source of errors. The lower accuracy at higher frequencies for ND6 cases is explained by considering that, at higher frequencies, the inductance of the suction line of the facility (L_C) becomes significantly more important than its resistance R_C for the evaluation of the oscillations, and so the ND7 design is more effective than the ND6 ones.

It is therefore demonstrated that, for most of the frequencies of actual interest, the simple insertion of a calibrated resistance in the suction line of the facility (between the tank and the upstream measurement section) could provide the second linearly independent condition necessary for the experimental evaluation of the transfer matrix. However, to obtain accurate results at higher excitation frequencies (more than 20 Hz), it should probably be necessary to add a long pipe section to the suction line (ND7 condition) in order to increase its inertance.

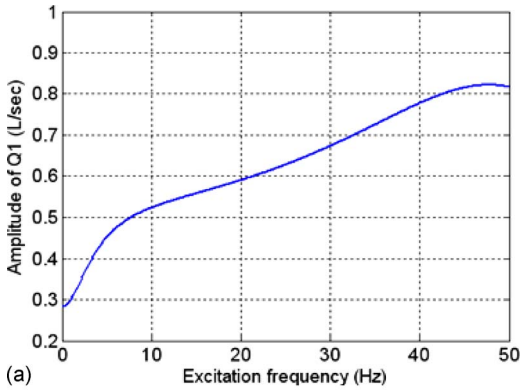

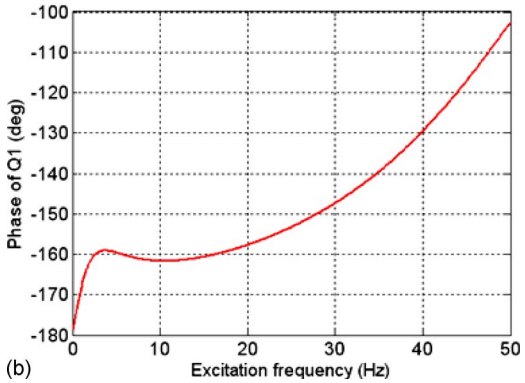

Fig. 9 Amplitude and phase of the upstream flow rate oscillations, as a function of the excitation frequency ω (cavitating conditions), for Ω=3000 rpm, σ=0.1, ϕ=0.078, and amplitude of the flow rate oscillations generated by the fluctuator equal to 1 l/s

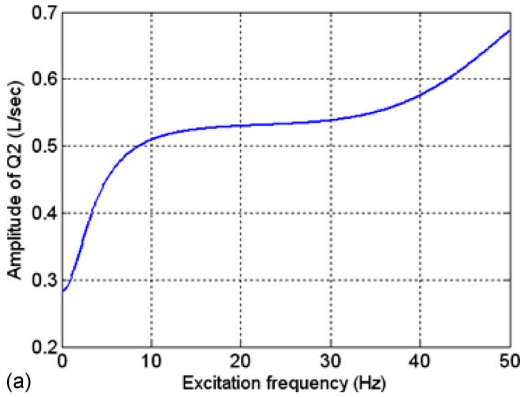

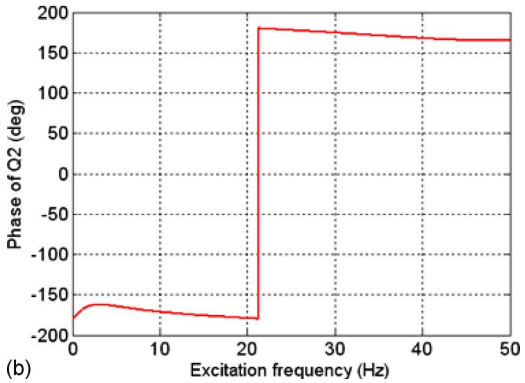

Fig. 10 Amplitude and phase of the downstream flow rate oscillations, as a function of the excitation frequency ω (cavitating conditions), for Ω=3000 rpm, σ=0.1, ϕ=0.078, and amplitude of the flow rate oscillations generated by the fluctuator equal to 1 l/s

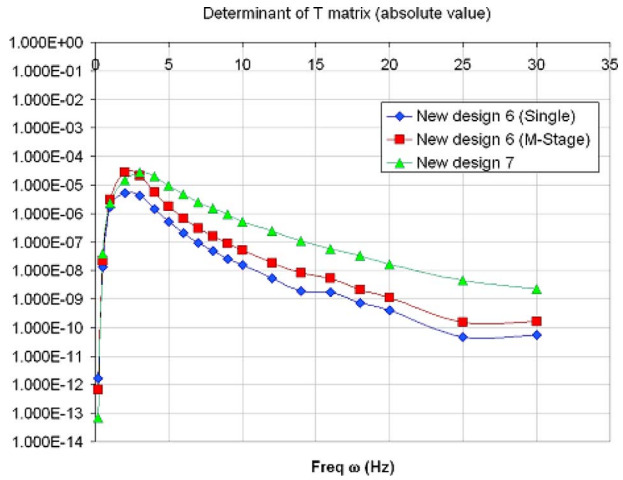

Fig. 11 Determinant of the evaluation matrix *T*, as a function of the excitation frequency ω, for Ω=3000 rpm, σ=0.1, ϕ=0.078, and amplitude of the flow rate oscillations generated by the fluctuator equal to 1 l/s

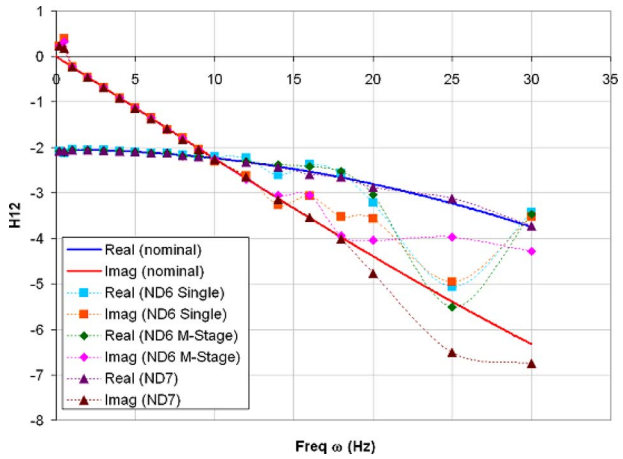

Fig. 12 Real and imaginary parts of the element HM_{12} of the dynamic matrix, as functions of the excitation frequency ω, for Ω=3000 rpm, σ=0.1, ϕ=0.078, and amplitude of the flow rate oscillations generated by the fluctuator equal to 1 l/s

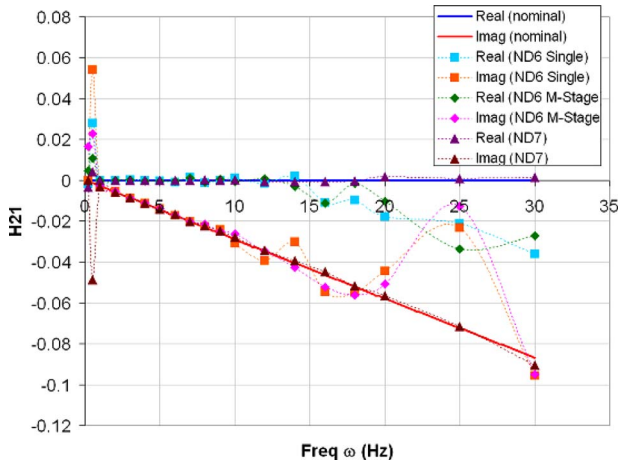

Fig. 13 Real and imaginary parts of the element HM_{21} of the dynamic matrix, as functions of the excitation frequency ω, for Ω=3000 rpm, σ=0.1, ϕ=0.078, and amplitude of the flow rate oscillations generated by the fluctuator equal to 1 l/s

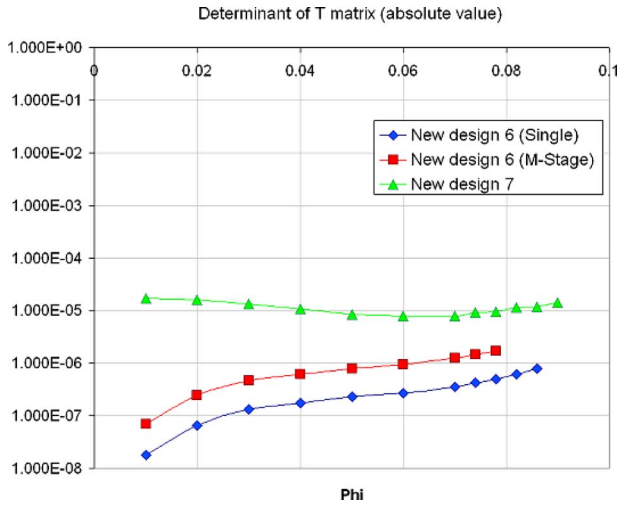

Fig. 14 Determinant of the evaluation matrix *T*, as a function of the flow coefficient ϕ, for $\Omega=3000$ rpm, $\sigma=0.1$, $\omega=5$ Hz, and amplitude of the flow rate oscillations generated by the fluctuator equal to 1 l/s

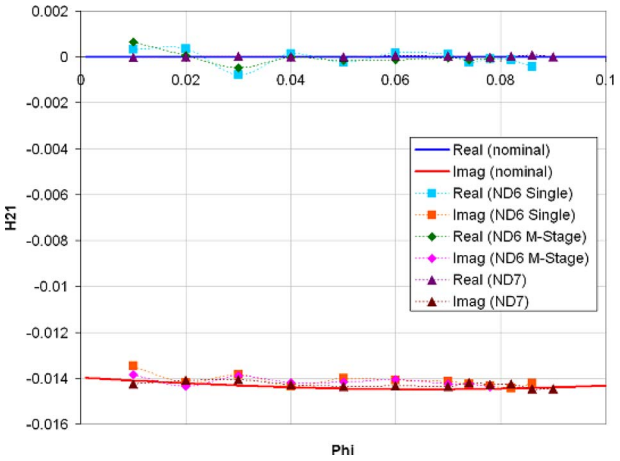

Fig. 16 Real and imaginary parts of the element HM_{21} of the dynamic matrix, as functions of flow coefficient ϕ, for $\Omega=3000$ rpm, $\sigma=0.1$, $\omega=5$ Hz, and amplitude of the flow rate oscillations generated by the fluctuator equal to 1 l/s

5 Conclusions

An analytical model for the evaluation of the dynamic matrix of a cavitating inducer facility has been proposed in the present paper. The model, even if extremely simplified and based on very strong assumptions, has shown to be a powerful tool for the design of the facility and the preparation of the experimental activity.

In particular, the backward calculation (utilization of the model results as simulated experimental data, after having opportunely added to them artificial error sources) can be used to get extremely useful indications about the effectiveness of different facility designs. Furthermore, the model equations showed that the only effective design changes for obtaining the second linearly independent condition, needed for the experimental evaluation of the dynamic matrix, are those related to the suction line of the facility (or, conversely, the discharge line if the external fluctuations are provided to the suction line).

Future improvements to the model could include, as an example, a better evaluation of the inducer dynamic matrix, based on more accurate models than the simple empirical-theoretical model proposed in this paper. As a useful tool to this purpose, an extensive experimental activity is foreseen during the next months, in order to measure the pressure and flow rate oscillations in the facility under several operating conditions and compare the obtained data to the results of the model.

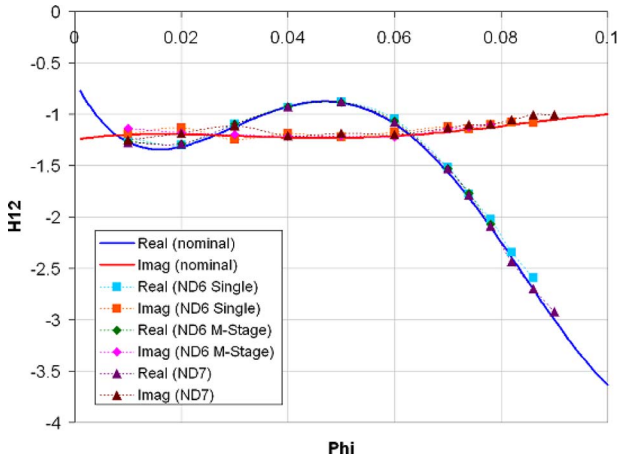

Fig. 15 Real and imaginary parts of the element HM_{12} of the dynamic matrix, as functions of flow coefficient ϕ, for $\Omega=3000$ rpm, $\sigma=0.1$, $\omega=5$ Hz, and amplitude of the flow rate oscillations generated by the fluctuator equal to 1 l/s

Acknowledgment

A.C. would like to acknowledge the support of Japan Society for the Promotion of Science (JSPS), which has funded his research program at Osaka University. He also expresses his gratitude to all the colleagues at Pisa University in Italy, and, in particular, Professor Luca d'Agostino and Professor Mariano Andrenucci, for their kind and constant encouragement.

Nomenclature

a_i = constants in cavity volume equation, $i=1-4$ (m^3)
A = pipe section (m^2)
C = compliance ($m^4\ s^2/kg$)
k = loss coefficient (dimensionless)
L = inertance (kg/m^4)
M = mass flow gain factor (s^{-1})
p = pressure (Pa)
H = generic dynamic matrix
HB = dynamic matrix outside the measurement section
HM = dynamic matrix of the measurement section
Q = flow rate (m^3/s)
Q_F = externally imposed flow oscillation (m^3/s)
R = resistance ($kg/m^4\ s$)
r_T = inducer tip radius (m)
S = real part of the pressure gain factor (dimensionless)
t = time (s)
T = characteristic matrix for backward calculation
V = volume (m^3)
V_C = cavity volume (m^3)
X = imaginary part of the pressure gain factor (s)
α_0 = void fraction (dimensionless)
β_b = inducer tip blade angle (rad)
$\Delta\psi$ = head loss at breakdown (dimensionless)
ϕ = flow coefficient (dimensionless)
γ = specific heat ratio (dimensionless)

λ = inertial length (m)
ψ = head coefficient (dimensionless)
ρ = density (kg/m^3)
σ = cavitation number (dimensionless)
σ_c = "choked" cavitation number (dimensionless)
ω = frequency of oscillations (Hz)
Ω = inducer rotating speed (rad/s)

Superscripts

$\hat{}$ = oscillating component of a given quantity
$\bar{}$ = steady component of a given quantity

Subscripts

a, b = linearly independent experimental conditions
A = pipework from measurement section to fluctuator
B = discharge line
C = suction line
d = downstream section (generic)
in = measurement section (upstream of inducer)
ind = inducer
m = total measurement section (including inducer)
out = measurement section (downstream of inducer)
T = main tank
u = upstream section (generic)
1 = upstream measurement point
2 = downstream measurement point
3 = point immediately after the fluctuator

References

[1] Stripling, L. B., and Acosta, A. J., 1962, "Cavitation in Turbopumps–Part 1," ASME J. Basic Eng., **84**, pp. 326–338.

[2] Kawata, Y., Takata, T., Yasuda, O., and Takeuchi, T., 1988, "Measurement of the Transfer Matrix of a Prototype Multi-Stage Centrifugal Pump," Paper No. C346/88.

[3] Tsujimoto, Y., Kamijo, K., and Yoshida, Y., 1993, "A Theoretical Analysis of Rotating Cavitation in Inducers," ASME J. Fluids Eng., **115**, pp. 135–141.

[4] Tsujimoto, Y., Watanabe, S., and Horiguchi, H., 1998, "Linear Analyses of Cavitation Instabilities of Hydrofoils and Cascades," Proceedings of the US-Japan Seminar: Abnormal Flow Phenomena in Turbomachinery, Osaka, Japan.

[5] Brennen, C. E., 1978, "Bubbly Flow Model for the Dynamic Characteristics of Cavitating Pumps," J. Fluid Mech., **89**, pp. 223–240.

[6] Ng, S. L., and Brennen, C. E., 1978, "Experiments on the Dynamic Behavior of Cavitating Pumps," ASME J. Fluids Eng., **100**, pp. 166–176.

[7] Otsuka, S., Tsujimoto, Y., Kamijo, K., and Furuya, O., 1996, "Frequency Dependence of Mass Flow Gain Factor and Cavitation Compliance of Cavitating Inducers," ASME J. Fluids Eng., **118**, pp. 400–408.

[8] Rubin, S., 2004, "An Interpretation of Transfer Function Data for a Cavitating Pump," Proceedings of the 40th AIAA/ASME/SAE/ASEE Joint Propulsion Conference, Fort Lauderdale, FL.

[9] Bhattacharyya, A., 1994, "Internal Flows and Force Matrices in Axial Flow Inducers," Ph.D. thesis, California Institute of Technology, Pasadena, CA.

[10] Jun, S. I., Tokumasu, T., and Kamijo, K., 2003, "Dynamic Response Analysis of High Pressure Rocket Pumps," Proceedings of CAV2003—Fifth International Symposium on Cavitation, Osaka, Japan.

[11] Yamamoto, K., and Tsujimoto, Y., 2008, "Backflow Vortex Cavitation and Its Effects on Cavitation Instabilities," *Proceedings of the WIMRC Cavitation Forum*, Warwick University, Coventry, UK.

[12] Shimiya, N., Fujii, A., Horiguchi, H., Uchiumi, M., Kurokawa, J., and Tsujimoto, Y., 2006, "Suppression of Cavitation Instabilities in an Inducer by J-Groove," Proceedings of CAV2006—Sixth International Symposium on Cavitation, Wageningen, The Netherlands.

[13] Brennen, C. E., 1994, *Hydrodynamics of Pumps*, Concepts ETI Inc., Norwich, VT/Oxford University Press, Oxford.

[14] Brennen, C. E., and Acosta, A. J., 1973, "Theoretical, Quasi-Static Analysis of Cavitation Compliance in Turbopumps," J. Spacecr. Rockets, **10**(3), pp. 175–179.

RANS Analyses of Turbofan Nozzles With Internal Wedge Deflectors for Noise Reduction

James R. DeBonis[1]
Inlet and Nozzle Branch,
NASA Glenn Research Center,
Cleveland, OH 44135
e-mail: james.r.debonis@nasa.gov

Computational fluid dynamics (CFD) was used to evaluate the flow field and thrust performance of a promising concept for reducing the noise at take-off of dual-stream turbofan nozzles. The concept, offset stream technology, reduces the jet noise observed on the ground by diverting (offsetting) a portion of the fan flow below the core flow, thickening and lengthening this layer between the high-velocity core flow and the ground observers. In this study a wedge placed in the internal fan stream is used as the diverter. Wind, a Reynolds averaged Navier–Stokes (RANS) code, was used to analyze the flow field of the exhaust plume and to calculate nozzle performance. Results showed that the wedge diverts all of the fan flow to the lower side of the nozzle, and the turbulent kinetic energy on the observer side of the nozzle is reduced. This reduction in turbulent kinetic energy should correspond to a reduction in noise. However, because all of the fan flow is diverted, the upper portion of the core flow is exposed to the freestream, and the turbulent kinetic energy on the upper side of the nozzle is increased, creating an unintended noise source. The blockage due to the wedge reduces the fan mass flow proportional to its blockage, and the overall thrust is consequently reduced. The CFD predictions are in very good agreement with experimental flow field data, demonstrating that RANS CFD can accurately predict the velocity and turbulent kinetic energy fields. While this initial design of a large scale wedge nozzle did not meet noise reduction or thrust goals, this study identified areas for improvement and demonstrated that RANS CFD can be used to improve the concept. [DOI: 10.1115/1.3089536]

1 Introduction

The concept of offsetting the fan stream of a dual flow turbofan nozzle to reduce jet noise was developed by Papamoschou at the University of California Irvine (UCI) [1–3]. The idea is to provide a thicker layer of fan flow on the lower (observer) side of the nozzle. The additional fan flow serves to extend the length of the fan stream covering or "shielding" a larger portion of the core flow on the lower side. This layer of low speed flow reduces the convective Mach number of the turbulent eddies generated by the high speed core flow. This reduces these turbulent structures' ability to generate strong acoustic waves that travel to the far field (on the lower side of the nozzle). Papamoschou's [1–3] initial concept was to physically offset the nozzle flow paths. This eccentric nozzle would be difficult to implement in a real system. He found that vanes and/or wedges placed in the fan stream can deflect the fan flow to the lower portion of the jet to achieve the desired flow field and resulting acoustics in a simple, easy to implement manner.

Papamoschou [1–3] tested these concepts in a small jet facility (1 in. (2.54 cm) fan exit diameter) and measured jet noise reductions of over 5.0 dB in the overall sound pressure level. These impressive results led the National Aeronautics and Space Administration (NASA) to examine this noise reduction concept at a larger scale. NASA developed the Offset Stream Technology (OST) program to design and test turbofan nozzles with devices to offset the fan flow. The program consisted of computational fluid dynamics (CFD) analysis to screen flow deflector design and placement and to estimate nozzle performance, design of experiments (DOE) methodology to reduce the number of experimental test points required, additional small scale testing, and large scale testing (9.63 in. (24.5 cm) fan exit diameter) in the NASA Glenn Nozzle Acoustic Test Rig (NATR) [4].

There are four other papers from the OST study that form a complete description of the program. A companion CFD study examining the vane deflector and s-duct nozzles was performed by Dippold et al. [5]. The experimental results from NATR, acoustics and particle image velocimetry (PIV)–based velocity measurements in the exhaust plume, were reported by Brown et al. [6], and a comparison of experimental results between UCI and NASA Glenn was detailed by Zaman et al. [7]. The results of the DOE study were reported by Henderson et al. [8].

The experimental results at NATR indicate that the wedge deflectors do reduce the noise on the lower side of the nozzle at downstream angles. However, at other angles on the lower side and at all angles on the sideline and upper side, the noise was increased. In general, the overall estimated perceived noise level (EPNL) increased relative to the baseline due to the higher noise at the other locations. One configuration, BPR=5.0, M_∞=0.0, showed a small noise reduction of 0.8 EPN dB. Based on measurements of turbulent kinetic energy, Brown et al. [6] concluded that the wedge designs tested were too aggressive.

Thrust performance is a critical factor in assessing low noise nozzle concepts. Papamoschou [1–3] estimated the thrust loss in nozzles with vane deflectors based on airfoil drag and nozzle flow deflection [2], and Papamoschou et al. [9] experimentally examined the aerodynamics of a wedge deflector in a simplified configuration. But up to this point, there has been no detailed examination of the performance of these nozzles. The NATR tests did not include force measurements. A key element of the CFD calculations presented here was to characterize the thrust of these nozzles and compare them to a baseline nozzle without deflectors. This work represents the highest fidelity estimates of Offset Stream nozzle performance to date.

This paper describes the CFD analyses performed to support the design and testing of turbofan nozzles with the wedge shaped

[1]Corresponding author.

Contributed by the Fluids Engineering Division of ASME for publication in the JOURNAL OF FLUIDS ENGINEERING. Manuscript received March 21, 2008; final manuscript received January 22, 2009; published online March 9, 2009. Assoc. Editor: Zvi Rusak. Paper presented at the AIAA Aerospace Sciences Meeting, 2008.

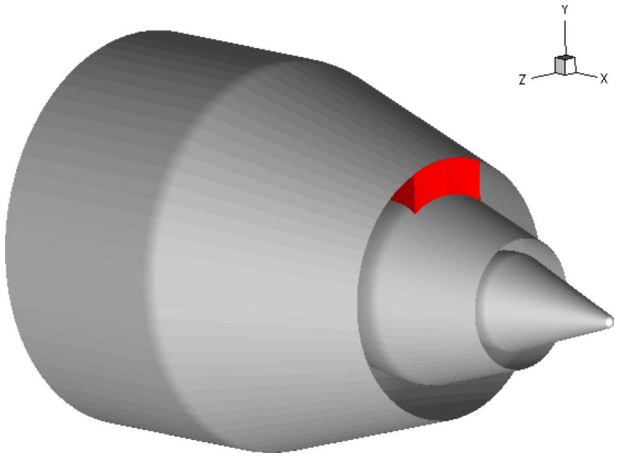

Fig. 1 Turbofan nozzle with wedge installed in the fan stream

flow deflectors. The CFD analyses consisted of three parts: (1) pretest predictions to verify the wedge design and its effect on the flow field, (2) performance calculations to examine the performance penalties due to the noise reduction scheme, and (3) validation of the CFD methodology against experimental data. While estimates of jet noise cannot be obtained directly from the CFD analyses, the predicted levels of turbulent kinetic energy can be used to infer the impact of the wedge deflector on the noise field at a rudimentary level.

2 Description of Nozzles and Flow Conditions

The nozzles used in this study were originally designed for NASA under the Advanced Subsonic Technology program for investigating mixing enhancement devices to reduce jet noise [10]. The baseline nozzles with no mixing devices were used here. For this study a wedge flow deflector was placed in the fan stream. The wedge sits completely inside the nozzle, and the base of the wedge is coincident with the nozzle exit (Fig. 1). Three different nozzles were analyzed: 3BB, 4BB, and 5BB (Fig. 2). The 3BB and 5BB nozzles both have an external nozzle plug in the core stream and have nozzle bypass ratios (BPR) of 5 and 8, respectively. These two nozzles share the same fan flow geometry. The core flow nozzle section was replaced to affect the bypass ratio change. The 4BB nozzle has an internal plug in the core flow and has a bypass ratio of 8. This nozzle was studied computationally but not tested in the experiment. All three nozzles have the same fan diameter of 9.63 in. (24.5 cm).

The shape of the wedge deflector studied here is the same as the wedge used by Papamoschou [1–3] in his initial studies. The wedge has a half angle of 11 deg and a base width of 3.44 in. (8.74 cm). The upper and lower surfaces of the wedge conform to the internal contours of the fan stream. The wedge reduces the exit area of the fan stream by 14%.

It is anticipated that the wedge deflector would be incorporated as a pair of flaps into the existing structure of the engine. For underwing mounted engines found on most large transport aircraft, the flaps could be placed in the pylon. For other installations, side mounted or more highly integrated installations, the flaps could be incorporated into a strut. In either case the flaps would deploy to form a wedge on take-off and retract for cruise. The pylons for underwing mounted engines already deflect some fan flow. However, additional flow deflection is probably necessary to maximize noise reduction.

The calculations performed for the pretest predictions and performance analyses were done using cycle data for a representative take-off condition. Details of the operating conditions are in Table 1. The experiment was run subsequent to the CFD analyses, and the data were taken at slightly different conditions. The analyses were rerun at these conditions for code validation purposes (Table 2). For the 3BB validation case, the nozzle was tested with static freestream conditions. This analysis was run with a freestream Mach number of 0.05 for numerical stability. Two 5BB cases were run, one with heated streams and one with cold streams. Both cases had a freestream Mach number of 0.20. Because the wedge deflectors will most likely be removed from the flow after take-off, only that flight condition was analyzed.

3 Analysis Procedure

3.1 Geometry Definition. The computational grids (Fig. 3) were generated using the Gridgen Version 15 software [11]. The database, which provides the geometry for the grid generator, was taken directly from the computer aided drafting (CAD) file used to design and build the experimental model hardware. The grids are a structured multiblock type, with separate grid blocks represent-

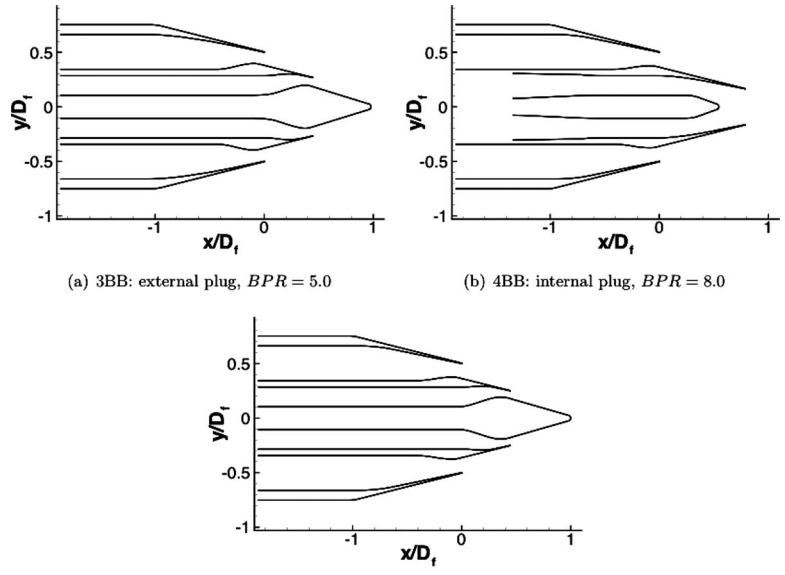

(a) 3BB: external plug, $BPR = 5.0$

(b) 4BB: internal plug, $BPR = 8.0$

(c) 5BB: external plug, $BPR = 8.0$

Fig. 2 Schematic drawings of NASA GRC turbofan nozzles

Table 1 Nozzle operating conditions for performance calculations

		Fan			Core			Freestream		
Nozzle	BPR	NPR	T_0 (K)	U (m/s)	NPR	T_0 (K)	U (m/s)	p_∞ (kPa)	T_∞ (K)	M_∞
3BB	5.0	1.83	364	340	1.68	833	480	98.6	294	0.29
4BB	8.0	1.57	347	290	1.52	844	437	98.6	294	0.29
5BB	8.0	1.62	356	303	1.42	832	399	98.6	294	0.29

Table 2 Nozzle operating conditions for comparison to experiment

		Fan			Core			Freestream		
Nozzle	BPR	NPR	T_0 (K)	U (m/s)	NPR	T_0 (K)	U (m/s)	p_∞ (kPa)	T_∞ (K)	M_∞
3BB hot	5.0	1.83	356	336	1.68	833	480	98.6	298	0.00[a]
5BB hot	8.0	1.62	356	303	1.42	832	399	98.6	298	0.20
5BB cold	8.0	1.42	298	239	1.86	298	311	98.6	298	0.20

[a]CFD analysis used M_∞=0.05 for numerical stability.

ing the following: (1) the internal primary flow path, (2) the external primary flow path including the plug, (3) the internal secondary flow path, (4) the external secondary flow path, (5) the nacelle, and (6) the jet plume region (Fig. 4). Dimensions of the grids are given in Table 3. At block interfaces the grids are not contiguous, and a Roe-based zone coupling algorithm is used to pass the fluxes between blocks.

The grids for the baseline nozzles with no wedge deflector were planar, taking advantage of the axisymmetric geometry. A total of 66,734 points were used. The grids for the nozzles with the wedge deflector were three dimensional: a 180 degree segment, taking advantage of the symmetry about the xy-plane (vertical streamwise) plane. A total of 6,072,794 grid points were used.

3.2 Flow Solution. The flow solver used for all the computations was Wind version 5.0 [12]. Wind is a general purpose Reynolds averaged Navier–Stokes (RANS) equation solver. All the calculations presented here used the same code options. The default numerical scheme was used: implicit time stepping and a second-order physical Roe scheme for stretched grids. Turbulence was modeled using the Menter [13] shear stress transport (SST) model. No additional corrections (i.e., compressibility corrections) were used in the model.

Grid sequencing in all three computational directions was used during the flow solution. Sequencing solves the equations on a reduced grid to speed convergence. The sequenced results are then interpolated onto the finer grid for continued processing. One level of sequencing involves removing every other grid point from the previous level. The solution started at two levels of sequencing and progressed to the full grid solution. Nozzle force measurements were monitored, and the sequencing was reduced when the nozzle force converged on that grid level. Nozzle force measurements between the final grid level and the next sequenced level

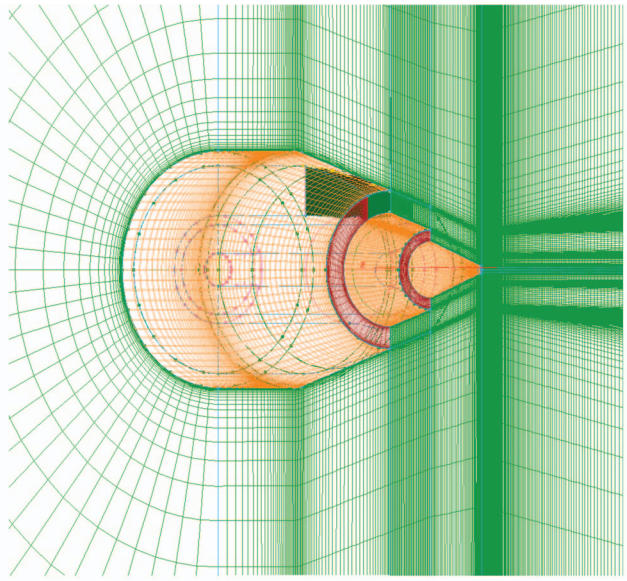

Fig. 3 Grid of the 5BB nozzle with wedge installed in the fan stream

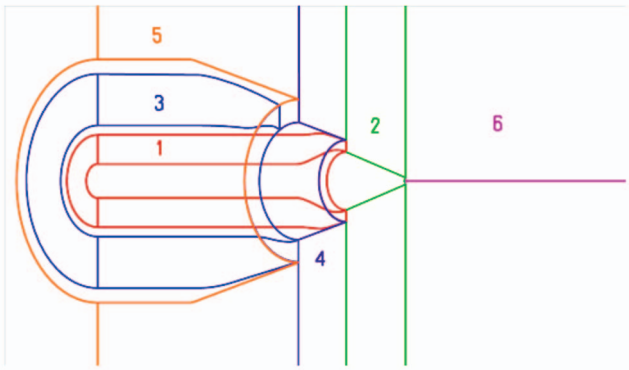

Fig. 4 Grid blocking structure

Table 3 Dimensions of the computational grid

Block	Axial	Radial	Azimuthal	Total
1	73	45	91	298,935
2	53	165	91	795,795
3	65	45	91	266,175
4	45	109	91	446,355
5	69	45	91	282,555
6	253	173	91	3,982,979
Wedge (3D)				6,072,794
Baseline				66,734

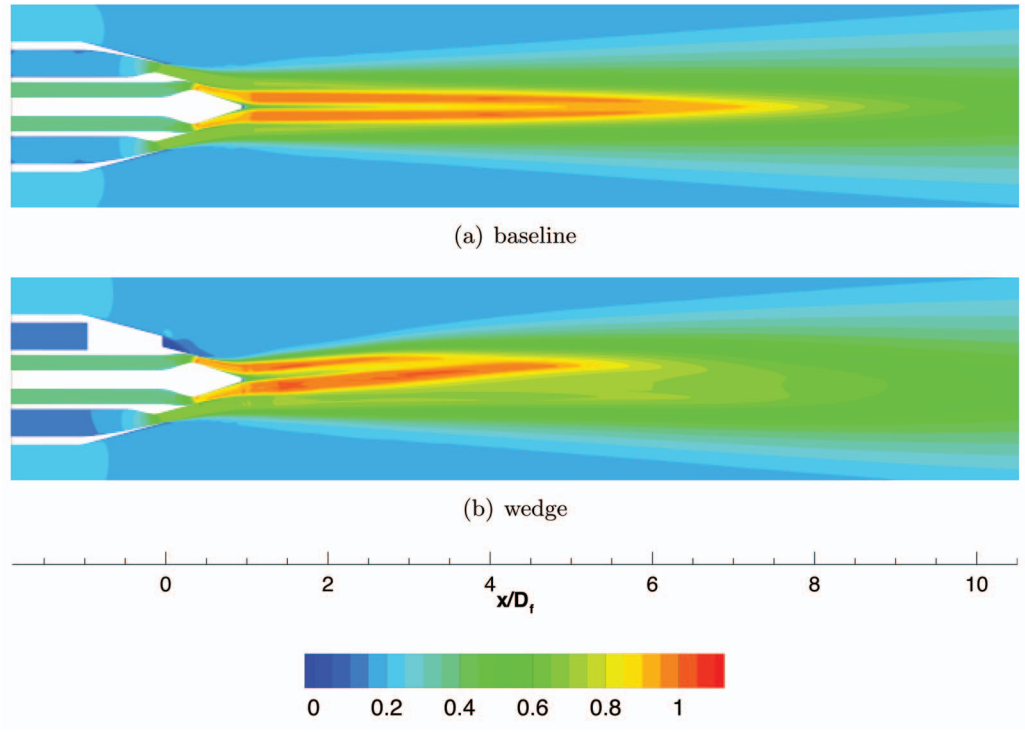

Fig. 5 Streamwise (*xy*-plane) contours of *u*-velocity, u/U_c, for 3BB nozzles

agreed within 1%, indicating that grid convergence was obtained. Local time stepping was used to achieve a steady state solution. For the 3BB case at near static ambient conditions (M_∞=0.05), the solution did not converge in this manner. For this case the solution was switched to global time stepping, and convergence to a steady state was achieved.

4 Results

4.1 Examination of the Flow Fields. The noise benefit of the offset fan stream concept is predicated on reducing the convective Mach number of the core stream instabilities by lengthening the fan stream to cover or shield a larger portion of the high speed

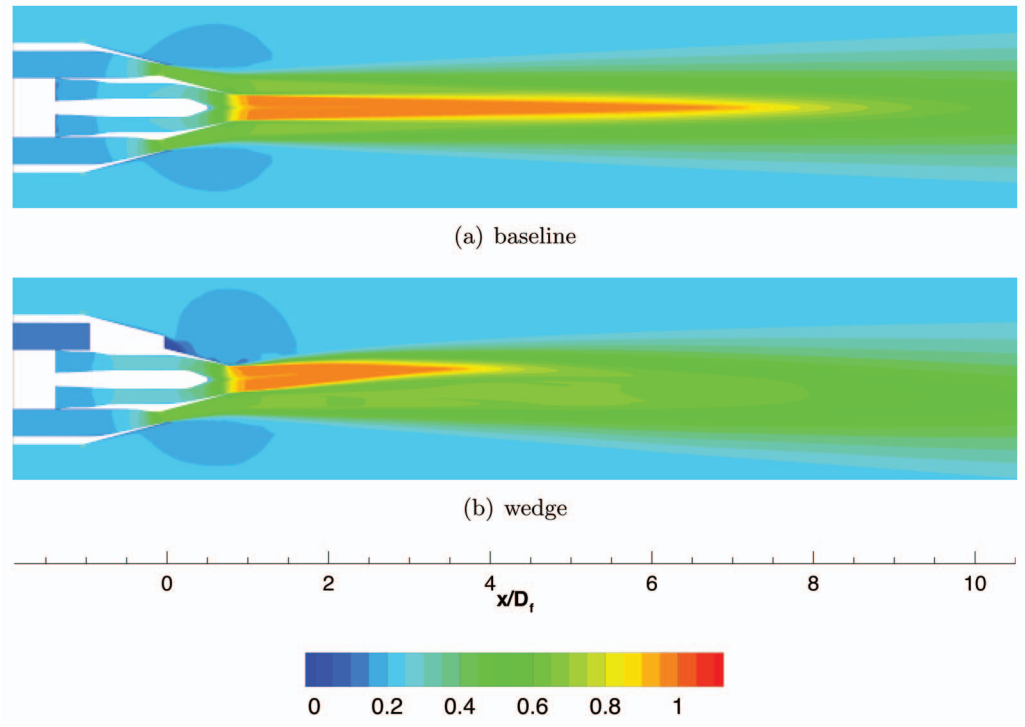

Fig. 6 Streamwise (*xy*-plane) contours of *u*-velocity, u/U_c, for 4BB nozzles

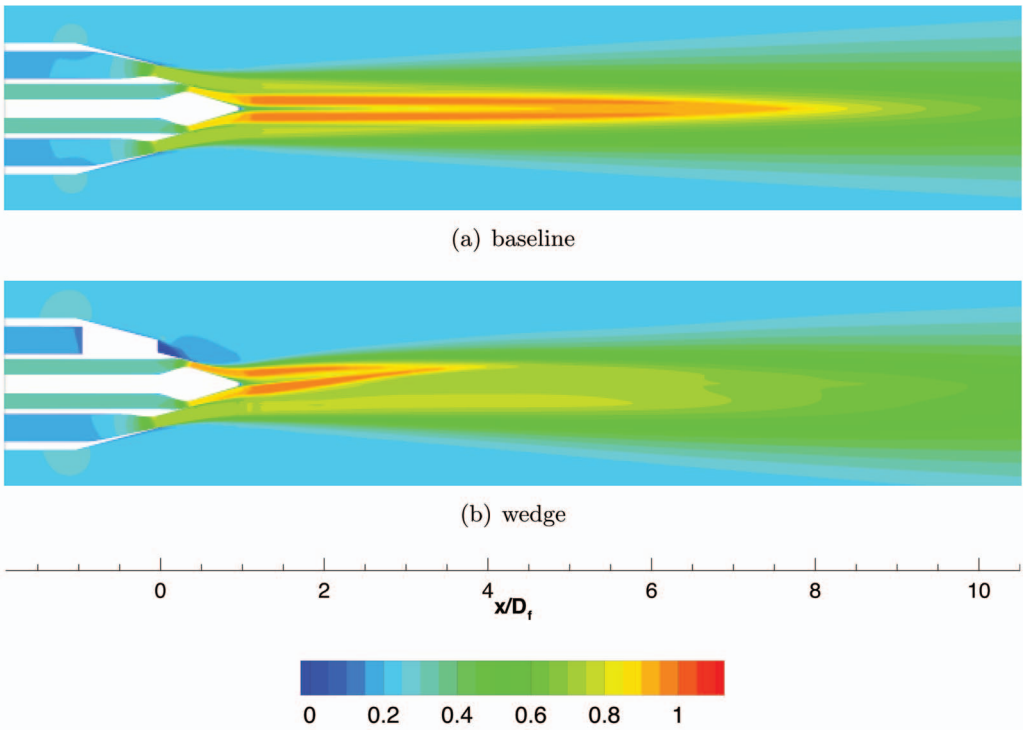

Fig. 7 Streamwise (*xy*-plane) contours of *u*-velocity, u/U_c, for 5BB nozzles

primary flow [14]. The increased interface between the primary and secondary streams reduces the region of large velocity gradients (between the core and surrounding flow) and thus reduces the convective Mach number and the strength of the noise sources. In the context of the CFD solutions presented, the reduced velocity gradient lowers the resultant turbulent kinetic energy, which can be related to the noise sources in jets [15]. This effect can be seen in the streamwise (*xy*-plane) velocity and turbulent kinetic energy contours in Figs. 5–10. Data are presented for all three nozzles (3BB, 4BB, and 5BB), and the results show that all three flow fields behave similarly.

Velocity contours in the streamwise planes compare the wedge nozzle to the baseline nozzle (Figs. 5–7). These contours show that the presence of the wedge directs the core flow upward and significantly shortens the core stream's potential core. The layer of fan flow on the underside of the jet plume is substantially thicker.

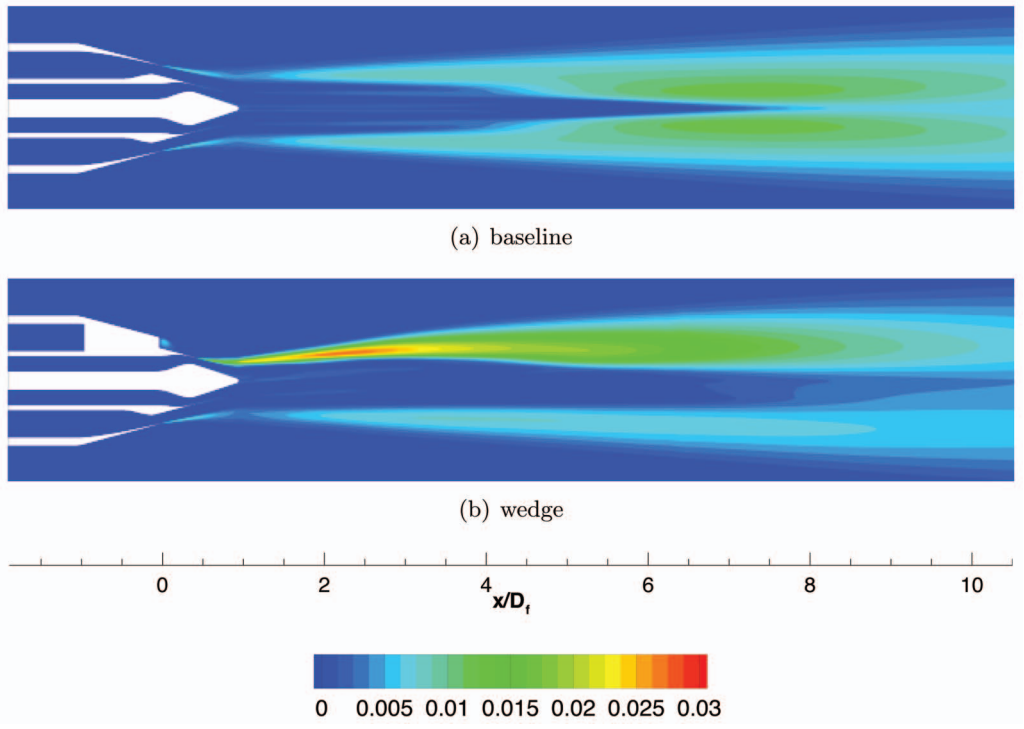

Fig. 8 Streamwise (*xy*-plane) contours of turbulent kinetic energy, k/U_c^2, for 3BB nozzles

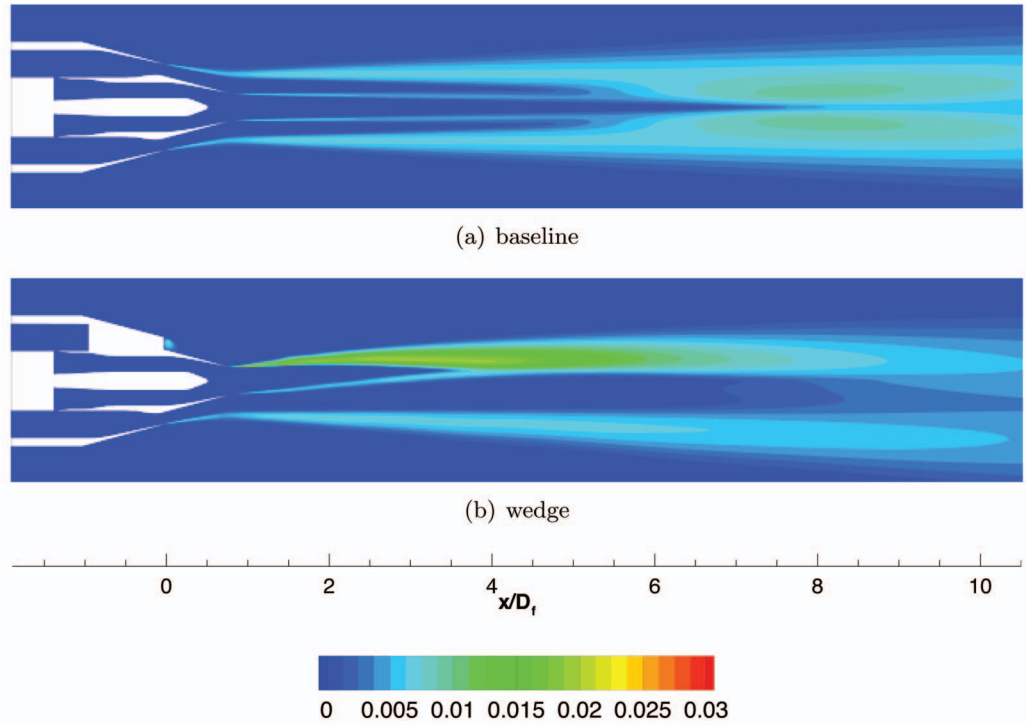

Fig. 9 Streamwise (*xy*-plane) contours of turbulent kinetic energy, k/U_c^2, for 4BB nozzles

While it is difficult to quantify, the fan flow does appear to have lengthened. This can be seen by the presence of large regions of flow near the fan exit velocity ($u/U_c=0.7$) as far downstream as $x/D_f=6$. A low-velocity region immediately behind the wedge indicates that a large recirculation region is present there.

Turbulent kinetic energy contours in the streamwise planes are shown in Figs. 8–10. On the upper side of the exhaust plume, levels of k/U_c^2 are increased and the peak level has moved upstream, closer to the nozzle exit. On the lower side of the exhaust plume, the levels of k/U_c^2 have been reduced. This is the desired effect. A small local peak in turbulence levels is seen directly behind the wedge, again indicating a separated region and potential noise source.

The movement of the fan flow induced by the wedge deflector is more easily seen in cross-planes downstream of the nozzle exit (Figs. 11–16). The fan flow moves to the lower half of the exhaust

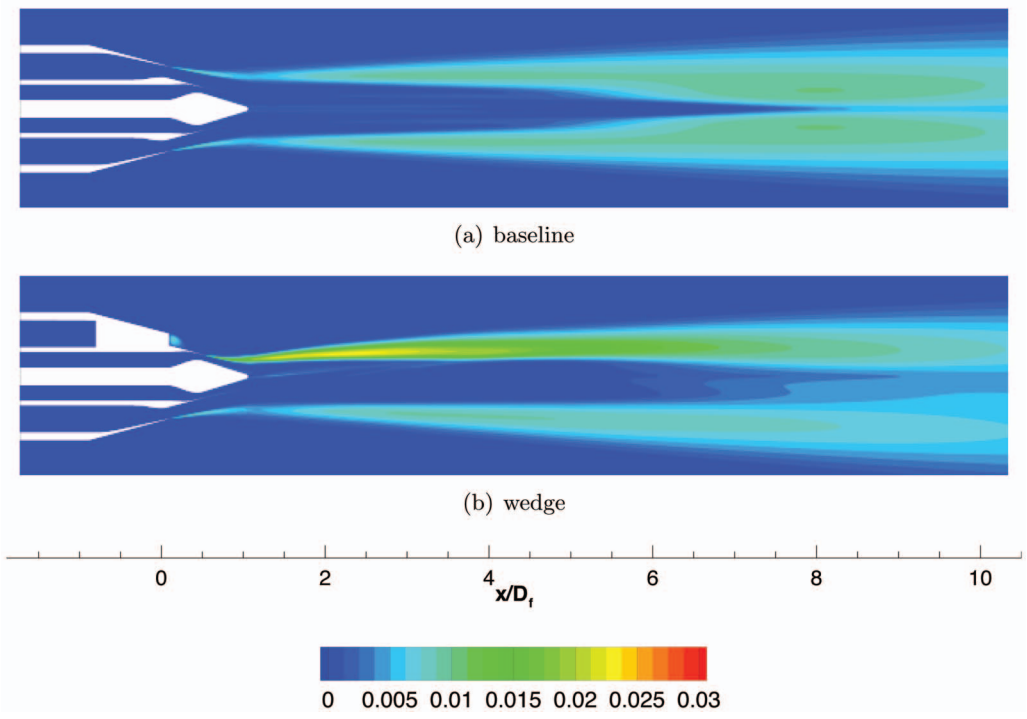

Fig. 10 Streamwise (*xy*-plane) contours of turbulent kinetic energy, k/U_c^2, for 5BB nozzles

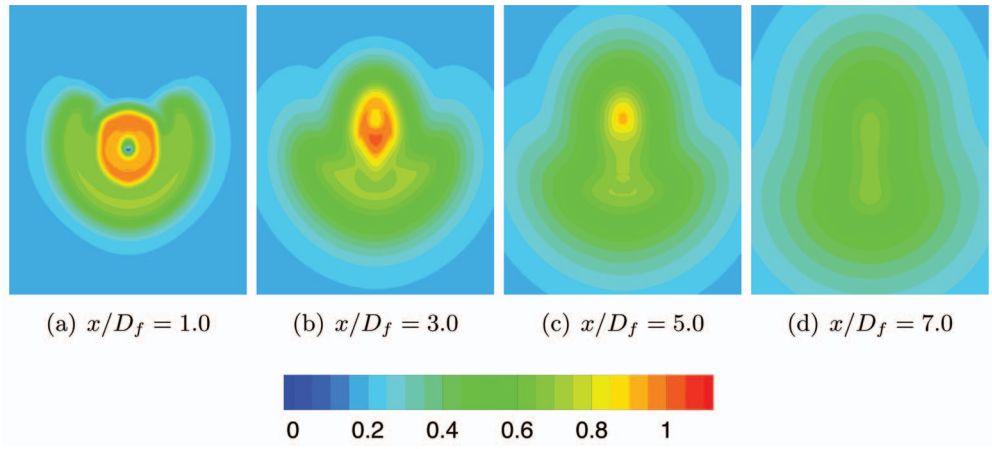

Fig. 11 Cross-plane (*yz*-plane) contours of *u*-velocity, u/U_c, for 3BB nozzles

plume, and at x/D_f=5.0 the fan stream is almost completely below the core flow. The upper portion of the core flow comes in direct contact with the freestream flow and is not buffered by the fan flow. This region of large velocity gradients results in high turbulence levels and will certainly increase the noise on this side of the nozzle. At x/D_f=3.0 high turbulence levels are present from the top of the nozzle down to the sideline position (0–90 deg, measured from the vertical). The turbulent kinetic energy levels resulting from the core stream interacting directly with the freestream are on the order of an isolated jet operating at the core stream conditions and could result in very high noise levels at sideline and above the nozzle. The lower side has much lower turbulence levels and should result in lower noise on this side of the exhaust plume. These conclusions correspond well with the findings in the experimental noise measurements [6]. It appears that the wedge moved too much fan flow, exposing the core flow to the freestream. A less aggressive wedge design may improve the noise characteristics of this device. Lower wedge angles

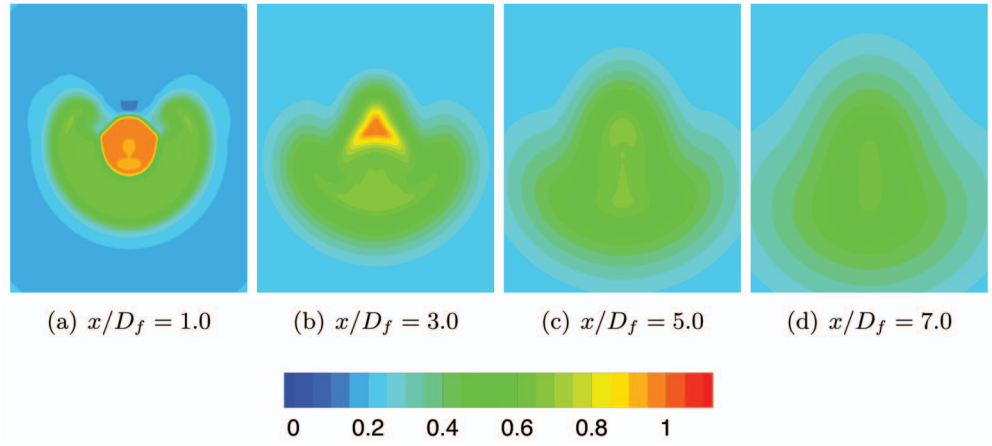

Fig. 12 Cross-plane (*yz*-plane) contours of *u*-velocity, u/U_c, for 4BB nozzles

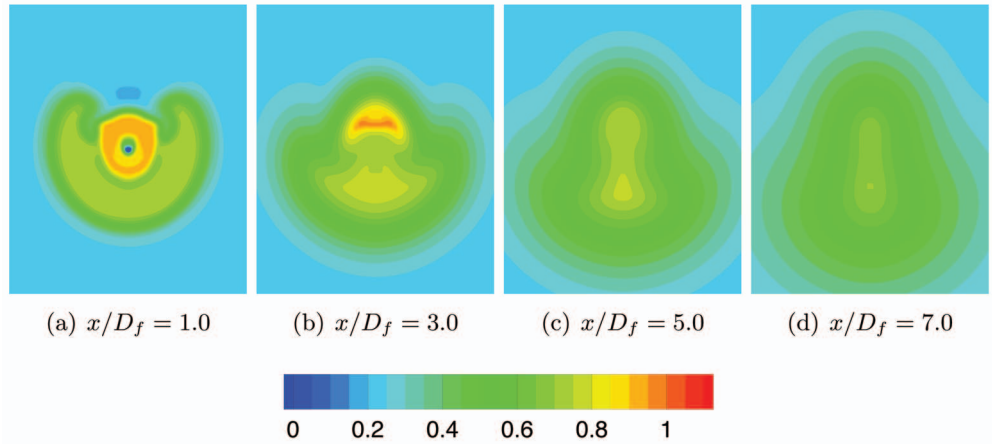

Fig. 13 Cross-plane (*yz*-plane) contours of *u*-velocity, u/U_c, for 5BB nozzles

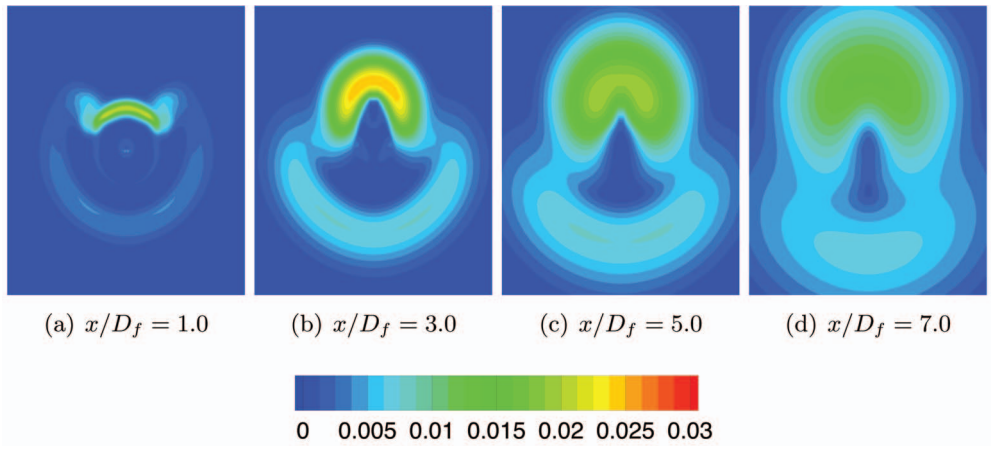

Fig. 14 Cross-plane (*yz*-plane) contours of turbulent kinetic energy, k/U_c^2, for 3BB nozzles

should be investigated to reduce the deflection of the fan flow. Also, shorter wedges that do not span the entire fan duct height may prevent the core flow from being completely exposed to the freestream.

4.2 Nozzle Performance

4.2.1 Calculation Procedure. Nozzle performance was computed using the Wind utility, CFPOST. Stream thrust was computed at the fan and core exits. Pressure and viscous forces were computed on the remaining surfaces: core nozzle lip, fan nozzle lip, plug, splitter between fan and core, nacelle, and wedge base.

Nozzle performance will be reported in two ways. First, the total thrust of the nozzle with wedge deflector will be expressed as a fraction of the baseline nozzle thrust

$$F/F_{\text{baseline}} \tag{1}$$

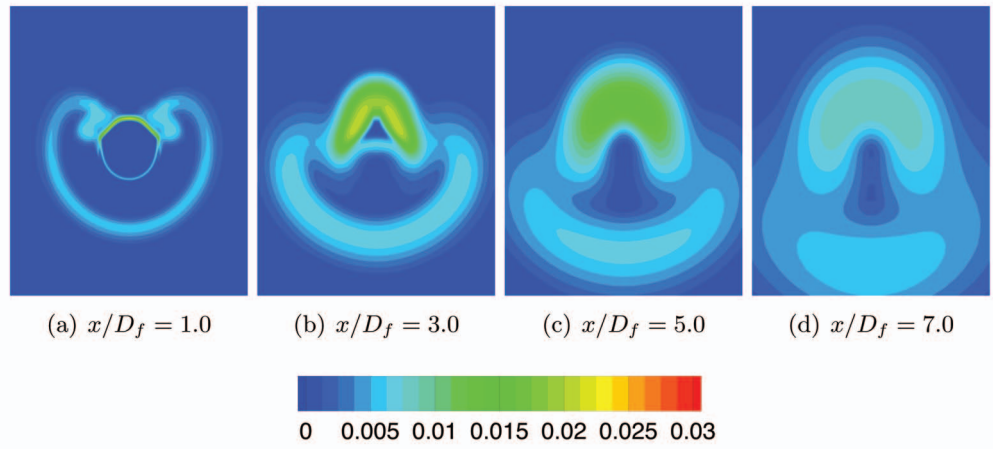

Fig. 15 Cross-plane (*yz*-plane) contours of turbulent kinetic energy, k/U_c^2, for 4BB nozzles

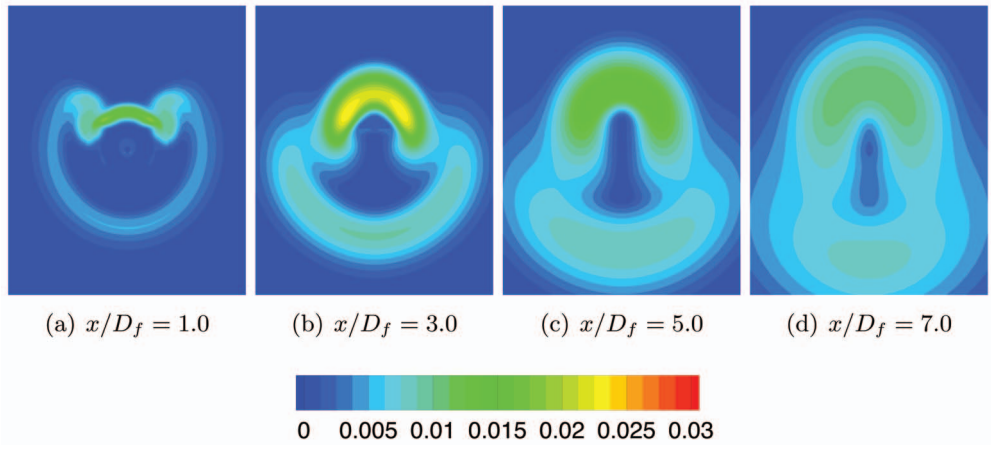

Fig. 16 Cross-plane (*yz*-plane) contours of turbulent kinetic energy, k/U_c^2, for 5BB nozzles

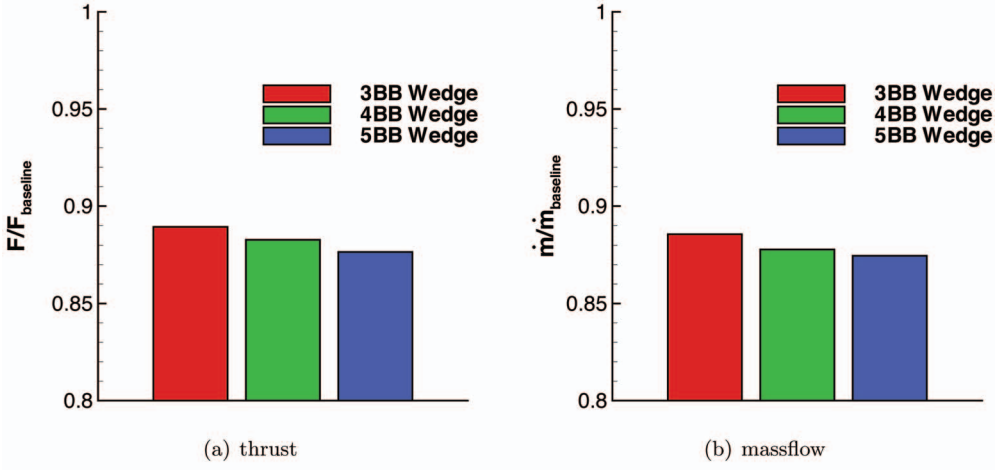

Fig. 17 Ratio of wedge nozzle to baseline nozzle performance

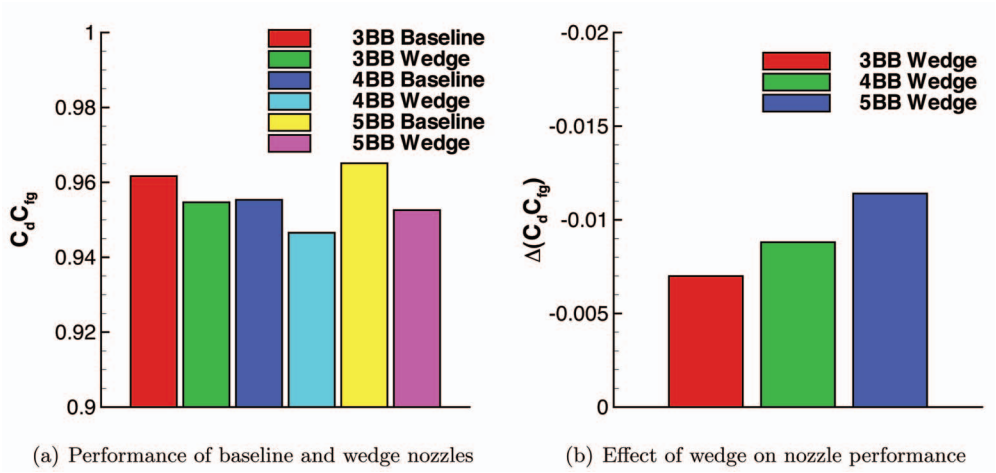

Fig. 18 Nozzle performance expressed as a thrust coefficient

Second, it will be expressed in terms of a thrust coefficient. Typically nozzle performance results are reported using the gross thrust coefficient,

$$C_{fg} = \frac{F_{\text{actual}}}{\dot{m}_{\text{actual}} U_{\text{ideal}}} \tag{2}$$

Using the actual mass flow in the denominator, C_{fg}, removes the deviation from the ideal mass flow from the performance measure. Discharge coefficient is a separate measure for the reduction in mass flow,

$$C_d = \frac{\dot{m}_{\text{actual}}}{\dot{m}_{\text{ideal}}} \tag{3}$$

For subsonic nozzles the mass flow through the nozzle can vary due to downstream effects, and the thrust coefficient does not give a true measure of nozzle performance. In these circumstances, the change in the measured thrust is caused by the change in the nozzle flow rate and not a change in the exit velocity. This is especially true for two-stream nozzles where the behavior of one stream can affect the flow rate of the other. Nozzles with noise suppressing features can also affect flow rates. Therefore, a thrust coefficient that accounts for the change in mass flow rate is used in this paper. It is simply a thrust coefficient based on the ideal mass flow rather than the actual mass flow. It can be conveniently written as the product of the gross thrust coefficient and discharge coefficient,

$$\frac{F_{\text{actual}}}{\dot{m}_{\text{ideal}} U_{\text{ideal}}} = \frac{\dot{m}_{\text{actual}}}{\dot{m}_{\text{ideal}}} \frac{F_{\text{actual}}}{\dot{m}_{\text{actual}} U_{\text{ideal}}} = C_d C_{fg} \tag{4}$$

For the cases where the wedge is installed in the nozzle, the ideal mass flow is computed using the reduced nozzle exit area.

A baseline case, no wedge, was calculated for each nozzle geometry. Performance of the wedge nozzles is referenced to the baseline and is reported as $\Delta(C_d C_{fg})$,

$$\Delta(C_d C_{fg}) = (C_d C_{fg})_{\text{wedge}} - (C_d C_{fg})_{\text{baseline}} \tag{5}$$

4.2.2 Performance Results. The thrust of the wedge nozzles expressed as a ratio to the baseline nozzle thrust is shown in Fig. 17(*a*). The wedge has created thrust losses between 11% and 13%. The reason for these losses is clear. Figure 17(*b*) shows the loss in mass flow of wedge nozzles, expressed as a ratio to the baseline nozzles. Total mass flow reduction also varies between 11% and 13%. This reduction is due entirely to the reduction in fan mass flow, which is approximately 14% for all three cases. These losses are a direct result of the blockage created by the wedge (14% of the fan exit area). For this noise reduction concept to be viable, the engine would have to be oversized to accommodate the performance penalty at take-off. Reducing the size of the wedge, as suggested for acoustic reasons, would reduce the thrust penalty. An alternative concept, placing the wedge external to the fan nozzle on the splitter, has been proposed and should eliminate this loss of fan mass flow [16].

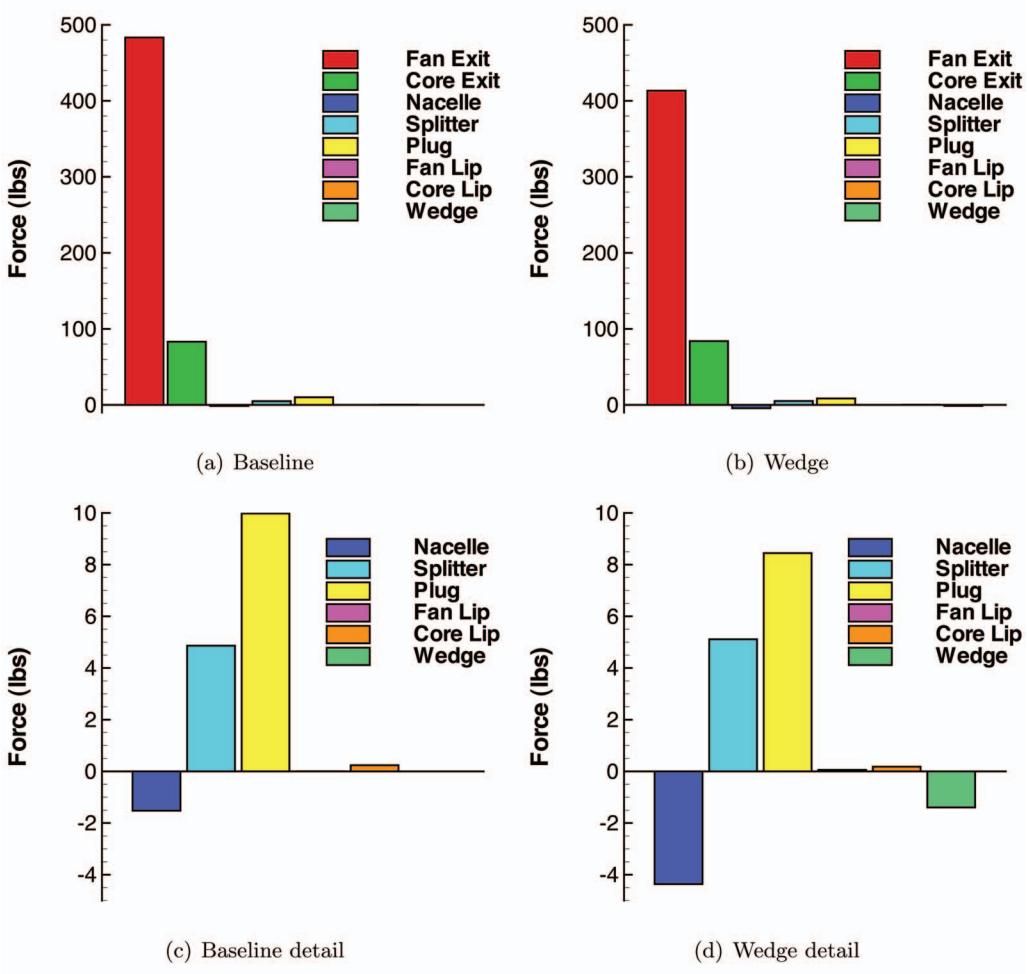

Fig. 19 Force breakout for 5BB baseline and wedge nozzles

Nozzle performance expressed as a thrust coefficient, $C_d C_{fg}$, for both the baseline and wedge configurations for all three nozzles is shown in Fig. 18(*a*). For the wedge nozzles, this performance measure uses the ideal conditions based on the actual exit area and therefore does not include the loss due to blockage. The external plug nozzles have uniformly higher performance than the internal plug nozzle. Figure 18(*b*) shows the decrement in performance due to the wedge. The losses due to the wedge vary

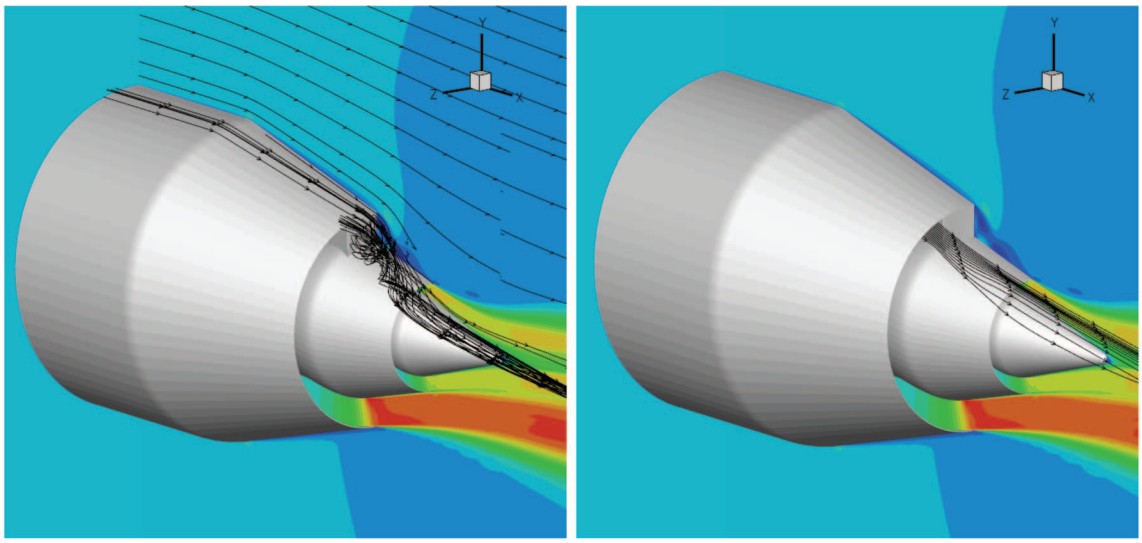

Fig. 20 Streamlines for the 5BB nozzle

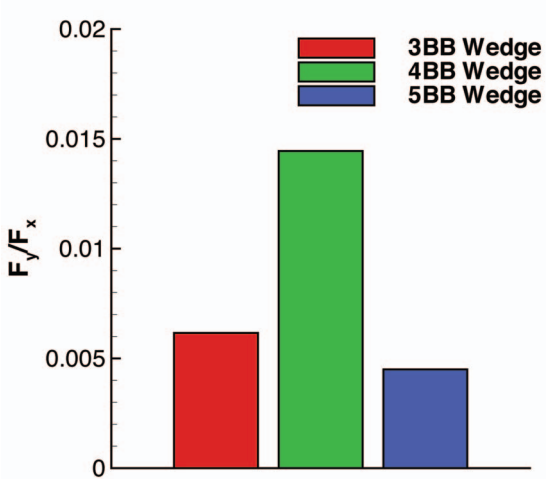

Fig. 21 Component of the vertical thrust

from about 0.7% to 1.1% and appear to be relatively low, considering the large base area created by the wedge. A detailed breakout of the forces that comprise the thrust calculation is shown for the 5BB baseline and wedge nozzles in Fig. 19. The figure confirms that the primary loss mechanism is the loss in fan stream thrust due to the reduced mass flow. The presence of the wedge reduces the positive force on the nozzle plug and increases the drag on the nacelle. The base drag on the wedge surface is a relatively minor component. This is somewhat surprising but can be explained by the streamlines in Fig. 20. The figure shows that the flow that separates and recirculates behind the base of the wedge is the external flow over the nacelle. This also shows the linkage between the presence of the wedge and the increased nacelle drag (Fig. 19). The fan flow, the primary contributor to the thrust, is turned by the wedge to create the offset stream but does not separate behind the wedge, which would result in large thrust losses.

By examining nozzle performance using the $C_d C_{fg}$ parameter, we can see that the losses created by the wedge deflector would be acceptable if the reduction in mass flow could be removed or accounted for in the nozzle design. The wedge deflector could be

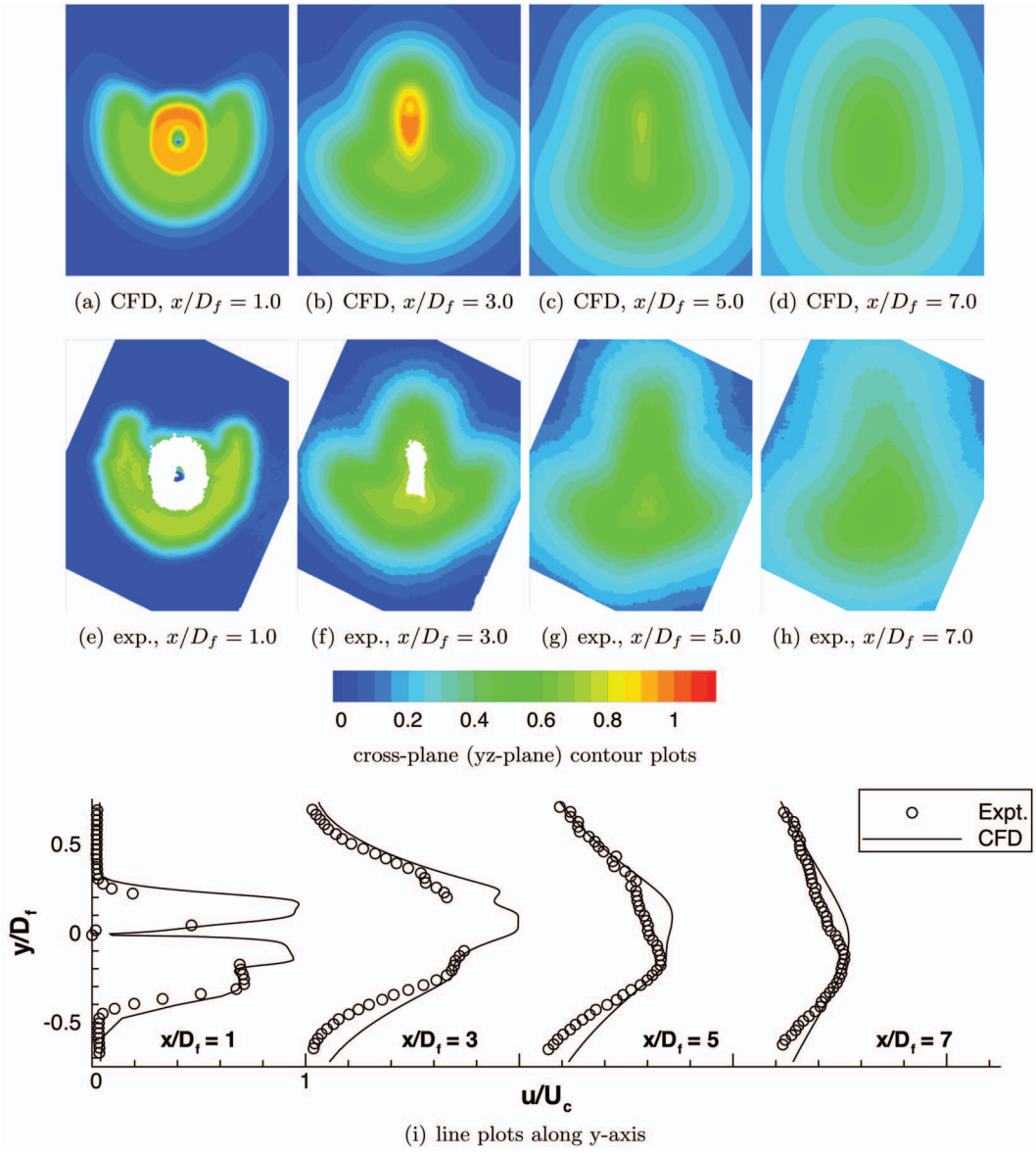

Fig. 22 Comparison to experiment; *u*-velocity, u/U_c, for the 3BB nozzle with wedge, hot conditions

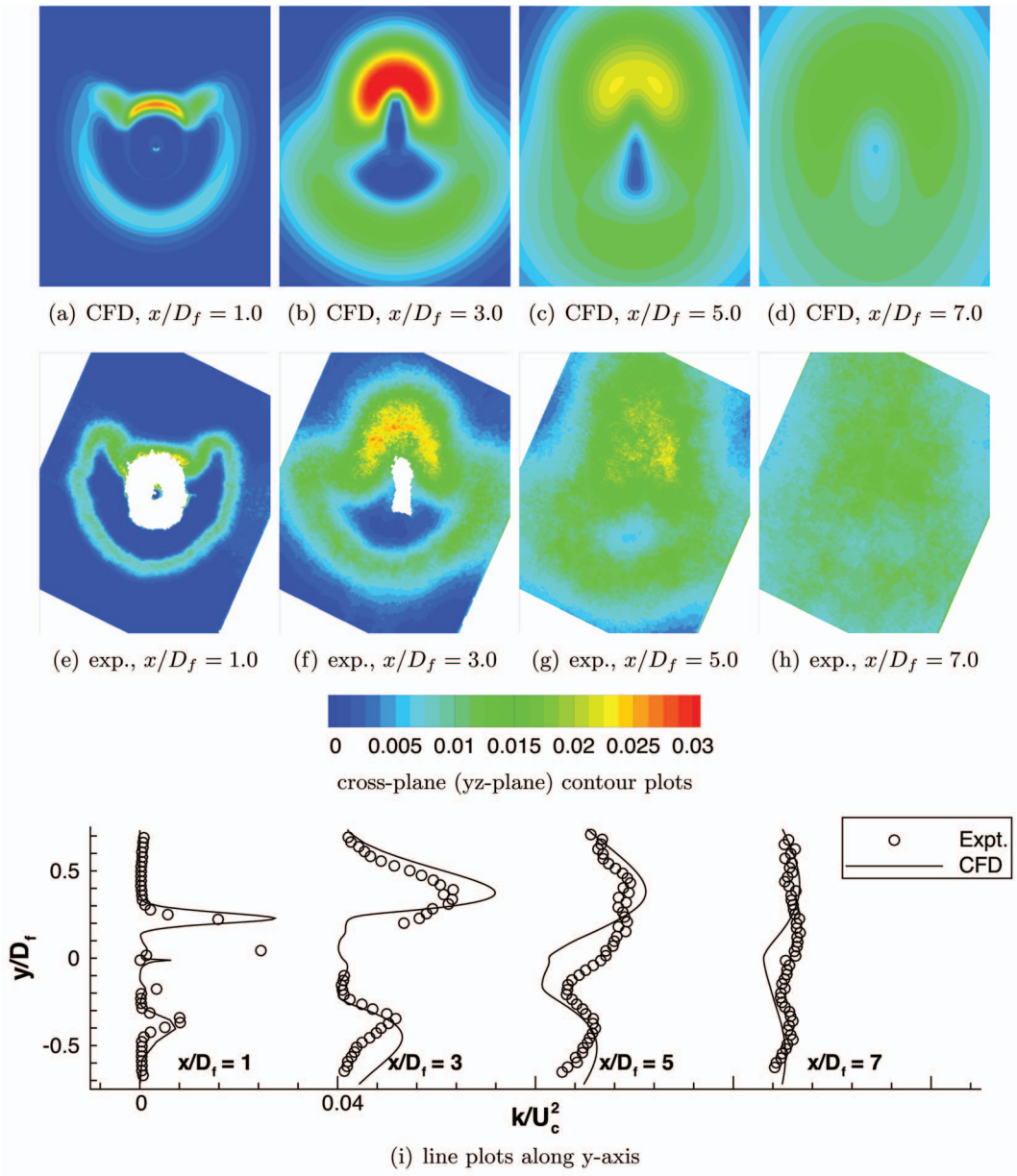

Fig. 23 Comparison to experiment; turbulent kinetic energy, k/U_c^2, for the 3BB nozzle with wedge, hot conditions

a viable noise reduction concept if the wedge size could be significantly reduced or if an external wedge that did not reduce the fan flow rate was employed.

The wedge induces a downward movement of the fan flow and a corresponding upward movement of the core flow. The resulting vertical component of the nozzle thrust is presented in Fig. 21. The data indicate that the wedge induces a very small vertical component to the thrust. The external plug nozzles have a smaller component, about 0.5% of the axial thrust, and the internal plug has a slightly larger component, approximately 1.5% of the axial thrust.

The wedge deflector was one of three devices used to offset the fan stream examined in NASA's OST program. The performance of the other two devices, vane deflectors and s-duct nozzles, were also analyzed using a similar CFD method [5]. The performance of all three devices are compared in the Appendix of Ref. [17].

4.3 Comparison to Experiment. Once the experimental test program was carried out, the CFD analyses were rerun to match the experimental conditions. The same computational grids, code version, and code options were used. The experimental data were withheld until the predictions were complete, and no attempts were made to adjust code parameters to better match the data.

The nozzles were tested in the NASA Glenn NATR facility [4]. The NATR is a 53 in. (135 cm) diameter free jet facility with a maximum Mach number of 0.30. The nozzles were mounted in the NATR on the high flow jet exit rig, which provides high pressure and high temperature air to both fan and core nozzle streams. The experimental data consisted of particle image velocimetry measurements of instantaneous velocity components in the nozzle plume [18]. The data were measured in planes parallel to the nozzle exit at distances of 1.0, 1.5, 2.0, 3.0, 5.0, and 7.0 fan diameters downstream of the fan nozzle exit. A complete description of the experiment including both the PIV shown here and the acoustic measurements is given by Brown et al. [6]. The measured u-velocity (axial component) and turbulent kinetic energy were

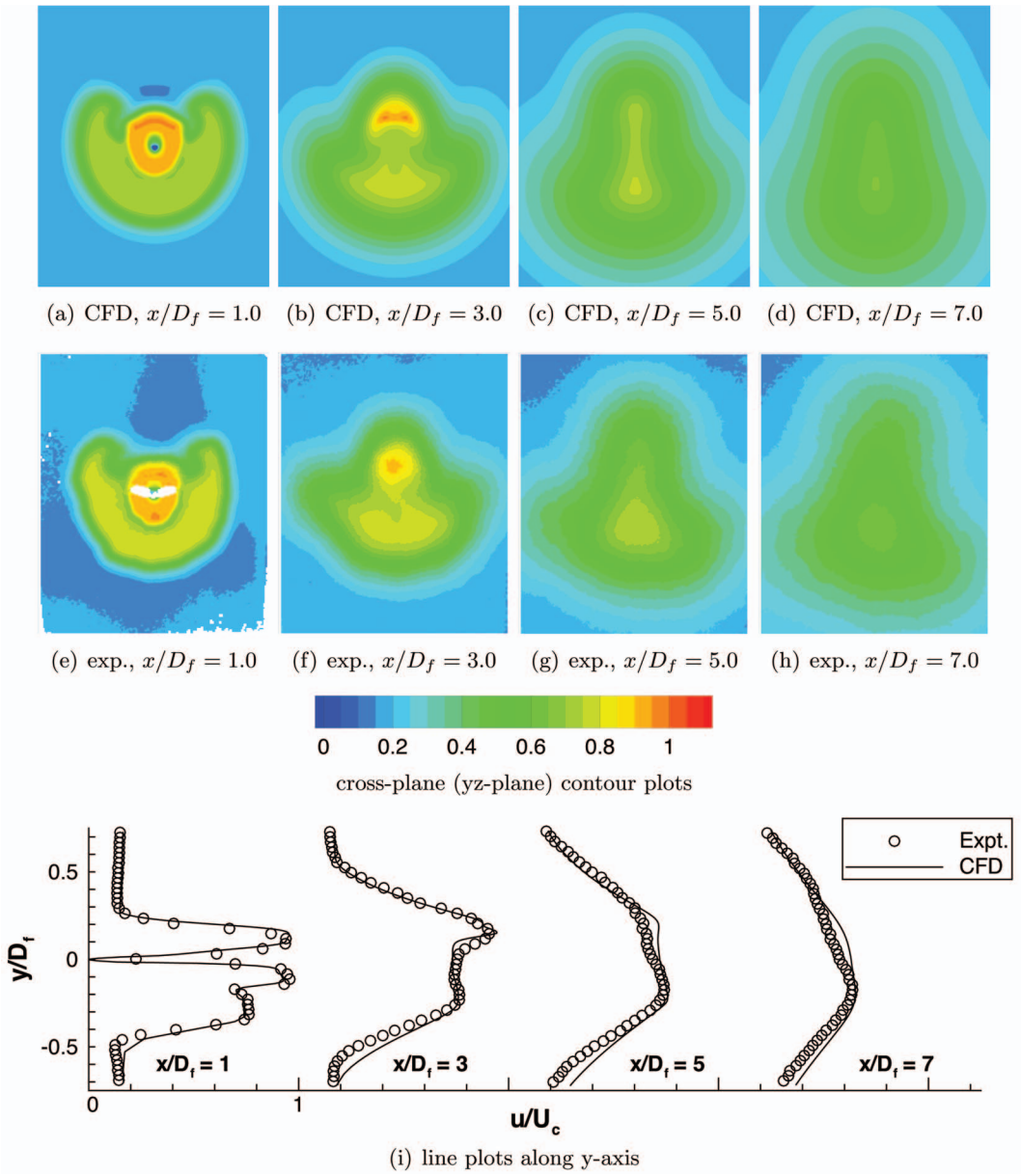

Fig. 24 Comparison to experiment; *u*-velocity, u/U_c, for the 5BB nozzle with wedge, hot conditions

compared with the predictions for three wedge nozzle cases listed in Table 2. Comparisons for the baseline nozzle cases can be found in Ref. [17].

The 3BB nozzle was tested at conditions similar to the pretest predictions, but with a static freestream. The CFD analysis used a small freestream velocity, M_∞=0.05, to prevent numerical instabilities. Plots showing the comparison between prediction and experiment for both axial velocity and turbulent kinetic energy are shown in Figs. 22 and 23. Near the fan exit plane at x/D_f=1.0 and 3.0, the proximity of the nozzle plug to the measurement planes caused a low signal to noise ratio in the experimental data. These data were removed, resulting in the white regions in the center of the plots. The white areas at the corners of the experimental data are due to the orientation of the nozzle relative to the PIV measurement plane. Overall, the agreement between CFD and experiment is very good. The contour plots indicate that the CFD does a good job of predicting the shape of the nozzle plume and the movement of diverted fan flow relative to the core. One does see that the CFD predicts a more diffuse plume shape compared with experiment. Line plots along the *y*-axis (vertical axis) show that the CFD does a good job of predicting the levels of both velocity and turbulent kinetic energy. For this case the Wind code predicts higher peak velocities. This is due to the inclusion of the forward velocity in the freestream for numerical reasons. This small coflow serves to reduce the nozzle mixing rate [19].

The 5BB nozzle was tested at two different flow conditions. The quality of the PIV data near the nozzle exit was much better with only small regions at x/D_f=1.0 where the data were removed. The first case had the same nozzle conditions as the pretest prediction, but the freestream Mach number was 0.20 instead of 0.29. The comparison is presented in Figs. 24 and 25. For this case agreement is very good for both velocity and turbulent kinetic energy. The contour plots show similar agreement in plume shape. The line plots show that there is excellent agreement in the prediction of both velocity and turbulence levels. The improved agreement in the levels over the 3BB case is most likely due to the fact that the CFD analysis matched the experimental freestream velocity. The second 5BB case was tested at cold nozzle temperatures and a Mach 0.20 freestream. The comparison for this case is presented in Figs. 26 and 27. Again, for all aspects agreement

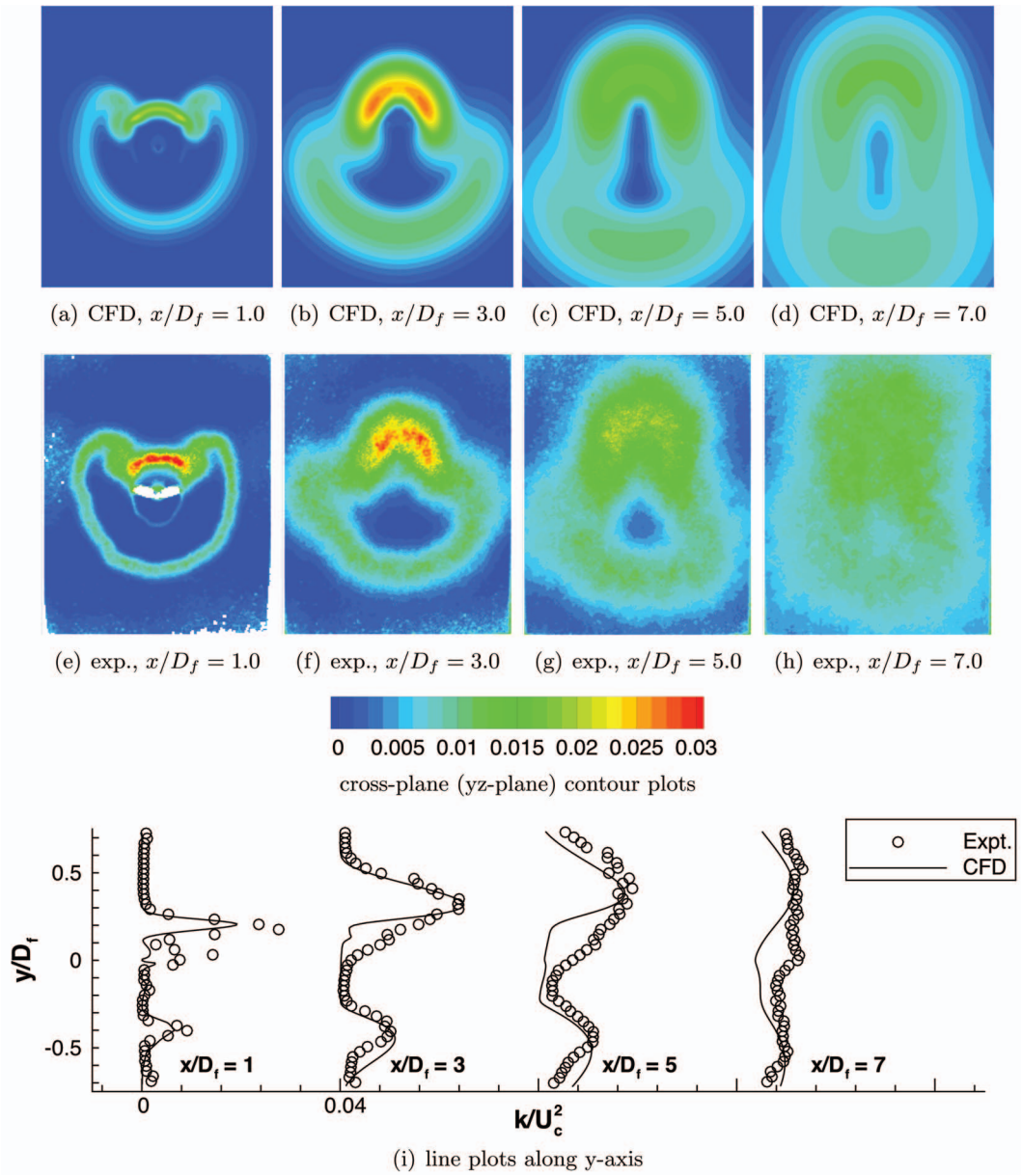

Fig. 25 Comparison to experiment; turbulent kinetic energy, k/U_c^2, for the 5BB nozzle with wedge, hot conditions

between experiment and predictions is very good.

In general for all the cases, very good agreement is achieved between the CFD and experiment in terms of plume shape, velocity levels, and turbulent kinetic energy levels. The CFD predicts slightly higher values of velocity and slightly lower values of turbulent kinetic energy at the downstream locations. This behavior is typical of RANS CFD predictions for jets using two-equation turbulence models [20]. The baseline nozzle cases reported in Ref. [17] similarly exhibit very good agreement. The favorable comparison between the analysis and the experiment is very encouraging and indicates that this RANS CFD technique can be used effectively to optimize the wedge nozzle design and accurately predict the resulting flow fields.

5 Summary and Conclusions

Detailed Reynolds averaged Navier–Stokes calculations of turbofan nozzles with wedge deflectors for noise reduction were carried out to support NASA's Offset Stream Technology program. The nozzles were designed to reduce jet noise at take-off conditions. The computational fluid dynamics calculations were intended to characterize the exhaust plume aiding in wedge design, predict nozzle thrust performance, and validate the computational technique against experimental data.

The predicted flow fields showed that the wedge deflector was effective at redirecting the fan flow to the underside of the exhaust plume, effectively reducing noise on this side of the nozzle. The predictions indicate that the wedge design is too aggressive, deflecting too much flow and exposing the core flow to the freestream on the top and sides of the plume. Predictions of turbulent kinetic energy suggest that noise levels at the sideline and upper side of the nozzle may approach those of an isolated jet at core flow conditions.

Nozzle performance calculations show that the thrust of the nozzle is significantly reduced relative to an unmodified nozzle. This thrust loss is caused by a reduction in mass flow of the fan stream, which is directly proportional to the area reduction of the fan exit caused by the wedge. Thrust losses imparted by the wedge not due to the fan flow reduction are relatively small. If the

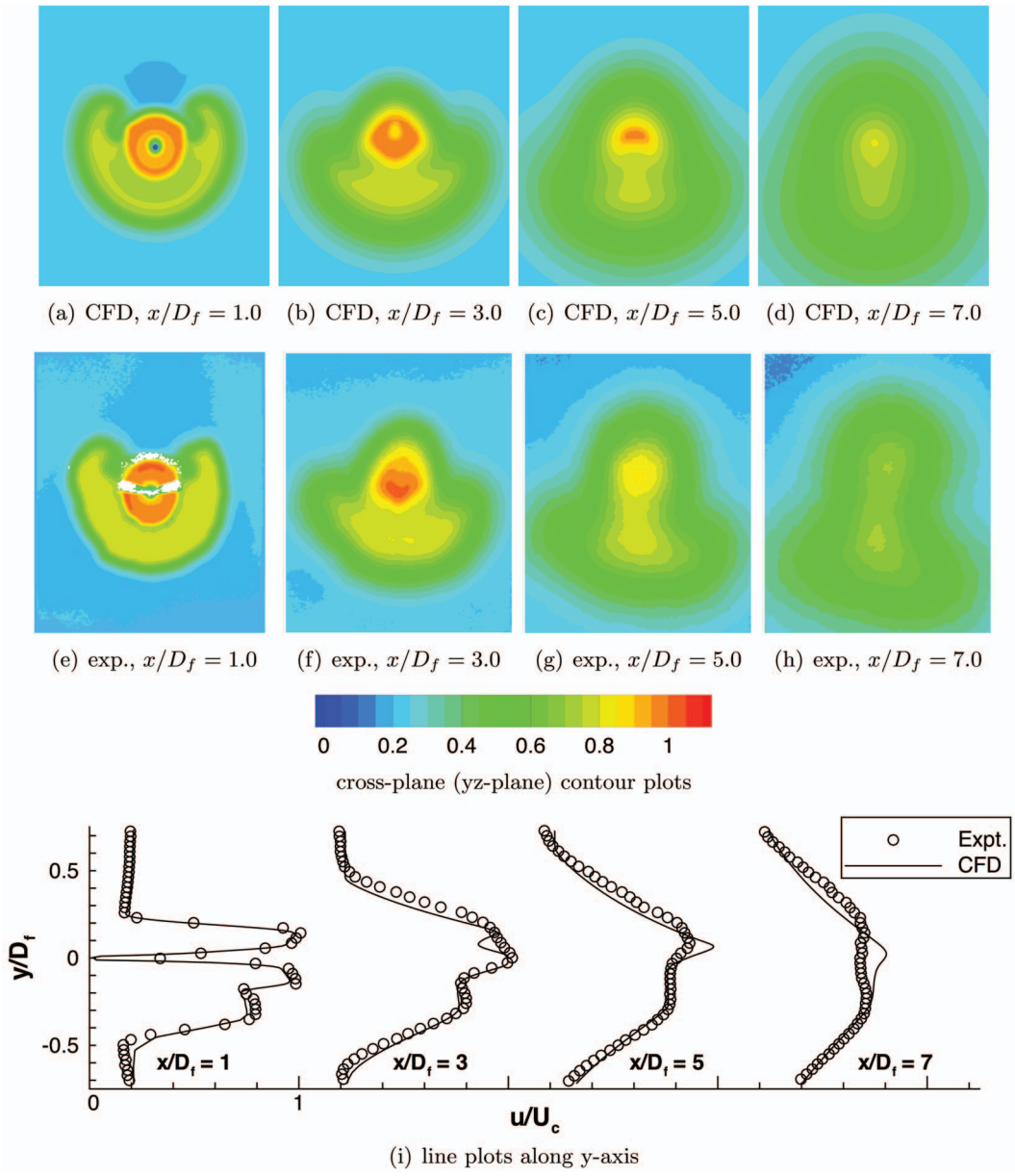

Fig. 26 Comparison to experiment; *u*-velocity, u/U_c, for the 5BB nozzle with wedge, cold conditions

loss in mass flow could be removed or accounted for in the nozzle design, the wedge concept would be viable in terms of performance.

Two of the nozzles considered here were tested at the NASA Glenn NATR. The calculations were rerun to match the experimental test conditions. Predictions of axial velocity and turbulent kinetic energy in several downstream planes parallel to the nozzle exit were compared with experimentally obtained data. The CFD did a very good job of predicting the offset stream nozzles' plume shape. Also, the agreement between the experiment and predicted levels of both axial velocity and turbulent kinetic energy was very good for all nozzle configurations, locations, and flow conditions considered.

Acoustic testing of the nozzles considered here showed that they did not achieve the desired noise reduction. The analyses presented here suggest a smaller, less aggressive wedge diverter would improve the thrust and noise characteristics. This echoes the conclusion from the experimental program. Based on the predicted flow fields, performance calculations, and agreement with experimental data, this study shows that the CFD methodology used here can be used to improve this nozzle concept.

Nomenclature

k = turbulent kinetic energy
$\dot{m}$ = mass flow
p = pressure
u = axial component of velocity
x, y, z = Cartesian coordinates
BPR = bypass ratio
C_d = discharge coefficient
C_{fg} = thrust coefficient
D = diameter
F = nozzle force (thrust)
M = Mach number
NPR = nozzle pressure ratio
T = temperature
U = ideal exit velocity

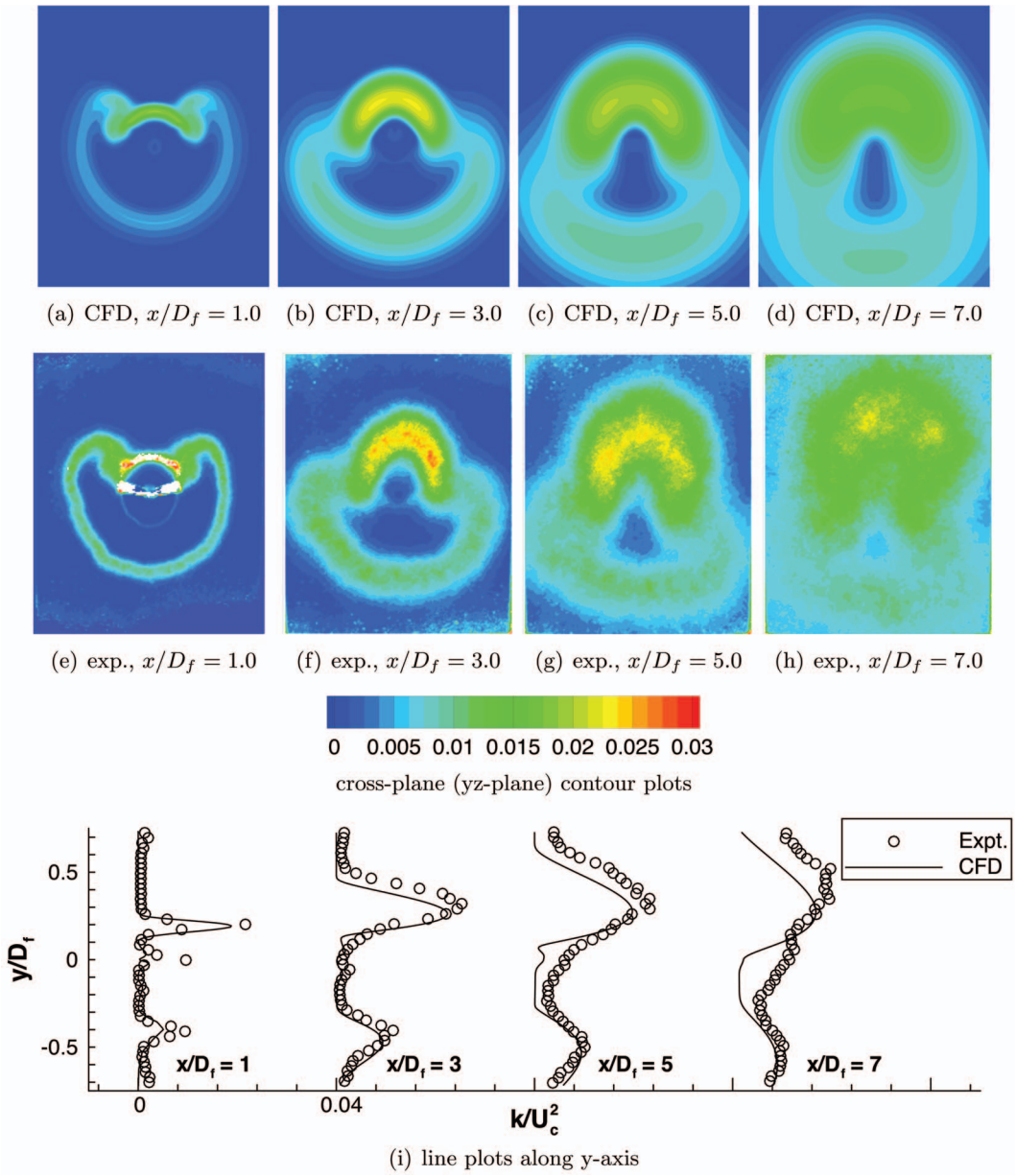

Fig. 27 Comparison to experiment; turbulent kinetic energy, k/U_c^2, for the 5BB nozzle with wedge, cold conditions

Subscripts

actual = measured quantity
baseline = nozzle without flow deflectors
ideal = isentropically expanded to freestream condition
c = core (primary)
f = fan (secondary)
0 = stagnation/total condition
∞ = freestream condition

References

[1] Papamoschou, D., 2002, "Noise Suppression in Moderate-Speed Multistream Jets," AIAA Paper No. 2002-2557.
[2] Papamoschou, D., 2004, "New Method for Jet Noise Reduction in Turbofan Engines," AIAA J., **42**(11), pp. 2245–2253.
[3] Papamoschou, D., and Nishi, K., 2005, "Jet Noise Suppression With Fan Flow Deflectors in Realistic-Shaped Nozzle," AIAA Paper No. 2005-993.
[4] Castner, R., 1994, "The Nozzle Acoustic Test Rig; An Acoustic and Aerodynamic Free-Jet Facility," NASA Report No. TM 106495.
[5] Dippold, V., Foster, L., and Wiese, M., 2007, "Computational Analyses of Offset Stream Nozzles for Noise Reduction," AIAA Paper No. 2007-3589.
[6] Brown, C., Bridges, J., and Henderson, B., 2007, "Offset Stream Technology Test—Summary of Results," AIAA Paper No. 2007-3664.
[7] Zaman, K., Bridges, J., and Papamoschou, D., 2007, "Offset Stream Technology—Comparison of Results From UC and GRC Experiments," AIAA Paper No. 2007-438.
[8] Henderson, B., Norum, T., and Bridges, J., 2006, "An MDOE Assessment of Nozzle Vanes for High Bypass Ratio Jet Noise Reduction," AIAA Paper No. 2006-2543.
[9] Papamoschou, D., Vu, A., and Johnson, A., 2006, "Aerodynamics of Wedge-Shaped Deflectors for Jet Noise Reduction," AIAA Paper No. 2006-3655.
[10] Janardan, B. A., Hoff, G. E., Barter, J. W., Martens, S., Gliebe, P. R., Mengle, V., and Dalton, W. N., 2000, "AST Critical Propulsion and Noise Reduction Technologies for Future Commercial Subsonic Engines Separate-Flow Exhaust System Noise Reduction Concept Evaluation," NASA Report No. CR 2000-210039.
[11] Pointwise, Inc., http://www.pointwise.com/gridgen/
[12] The NPARC Alliance, http://www.grc.nasa.gov/www/winddocs/
[13] Menter, F. R., 1994, "Two-Equation Eddy-Viscosity Turbulence Models for Engineering Applications," AIAA J., **32**(8), pp. 1598–1605.
[14] Papamoschou, D., 2003, "A New Method for Jet Noise Reduction in Turbofan Engines," AIAA Paper No. 2003-1059.
[15] Khavaran, A., and Kenzakowski, D. C., 2007, "Noise Generation in Hot Jets," NASA Report No. CR 2007-214924.

[16] Papamoschou, D., 2006, "Fan Flow Deflection in Simulated Turbofan Exhaust," AIAA J., **44**(12), pp. 3088–3097.
[17] DeBonis, J., 2008, "RANS Analyses of Turbofan Nozzles With Wedge Deflectors for Noise Reduction," AIAA Paper No. 2008-0041.
[18] Wernet, M., and Bridges, J., 2002, "Application of DPIV to Enhanced Mixing Heated Nozzle Flows," AIAA Paper No. 2002-0691.
[19] Dembowski, M. A., and Georgiadis, N. J., 2002, "An Evaluation of Parameters Influencing Jet Mixing Using the WIND Navier-Stokes Code," NASA Report No. TM 2002-211727.
[20] Georgiadis, N. J., and DeBonis, J. R., 2006, "Navier-Stokes Analysis Methods for Turbulent Jet Flows With Application to Aircraft Exhaust Nozzles," Prog. Aerosp. Sci., **42**, pp. 377–418.

Choking Phenomena in a Vortex Flow Passing a Laval Tube: An Analytical Treatment

Theo Van Holten
e-mail: t.vanholten@tudelft.nl

Monique Heiligers

Annemie Jaeken

Department of Design, Integration and Operation of Aircraft and Rotorcraft,
Faculty of Aerospace Engineering,
Delft University of Technology,
Kluyverweg 1,
2629 HS Delft, The Netherlands

The behavior of a vortex flow through a Laval nozzle was studied in connection with the purification of natural gas. By creating a vortex and passing it through a Laval nozzle, the gas will be cooled, and water droplets will form and will be centrifuged out of the gas. This system is named the Condi-Cyclone. An analytical theory is developed to reveal the most important phenomena of the flow, to first order accuracy. Experiments have been performed with a prototype of the Condi-Cyclone. A Euler numerical simulation was performed, using the geometry of the test channel. This paper presents an analytical theory for a vortex flow through a Laval nozzle. It will demonstrate that when a vortex is present the total velocity reaches sonic conditions upstream of the nozzle throat, that the axial component of the velocity in the nozzle throat is equal to the local speed of sound and that the mass flow through the Laval nozzle decreases with increasing vortex strength. The predictions of the analytical theory have been compared with the results of the experiments and the Euler numerical simulation, and it can be concluded that the analytical theory describes the main characteristics of the flow very well.
[DOI: 10.1115/1.3089532]

Keywords: Laval nozzle, vortex flow, natural gas, Condi-Cyclone

1 Introduction

The behavior of a vortex flow through a Laval nozzle was studied in connection with the purification of natural gas. Water normally present in natural gas needs to be extracted because it can have damaging effects on the installations and pipelines further downstream. The steps of dehydration and hydrocarbon removal are normally achieved in multiple process stages, for example, in turbo-expanders or with added chemicals, notably glycol or methanol [1]. In addition to requiring large vessels and complex operation, processes such as glycol regeneration can also produce toxic atmospheric emissions, including benzene, toluene, ethylene, and xylene [1].

To solve these problems a radical new means to purify natural gas has been invented: the Condi-Cyclone. By creating a vortex in a Laval nozzle, the gas will be cooled, and water droplets will form and will be centrifuged out of the gas. This paper will present an analytical theory describing the basic process of a vortex flow through a Laval nozzle.

Section 2 will provide a brief explanation of the Condi-Cyclone and its lay-out. Section 3 will present the actual analytical theory. To verify the predictions of the analytical theory, both Euler numerical simulation and full scale tests with the Condi-Cyclone have been performed. The results of the full scale tests will be presented in Sec. 4; the results of the numerical simulation in Sec. 5. The different results will be compared with the analytical theory in Sec. 6, and finally the conclusions are presented in Sec. 7.

2 Condi-Cyclone Lay-Out

The Condi-Cyclone accelerates the natural gas to supersonic levels and at the same time introduces a strong vortex. By accelerating the gas, the gas will cool down, the water will start to condensate, and small water droplets will form. These water droplets will be centrifuged to the wall of the Condi-Cyclone by the vortex and can then be extracted from the flow. A schematic lay-out of the Condi-Cyclone is given in Fig. 1.

After the natural gas enters the inlet of the Condi-Cyclone, a static center-body directs the gas flow past a static array of blades. This static array of blades deflects the flow and thereby generates the vortex. This part of the Condi-Cyclone is also referred to as the subsonic vortex generator (SVG). The next step is an acceleration of the flow by means of a Laval nozzle. The flow will become supersonic, and when the temperature drop is sufficient, water droplets will start to form. When the water droplets have grown sufficiently, they are driven toward the nozzle wall by the centrifugal forces and are extracted from the flow in the recovery section. When the flow has passed the recovery section, it is slowed down. The cleaned gas then flows straight into the remaining processes.

3 Analytical Theory

The purpose of the analytical theory is to reveal the most important phenomena of the flow, to first order accuracy. In the case of rocket nozzles and the design of supersonic windtunnels, it is well known that the assumption of quasi-one-dimensional isentropic flow may give a useful first indication of the global flow properties. For this reason it was attempted to develop a theory for the Condi-Cyclone flow based on similar assumptions. The validity of such an extremely simplified theory will depend on how strong viscous effects are or on how much the flow is affected by local shocks. Comparisons with experiments (Sec. 4) are therefore essential before conclusions can be drawn concerning the validity of the assumptions. Further insight into details such as the occurrence of local shocks will be provided by Euler numerical simulations (Sec. 5). The analytical theory for a vortex flow through a Laval nozzle will be presented in this section. Among others it will be shown that the total velocity reaches the local speed of sound *upstream* of the throat and that the mass flow is a function of the vortex strength.

Contributed by the Fluids Engineering Division of ASME for publication in the JOURNAL OF FLUIDS ENGINEERING. Manuscript received July 28, 2006; final manuscript received January 31, 2008; published online March 6, 2009. Assoc. Editor: Phillip M. Ligrani. Paper presented at the 45th AIAA Aerospace Sciences Meeting and Exhibit 2007.

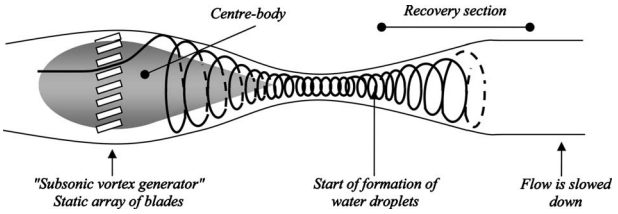

Fig. 1 Schematic lay-out of the Condi-Cyclone

3.1 Basic Equations and Assumptions. The following basic assumptions have been made. The flow is considered to be isentropic and a calorically perfect gas is assumed, implying that the following flow equations can be used:

$$\frac{T_t}{T} = 1 + \frac{\gamma - 1}{2} M^2 \tag{1}$$

$$\frac{p_t}{p} = \left(1 + \frac{\gamma - 1}{2} M^2\right)^{\gamma/\gamma - 1} \tag{2}$$

$$\frac{\rho_t}{\rho} = \left(1 + \frac{\gamma - 1}{2} M^2\right)^{1/\gamma - 1} \tag{3}$$

$$a^2 = \gamma RT = \gamma RT_t \left(1 + \frac{\gamma - 1}{2} M^2\right)^{-1} = a_t^2 \left(1 + \frac{\gamma - 1}{2} M^2\right)^{-1}$$

$$= a_t^2 - \frac{\gamma - 1}{2} V^2 \tag{4}$$

in which T_t is the total temperature, T is the static temperature, γ is the ratio of specific heats, M is the Mach number, p_t is the total pressure, p is the actual pressure, ρ_t is the total air density, ρ is the actual air density, a is the speed of sound, a_t is the total speed of sound, and V is the velocity. Furthermore, the flow is considered to be rotationally symmetric. Quasi-one-dimensional flow is assumed, i.e., it is assumed that the flow properties depend on the axial coordinate only. For the flow around the central body, this is an acceptable assumption; the variation in the velocity in the radial direction will indeed be very small in the narrow annular channel. For the flow downstream of the center-body this assumption will not be valid anymore; therefore in this part of the Laval nozzle the analytically calculated velocities will merely be treated as an indication of the average velocities.

The definition of the annulus and the corresponding velocities are clarified in Fig. 2. V_{ax} is the axial velocity component, parallel to the axis of the Laval nozzle. V_{tan} is the tangent velocity due to the vortex. It is tangent to the mean radius of the annulus r. The angle between the total velocity V and the axial velocity V_{ax} is α, and the area of the annulus is A.

The basic equations that will be used for the analytical calculations are conservation of angular momentum and the continuity equation:

$$\dot{m} = \rho V_{ax} A = \text{constant} \tag{5}$$

$$I = \dot{m} V_{tan} r = \text{constant} \tag{6}$$

in which $\dot{m}$ is the mass flow and I is the angular momentum.

3.2 Throat Conditions. As a preliminary the local Mach number is expressed as a function of the velocity components V_{ax} and V_{tan}. Using Eqs. (1) and (4),

$$a_t^2 - a^2 = \gamma RT\left(\frac{T_t}{T} - 1\right) = a^2 \frac{\gamma - 1}{2} M^2 = \frac{\gamma - 1}{2} V^2 \tag{7}$$

so that

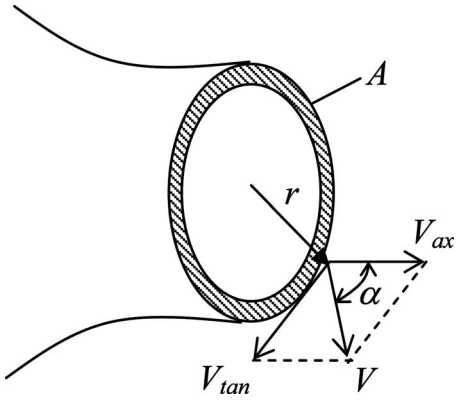

Fig. 2 Definition of annulus and corresponding velocities

$$M^2 = \frac{V^2}{a^2} = \frac{V_{tan}^2 + V_{ax}^2}{a_t^2 - \frac{\gamma - 1}{2}(V_{tan}^2 + V_{ax}^2)} \tag{8}$$

By definition the throat is given by $dA/dx = 0$. This implies that $dr/dx = 0$ and thus, on account of Eq. (6), $dV_{tan}/dx = 0$. Equation (5) states,

$$A = \frac{\dot{m}}{\rho V_{ax}} \tag{9}$$

which yields upon differentiation.

$$\frac{dA}{dx} = -\frac{\dot{m}}{\rho V_{ax}}\left[\frac{1}{\rho}\frac{d\rho}{dM^2}\left\{\frac{\partial M^2}{\partial V_{ax}}\frac{dV_{ax}}{dx} + \frac{\partial M^2}{\partial V_{tan}}\frac{dV_{tan}}{dx}\right\} + \frac{1}{V_{ax}}\frac{dV_{ax}}{dx}\right] \tag{10}$$

Substituting the throat conditions $dA/dx = 0$ and $dV_{tan}/dx = 0$ yields,

$$0 = \frac{1}{\rho}\frac{d\rho}{dM^2}\left\{\frac{\partial M^2}{\partial V_{ax}}\right\} + \frac{1}{V_{ax}} \tag{11}$$

According to Eqs. (3) and (4) the derivative $d\rho/dM^2$ is given by

$$\frac{d\rho}{dM^2} = -\frac{1}{2}\rho_t\left(1 + \frac{\gamma - 1}{2} M^2\right)^{-\gamma/\gamma - 1} = -\frac{1}{2}\rho\left(1 + \frac{\gamma - 1}{2} M^2\right)^{-1}$$

$$= -\frac{1}{2}\rho\frac{a^2}{a_t^2} \tag{12}$$

The other derivative $\partial M^2/\partial V_{ax}$ occurring in Eq. (11) is found using Eqs. (7) and (8):

$$\frac{\partial M^2}{\partial V_{ax}} = \frac{2V_{ax}a_t^2}{\left[a_t^2 - \frac{\gamma - 1}{2}(V_{tan}^2 + V_{ax}^2)\right]^2} = 2V_{ax}\frac{a_t^2}{a^4} \tag{13}$$

After substituting Eqs. (12) and (13) into Eq. (11), the following result is found for the flow in the throat:

$$[V_{ax} = a]_{throat} \tag{14}$$

The total Mach number of the flow in the throat section, taking into account that there is an additional velocity component V_{tan}, apparently is larger than unity.

$$M_{thr} > 1 \quad \text{if } V_{tan} > 0$$

In fact, the Mach number in the throat is uniquely determined by the value of V_{tan}, as shown by the following expressions:

$$M_{thr}^2 = \frac{V_{tan}^2 + V_{ax}^2}{a^2} = 1 + \frac{V_{tan}^2}{a_t^2}\left(1 + \frac{\gamma - 1}{2} M_{thr}^2\right) \tag{15}$$

from which M_{thr} can be made explicit as follows:

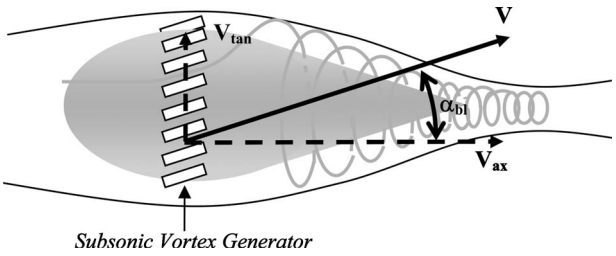

Fig. 3 Flow angle just downstream of the subsonic vortex generator and the resulting velocities

$$M_{\text{thr}}^2 = \frac{1 + \dfrac{V_{\tan}^2}{a_t^2}}{\left(1 - \dfrac{\gamma - 1}{2}\dfrac{V_{\tan}^2}{a_t^2}\right)} \tag{16}$$

The latter equation again clearly shows that the Mach number in the throat is larger than unity if a vortex flow is present. Under such conditions the transition from sub-to supersonic flow occurs at a position upstream of the throat.

3.3 Mass Flow Through the Channel. Making use of the property (14) and Eq. (5), the mass flow through the throat section (and therefore the mass flow in every section) may be expressed as follows:

$$\dot{m} = \rho V_{\text{ax}} A = \rho_{\text{thr}} a_{\text{thr}} A_{\text{thr}} \tag{17}$$

Using Eqs. (1), (3), and (4), the right-hand side of this equation can be written as a function of M_{thr} only.

$$\dot{m} = \rho_t a_t A_{\text{thr}} \left[1 + \frac{\gamma - 1}{2} M_{\text{thr}}^2\right]^{-\gamma + 1/2(\gamma - 1)} \tag{18}$$

If, for example, γ is taken equal to the value for air ($\gamma = 1.4$), the exponent in Eq. (18) will equal to -3. It can thus be seen that increasing M_{thr} will lead to a reduced mass flow. In other words, increasing the vortex strength will "throttle" the Laval nozzle, as a consequence of the additional $V_{\tan}$ and the resulting increased Mach number in the throat. This throttling effect is quite large, as will be seen later from some experimental results used to determine the validity of the above given theory.

Using the average radius r_{thr} of the flow annulus in the throat (see the earlier remarks about the quasi-one-dimensional approximation underlying the developed theory), Eq. (6) yields for the conditions in the throat:

$$V_{\tan,\text{thr}} = \frac{I}{\dot{m} r_{\text{thr}}} \tag{19}$$

The set of equations (16), (18), and (19) determines a relation between the mass flow $\dot{m}$ and the angular momentum I, although an actual calculation will be iterative. In order to complete the quantification of the flow properties, a second relation between $\dot{m}$ and I will be needed.

3.4 Flow Conditions at the Blades of the Vortex Generator. A second relation between the mass flow and angular momentum is provided by a consideration of the flow through the array of blades at the entrance of the channel (see Fig. 3), called the subsonic vortex generator. The blade angle determines the flow angle α_{bl} just downstream of the subsonic vortex generator.

In terms of the flow properties just downstream of the blades, the mass flow (Eq. (5)) may be written as

$$\dot{m} = \rho_{\text{bl}} M_{\text{bl}} a_{\text{bl}} \cos\alpha_{\text{bl}} A_{\text{bl}} = \rho_t a_t \cos\alpha_{\text{bl}} A_{\text{bl}} M_{\text{bl}} \times \left(1 + \frac{\gamma - 1}{2} M_{\text{bl}}^2\right)^{-\gamma + 1/2(\gamma - 1)} \tag{20}$$

Likewise the angular momentum may be expressed in terms of the flow condition just downstream of the vortex generator as follows:

$$I = \dot{m} M_{\text{bl}} a_{\text{bl}} \sin\alpha_{\text{bl}} r_{\text{bl}} = \dot{m} a_t \sin\alpha_{\text{bl}} r_{\text{bl}} M_{\text{bl}} \left(1 + \frac{\gamma - 1}{2} M_{\text{bl}}^2\right)^{-1/2} \tag{21}$$

Equations (20) and (21) contain the three variables $\dot{m}$, I, and M_{bl}, apart from the constants that specify the reservoir- (or total-) conditions of the gas and the geometry of the channel. The set (Eqs. (20) and (21)) therefore provides a second relation between mass flow and angular momentum.

At this point there are two separate relations available between $\dot{m}$ and I; the first one derived from the throat conditions and the second one given by the inflow conditions. The calculation of the values of $\dot{m}$ and I can thus be completed.

3.5 Computational Scheme to Determine Mass Flow and Angular Momentum. The two relations between mass flow $\dot{m}$ and angular momentum I provided by the two sets of equations (16), (18), and (19) on the one hand, and Eqs. (20) and (21) on the other hand consist of nonlinear algebraic equations and do not allow for an explicit solution. The following is an efficient iterative calculation scheme:

Step 1. Guess a value of M_{thr}.

Step 2. The corresponding estimate of the mass flow is given by Eq. (18), describing the throat condition.

Step 3. Eq. (20) will provide the Mach number just downstream of the vortex generator. Equation (20) may conveniently be solved for M_{bl} using a Newton–Raphson procedure.

Step 4. The angular momentum I brought into the flow by the vortex generator is given by Eq. (21).

Step 5. The tangential velocity in the throat $V_{\tan,\text{thr}}$ is known from Eq. (19)

Step 6. An improved estimate for M_{thr} is finally obtained from Eq. (16), and, if necessary, the iteration can proceed by returning to step 1.

3.6 Calculation of Flow Conditions at Each Axial Station. Now the mass flow and the angular momentum have been calculated, and since the flow area $A(x)$ and radius $r(x)$ as functions of the axial coordinate x are given, the flow conditions at each axial station can be calculated. The tangent velocity is still given by Eq. (6). The total velocity, axial velocity, and Mach number at each axial station can be calculated by combining the following four equations:

$$V(x) = M(x) a(x) = \frac{M(x) a_t}{\sqrt{1 + \dfrac{\gamma - 1}{2} M^2(x)}} \tag{22}$$

$$V(x) = \sqrt{V_{\tan}^2(x) + V_{\text{ax}}^2(x)} \tag{23}$$

Equations (22) and (23) give the following expression for the axial velocity:

$$V_{\text{ax}}(x) = \sqrt{\frac{M(x)^2 a_t^2}{1 + \dfrac{\gamma - 1}{2} M^2(x)} - V_{\tan}^2(x)} \tag{24}$$

An expression for the Mach number can be derived from Eq. (9) by substituting Eqs. (24) and (3), as follows:

Table 1 Input and output of the analytical calculations

Analytical results						
Input			Output			
α_{bl} (deg)	p_t (bar)	T_t (K)	m (kg/s)	Γ (m^2/s)	$T_{end\ nozzle}$ (K)	$M_{end\ nozzle}$
20	1.5	300	1.07	25.10	180	1.9
25	1.5	300	0.98	28.91	175	1.9
30	1.5	300	0.89	32.27	165	2.0
40	1.5	300	0.73	38.14	155	2.2

$$\rho_t\left(1+\frac{\gamma-1}{2}M^2(x)\right)^{-1/\gamma-1}\sqrt{\frac{M^2(x)a_t^2}{1+\frac{\gamma-1}{2}M^2(x)}-V_{tan}^2(x)}=\frac{\dot{m}}{A(x)} \tag{25}$$

Solving Eq. (25) will give the Mach number for each axial coordinate: substitution of the Mach number for each axial coordinate into Eq. (22) will give the total velocity for each axial coordinate. Finally substitution of the Mach number into Eq. (24) will give the axial velocity for each axial coordinate.

3.7 Analytical Calculations and Results. Using the analytical theory calculations have been performed on the Condi-Cyclone test setup that was used during the experiments (see Sec. 4). Section 4 will also describe the geometry of the Condi-Cyclone. Here, the analytical results for four different blade angles (α_{bl}) are already given (see Table 1). The input parameters are the total pressure and total temperature at the location of the blades of the subsonic vortex generator. The output parameters are the mass flow, vortex strength Γ, temperature at the end of the nozzle $T_{end\ nozzle}$, and Mach number at the end of the nozzle $M_{end\ nozzle}$.

4 Experiments

Experiments have been performed with a prototype of the Condi-Cyclone. The purpose of these tests was to obtain an impression about the validity of the above described simplified analytical theory, taking into account the limited scope of such a theory as stated in the introduction of Sec. 3. Therefore, tests were run with dry air. Since the mass flow is of primary importance for the designer, the measurements concentrated on this property. Mass flow could be determined relatively accurately ($\pm 2\%$) from the total and static pressures in the subsonic part of the channel upstream of the subsonic vortex generator. As a matter of interest an attempt was done to get an impression of the angular momentum and the variation in the Mach number along the length of the channel. It should be realized, however, that the latter properties vary strongly in the radial direction in the region of the throat (see Sec. 5), so that very accurate measurements were not considered to be useful; results are therefore not discussed in this paper. This section will describe the test setup and test conditions, followed by the experimental results.

Table 2 Experimental results

Experimental results				
α_{SVG} (deg)	p_t (bar)	T_t (K)	$\dot{m}$ ($\pm$ 2%) (kg/s)	Γ ($\pm$ 20%) (m^2/s)
20	1.5	300	1.04	26
25	1.5	300	0.95	24
30	1.5	300	0.887	31
40	1.5	300	No result	No result

4.1 Description of the Experiment. Figure 4 shows the general geometry of the channel. The step in the radial contour of the center-body has no significance. It was caused by the fact that the hardware for the test made use of parts of an earlier experiment with different dimensions. Within the scope of the analytical theory the mass flow $\dot{m}$ and the angular momentum I are determined solely by the entrance conditions and the dimension of the throat. For the purpose of comparison with the analytical theory, the experimental setup is therefore defined by the following data.

4.1.1 Entrance Geometry. The radius of the center-body at the station of the vortex generator was 0.23 m, with a channel width at that station (equal to the span of the blades of the vortex generator) of 0.01 m.

The blades of the array consisted of simple cambered plates. Due to the camber the deflection angle of the flow was slightly larger than the nominal setting, the latter defined by the orientation of the chord. The nominal setting angles were 20 deg, 25 deg, 30 deg, and 40 deg. The effective deflection angles were estimated to be 2 deg larger in each case.

4.1.2 Throat. The entire channel had a circular cross section. The narrowest part of the channel (located at the 0.5 m station) had a radius of 0.035 m, although boundary layer effects, in principle, slightly affect the effective radius. The effect of viscosity might show up in the measured mass flow. In order to judge the magnitude of this effect (when compared with the experimental results), the throat radius of 0.035 m was substituted in the analytical calculations.

4.1.3 Reservoir Conditions. The experiment was fed by pressurized air, which could be considered to be sufficiently clean and dry for this purpose. Total pressure was $p_t=1.5\times10^5$ Pa, and total temperature was $T_t=300$ K.

4.1.4 Instrumentation. An array of static pressure holes, running from the subsonic part of the channel through the throat to a station well downstream of the throat section, provided the information needed to determine the mass flow and to obtain an impression about the variation of the average Mach number in the

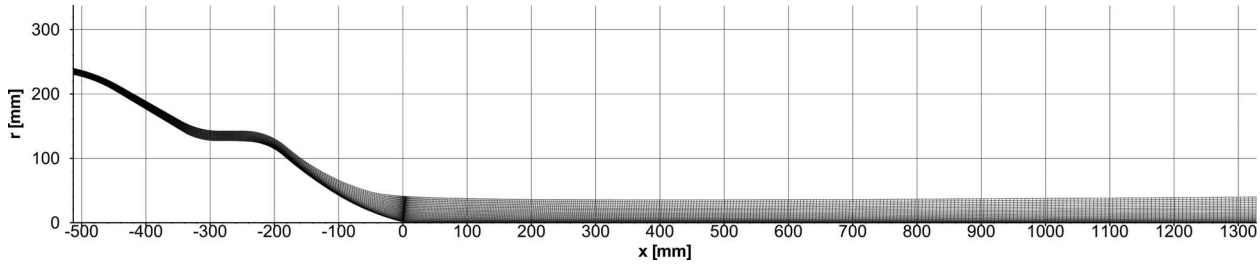

Fig. 4 General geometry of the channel with axisymmetric mesh. The zero station is located at the end of the center-body; the throat is located at the 0.5 m station.

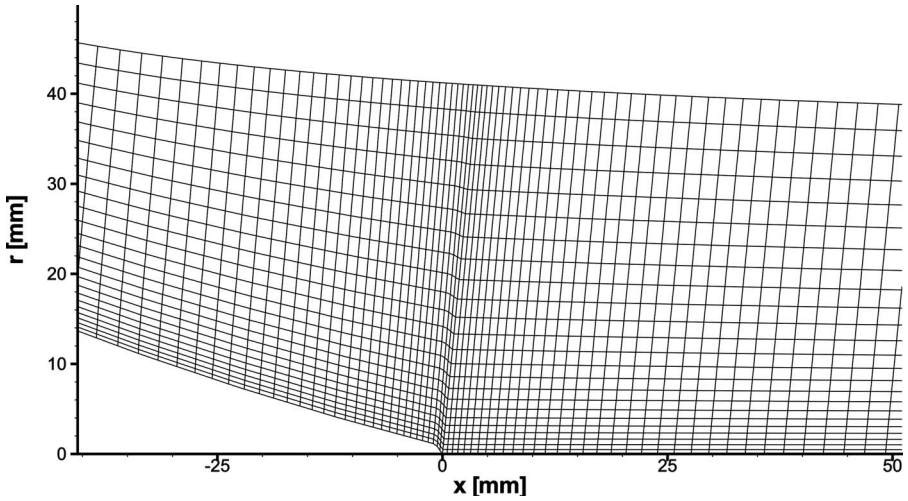

Fig. 5 Axisymmetric mesh; zoomed in at the end of the center-body

channel.

A crude check on the magnitude of the swirl was made by mounting a three-hole pressure tube in the widest part of the channel near the aft end of the central body. This pitot tube could be rotated in such a way that it was roughly aligned with the flow direction. From this device the flow angle α was derived on the mean radius of this particular station.

The measured vortex strength was expressed in terms of the circulation Γ defined as

$$\Gamma = 2\pi r V_{\tan} = 2\pi r_{\mathrm{bl}} M_{\mathrm{bl}} a_{\mathrm{bl}} \sin \alpha_{\mathrm{bl}} \tag{26}$$

The expected accuracy is not more than 20% due to the uncertainties in the measurement techniques. On account of the quasi-one-dimensional assumption underlying the analytical theory, the circulation is related to the angular momentum I by the expression

$$I = \frac{\dot{m}}{2\pi}\Gamma \tag{27}$$

4.2 Experimental Results. Experiments with the Condi-Cyclone have been performed at the Stork Product Engineering TM620-Air/Water test facility [2,3]. The results of the test for different blade angle deflections are given in Table 2. With increasing blade deflection angle and thus with increasing vortex strength, the mass flow through the nozzle decreases. At the highest blade deflection angle (40 deg) the test setup started to vibrate heavily, and the mass flow was severely limited. Because of the vibrations the test was aborted and therefore no results are available for this blade deflection angle. Either vortex breakdown or the stalling of the blades of the SVG is thought to be the probable cause for these vibrations.

5 Euler Numerical Simulation

The Euler numerical simulation [4] was performed using the geometry of the test channel. The purpose was to obtain information on the radial variations in the flow, which may be expected to have occurred during the experiment. Another goal was to check whether local shocks on the tail of the center-body could have occurred, thus causing the breakdown of the experiment with the largest vane angles. For this specific purpose the Euler numerical simulation was considered adequate.

5.1 Mesh Generation. Meshes have been generated to perform dry air Euler numerical simulations for the Condi-Cyclone

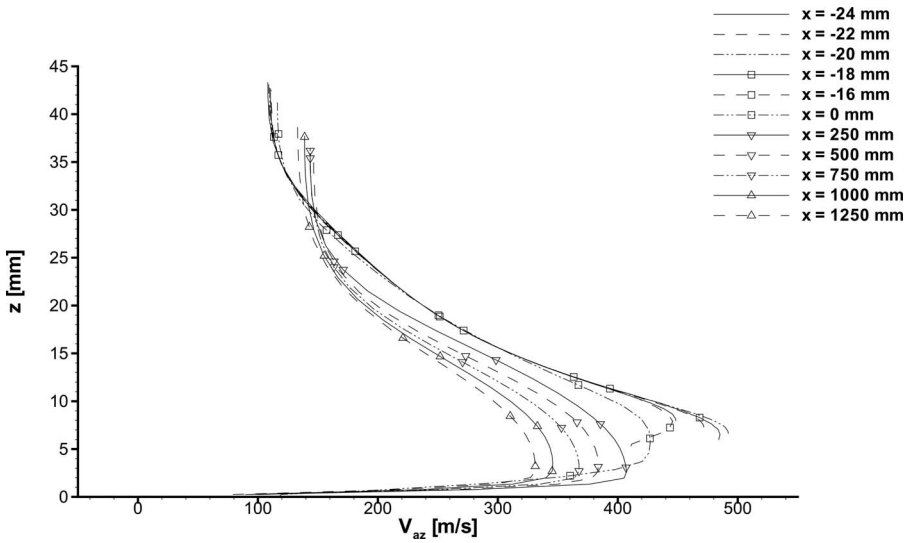

Fig. 6 Tangential velocity (horizontal axis) as a function of radial distance (vertical axis) for several stations

Table 3 Input and output of the Euler numerical simulation

Numerical results							
Input				Output			
α_{SVG} (deg)	M_{bl}	p_t (bar)	T_t (K)	m (kg/s)	Γ (m^2/s)	$T_{end\ nozzle}$ (K)	$M_{end\ nozzle}$
20	0.14	1.5	300	1.12	23.31	186	1.75
25	0.13	1.5	300	1.02	27.37	180	1.80
30	0.13	1.5	300	0.91	32.68	174	1.85
40	0.12	1.5	300	0.69	39.07	168	1.95

SVG with various blade deflection angles. An axisymmetric mesh was used (starting just downstream of the static array of blades and running through the throat until well downstream of the throat).

Because an axisymmetric flow is assumed, it was only necessary to generate a two-dimensional mesh. The mesh is a structured H-type mesh with dimensions of 124×24 cells for the first block (running from just downstream of the blades until halfway of the center-body). The remainder of the channel consisted of four blocks of each 108×24 cells. The distribution of mesh points has been chosen in such a way that the width of the cells approximates the height of the cells and that a refinement can be found at the end of the center-body and along the nozzle axis of symmetry (see Fig. 5). Numerical simulations have also been performed with finer meshes. However mesh convergence was reached, and therefore results for these finer meshes have been omitted. The inflow boundary conditions, just downstream of the swirl vanes, were chosen to correspond to the flow conditions determined by the analytical calculations.

5.2 Results of Numerical Analysis. The main findings of the numerical simulations are the following: The vortex causes the flow to reach sonic conditions well upstream of the nozzle throat in the region of the tail of the center-body. In the nozzle throat the axial velocity is equal to the local speed of sound, as predicted by the analytical theory. In the nozzle a vortex structure is found with a solid body rotation at the axis of symmetry and a "1 over r" behavior toward the nozzle wall (see Fig. 6). A severe pressure drop is present in the region of the solid body rotation.

With increasing blade deflection angle the mass flow decreases, the vortex strength increases, a higher Mach number at the end of the nozzle is achieved, and a slightly larger temperature drop occurs (see Table 3). With increasing blade deflection angles the solid body rotation region expands, the supersonic region at the end of the center-body moves upstream, and the effective cross section of the channel decreases. At the highest vane angle of 40 deg a flow disturbance at the very end of the center-body was clear (see Fig. 7), showing up as a region of back-flow near the center-line and possibly involving a small shock. It was therefore recommended to use in later configurations center-bodies with a pluglike tail shape.

6 Comparison of Analytical, Numerical, and Experimental Results

The results of the analytical theory, experiments, and numerical simulation as explained in Secs. 3–5 will be compared.

6.1 Mass Flow and Vortex Strength. The mass flow and vortex strength as predicted by the analytical theory, calculated by the numerical simulation, and measured during the experiments are plotted as a function of the blade deflection angle in Fig. 8. As can be seen from this figure, the results correspond reasonably well, especially when taking into account that the experimentally obtained values for the vortex strength have an accuracy of only 20%. The measured mass flow does not seem to be affected appreciably by viscosity effects.

6.2 Axial Velocity, Temperature, and Mach Number. Both the analytical results and the numerical results show that the total

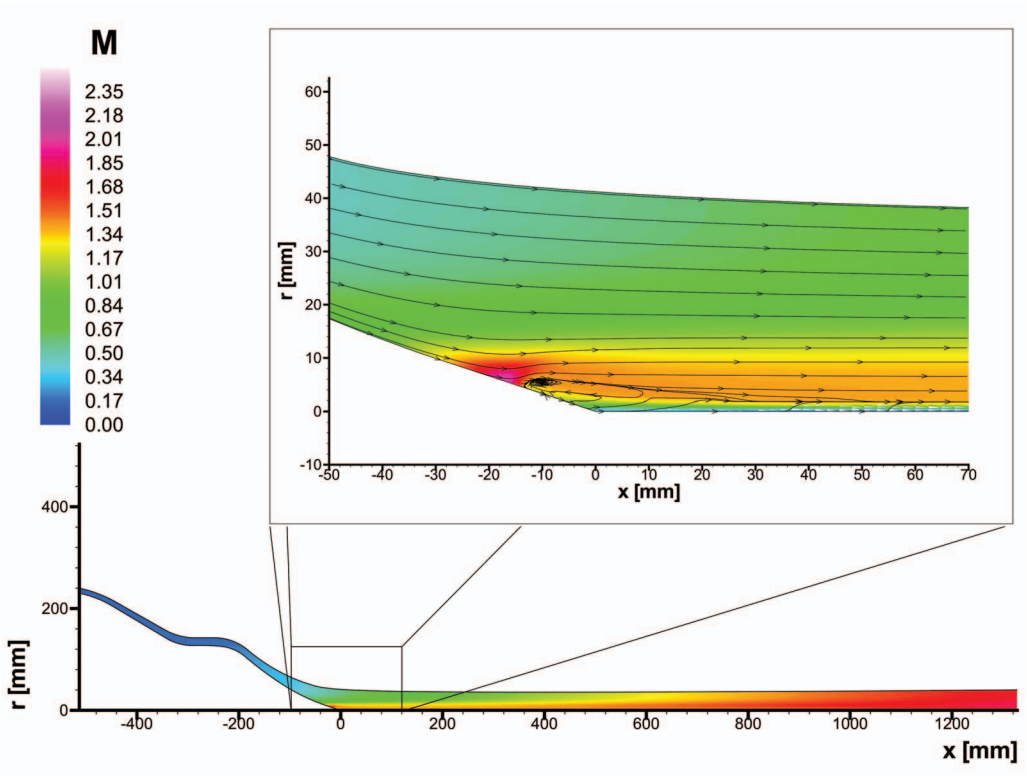

Fig. 7 Calculated back-flow at the end of the center-body

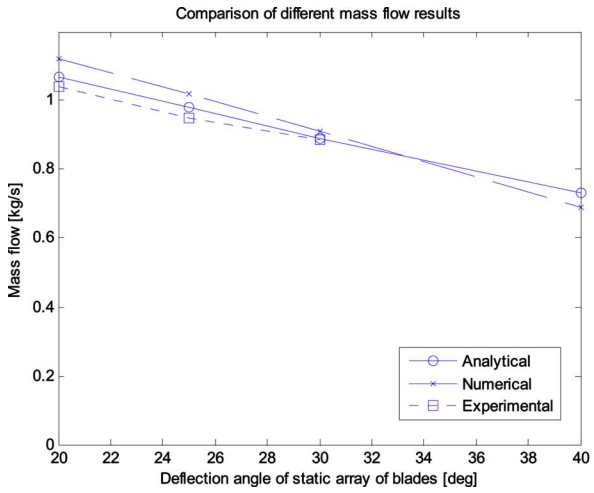

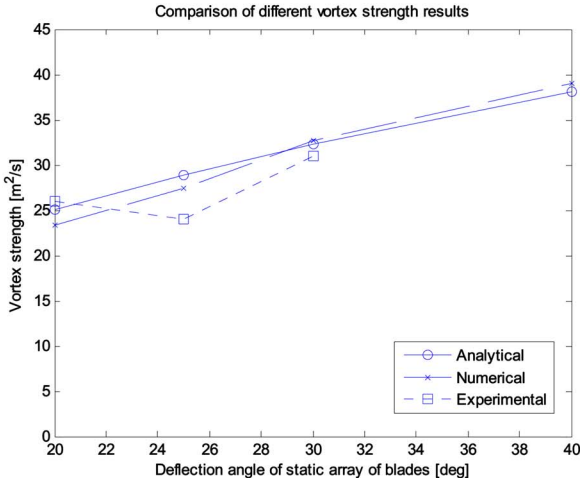

Fig. 8 Mass flow and vortex strength as a function of the blade deflection angle

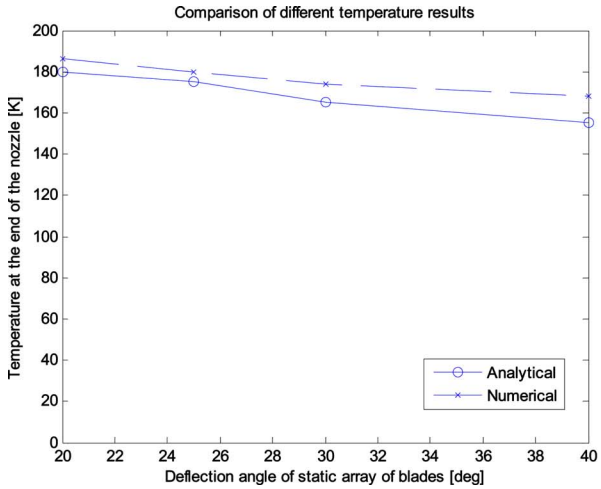

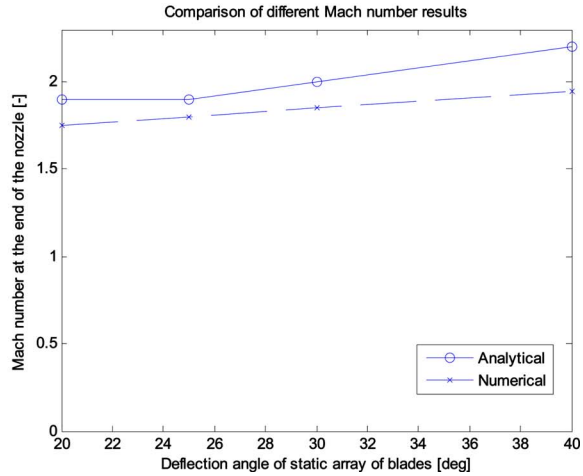

Fig. 9 Temperature and Mach number at the end of the nozzle as a function of the blade deflection angle

Mach number becomes supersonic well before the throat, just upstream of the end of the center-body. Both results also show that the axial velocity in the throat is equal to the local speed of sound. The Mach number and temperature at the end of the nozzle (station 1.3 m downstream of the center-body) as predicted by the analytical theory and calculated by the numerical simulation are plotted in Fig. 9.

7 Conclusions

The analytical theory developed to describe a vortex flow through a Laval nozzle predicts that the axial velocity in the throat will be equal to the local speed of sound and that the total velocity will be larger than the local speed of sound. The total velocity will reach $M=1$ upstream of the throat. Furthermore, the theory predicts that the mass flow through the nozzle depends on the conditions in the throat and also on the vortex strength. The predictions from a simplified analytical theory have been compared with the results of a numerical simulation and experiments and correspond very well.

8 Epilogue

After some modifications were applied to the Condi-Cyclone (a change in the end of the center-body and a redesign of the static array of blades), the concept performed very well during the experiments. The Condi-Cyclone concept has been patented by Stork Product Engineering and has been further developed by Twister BV to make the technology commercially available to the wider industry. A Twister demonstration unit has been operational in Nigeria since early 2001, successfully performing water and hydrocarbon separation, while confirming the ability of Twister to run virtually without supporting systems (Twister BV). Earlier units have been in operation in the Netherlands in Zuiderveen en Barendrecht since 1997 [5].

References

[1] Knott, T., 2000, "Twist in the Tale," Offshore Engineer, http://www.oilonline.com/news/features/oe/20000701.Twist_in.67.asp.
[2] Mertens, S., 1999, "Test Report: Subsonic Vortex Generation (20 & 40 Degrees Turbine Ring)," Stork Product Engineering, Amsterdam, The Netherlands, Technical Report No. SPE-CON-RP-102 (1/0).
[3] Mertens, S., 1999, "Test report: Subsonic Vortex Generation (25 & 30 Degrees Turbine Ring)," Stork Product Engineering, Amsterdam, The Netherlands, Technical Report No. SPE-CON-RP-113 (1/0).
[4] Schoones, M. M. J., and Van Holten, Th., 1999, "Euler Numerical Simulation of Channel Flow With a Superimposed Vortex," Faculty of Aerospace Engineering, Delft University of Technology, The Netherlands, Technical Report No. FM&P-99.001.
[5] Twister, B. V., http://www.twisterbv.com/

Mohsen Akbari[1]
Ph.D. Candidate
Mechatronic System Engineering,
School of Engineering Science,
Simon Fraser University,
Surrey, BC, V3T 0A3, Canada
e-mail: maa59@sfu.ca

David Sinton
Associate Professor
Department of Mechanical Engineering,
University of Victoria,
Victoria, BC, V8W 2Y2, Canada

Majid Bahrami
Assistant Professor
Mem. ASME
Mechatronic System Engineering,
School of Engineering Science,
Simon Fraser University,
Surrey, BC, V3T 0A3, Canada

Pressure Drop in Rectangular Microchannels as Compared With Theory Based on Arbitrary Cross Section

Pressure driven liquid flow through rectangular cross-section microchannels is investigated experimentally. Polydimethylsiloxane microchannels are fabricated using soft lithography. Pressure drop data are used to characterize the friction factor over a range of aspect ratios from 0.13 to 0.76 and Reynolds number from 1 to 35 with distilled water as working fluid. Results are compared with the general model developed to predict the fully developed pressure drop in arbitrary cross-section microchannels. Using available theories, effects of different losses, such as developing region, minor flow contraction and expansion, and streaming potential on the measured pressure drop, are investigated. Experimental results compare well with the theory based on the presure drop in channels of arbitrary cross section. [DOI: 10.1115/1.3077143]

1 Introduction

Advances in microfabrication make it possible to build microchannels with micrometer dimensions. Micro- and minichannels show potential and have been incorporated in a wide variety of unique, compact, and efficient cooling applications in microelectronic devices [1]. These microheat exchangers or heat sinks feature extremely high heat transfer surface area per unit volume ratios, high heat transfer coefficients, and low thermal resistances. In biological and life sciences, microchannels are used widely for analyzing biological materials such as proteins, DNA, cells, embryos, and chemical reagents [2]. Various microsystems, such as microheat sinks, microbiochips, microreactors, and micronozzles have been developed in recent years [3–6]. Since microchannels are usually integrated into these microsystems, it is important to determine the characteristics of the fluid flow in microchannels for better design of various microflow devices.

In parallel to the recent advances in microfluidic devices, microfabrication techniques have evolved. Some of the important fabrication techniques include lithography (soft and photolithography), lamination, injection molding, hot embossing, laser micromachining, and electrochemical or ultrasonic technologies [2,7–10]. Together with new methods of fabrication, it is possible to exploit certain fundamental differences between the physical properties of fluids moving in large channels and those traveling through micrometer-scale channels [2]. In recent years, a large number of papers have reported pressure drop data for laminar fully developed flow of liquids in microchannels with various cross sections [11–32]. Rectangular cross sections have been extensively studied as they are employed in many applications [11–16]. However, published results are often inconsistent. Some authors reported a huge deviation from the conventional theories and attributed it to an early onset of laminar to turbulent flow transition or surface phenomena such as surface roughness, electrokinetic forces, viscous heating effects, and microcirculation near the wall [12–26].

Jiang et al. [28] conducted an experimental investigation of water flow through different microchannel cross sections including circular, rectangular, trapezoidal, and triangular. The hydraulic diameter of microchannels varied from 8 μm to 42 μm. They collected experimental data with the Reynolds number ranging from 0.1 to 2, and concluded that there was less influence of the cross-sectional shape on the microflow in the microchannel and that the experimental data agreed well with the prediction of the conventional theory. Baviere et al. [29] performed an experimental study on the water flow through smooth rectangular microchannels. Their channels were made of a silicon engraved substrate anodically bonded to a Pyrex cover. Their results showed that in smooth microchannels, the friction law is correctly predicted by conventional theories. Judy et al. [15] and Bucci et al. [30] showed that their experimental results were in good agreement with conventional theories in the laminar regime. Also Wu and Cheng [31], Liu and Garimella [32], and Gao et al. [33] reported good agreement between experimental data with conventional theories.

Low Reynolds numbers characterize many microscale liquid flows [34]. Hence, nonlinear terms in the Navier–Stokes equation disappear for fully developed flow, resulting in Poisson's equation

$$\nabla^2 u = \frac{1}{\mu}\frac{dp}{dz}, \quad u = 0 \text{ on } \Gamma \tag{1}$$

where u is the fluid velocity, z is the flow direction, and Γ is the perimeter of the channel. Exact solution for Eq. (1) in rectangular cross-section channels can be found in fluid mechanics textbooks such as Ref. [35]. The original analytical solution for the mean velocity in rectangular channels is in the form of a series, but it has been shown that using the first term of the series results in errors less than 0.7%.

Recently, Bahrami et al. [1,36] developed a general model for prediction of pressure drop in microchannels of arbitrary cross section. Using the analytical solution of elliptical duct and the concept of Saint-Venant principal in torsion [37], they showed that the Poiseuille number, $f\ \mathrm{Re}_{\sqrt{A}}$, is a function of the polar moment of inertia, I_P, area, A, and perimeter of the cross section of the channel, Γ. Their model showed good agreement with experimental and numerical data for a wide variety of channel cross sections such as rectangular, trapezoidal, triangular, circular, and moon shaped.

[1]Corresponding author.

Contributed by the Fluids Engineering Division of ASME for publication in the JOURNAL OF FLUIDS ENGINEERING. Manuscript received June 11, 2008; final manuscript received December 5, 2008; published online March 6, 2009. Assoc. Editor: James A. Liburdy. Paper presented at the ECI International Conference on Heat Transfer and Fluid Flow in Microscale III, Whistler, BC, Canada, September 21–26, 2008.

However, they [1,36] did not perform any experiment to verify this model, thus they could not investigate all issues and effects of different parameters. As a result the goal of the present work is to independently validate the general model of Bahrami et al. [1,36]. Moreover, effects of different parameters, including microchannel dimensions, minor and developing region losses, viscous heating, electroviscous phenomena, and channel deformation on the measured pressure drop, have been discussed. By successfully validating the model, it will be used in more complicated channel geometries such as variable cross-section microchannels.

2 Theory

Selection of the characteristic length is an arbitrary choice and will not affect the final solution. However, an appropriate length scale leads to more consistent results, especially when a general cross section is considered. A circular duct is fully described with its diameter, thus the obvious length scale is the diameter (or radius). For noncircular cross sections, the selection is not as clear; many textbooks and researchers have conventionally chosen the hydraulic diameter as the characteristic length. Yovanovich [38] introduced the square root of area as a characteristic length scale for heat conduction and convection problems. Later, Muzychka and Yovanovich [39] proposed the use of $\sqrt{A}$ for the fully developed flow in noncircular ducts. Bahrami et al. [1,37] showed that the square root of area appears in the solution of fully developed flow in noncircular ducts. They also compared both D_h and $\sqrt{A}$ and observed that using $\sqrt{A}$ as the characteristic length scale results in similar trends in Poiseuille number for microchannels with a wide variety of cross sections. Therefore, in this study, $\sqrt{A}$ is selected consistently as the length scale throughout the analysis.

According to the model of Bahrami et al. [1], pressure drop of laminar fully developed flow in arbitrary cross-section microchannels can be obtained from

$$\Delta P = 16\pi^2 \mu Q I_p^* \frac{L}{A^2} \tag{2}$$

where $I_p^* = I_p/A$ is the specific polar momentum of inertia of the microchannel cross section, $\Gamma = 4(W+H)$ is the microchannel cross-section perimeter, L is the fully developed length, and Q is the the volumetric flow rate. Substituting for the geometrical parameters in Eq. (2) for microchannels of rectangular cross section and the definition of the Poiseuille number yields [1]

$$f\ \mathrm{Re}_{\sqrt{A}} = \frac{4\pi^2(1+\varepsilon^2)}{3\sqrt{\varepsilon}(1+\varepsilon)} \tag{3}$$

As can be seen the only parameter effects the Poiseuille number in rectangular channels is the cross-section aspect ratio, consistent with previous works [35,40]. For rectangular microchannels, two asymptotes can be recognized, i.e., very narrow rectangular and square channels

$$f\ \mathrm{Re}_{\sqrt{A}} = \frac{4\pi^2}{3\sqrt{\varepsilon}}; \quad \varepsilon \to 0$$

$$f\ \mathrm{Re}_{\sqrt{A}} = 13.16; \quad \varepsilon = 1 \tag{4}$$

3 Experimental Setup

3.1 Chemicals and Materials. De-ionized water was used as the testing liquid. SU-8 photoresist (Microchem, Newton, MA) and diacetone-alcohol developer solution (Sigma-Aldrich, St. Louis, MO) were used in the making of the positive relief masters by the procedure outlined below. Polydimethylsiloxane (PDMS) casts were prepared by thoroughly mixing the base and curing agent at a 10:1 ratio as per the manufacturer's instructions for the Sylgard 184 silicon elastomer kit (Dow Corning, Midland, MI). Caution was used to avoid contact between the liquid PDMS and latex rubber (gloves), as this was found to inhibit curing [41].

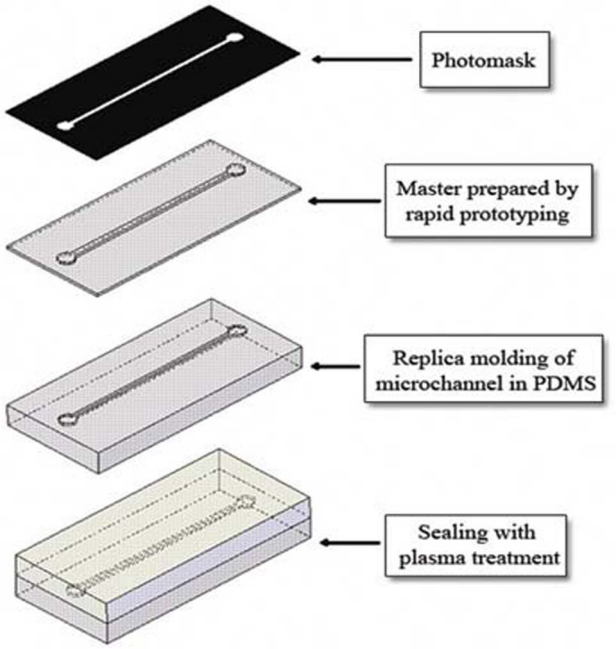

Fig. 1 Schematic of the soft lithography technique

3.2 Microfabrication. The PDMS/PDMS microchannels used in this study have been manufactured using the soft lithography technique [42] described by Erickson et al. [41]. A schematic of the process is provided in Fig. 1. Photomasks were designed by AUTOCAD software[2] and printed with a 3500DPI printer (Island Graphics Ltd., Victoria, BC, Canada). Masters containing the desired microchannel pattern have been made by spin coating of SU-8 negative photoresist on a glass slide to the desired thickness. The photoresist film was then hardened through a two-stage direct contact pre-exposure bake procedure (65 °C for 5 min and 95 °C for 30 min) and exposed to UV light for 100 s through the mask containing the channel pattern. A two-stage postexposure bake procedure (65 °C for 5 min and 95 °C for 30 min) was then used to enhance cross linking in the exposed portion of the film. The slide was then placed in quiescent developer solution for 10 min to dissolve the unexposed photoresist, leaving a positive relief containing the microchannel pattern.

Liquid PDMS was then poured over the master and exposed to vacuum condition (1 h) to extract all the bubbles in it and cured at 85 °C for 15–20 min yielding a negative cast of the microchannel pattern. An enclosed microchannel was then formed by bonding the PDMS cast with another piece of PDMS via plasma treatment.

Five microchannels were made with a range of aspect ratios, $0.13 < \varepsilon < 0.76$, and tested in this study. Dimensions of the microchannels are shown in Table 1. The channels' names in the table indicate the channel material, cross-sectional shape, and the aspect ratio (i.e., PPR-0.13 corresponds to the PDMS/PDMS chip with rectangular cross section and the aspect ratio of 0.13). As can be seen, channels were designed long enough so that fully developed flow is dominant. Since the microchannel dimensions have a major effect on the friction factor calculation [13,15,33], a destructive careful measurement was performed after the experiments. Channels were cut carefully at three random cross sections. The cutting lines were perpendicular to the channel to ensure a 90 deg viewing angle. Dimensions of the channel were measured by an image processing method. To do so, a Leica DMI 6000B (Leica Microsystems, Richmond Hill, ON, Canada) microscope with a 10×, 0.4 N.A. objective was used. Images of the channel cross

[2] www.usa.autodesk.com.

Table 1 Dimensions of the fabricated microchannels

Channel	Width, $2W$ (μm)	Depth, $2H$ (μm)	Length, L (mm)	$\varepsilon = H/W$	$L_{D,\max}/L$ (%)
PPR-0.13	780	110	50	0.13	3.47
PPR-0.17	581	101	50	0.17	4.03
PPR-0.4	480	192	58.8	0.4	5.55
PPR-0.6	189	113	55.5	0.6	6.75
PPR-0.76	134	103	50	0.76	7.86

section were captured by a high resolution high sensitivity CCD camera (Hamamatsu Orca AG, NJ) and imported into a photo editing software, ADOBE PHOTOSHOP 8.0. Dimensions of the channel were then measured by pixel counting. Size of each pixel was calibrated using a known dimension provided by the microscope image acquisition software. Accuracy of this method was found to be ± 3.6 μm. Due to the microfabrication process, the microchannel cross section has some deviations from the rectangular shape. Height and width measurements were conducted at different random positions for each cross section and the average value was determined. This measurement was also performed at several cross sections. Mean values are reported in Table 1. It was observed that both microchannel depth and width were different from the expected values in the fabrication process. From our measurements, channel height, and width deviated less than 4% and 3% from the designed sizes, respectively. Since smooth surfaces were observed by the image processing technique described above, the roughness of the channels was estimated to be less than the accuracy of the image processing method. Hence, the relative channel roughness (channel roughness/channel length scale) was found to be less than 3%. As a result the effect of roughness on the pressure drop of the fully developed flow can be neglected [27].

3.3 Experimental Procedure. An open loop syringe pump system, as illustrated in Fig. 2, was designed for this work. A syringe pump (Harvard Apparatus, QC, Canada) provided constant flow rate with $\pm 0.5\%$ accuracy. A range of Reynolds numbers was covered by changing the volumetric flow rate from 40 μl/min to 240 μl/min. Water was forced to flow through a submicron filter (Aktreingeselchaf Co., Germany) before entering the channel. To measure the pressure drop, a gauge pressure transducer (Omega Inc., Laval, QC, Canada) was fixed at the channel inlet while the channel outlet was opened to the atmosphere. Teflon tubing (Scientific Products And Equipment, North York, ON, Canada) was employed to connect the pressure transducer to the syringe pump and the microchannel. Measured pressure was then monitored and recorded with a computerized data acquisition system (LABVIEW 8.5, National Instruments, USA[3]). The flow was considered to have reached a steady state condition when the readings of the pressure drop did not change with time. For a given channel, the measurement of pressure drop was repeated three times for each flow rate. An arithmetic averaging method [43] was performed to determine the final results.

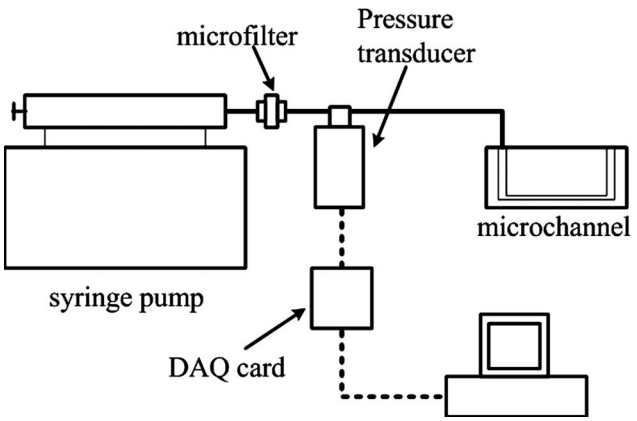

Fig. 2 Schematic of the test section

4 Analysis of Experimental Data

Reynolds number was calculated knowing the volumetric flow rate, Q, and the cross-sectional area, A, from

$$\mathrm{Re}_{\sqrt{A}} = \frac{\rho Q}{\mu \sqrt{A}} \tag{5}$$

Viscous dissipation effect was neglected since the dimensionless number $4\ \mathrm{Ec}[L^* f\ \mathrm{Re}_{\sqrt{A}}]/\mathrm{Re}_{\sqrt{A}} = 0.006$ is much smaller than 1. The value of $\Delta T_{\mathrm{ref}} = 1\,^\circ\mathrm{C}$ was used to calculate the Eckert number, Ec, for water as a working fluid [26]. Hence, the properties of the water was assumed to be constant.

Total measured pressure drop during the experiment, $\Delta P_{\mathrm{measured}}$ is

$$\Delta P_{\mathrm{measured}} = \Delta P_c + \Delta P_{\mathrm{in}} + \Delta P_D + \Delta P_{\mathrm{FD}} + \Delta P_{\mathrm{ex}} + 2\Delta P_b + \Delta P_{\mathrm{ev}} \tag{6}$$

where ΔP_c is the pressure loss due to the flow in the connecting tubes, ΔP_{in} and ΔP_{ex} are the inlet and exit losses, ΔP_D is the developing region loss, ΔP_{FD} is the pressure drop in the fully developed region, ΔP_b is the pressure drop due to 90 deg bends, and ΔP_{ev} is the pressure drop corresponds to the electroviscous effect. Since fully developed pressure drop is the focus of this study, right hand side losses except ΔP_{FD} must be subtracted from the measured pressure drop.

4.1 Connecting Tube Pressure Loss, ΔP_c. The connecting tube pressure drop includes the losses due to all fittings and the capillary tube from the transducer to the microchannel inlet. We measured this loss directly at each flow rate when there was no microchannel at the end of the tubing. The measurements were carefully conducted with the conditions identical to the case when a microchannel was added to the end of the connecting tube to avoid the effects of hydrostatic pressure.

4.2 Developing Region, ΔP_D. Since the viscous boundary layer inherently grows faster in microchannels than in macroscales, the developing region in most cases is negligible. There are few references that can be found in literature, in which the effect of inlet region was considered [40,44,45]. Phillips [44] showed that the length of the hydrodynamic developing region, L_D, depends on the aspect ratio of rectangular cross-section microchannels; the higher the aspect ratio, the longer the developing length. Maximum value of L_D can be obtained from Eq. (7)

$$L_D = \frac{4\varepsilon}{(1+\varepsilon)^2}\frac{\rho Q}{\mu} \tag{7}$$

This equation shows that the developing length depends on the flow rate and the channel aspect ratio. The higher the aspect ratio and/or flow rate, the higher the developing length. Ratio of the maximum developing length over the total length of the microchannel is listed in Table 1 for different channels. Obviously this length occurs in the maximum flow rate. Pressure drop associated with the entrance region after changing the length scale to $\sqrt{A}$ is [46]

$$\Delta P_D = \frac{(f\ \mathrm{Re}_{\sqrt{A}})\mu Q \Gamma}{2A\sqrt{A}} L_D + K\frac{\rho Q^2}{2A^2} \tag{8}$$

where $K = 0.6796 + 1.2197\varepsilon + 3.3089\varepsilon^2 - 9.5921\varepsilon^3 + 8.9089\varepsilon^4$

[3] www.ni.com.

Table 2 Ratio of the developing region pressure drop over the measured pressure drop of the microchannel

	$\Delta P_D/\Delta P_{\text{measured}}$ (%)				
Q (μl/min)	ε=0.13	ε=0.17	ε=0.4	ε=0.6	ε=0.76
40	0.01	0.01	0.04	0.03	0.04
60	0.01	0.02	0.03	0.04	0.06
80	0.01	0.02	0.04	0.06	0.08
100	0.02	0.01	0.06	0.07	0.10
120	0.02	0.02	0.06	0.08	0.11
240	0.03	0.05	0.10	0.20	0.24

$-2.9959\varepsilon^5$.

In Eq. (8), $f\ \mathrm{Re}_{\sqrt{A}}$ was calculated based on the measured pressure drop. Table 2 lists the relative pressure loss of the developing region with respect to the measured pressure drop. As can be seen, the values are small, less than 0.3%, and can be neglected for the range of Reynolds numbers studied in this work ($1<\mathrm{Re}_{\sqrt{A}}<35$). For the higher Reynolds numbers ($\mathrm{Re}\sim 100$), the developing pressure drop, ΔP_D, was found to be less than 2% of the fully developed pressure drop obtained from Eq. (3).

4.3 Minor Losses, ΔP_{min}. Other pressure losses associated with the measured pressure drop are inlet, exit, and bend losses. These losses are usually obtained from the traditional relationships used in macroscale [15,44,46,47]. Phillips [44] showed that the minor pressure losses can be obtained from

$$\Delta P_{\text{min}} = \Delta P_{\text{in}} + \Delta P_{\text{ex}} + 2\Delta P_b = \frac{\rho Q^2}{2A}\left[K_c + K_e + 2K_b\left(\frac{A}{A_t}\right)^2\right] \tag{9}$$

where A and A_t are the channel and connecting tube cross-sectional areas, respectively. K_b is the loss coefficient for the bend, and K_c and K_e represent the contraction and expansion loss coefficients due to area changes. Phillips [44] recommended K_b to be approximately 1.2 for a 90 deg bend. Assuming equal cross-sectional areas for the channel and connecting tubes and also maximum possible values for K_c and K_e [48], relative minor losses with respect to the measured pressure drop are listed in Table 3. As can be seen, these losses are negligible compared with the measured pressure drop. For higher Reynolds numbers ($\mathrm{Re}\sim 100$), minor pressure drop, ΔP_{min}, was found to be less than 5% of the fully developed pressure drop obtained from Eq. (3).

4.4 Electroviscous Effect, ΔP_{ev}. When a liquid is forced through a narrow channel under an applied pressure gradient, the counterions in the diffusive layer of EDL (electric double layer) are moving toward the downstream end and a potential gradient is induced in the flow [49]. This so called streaming potential acts to drive the counterions in the diffuse layer of the EDL to move in the direction opposite to the pressure-driven flow. The overall result is a reduced flow rate for a constant pressure gradient or increase in pressure drop for a given flow rate. This phenomenon, which gives the appearance of an increased viscosity, μ_a, is called the electroviscous effect [50]. The ratio of this apparent viscosity to the actual fluid viscosity for circular cross-section capillaries can be found from [50]

$$\frac{\mu_a}{\mu} \approx 1 + \frac{32\mu}{\sigma_b D^2}\mu_{\text{eo}}^2 \tag{10}$$

where D is the capillary diameter, μ is the fluid viscosity, σ_b is the liquid electrical conductivity, and a is the radius of the capillary. $\mu_{\text{eo}}=\varepsilon_0\varepsilon_r\zeta/\mu$ is the electro-osmotic mobility, where $\varepsilon_0=8.854\times10^{-12}$ $\mathrm{C^2\ V^{-1}\ m^{-1}}$ is the permittivity of vacuum, $\varepsilon_r=78.3$ is the relative permittivity for water at 25°C [49], and ζ is the zeta potential of the surface. Approximating the rectangular cross-section microchannel with a capillary of the same cross-sectional area, $\sigma_b=5.6\times10^{-6}$ $\mathrm{S\ m^{-1}}$ [51] and $\mu_{\text{eo}}=5.9\times10^{-8}$ $\mathrm{m^2\ V^{-1}\ s^{-1}}$ [52] for PDMS, value of μ_a/μ was found to be less than 1.03 for the channel sizes in this study.

Table 3 Ratio of the minor pressure loss over the measured pressure drop of the microchannel

	$\Delta P_{\text{min}}/\Delta P_{\text{measured}}$ (%)				
Q (μl/min)	ε=0.13	ε=0.17	ε=0.4	ε=0.6	ε=0.76
40	0.04	0.04	0.12	0.09	0.11
60	0.05	0.07	0.10	0.13	0.17
80	0.07	0.10	0.14	0.17	0.23
100	0.08	0.07	0.21	0.22	0.28
120	0.09	0.10	0.19	0.25	0.35
240	0.16	0.24	0.35	0.51	0.70

4.5 Effect of Channel Deformation Under Pressure-Driven Flow. Effect of channel deformation becomes important since it can change the microchannel cross-sectional area and as a result the pressure drop. In all equations used in Secs. 1–3, we assumed that the channel cross section did not change under pressure-driven flow. Few works have discussed the importance of bulk deformation in rectangular microchannels. Holden et al. [53] measured the PDMS bulk deformation under high pressure drops ($\sim$1 bar) using the change in fluorescence intensity. Gervais et al. [54] studied the elastic deformation of PDMS microchannels under imposed flow rates. They demonstrated that the channel deformation can effect the the laminar flow profile and pressure distribution within the channels with low aspect ratios and high pressure drops. In a bulged microchannel, measured pressure drop no longer changes linearly with the flow rate [53]. This is because the microchannel cross section varies due to deformation, and for a constant flow rate, pressure drop changes. Figure 3 shows the variation in the channel pressure drop with flow rate for present work. Experimental results properly follow the linear behavior of theoretical profiles. Thus one can conclude that the channel deformation has negligible effect on the results in this work. However, a careful experimental and theoretical investigation is required to study the effect of the channel deformation on the pressure drop of moderate and high aspect ratio rectangular cross-section microchannels.

4.6 Uncertainty Analysis. A careful analysis of the experimental uncertainty in this study is critical to the interpretation of experimental data of Poiseuille number, Po, and exploration of deviations from the macroscale theory. Neglecting the developing region, minor losses, electroviscous effects, and considering that the channel deformation is not significant, the experimental Poiseuille number can be obtained from

$$\mathrm{Po}_{\text{exp}} = \frac{4}{\mu Q}\left(\frac{A^2\sqrt{A}}{L\Gamma}\right)\Delta P_{\text{FD}} \tag{11}$$

where $\Delta P_{\text{FD}}=\Delta P_{\text{measured}}-\Delta P_c$. The uncertainty associated with Po_{exp} based on the measured variables, and the method provided in Ref. [43] is then given by

$$\frac{\omega_{\mathrm{Po}_{\text{exp}}}}{\mathrm{Po}_{\text{exp}}} = \left[\left(\frac{\omega_{\Delta P}}{\Delta P}\right)^2 + \left(\frac{\omega_L}{L}\right)^2 + \left(\frac{\omega_\Gamma}{\Gamma}\right)^2 + \frac{25}{4}\left(\frac{\omega_A}{A}\right)^2 + \left(\frac{\omega_Q}{Q}\right)^2\right]^{1/2} \tag{12}$$

where ω values indicate uncertainty associated with each variable as subscribed, $\omega_A=4[(H\omega_W)^2+(W\omega_H)^2]^{1/2}$ and $\omega_\Gamma=4[\omega_W^2+\omega_H^2]^{1/2}$ (see Appendix for details of calculations). In this equation we

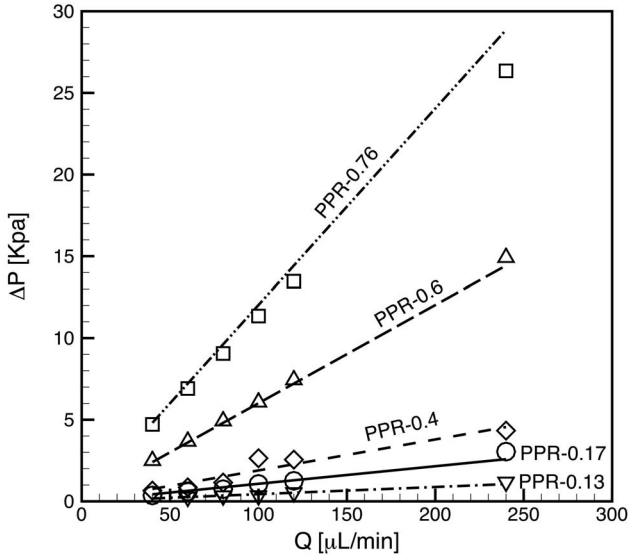

Fig. 3 Channel pressure drop as a function of flow rate. Lines show the theoretical prediction of pressure drop using Eq. (3) and symbols show the experimental data.

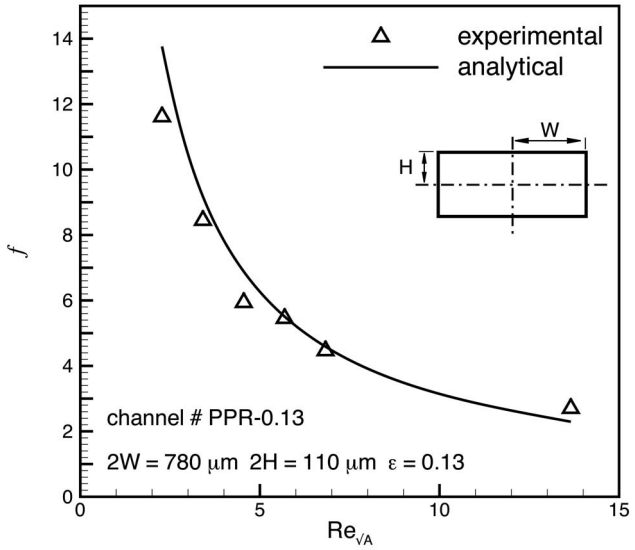

Fig. 4 Variation in friction factor with Reynolds number for sample no. PPR-0.13

assumed that the fluid properties remained constant. Equation (12) shows that the channel dimensions play an important role in determination of uncertainty by effecting three terms. Also for small Reynolds numbers, the accuracy of the flow rate becomes more significant. The uncertainty in the measurement of each parameter is listed in Table 4. Using Eq. (12) minimum uncertainties for the samples of PPR-0.13, PPR-0.17, PPR-0.4, PPR-0.6, and PPR-0.76 are 8.7%, 9.3%, 8.9%, 9.3%, and 11.1%, respectively.

5 Results and Discussion

Figures 4 and 5 show the comparison between friction factor obtained from Eq. (3), the solid line, and experimental data for two typical samples of PPR-0.13 and PPR-0.76, respectively. As shown, the trend and the values of experimental data are well predicted by the theoretical model. Consistent with the laminar flow in channels friction factor decreases with the Reynolds number.

Variation in the Poiseuille number, $f\ \mathrm{Re}_{\sqrt{A}}$, with the Reynolds number for different channels is shown in Fig. 6. Experimental data are normalized by the analytical model obtained from Eq. (3). The solid line shows the analytical model. From Eq. (3), it is clear that the Poiseuille number does not depend on the Reynolds number and it only varies with the aspect ratio of the channel cross section. The same trend can be observed in the experimental data. Large deviations from this trend in the very low Reynolds numbers attributed to the large uncertainties occur due to small flow rates and pressure drops. The Reynolds number can be a result of the small cross-sectional area and/or flow rate, with both parameters increasing the uncertainty in the value of the Poiseuille number, see Eq. (12). As can be seen, most of the experimental points fall within ±10% bounds of the analytical model.

Table 4 Uncertainty values for measured parameters

Parameter	Uncertainty
ΔP	±0.25% of full scale
L	±0.02 mm
W	±3.6 μm
H	±3.6 μm
Q	±0.5%

Another comparison of the present experimental work with analytical model is illustrated in Fig. 7. Since the Poiseuille number, $f\ \mathrm{Re}_{\sqrt{A}}$, remains constant for the laminar regime as the Reynolds number varies, the experimental data for each set were averaged over the laminar region. The ±10% bounds of the model are also shown in the plot to better demonstrate the agreement between the data and the model.

As shown in Eq. (3), the Poiseuille number, $f\ \mathrm{Re}_{\sqrt{A}}$, is only a function of the aspect ratio, which is a geometrical parameter. This dependency is plotted in Fig. 8. Averaged values over the studied range of the Reynolds number were used in this plot. It can be observed that for smaller aspect ratios, the Poiseuille number, $f\ \mathrm{Re}_{\sqrt{A}}$, increases sharply. To better show the trend of the analytical model, two asymptotes of very narrow and square cross sections are also included in Fig. 8. As can be seen, when $\varepsilon \to 0$, parallel plate, the Poiseuille number asymptotically approaches $4\pi^2/3\sqrt{\varepsilon}$.

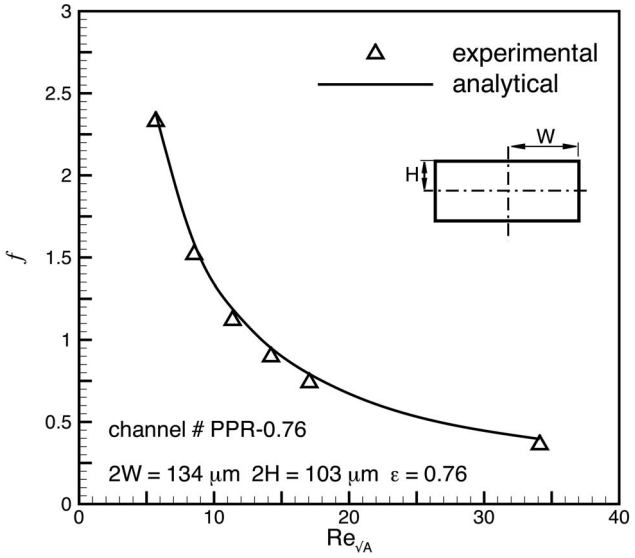

Fig. 5 Variation in friction factor with Reynolds number for sample no. PPR-0.76

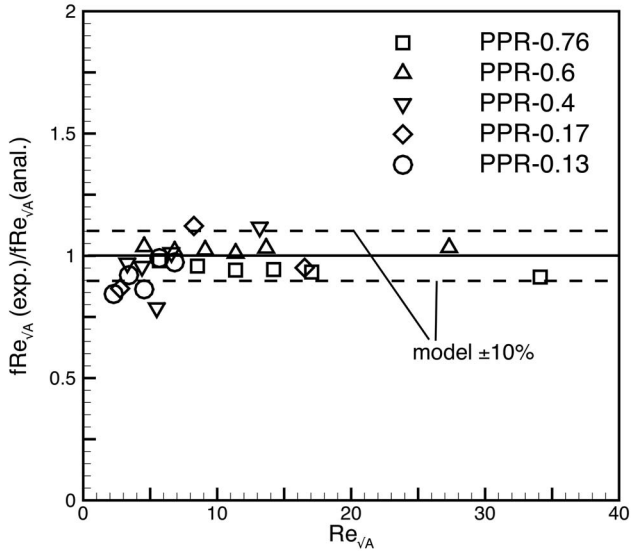

Fig. 6 Variation in Poiseuille number, $f\ \mathrm{Re}_{\sqrt{A}}$, with Reynolds number

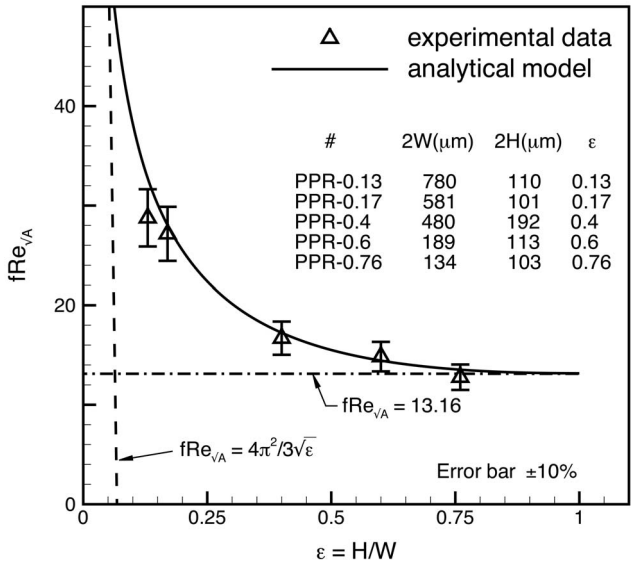

Fig. 8 Variation in Poiseuille number, $f\ \mathrm{Re}_{\sqrt{A}}$, with Reynolds number

It is beneficial to compare the results of present work with the existing data of rectangular microchannels. Data were collected from the works of Wu and Cheng [31], Lu and Garimella [32], and Gao et al. [33]. As shown in Fig. 9, the collected data cover a wide range of the aspect ratio for almost three decades. The solid line represents the analytical model of Bahrami et al. [1]. As can be seen, the analytical model agrees well with the experimental data over the wide range of microchannel cross-section aspect ratio.

6 Summary and Conclusions

The general model developed by Bahrami et al. [1,36] was experimentally validated for the case of rectangular cross-section microchannels. Frictional pressure drop measurements were conducted over a range of Reynolds numbers from 1 to 35 for rectangular cross-section microchannels fabricated with soft lithography method in the aspect ratio range of $0.13 < \varepsilon < 0.76$. A careful measurement of pressure drop and channel dimensions was conducted, and the pressure drops due to the developing region, minor losses, and electroviscous effect were estimated using available models in literature. Channel deformation due to the pressure inside the microchannel was found to be negligible since the pressure drop changes linearly with the flow rate. Comparing the results with the general theoretical model shows good agreement between the model and experimental data.

Uncertainty analysis showed that the measurement of channel dimensions and flow rate is critical in microscales. Here, microchannel cross-section geometry was determined through processing high quality images of the channel cross section.

According to the analytical model and experimental data of present work, the Poiseuille number, $f\ \mathrm{Re}_{\sqrt{A}}$, was found to be only a function of microchannel geometry in the range of Reynolds numbers studied in this work. For rectangular cross sections, the channel aspect ratio is the only parameter that affects the Poi-

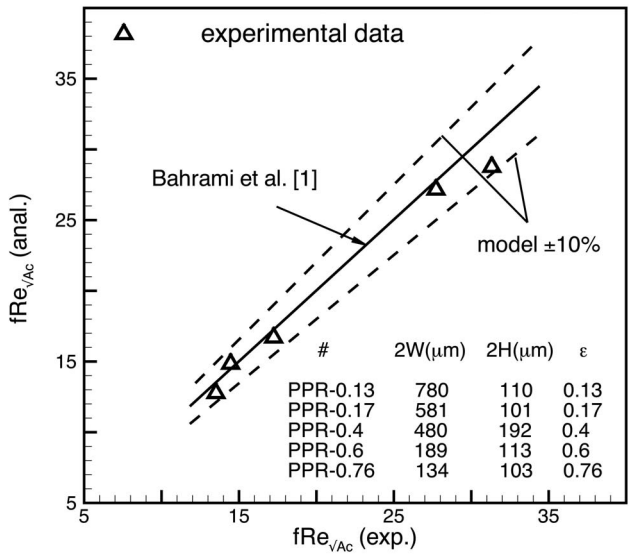

Fig. 7 Comparison of experimental data of present work with analytical model of Bahrami et al. [1]

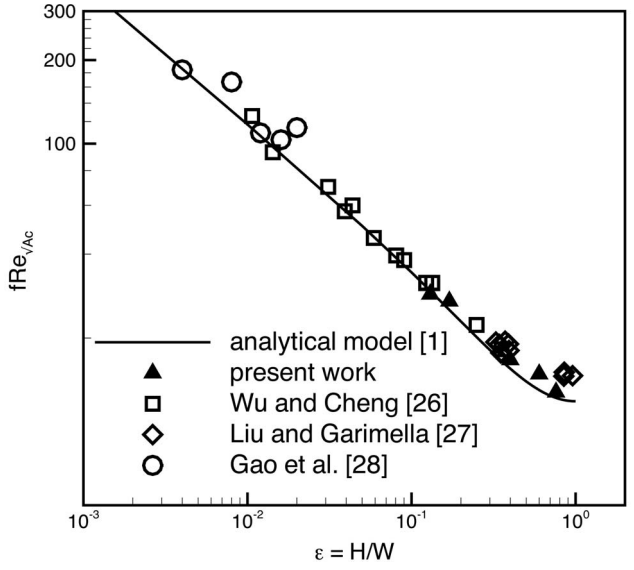

Fig. 9 Comparison between experimental data of present study and previous works

seuille number. The analytical model employed in this work will be applied to other channel geometries such as variable cross-section microchannels in our future work.

Acknowledgment

The authors gratefully acknowledge the financial support of the Natural Sciences and Engineering Research Council of Canada (NSERC). Also they thank Dr. Viatcheslav Berejnov and Mr. Ali K. Oskooi for their assistance.

Nomenclature

A = microchannel cross-sectional area, m^2
A_t = tubing cross-sectional area, m^2
c_p = fluid specific heat, J/kg K
Ec = Eckert number, $W^2/(2c_p\Delta T_{\text{ref}})$
f = Fanning friction factor
H = channel half height, m
I_p = polar momentum of inertia, m^4
I_p^* = specific polar momentum of inertia, I_p/A^2
K_b = loss coefficient for bend
K_c = flow contraction loss coefficient
K_e = flow expansion loss coefficient
L = channel length, m
L_D = developing region length, m
L^* = dimensionless length $L/\sqrt{A}$
Po = Poiseuille number, $f\ \text{Re}_{\sqrt{A}}$
Q = volumetric flow rate, m^3/s
$\text{Re}_{\sqrt{A}}$ = Reynolds number, $\rho Q/\mu\sqrt{A}$
W = channel half width, m

Greek

ΔP_b = bend pressure loss, Pa
ΔP_c = connecting tube pressure loss, Pa
ΔP_D = developing region pressure loss, Pa
ΔP_{ex} = exit pressure loss, Pa
ΔP_{FD} = fully developed pressure loss, Pa
ΔP_{ev} = pressure loss due to electroviscous effect, Pa
ΔP_{in} = inlet pressure loss, Pa
ε = channel aspect ratio, $2H/2W$
Γ = channel cross-section perimeter, m
μ = fluid viscosity, kg/m s
μ_a = apparent viscosity, kg/m s
μ_{eo} = electro-osmotic mobility, m^2/V s
ρ = fluid density, kg/m^3
σ_b = fluid electrical conductivity, S/m
ω = uncertainty

Appendix: Uncertainty Formulation

To calculate the uncertainty associated with the experimental measurements the following relation is used [43]:

$$\omega_R = \left[\sum \left(\frac{\partial R}{\partial x_i}\omega_i\right)^2\right]^{1/2} \tag{A1}$$

where ω_R is the uncertainty in results, $R(x_1, x_2, \ldots, x_n)$, and ω_i is the uncertainty of the independent variable x_i. If the results function, $R(x_1, x_2, \ldots, x_n)$, takes the form of a product of the independent variables, $R = x_1^{a_1} x_2^{a_2}, \ldots, x_n^{a_n}$, Eq. (A1) can be rewritten as

$$\frac{\omega_R}{R} = \left[\sum \left(\frac{a_i}{x_i}\omega_i\right)^2\right]^{1/2} \tag{A2}$$

The final form of the uncertainty of the Poiseuille number, Eq. (12), is obtained using Eqs. (10) and (A2).

To calculate the uncertainty of the channel cross section, $A = 4W \times H$, and perimeter, $\Gamma = 4(W+H)$, Eq. (A1) is employed

$$\omega_A = \left[\left(\frac{\partial A}{\partial W}\omega_W\right)^2 + \left(\frac{\partial A}{\partial H}\omega_H\right)^2\right]^{1/2} \tag{A3}$$

$$\omega_\Gamma = \left[\left(\frac{\partial \Gamma}{\partial W}\omega_W\right)^2 + \left(\frac{\partial \Gamma}{\partial H}\omega_H\right)^2\right]^{1/2} \tag{A4}$$

where $\partial A/\partial W = 4H$, $\partial A/\partial H = 4W$, $\partial \Gamma/\partial W = 4$, and $\partial \Gamma/\partial H = 4$.

References

[1] Bahrami, M., Yovanovich, M. M., and Culham, J. R., 2006, "Pressure Drop of Laminar, Fully Developed Flow in Microchannels of Arbitrary Cross-Section," ASME J. Fluids Eng., **128**, pp. 1036–1044.
[2] Whitesides, G. M., 2006, "The Origins and the Future of Microfluidics," Nature (London), **442**, pp. 368–372.
[3] Grushka, E., McCormick, R. M., and Kirkland, J. J., 1989, "Effect of Temperature Gradients on the Efficiency of Capillary Zone Electrophoresis Separations," Anal. Chem., **61**, pp. 241–246.
[4] Fletcher, P. D. I., Haswell, S. J., Pombo-Villar, E., Warrington, B. H., Watts, P., Wong, S., and Zhang, X., 2002, "Micro Reactors: Principles and Applications in Synthesis," Tetrahedron, **58**, pp. 4735–4757.
[5] DeWitt, S., 1999, "Microreactors for Chemical Synthesis," Curr. Opin. Chem. Biol., **3**(3), pp. 350–356.
[6] Miyake, R., Lammerink, S. J., Elwenspoek, M., and Fluitman, H. J., 1993, "Micro Mixer With Fast Diffusion," MEMS '93, Fort Lauderdale, FL, pp. 248–253.
[7] Weigl, B. H., Bardell, R. L., and Cabrera, C. R., 2003, "Lab-on-a-Chip for Drug Development," Adv. Drug Delivery Rev., **55**, pp. 349–377.
[8] Becker, H., and Locascio, L. E., 2002, "Polymer Microfluidic Devices," Talanta, **56**, pp. 267–287.
[9] Chovan, T., and Guttman, A., 2002, "Microfabricated Devices in Biotechnology and Biochemical Processing," Trends Biotechnol., **20**(3), pp. 116–122.
[10] Ehrfeld, W., 2003, "Electrochemistry and Microsystems," Electrochim. Acta, **48**, pp. 2857–2868.
[11] Bayraktar, T., and Pidugu, S. B., 2006, "Characterization of Liquid Flows in Microfluidic Systems," Int. J. Heat Mass Transfer, **49**, pp. 815–824.
[12] Peng, X. F., Peterson, G. P., and Wang, B. X., 1994, "Frictional Flow Characteristics of Water Flowing Through Rectangular Microchannels," Exp. Heat Transfer, **7**, pp. 249–64.
[13] Xu, B., Ooi, K. T., and Wong, N. T., 2000, "Experimental Investigation of Flow Friction for Liquid Flow in Microchannels," Int. Commun. Heat Mass Transfer, **27**, pp. 1165–1176.
[14] Ren, C. L., and Li, D., 2004, "Electroviscous Effects on Pressure-Driven Flow of Dilute Electrolyte Solutions in Small Microchannels," J. Colloid Interface Sci., **274**, pp. 319–330.
[15] Judy, J., Maynes, D., and Webb, B. W., 2002, "Characterization of Frictional Pressure Drop for Liquid Flows Through Microchannels," Int. J. Heat Mass Transfer, **45**, pp. 3477–3489.
[16] Tuckerman, D. B., and Peace, R. F. W., 1981, "High-Performance Heat Sinking for VLSI," IEEE Electron Device Lett., **2**, pp. 126–129.
[17] Mala, G. M., and Li, D., 1999, "Flow Characteristics of Water in Microtubes," Int. J. Heat Mass Transfer, **20**, pp. 142–148.
[18] Pfhaler, J., Harley, J., and Bau, H., 1990, "Liquid Transport in Micron and Submicron Channels," Sens. Actuators, A, **A21–A23**, pp. 431–434.
[19] Pfhaler, J., Harley, J., Bau, H., and Zemel, J. N., 1991, "Gas and Liquid Flow in Small Channels Micromechanical Sensors, Actuators, and Systems," ASME Dyn. Syst. Control Div., **32**, pp. 49–60.
[20] Urbanek, W., Zemel, J. N., and Bau, H. H., 1993, "An Investigation of the Temperature Dependence of Poiseuille Numbers in Microchannel Flow," J. Micromech. Microeng., **3**, pp. 206–208.
[21] Qu, W., Mala, G. M., and Li, D., 2000, "Pressure-Driven Water Flows in trapezoidal Silicon Microchannels," Int. J. Heat Mass Transfer, **43**, pp. 3925–3936.
[22] Papautsky, I., Brazzle, J., Ameel, T., and Frazier, A. B., 1999, "Laminar Fluid Behavior in Microchannels Using Micropolar Fluid Theory," Sens. Actuators, A, **73**, pp. 101–108.
[23] Ren, C. L., and Li, D., 2005, "Improved Understanding of the Effect of Electrical Double Layer on Pressure-Driven Flow in Microchannels," Anal. Chim. Acta, **531**, pp. 15–23.
[24] Weilin, Q., Mala, H. M., and Li, D., 2000, "Pressure-Driven Water Flows in Trapezoidal Silicon Microchannels," Int. J. Heat Mass Transfer, **43**, pp. 353–364.
[25] Guo, Z., and Li, Z., 2003, "Size Effect on Microscale Single-Phase Flow and Heat Transfer," Int. J. Heat Mass Transfer, **46**, pp. 149–159.
[26] Morini, G. L., 2005, "Viscous Heating in Liquid Flows in Microchannels," Int. J. Heat Mass Transfer, **48**, pp. 3637–3647.
[27] Bahrami, M., Yovanovich, M. M., and Culham, J. R., 2006, "Pressure Drop of Laminar, Fully Developed Flow in Rough Microtubes," ASME J. Fluids Eng., **128**, pp. 632–637.
[28] Jiang, X. N., Zhou, Z. Y., Huang, X. Y., and Liu, C. Y., 1997, "Laminar Flow Through Microchannels Used for Microscale Cooling Systems," IEEE/CPMT Electronic Packaging Technology Conference, pp. 119–122.
[29] Baviere, R., Ayela, F., Le Person, S., and Favre-Marinet, M., 2005, "Experimental Characterization of Water Flow Through Smooth Rectangular Microchannels," Phys. Fluids, **17**, p. 098105.
[30] Bucci, A., Celata, G. P., Cumo, M., Serra, E., and Zummo, G., 2003, "Water Single-Phase Fluid Flow and Heat Transfer in Capillary Tubes," International Conference on Microchannels and Minichannels, Vol. 1, pp. 319–326, ASME Paper No. 1037.

[31] Wu, H. Y., and Cheng, P., 2003, "Friction Factors in Smooth Trapezoidal Silicon Microchannels With Different Aspect Ratios," Int. J. Heat Mass Transfer, **46**, pp. 2519–2525.
[32] Liu, D., and Garimella, S., 2004, "Investigation of Liquid Flow in Microchannels," J. Thermophys. Heat Transfer, **18**, pp. 65–72.
[33] Gao, P., Le Person, S., and Favre-Marinet, M., 2002, "Scale Effects on Hydrodynamics and Heat Transfer in Two-Dimensional Mini and Microchannels," Int. J. Therm. Sci., **41**, pp. 1017–1027.
[34] Squires, T. M., and Quake, S. R., 2005, "Micro Fluidics: Fluid Physics at Nanoliter Scale," Rev. Mod. Phys., **77**, pp. 977–1026.
[35] White, F. M., 1974, *Viscous Fluid Flow*, McGraw-Hill, New York, Chap. 3.
[36] Bahrami, M., Yovanovich, M. M., and Culham, J. R., 2007, "A Novel Solution for Pressure Drop in Singly Connected Microchannels," Int. J. Heat Mass Transfer, **50**, pp. 2492–2502.
[37] Timoshenko, S. P., and Goodier, J. N., 1970, *Theory of Elasticity*, McGraw-Hill, New York, Chap. 10.
[38] Yovanovich, M. M., 1974, "A General Expression for Predicting Conduction Shape Factors," *AIAA Prog. in Astro. and Aeronautics: Thermophysics and Space Craft Control*, Vol. 35, R. G. Hering, ed., MIT Press, Cambridge, MA, pp. 265–291.
[39] Muzychka, Y. S., and Yovanovich, M. M., 2002, "Laminar Flow Friction and Heat Transfer in Non-Circular Ducts and Channels Part 1: Hydrodynamic Problem," Proceedings of Compact Heat Exchangers, A Festschrift on the 60th Birthday of Ramesh K. Shah, Grenoble, France, pp. 123–130.
[40] Shah, R. K., and London, A. L., 1978, *Laminar Flow Forced Convection in Ducts, Supplement to Advances in Heat Transfer*, Academic, New York.
[41] Erickson, D., Sinton, D., and Li, D., 2003, "Joule Heating and Heat Transfer in Poly(dimethylsiloxane) Microfluidic Systems," Lab Chip, **3**, pp. 141–149.
[42] McDonald, J. C., Duffy, D. C., Anderson, J. R., Chiu, D. T., Wu, H., Schueller, O. J. A., and Whiteside, G., 2000, "Fabrication of Microfluidic Systems in Poly(dimethylsiloxane)," Electrophoresis, **21**, pp. 27–40.
[43] Holman, J. P., 2001, *Experimental Methods for Engineering*, 7th ed., McGraw-Hill, New York, Chap. 3.
[44] Phillips, R. J., 1990, *Microchannel Heat Sinks, Advances in Thermal Modeling of Electronic Components and Systems*, Hemisphere, New York, Chap. 3.
[45] Sharp, K. V., Adrian, R. J., Santiago, J. G., and Molho, J. I., 2005, *Liquid Flows in Microchannels, MEMS Hand Book: Introduction and Fundamentals*, 2nd ed., Taylor & Francis, New York.
[46] Kandlikar, S. G., Garimella, S., Li, D., Colin, S., and King, M. R., 2006, *Heat Transfer and Fluid Flow in Minichannels and Microchannels*, Elsevier, Oxford.
[47] Steinke, M. E., and Kandlikar, S. G., 2006, "Single-Phase Liquid Friction Factors in Microchannels," Int. J. Therm. Sci., **45**, pp. 1073–1083.
[48] Kays, W. M., and London, A. L., 1984, *Compact Heat Exchangers*, McGraw-Hill, New York.
[49] Probstein, R. F., 1994, *Physicochemical Hydrodynamics*, 2nd ed., Wiley, New York.
[50] Masliyah, J. H., and Bhattacharjee, S., 2006, *Electrokinetic and Colloid Transport Phenomena*, Wiley, Englewood Cliffs, NJ.
[51] Lide, D., and Kehiaian, H. V., 1994, *CRC Handbook of Thermophysical and Thermochemical Data*, 1st ed., CRC Press, Florida.
[52] Lee, J. S. H., Hu, Y., and Li, D., 2005, "Electrokinetic Concentration Gradient Generation Using a Converging-Diverging Microchannel," Anal. Chim. Acta, **543**, pp. 99–108.
[53] Holden, M. A., Kumar, S., Beskok, A., and Cremer, P. S., 2003, "Microfluidic Diffusion Diluter: Bulging of PDMS Microchannels Under Pressure Driven Flow," J. Micromech. Microeng., **13**, pp. 412–418.
[54] Gervais, T., El-Ali, J., Gunther, A., and Jensen, K., 2006, "Flow-Induced Deformation of Shallow Microfluidic Channels," Lab Chip, **6**, pp. 500–507.

Numerical Modeling of Laminar Pulsating Flow in Porous Media

S.-M. Kim[1,2]
e-mail: kim698@purdue.edu

S. M. Ghiaasiaan[1]
e-mail: mghiaasiaan@gatech.edu

G. W. Woodruff School of Mechanical Engineering,
Georgia Institute of Technology,
Atlanta, GA 30332-0405

The laminar pulsating flow through porous media was numerically studied. Two-dimensional flows in systems composed of a number of unit cells of generic porous structures were simulated using a computational fluid mechanics tool, with sinusoidal variations in flow with time as the boundary condition. The porous media were periodic arrays of square cylinders. Detailed numerical data for the porosity ranging from 0.64 to 0.84, with flow pulsation frequencies of 20–64 Hz were obtained. Based on these numerical data, the instantaneous as well as the cycle-average permeability and Forchheimer coefficients, to be used in the standard unsteady volume-averaged momentum conservation equation for flow in porous media, were derived. It was found that the cycle-average permeability coefficients were nearly the same as those for steady flow, but the cycle-average Forchheimer coefficients were significantly larger than those for steady flow and were sensitive to the flow oscillation frequency. Significant phase lags were observed between the volume-averaged velocity and the pressure waves. The phase difference between pressure and velocity waves, which is important for pulse tube cryocooling, depended strongly on porosity and the mean-flow Reynolds number.
[DOI: 10.1115/1.3089541]

Keywords: porous media, pulsating flow, permeability, Forchheimer coefficient, phase shift

1 Introduction

Pulsating and periodic flows in porous media are poorly understood. An important area of application of such flow is in the Stirling and pulse tube cryocooler systems. In these systems, microporous structures constitute cold and warm heat exchangers, and more importantly a regenerator, all of which are subject to a periodic flow of a gas (usually helium).

The fluid-solid interactions in these microporous structures, in particular, the regenerator, are important with respect to the performance of the cryocooler system. The frictional losses, in particular, adversely affect the overall system performance. A number of experimental investigations dealing with friction in commonly-used cryocooler regenerator material have been reported in the recent past [1–6]. These investigations have all dealt with the macroscopic aspects of friction in porous media subject to periodic flow and have shown that, except at very low frequencies, the closure parameters that represent friction between the fluid and solid are different in steady and periodic flows. However, no systematic study of pore-level phenomena during periodic or pulsating flows through porous media has been reported in the past. It is thus the objective of this investigation to study the pore-level phenomena in a pulsating flow through a generic two-dimensional porous medium by numerical analysis, and from there examine the effects of flow pulsations on the closure parameters that are encountered in the standard volume-averaged momentum equation for porous media. We have chosen the pulsating flow as an intermediate step toward the more difficult problem of periodic flow.

Since pore-level analysis in general is not feasible for the usual design and analysis calculations for flow through porous media, model equations are often applied instead. The most widely used method for the derivation of tractable model equations for porous media is volume averaging, where surface integrals and integrals involving dispersion and tortuosity are replaced with tractable model terms [7–11]. The model equations derived in this way will include terms with unknown coefficients that must be found by experiments or numerical simulations aimed at pore-level analysis. For the pore-level analysis, the exact pore structure is needed, however, which is often complex, nonuniform, and even unknown. Nevertheless, valuable information about the flow in porous media can be obtained by direct pore-level simulation of idealized generic porous media composed of periodically-configured circular or square cylinders. Published investigations in this area include Refs. [12–18].

These investigations have all addressed steady flow, however, it appears that transient flows in porous media and, in particular, pulsating or periodic flow have thus far not been systematically studied by numerical simulation of pore-level flow and heat/mass transport phenomena.

2 Geometric Configuration

For the numerical simulation of flow through porous media, two-dimensional periodic arrays of cylindrical or rectangular cylinders are usually assumed [12–18]. In this study, the porous medium is simulated by an array of square cylinders. Figure 1 depicts the unit cells and dimensions of all the configurations considered. The flow everywhere is from left to right along the x coordinate. The geometric dimensions have been chosen such that porosity ranging from 0.64 to 0.84 is covered, where evidently (see Fig. 2)

$$\varepsilon = 1 - (D/L)^2 \tag{1}$$

Figure 2 displays the generic computational domain, which is composed of six unit cells in series. Past studies have shown that the end effects typically extend for a few unit cells in porous media, and an array of several unit cells is an adequate computational domain [9,12]. The forthcoming simulation results confirm that by using six unit cells in series and investigating in detail the flow field in the fifth unit cell, the end effects are effectively eliminated in the simulations.

[1]Corresponding author.
[2]Present address at Boiling and Two-Phase Flow Laboratory, School of Mechanical Engineering, Purdue University, West Lafayette, IN 47907-1288
Contributed by the Fluids Engineering Division of ASME for publication in the JOURNAL OF FLUIDS ENGINEERING. Manuscript received August 8, 2008; final manuscript received January 5, 2009; published online March 9, 2009. Assoc. Editor: Neelesh A. Patankar.

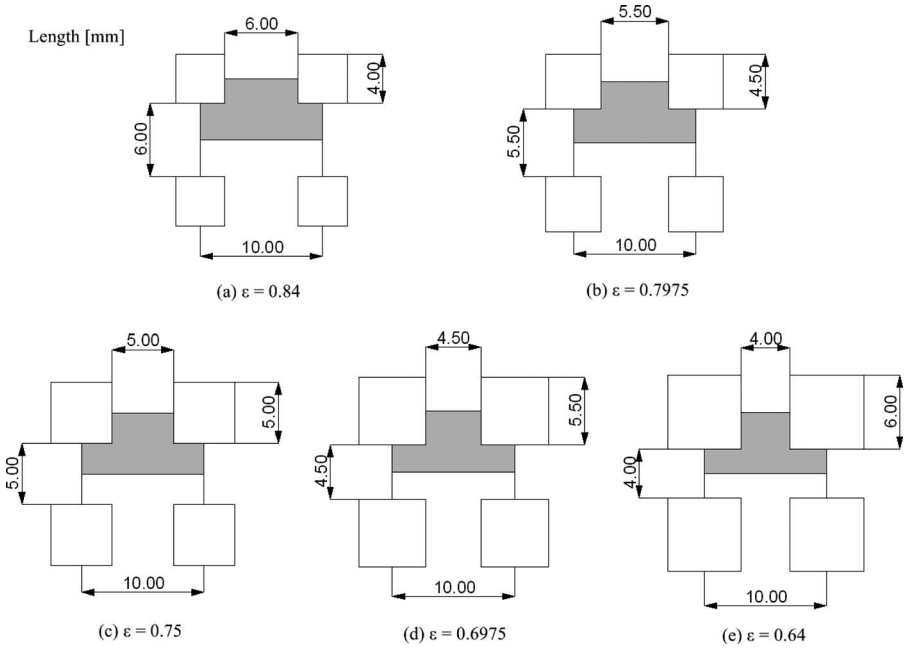

Fig. 1 Different porous structure geometries showing a unit cell of continuous porous structures

Figure 3 shows a sample grid system for the porous structure with $\varepsilon=0.84$, where each unit cell is represented with a 20×40 grid structure. Since the location of the inlet and outlet can affect the convergence and the accuracy of the simulations, following several numerical tests, it was found out that the inlet and outlet should be separated from the computational domain by buffer zone lengths of $2L$ and $7L$, respectively. With these separation lengths the simulation results became effectively independent of the inlet and outlet locations.

3 Governing Equations

Two separate sets of conservation equations are solved for the system shown in Fig. 3. The Navier–Stokes equations are solved for detailed pore-level simulations. These will be referred to as the microscopic-level equations. The results obtained with the microscopic-level equations will be compared with the solution of volume-average porous media-type equations. The latter equations will be referred to as the macroscopic-level equations.

Assuming incompressible and constant-property fluid, the microscopic-level equations will be the following:

$$\nabla \cdot \boldsymbol{u} = 0 \tag{2}$$

$$\frac{\partial \boldsymbol{u}}{\partial t} + \boldsymbol{u} \cdot \nabla \boldsymbol{u} = -\frac{1}{\rho} \nabla P + \nu \nabla^2 \boldsymbol{u} \tag{3}$$

where properties all belong to the fluid.

The macroscopic-level conservation equations will be the commonly-used model equations for flow in porous media [19–21]. The superficial volume-average velocity is defined as

$$\langle \boldsymbol{u} \rangle = \frac{1}{V} \int_{V_f} \boldsymbol{u} dV \tag{4}$$

where V and V_f denote the averaging control volume and the fluid volume contained within the averaging control volume, respectively (see Fig. 2). The intrinsic volume-average fluid velocity is defined as

$$\langle \boldsymbol{u} \rangle^f = \frac{1}{V_f} \int_{V_f} \boldsymbol{u} dV \tag{5}$$

Clearly, $\varepsilon = V_f/V = \langle \boldsymbol{u} \rangle / \langle \boldsymbol{u} \rangle^f$. The macroscopic-level momentum conservation equation will be as follows [17,20,21]:

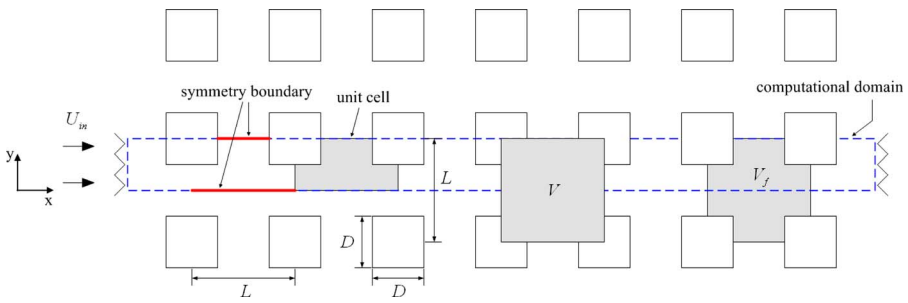

Fig. 2 Computational domain with boundary conditions

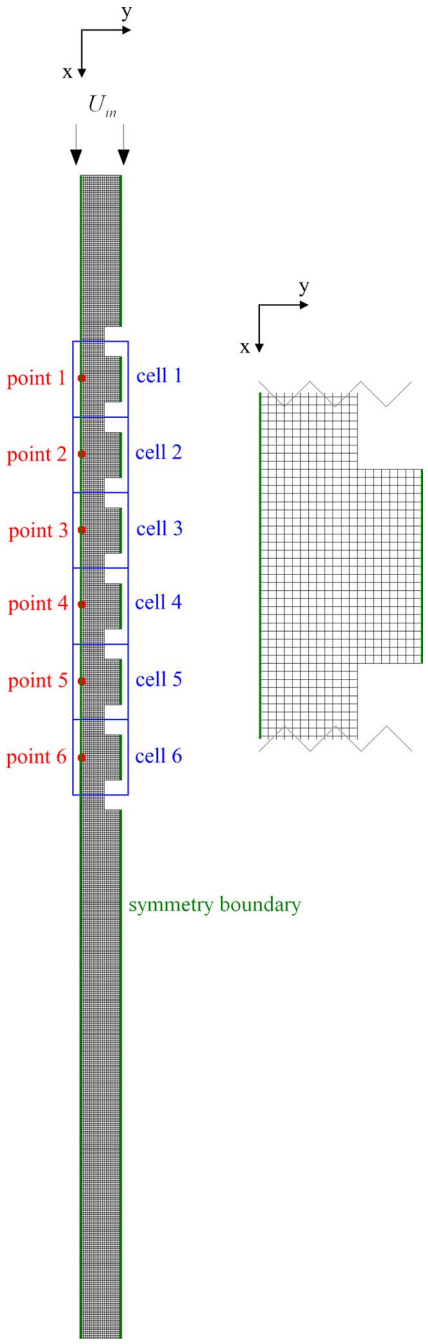

Fig. 3 Sample grid system for $\varepsilon=0.84$

$$\rho\left(\frac{\partial\langle\boldsymbol{u}\rangle^f}{\partial t}+\langle\boldsymbol{u}\rangle^f\cdot(\nabla\langle\boldsymbol{u}\rangle^f)\right)=-\nabla\langle P\rangle^f+\mu\nabla^2\langle\boldsymbol{u}\rangle^f-\frac{\varepsilon\mu}{\bar{\bar{K}}}\cdot\langle\boldsymbol{u}\rangle^f-\varepsilon^2\rho\bar{\bar{B}}\cdot|\langle\boldsymbol{u}\rangle^f|\langle\boldsymbol{u}\rangle^f \tag{6}$$

where $\varepsilon\mu/\bar{\bar{K}}\cdot\langle\boldsymbol{u}\rangle^f$ will be referred to as the Darcy term, which accounts for the viscous effect; $\mu\nabla^2\langle\boldsymbol{u}\rangle^f$ is the Brinkman term, which is important only in the interface between the porous medium and other solid boundaries, such as a wall or an adjacent fluid region, where the effective viscosity μ_e of the porous medium is assumed as $\mu_e\approx\mu$; and $\varepsilon^2\rho\bar{\bar{B}}\cdot|\langle\boldsymbol{u}\rangle^f|\langle\boldsymbol{u}\rangle^f$ is referred to as the Forchheimer term, which accounts for the inertial effects, and becomes dominant when $\langle\boldsymbol{u}\rangle^f$ is large. Under macroscopically fully developed flow, the Darcy and Forchheimer terms depend only on the geometry of the porous medium, and the Forchheimer effect can be negligible when the flow rate becomes vanishingly small.

For the porous structures shown in Fig. 3, the x coordinate is a principle direction. As a result, when a pressure gradient in the x direction is imposed, the flow on a macroscopic scale will also be in the x direction only. With respect to a coordinate system that coincides with the principle directions, the tensors $\bar{\bar{K}}$ and $\bar{\bar{B}}$ are both diagonal. Thus, Eq. (6) can be cast for flow in x direction as

$$\rho\left(\frac{\partial\langle u_x\rangle^f}{\partial t}+\langle u_x\rangle^f\frac{\partial\langle u_x\rangle^f}{\partial x}\right)=-\frac{\partial\langle P\rangle^f}{\partial x}+\mu\frac{\partial^2\langle u_x\rangle^f}{\partial x^2}-\frac{\varepsilon\mu}{K_{xx}}\langle u_x\rangle^f-\varepsilon^2\rho B_{xx}|\langle u_x\rangle^f|\langle u_x\rangle^f \tag{7}$$

where K_{xx} and B_{xx} are the x components of the diagonal tensors $\bar{\bar{K}}$ and $\bar{\bar{B}}$, respectively. In case of steady macroscopic flow in the x direction, Eq. (7) leads to the Forchheimer-extended Darcy equation.

$$0=-\frac{\partial\langle P\rangle^f}{\partial x}-\left(\frac{\mu}{K_{xx,st}}\langle u_x\rangle+\rho B_{xx,st}|\langle u_x\rangle|\langle u_x\rangle\right) \tag{8}$$

This equation can be written in nondimensional form as

$$\xi=\frac{L^2}{K_{xx,\mathrm{st}}\,\mathrm{Re}_L}+B_{xx,\mathrm{st}}L \tag{9}$$

where

$$\mathrm{Re}_L=\frac{\rho|\langle\boldsymbol{u}\rangle|L}{\mu} \tag{10}$$

and

$$\xi=-\frac{\partial\langle P\rangle^f}{\partial x}\frac{L}{\rho|\langle u_x\rangle|^2} \tag{11}$$

4 Numerical Solution Method

The microscopic-level equations are solved using the FLUENT 6.3 computational fluid dynamics (CFD) code [22]. The density-based Navier–Stokes coupled solution algorithm of FLUENT, which includes low-Mach number preconditioning, artificial compressibility, and dual time-stepping for the solution of unsteady incompressible flow, solves the governing equations of continuity and momentum simultaneously [22,23]. The first-order upwind discretization scheme is used to treat the convection terms. For the diffusion terms, the central difference scheme is used.

The two-dimensional mesh (as depicted in Fig. 3) was created by using the GAMBIT 2.2 software [24]. Detailed numerical data representing the oscillating velocity and pressure variations are obtained from the calculation of the microscopic-level governing equations. Then the volume-averaged velocities and pressures of each unit cell are used to numerically calculate the instantaneous as well as the cycle-average permeability and Forchheimer coefficients, as described below. For this purpose, a program was developed in C++. This program solves the unsteady volume-averaged momentum equation implicitly by using the finite-difference method.

To obtain the volume-averaged velocities and pressures at each unit cell of the generic porous structures, a user defined function (UDF) was coded in the C++ programming language. The numerical simulations are conducted with air as the working fluid, assuming $\rho=1.225$ kg/m^3 and $\mu=1.7894\times10^{-5}$ kg/(m s). The sinusoidal pulsating area-averaged velocity at inlet boundary, to be discussed later, was also implemented by a UDF of FLUENT 6.3 [22].

Equation (7) is numerically solved for the macroscopic-level analysis, using the backward in time and central in space (BTCS) finite-difference scheme, where a first-order backward-

differencing for the time derivative and a second-order central differencing for the spatial derivative are used. Thus, for unit cell i,

$$\rho\left(\frac{\langle u\rangle_i^{f,n}-\langle u\rangle_i^{f,n-1}}{\Delta t}+\langle u\rangle_i^{f,n}\frac{\langle u\rangle_{i+1}^{f,n}-\langle u\rangle_{i-1}^{f,n}}{2\Delta x}\right)=-\frac{\langle P\rangle_{i+1}^{f,n}-\langle P\rangle_{i-1}^{f,n}}{2\Delta x}$$
$$+\mu\frac{\langle u\rangle_{i+1}^{f,n}-2\langle u\rangle_i^{f,n}+\langle u\rangle_{i-1}^{f,n}}{(\Delta x)^2}-\frac{\varepsilon\mu}{K_{xx,\mathrm{inst}}(t)}\langle u\rangle_i^{f,n}-\varepsilon^2\rho B_{xx,\mathrm{inst}}(t)$$
$$\times|\langle u\rangle_i^{f,n}|\langle u\rangle_i^{f,n}+O[(\Delta t),(\Delta x)^2] \tag{12}$$

where subscript n and superscript i are time step and grid point indices, respectively. Note that u in the above equation implies u_x, and the subscript x has been left out for convenience.

The calculation procedure for extracting the permeability and Forchheimer coefficients from the microscopic-level solutions for pulsating flow is as follows. We note that at the limit of $\langle u\rangle^f\to 0$, the Forchheimer term in Eq. (7) or Eq. (12) can be neglected. Thus, for each of the configurations in Fig. 1, the following steps are followed:

(1) Obtain $\langle u\rangle_i^{f,n}$ and $\langle P\rangle_i^{f,n}$ for $i=1-6$ and during n equally-spaced time snapshots.
(2) Solve the following equation for the time snapshots covering two pulsation cycles for the low-flow simulations, and thereby obtain $K_{xx,\mathrm{inst}}(t)$.

$$\rho\left(\frac{\langle u\rangle_i^{f,n}-\langle u\rangle_i^{f,n-1}}{\Delta t}+\langle u\rangle_i^{f,n}\frac{\langle u\rangle_{i+1}^{f,n}-\langle u\rangle_{i-1}^{f,n}}{2\Delta x}\right)=$$
$$-\frac{\langle P\rangle_{i+1}^{f,n}-\langle P\rangle_{i-1}^{f,n}}{2\Delta x}+\mu\frac{\langle u\rangle_{i+1}^{f,n}-2\langle u\rangle_i^{f,n}+\langle u\rangle_{i-1}^{f,n}}{(\Delta x)^2}$$
$$-\frac{\varepsilon\mu}{K_{xx,\mathrm{inst}}(t)}\langle u\rangle_i^{f,n} \tag{13}$$

(3) Obtain the cycle-average permeability coefficient $K_{xx,\mathrm{avg}}$.
(4) Solve Eq. (12) for the time snapshots covering two pulsation cycles for the high-flow simulations by treating $K_{xx,\mathrm{inst}}(t)$ as known, and thereby obtain $B_{xx,\mathrm{inst}}(t)$.
(5) Obtain the cycle-average Forchheimer coefficient $B_{xx,\mathrm{avg}}$.

The cycle-average parameters are calculated from the following:

$$K_{xx,\mathrm{avg}}=f\int_{t_o}^{t_o+1/f}K_{xx,\mathrm{inst}}(t)dt \tag{14}$$

$$B_{xx,\mathrm{avg}}=f\int_{t_o}^{t_o+1/f}B_{xx,\mathrm{inst}}(t)dt \tag{15}$$

A similar but simpler procedure is used for the calculation of K_{xx} and B_{xx} under steady-flow conditions (see Ref. [25] for details).

The boundary conditions for the simulations are now discussed. The inlet boundary is located at a distance $2L$ upstream from the inlet to the first unit cell, where the velocity has a uniform profile. The no-slip boundary condition is applied on the wall. Referring to Fig. 2, in view of symmetry with respect to the x-axis, only half of the physical domain that represents the six unit cells is considered, and at the top and bottom faces of a unit cell, the normal gradients of all variables are prescribed as zero. The outflow boundary is located at a distance $7L$ downstream from the exit of the last unit cell, where a zero-gradient is imposed for all dependent variables.

The Re_L ranging from 0.1 to 1000 is used for the steady-flow simulations. The converged steady-state results are used as the initial values for the relevant unsteady calculations. For the pulsating flow simulations, the mean Reynolds numbers based on the mean superficial (Darcy) velocity U_m of $\mathrm{Re}_{m,L}=0.11$ and 560 are selected for the calculation of the instantaneous permeability and Forchheimer coefficients, respectively. The velocity at the inlet of the computational domain in pulsating flow simulations is

$$U_{\mathrm{in}}=U_m[1+a\sin(2\pi ft)],\quad a=0.4 \tag{16}$$

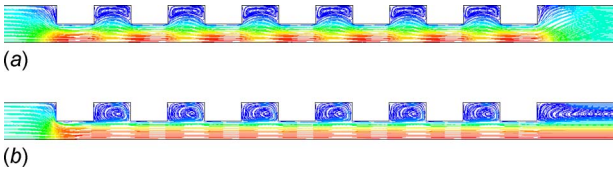

Fig. 4 Steady-state streamline patterns for (*a*) $\mathrm{Re}_L=0.11$ and (*b*) $\mathrm{Re}_L=560$ in the case of $\varepsilon=0.75$

5 Steady Flow

For CFD simulations, a convergence criterion of 10^{-6} was applied to the residuals of the continuity and momentum equations. Grid independence was examined by using two grid systems with 20×40 and 40×80 per unit cell. The two simulations showed nearly identical velocity and pressure distributions for the pairs of simulations with the maximum difference between the volume-averaged pressure gradients within 1%. For calculation efficiency, a grid system with 20×40 per unit cell was chosen for all the subsequent simulations.

Figure 4 represents the typical steady-state streamline patterns. The streamline patterns are similar for all the unit cells. The flow details in the unit cells 4, 5, and 6 are virtually identical, indicating a fully developed state. It is seen that for the low Reynolds number flow, a pair of small vortices appears between the adjacent square rods. For the high Reynolds number flow, the position of the vortex center in the cavity is shifted slightly downstream.

The pressure drop characteristics along the flow direction are presented in terms of the nondimensional pressure gradient ξ in Fig. 5. The nondimensional pressure gradient undergoes a large change in the entrance region and reaches an almost constant value along the flow direction. At very low Reynolds numbers ($\mathrm{Re}_L<1$), it is observed that the hydrodynamically fully developed regime is reached just after the second unit cell. However, in case of high Reynolds numbers, the pressure gradient still varies slightly from the third to fourth unit cells, and the change in pressure gradient from one unit cell to the next is decreased as the fully developed condition is reached further downstream. Similar

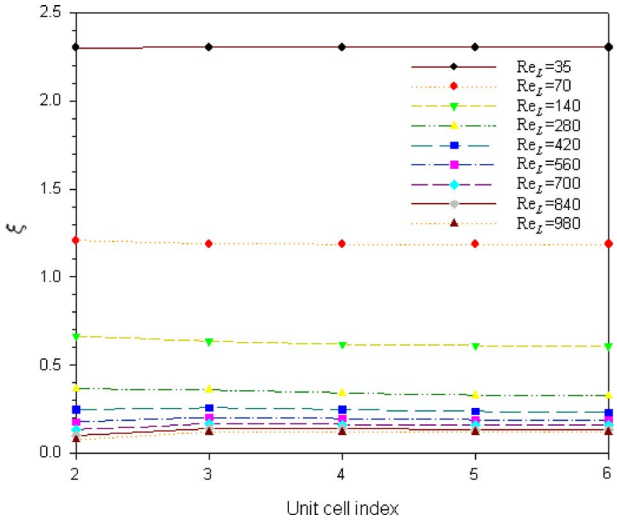

Fig. 5 Nondimensional pressure gradient along the flow direction with Reynolds number for the steady flow

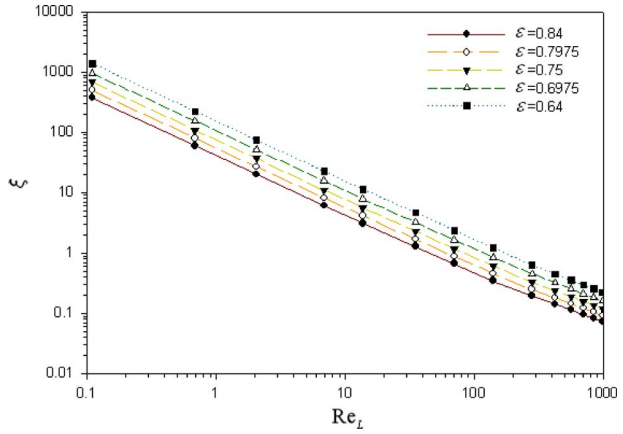

Fig. 6 Nondimensional pressure gradient as a function of Reynolds number for steady flow

trends have also been observed experimentally and numerically by many researchers, including Coulaud et al. [12], Benarji et al. [26], Raju and Narasimhan [27], and Sahiti et al. [28]. It was found that the change in nondimensional pressure gradient between the fourth and fifth unit cells is 0.04% and 1.7% for Re_L =35 and 980, respectively. Therefore, the flow after the fourth unit cell is considered to be fully developed, and the following results and observations are based on the fifth unit cell.

Figure 6 shows the variation in dimensionless pressure gradient ξ with Re_L, while the dependence of the Forchheimer term on Re_L is displayed in Fig. 7. Evidently, for $\mathrm{Re}_L \gtrsim 200$, the Forchheimer term approaches a constant that depends on ε and, as expected, it vanishes as $\mathrm{Re}_L \to 0$.

The permeability and Forchheimer terms for steady flow are shown in Table 1. The table also contains parameter values for pulsating flow, which will be discussed later. Nakayama et al. [16] performed numerical simulations for steady flow in a generic porous medium similar to Fig. 1(*c*). Our calculations show $L^2/K_{xx,\mathrm{st}}=75$ for $\varepsilon=0.75$, which agrees well with $L^2/K_{xx,\mathrm{st}}=76$ reported by Nakayama et al. [16]. However, we obtained $B_{xx,\mathrm{st}}L$ =0.049, which is one-quarter of $B_{xx,\mathrm{st}}L=0.2$ reported in Ref. [16].

6 Pulsating Flow

The pulsating flow CFD simulations are started from an initial condition represented by the aforementioned steady-flow simulations and are continued until steady-pulsating flow conditions are achieved. Steady-pulsating flow is assumed when all calculated

Table 1 The permeability and Forchheimer coefficients for steady and pulsating flows

ε	$\frac{L^2}{K_{xx,\mathrm{st}}}$	$\frac{L^2}{K_{xx,\mathrm{avg}}}$	$B_{xx,\mathrm{st}}L$	$B_{xx,\mathrm{avg}}L$
0.64	153	159	0.071	0.121
0.6975	105	113	0.058	0.108
0.75	75	79	0.049	0.096
0.75[a]	75	80	0.049	0.078
0.75[b]	75	80	0.049	0.088
0.7975	55	59	0.041	0.085
0.84	41	47	0.036	0.077

[a]20 Hz.
[b]64 Hz,

quantities at t and $t+T$ are identical for points 1–6 in Fig. 3. Similar to steady-flow simulations, two grid systems with 20 $\times$40 and 40$\times$80 nodes per unit cell were generated, and grid independence was investigated by comparing the volume-averaged pressure gradients. The maximum difference in volume-averaged pressure gradient between the two grid systems was 2.8% at the first unit cell. Additionally, the effect of the time step size was studied by using three time step sizes $\Delta t=2.5\times10^{-4}$ s $(T/100)$, 1.25×10^{-4} s $(T/200)$, and 6.25×10^{-5} s $(T/400)$, in simulations where the period of oscillation T was 0.025 s. Figure 8 compares the instantaneous area-averaged velocities at inlet and outlet for $\varepsilon=0.75$ with a grid size of 20$\times$40 per unit cell, for the aforementioned three time step sizes. Evidently, there is essentially no difference among the model predictions for the three time steps. Therefore, a time step size of $1.25\times10^{-4}(T/200)$s and a grid size of 20$\times$40 per unit cell are used in the forthcoming calculations.

Figure 9 shows the instantaneous velocities and pressures along the flow direction for a typical run. Although the calculations are continued for 0.375 s, the cyclic steady state was obtained after only 7 cycles, or 0.175 s. The convergence criterion was the relative error in the oscillating velocity component, which was required to be smaller than 10^{-3}.

Figures 10 and 11 display typical instantaneous velocities and pressures for steady-pulsating flow condition for $\mathrm{Re}_{m,L}=0.11$ and $\mathrm{Re}_{m,L}=560$, respectively. Although the pulsating inlet velocity is sinusoidal, the calculated velocity and pressure waves are not exactly sinusoidal. Furthermore, the amplitudes of velocity and pressure waves are attenuated along the flow direction, and a phase shift develops between instantaneous velocity and pressure waves. For the low pulsating Reynolds number flow, the amplitudes of

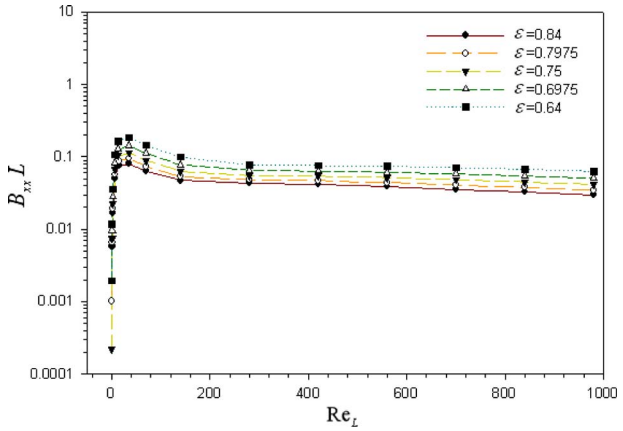

Fig. 7 The Forchheimer term as a function of Reynolds number for steady flow

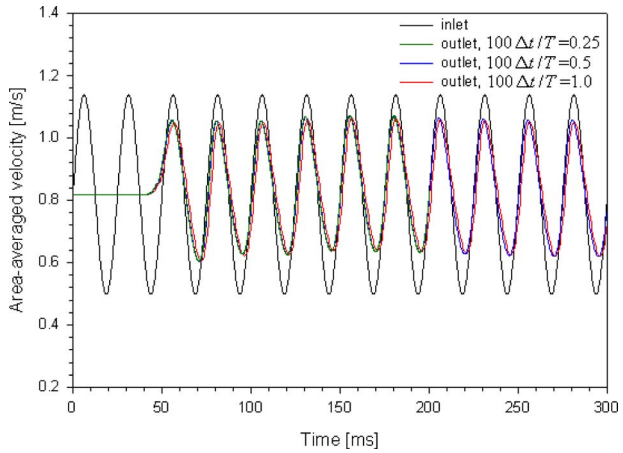

Fig. 8 Time independence test for the base case of $\varepsilon=0.75$ with the grid size of 20$\times$40 per unit cell

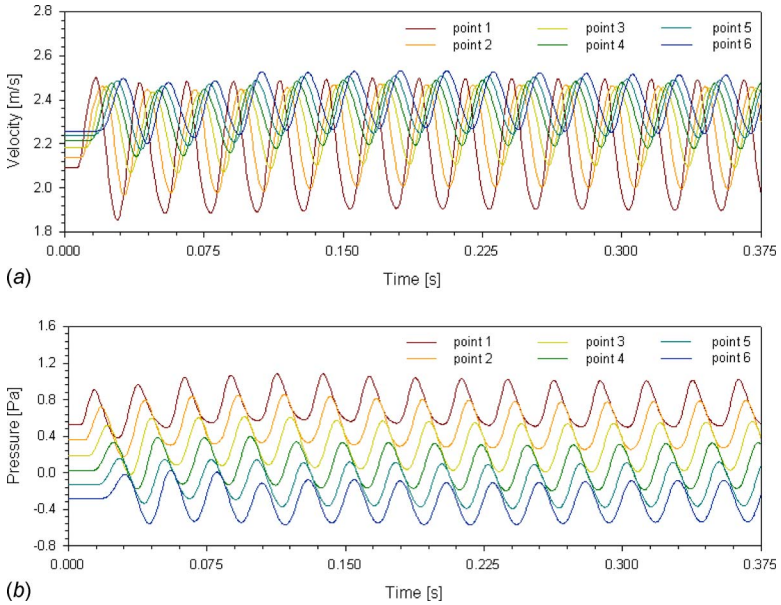

Fig. 9 Convergence check for $\varepsilon=0.75$ with 20×40 nodes per unit cell for (*a*) velocity and (*b*) pressure

instantaneous pressure waves along the flow direction decrease notably; whereas for high $Re_{m,L}$ cases, the reduction in instantaneous pressure amplitudes is insignificant along the flow direction, and the waves are flattened with decreasing porosity. The results also show that the cycle-average instantaneous velocities at the measured points increase as the porosity decreases, and as the

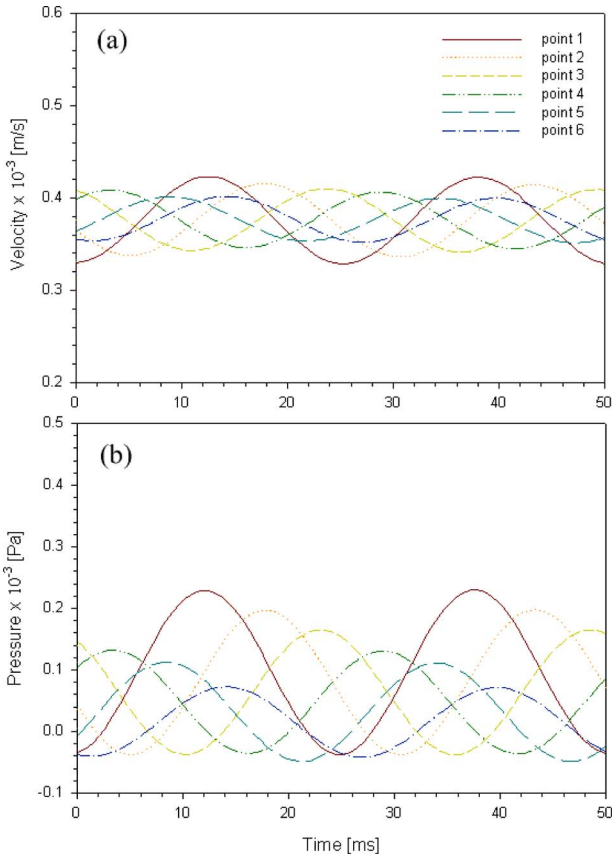

Fig. 10 Variation in the instantaneous (*a*) velocity and (*b*) pressure waves along the flow direction for $Re_{m,L}=0.11$ and $\varepsilon=0.7975$

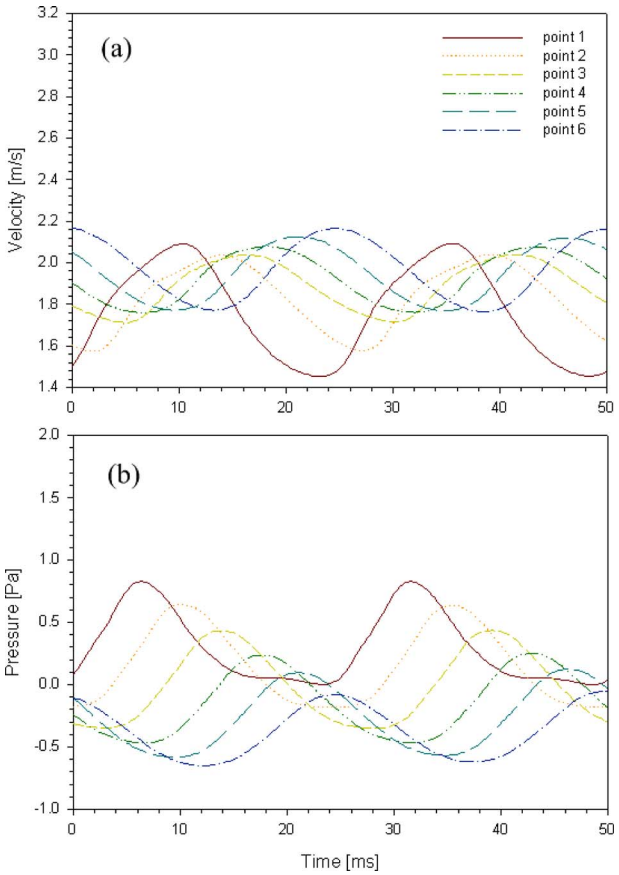

Fig. 11 Variation in the instantaneous (*a*) velocity and (*b*) pressure waves along the flow direction for $Re_{m,L}=560$ and $\varepsilon=0.84$

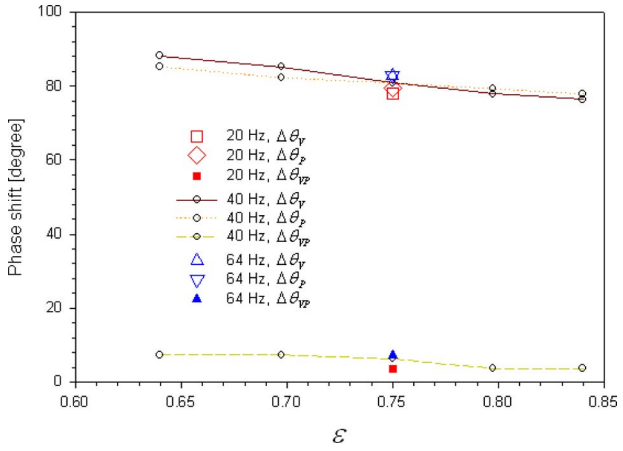

Fig. 12 Phase shifts $\Delta\theta_V$, $\Delta\theta_P$, and $\Delta\theta_{VP}$ in terms of porosities for pulsating low Reynolds number flow ($Re_{m,L}=0.11$)

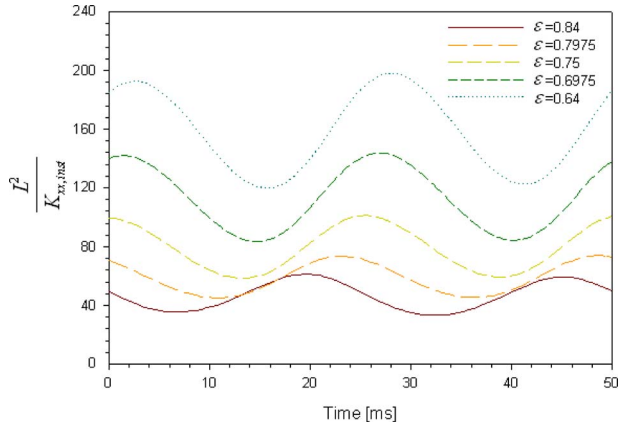

Fig. 14 Variation in the instantaneous permeability coefficients for different porosities (f=40 Hz calculated from $Re_{m,L}$ =0.11)

porosity decreases the differences in cycle-average instantaneous pressures between adjacent two unit cells increase.

Figures 12 and 13 display the velocity phase shift $\Delta\theta_V$, pressure phase shift $\Delta\theta_P$, and the phase difference between velocity and pressure $\Delta\theta_{VP}$ at low and high Reynolds numbers, respectively. The aforementioned phase shifts are defined as follows:

$$\Delta\theta_V = (\theta_{V,\text{pt6}} - \theta_{V,\text{pt1}})/5 \tag{17}$$

$$\Delta\theta_P = (\theta_{P,\text{pt6}} - \theta_{P,\text{pt1}})/5 \tag{18}$$

$$\Delta\theta_{VP} = (\Delta\theta_{VP,\text{pt1}} + \Delta\theta_{VP,\text{pt6}})/2 \tag{19}$$

where subscripts 1 and 6 refer to points 1 and 6 in Fig. 3; θ_V and θ_P represent the phase angles associated with the velocity and pressure waves; and $\Delta\theta_{VP}=\theta_V-\theta_P$. The phase shifts $\Delta\theta_V$ and $\Delta\theta_P$ thus represent the average phase lags, per unit cell, which occur to the velocity and pressure, respectively, and $\Delta\theta_{VP}$ is the average phase shift between velocity and pressure. As noted, at low $Re_{m,L}$, $\Delta\theta_V$, $\Delta\theta_P$, and $\Delta\theta_{VP}$ are all relatively insensitive to both frequency and ε. However, for high $Re_{m,L}$ (Fig. 13), the aforementioned phase shift parameters all depend on ε and frequency. The dependence of $\Delta\theta_V$ and $\Delta\theta_{VP}$ on ε is not monotonic, and for the 40 Hz frequency their maxima occur at ε=0.75 and 0.7975, respectively. The parameters $\Delta\theta_V$ and $\Delta\theta_P$ for the low $Re_{m,L}$ are significantly larger than those for the high $Re_{m,L}$ cases.

The permeability and Forchheimer terms are now discussed. Figures 14 and 15 display the instantaneous permeability and Forchheimer terms. These terms were calculated following the procedure described in Sec. 4. As noted, for the instantaneous permeability coefficient, the amplitude and the cycle-average value of permeability coefficient increase with decreasing porosity. An interesting observation in Fig. 15 is that during a portion of each cycle, the values of instantaneous Forchheimer coefficient were negative, since the left hand side of the unsteady volume-averaged momentum equation (Eq. (7)), which presents the local and convective acceleration terms, is less than the pressure drop term in the same equation. With increasing porosity, the portion of the cycle in which the value of instantaneous Forchheimer coefficient is negative is extended. The negative values for the Forchheimer coefficient are, of course, a result of the phase difference between the pressure and velocity waves. It should also be emphasized that the form of the volume-averaged porous-media momentum equation is theoretically plausible only for quasisteady (i.e., relatively slow transient) processes [9]. For fast transients, theory would indicate that additional higher-order terms may be needed in the equation. Inclusion of such additional higher-order terms is not feasible at this time, however, since such terms would require additional unknown closure relations and parameters. The standard Darcy–Forchheimer volume-averaged equations are therefore generally used in the analysis of transient processes.

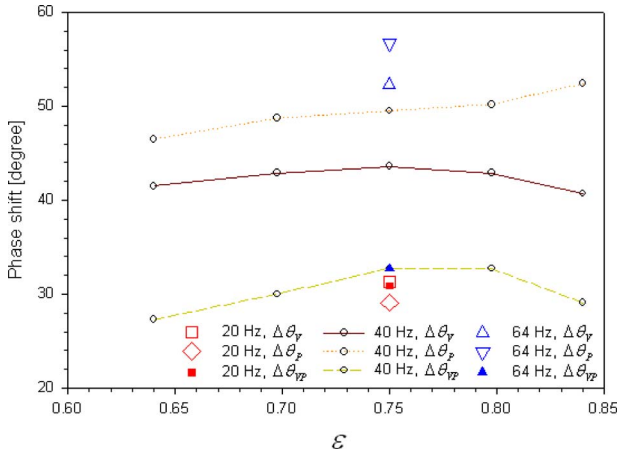

Fig. 13 Phase shifts $\Delta\theta_V$, $\Delta\theta_P$, and $\Delta\theta_{VP}$ in terms of porosities for pulsating high Reynolds number flow ($Re_{m,L}=560$)

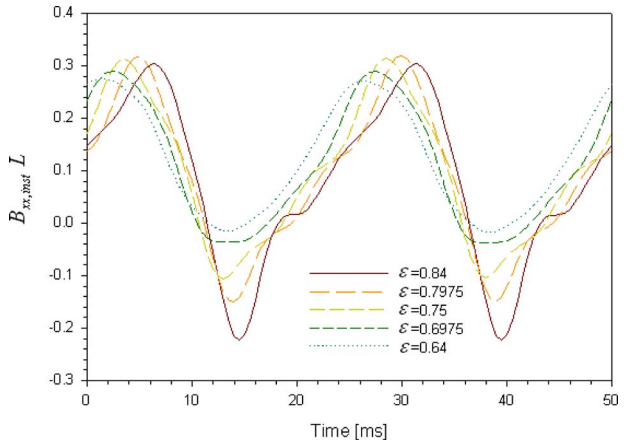

Fig. 15 Variation in the instantaneous Forchheimer coefficients for different porosities (f=40 Hz calculated from $Re_{m,L}$ =0.11 and 560)

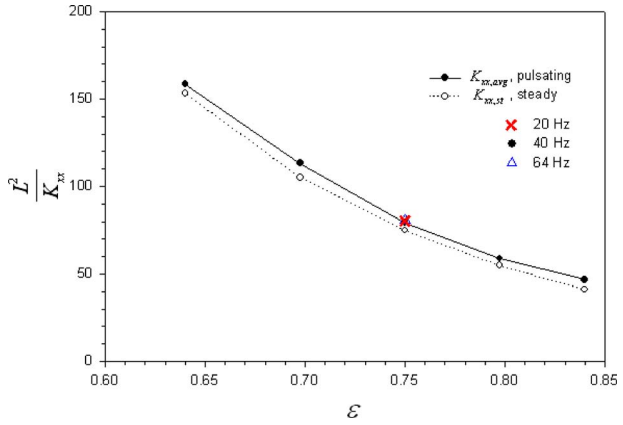

Fig. 16 Comparison of the permeability coefficients between the steady and pulsating flow for different porosities

The cycle-average permeability and Forchheimer terms are shown in Figs. 16 and 17, respectively, and their numerical values are provided in Table 1. In both figures, model predictions are shown for $f=40$ Hz for all porosities of interest. For $\varepsilon=0.75$, however, model predictions for $f=20$ Hz and 60 Hz are also depicted. Furthermore, in both figures the parameters representing steady-flow conditions are also shown for comparison. The permeability parameter, as noted in Fig. 16, is a strong function of porosity and monotonically decreases as porosity is increased. More importantly, furthermore, the cycle-average permeability parameter for pulsating flow is only slightly larger than the permeability parameter for steady flow (or, equivalently, the permeability for pulsating flow is only slightly larger than the permeability for steady flow). On the other hand, as noted in Fig. 17, the cycle-average Forchheimer coefficients decrease with increasing porosity and are about two times larger than those for steady flow at the same porosity. It is also noted in Fig. 17 that the Forchheimer parameter depends on the frequency, and its dependence on frequency is not monotonic. Our simulation results, although relatively limited in scope and parametric range, thus suggest that the application of the Darcy–Forchheimer model equations with steady-flow parameters to pulsating flow is, in general, incorrect. While the permeability is likely to be approximately the same for steady and pulsating flow conditions, the Forchheimer coefficient can have significantly different values for steady-flow and pulsating flow conditions. More comprehensive investigations are recommended for better understanding the trends and dependencies in pulsating flow.

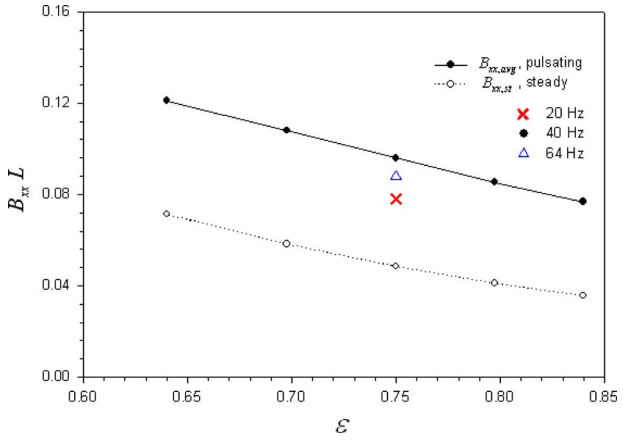

Fig. 17 Comparison of the Forchheimer coefficients between the steady and pulsating flow for different porosities

7 Conclusions

We have investigated, by numerical simulation, the momentum transfer parameters associated with pulsating laminar flow through generic porous media made of periodic square cylinders patterned on a rectangular pitch, for flow pulsation frequencies of 20–64 Hz and the porosity ranging from 0.64–0.84. Detailed numerical data representing the oscillating two-dimensional velocity and pressure variations were obtained by solving the Navier–Stokes using the CFD code FLUENT 6.3. These numerical data were then utilized for the calculation of various volume-averaged properties to be used in the standard Darcy-extended Forchheimer momentum equation. Instantaneous and cycle-average parameters were both extracted and displayed. The results indicated that the application of the Darcy-extended Forchheimer momentum equation with coefficients representing steady flow to pulsating flow conditions is only adequate at very low-flow (low frequency) conditions and is otherwise incorrect. Within the range of parameters studied in this investigation, the pulsating flow cycle-average permeabilities were a strong function of porosity, but they were only slightly larger than the permeabilities for steady flows. The cycle-average Forchheimer coefficients for pulsating flows strongly depended on frequency, however, and were significantly larger than steady-flow Forchheimer coefficients.

The results also showed that the velocity and pressure phase shifts are sensitive to the mean-flow Reynolds number. The velocity phase shifts $\Delta\theta_V$ and pressure phase shifts $\Delta\theta_P$ for low mean-flow Reynolds numbers ($\mathrm{Re}_{m,L}=0.11$) were significantly larger than those for the high-flow Reynolds number ($\mathrm{Re}_{m,L}=560$) flows. However, the phase shifts between velocity and pressure $\Delta\theta_{VP}$ for $\mathrm{Re}_{m,L}=560$ were several times larger than those for the $\mathrm{Re}_{m,L}=0.11$ case.

Nomenclature

a = normalized amplitude of velocity
A = constant
B = Forchheimer coefficient (1/m)
$B_{xx,\mathrm{avg}}$ = cycle-average Forchheimer coefficient (m^2)
$B_{xx,\mathrm{inst}}$ = instantaneous Forchheimer coefficient along the x direction for pulsating flow (m^2)
$B_{xx,\mathrm{st}}$ = Forchheimer coefficient along the x direction for steady flow (m^2)
$\bar{\bar{B}}$ = Forchheimer coefficient tensor (1/m)
D = side of square rod (m)
f = frequency (Hz)
I = identity tensor
K = permeability coefficient (m^2)
$K_{xx,\mathrm{avg}}$ = cycle-average permeability coefficient (m^2)
$K_{xx,\mathrm{inst}}$ = instantaneous permeability coefficient along the x direction for pulsating flow (m^2)
$K_{xx,st}$ = permeability coefficient along the x direction for steady flow (m^2)
$\bar{\bar{K}}$ = permeability tensor (m^2)
L = length of unit cell (m)
P = static pressure ($\mathrm{N/m}^2$)
$\langle P\rangle^f$ = intrinsic volume-average fluid static pressure over V_f ($\mathrm{N/m}^2$)
Re_L = Reynolds number based on a unit cell length L in steady flow
$\mathrm{Re}_{m,l}$ = Reynolds number based on mean velocity and unit cell length (pulsating flow)
t = time (s)
T = period of pulsation (s)
u, U = velocity (m/s)
$\langle \boldsymbol{u}\rangle$ = superficial volume-average fluid velocity (m/s)
$\langle \boldsymbol{u}\rangle^f$ = intrinsic volume-average fluid velocity (m/s)
V = averaging control volume (m^3)

V_f = fluid volume in an averaging control volume (m^3)
Δt = time step size (s)

Greek Letters

ε = porosity of medium
μ = molecular viscosity (kg/m s)
ν = kinematic viscosity (m^2/s)
θ = phase angle (deg)
ρ = density (kg/m^3)
$\Delta\theta_V$ = phase shift of velocity (deg)
$\Delta\theta_P$ = phase shift of pressure (deg)
$\Delta\theta_{VP}$ = phase shift between velocity and pressure (deg)
ξ = nondimensional pressure gradient

Subscripts

avg = cycle-average value
e = effective
exit = exit
i = grid point index
in = inlet
inst = instantaneous value
m = mean value
st = steady state
x, xx = x direction

Superscripts

f = fluid
n = time step index
= = tensor

References

[1] Ju, Y. L., Wang, C., and Zhou, Y., 1998, "Numerical Simulation and Experimental Verification of the Oscillating Flow in Pulse Tube Refrigerator," Cryogenics, **38**, pp. 169–176.
[2] Hsu, C. T., Fu, H. L., and Cheng, P., 1999, "On Pressure Velocity Correlation of Steady and Oscillating Flows in Regenerators Made of Wire-Screens," ASME J. Fluids Eng., **121**, pp. 52–56.
[3] Nam, K., and Jeong, S., 2002, "Experimental Study on the Regenerator Under Actual Operating Conditions," Adv. Cryog. Eng., **47**, pp. 977–984.
[4] Jeong, S., Nam, K., and Jung, J., 2002, "Regenerator Characterization Under Oscillating Flow and Pulsating Pressure," Cryocoolers, **12**, pp. 531–537.
[5] Cha, J. S., Ghiaaisiaan, S. M., Desai, P. V., Harvey, J. P., and Kirkconnell, C. S., 2006, "Multi-Dimensional Flow Effects in Pulse Tube Refrigerators," Cryogenics, **46**, pp. 658–665.
[6] Clearman, W. M., Cha, J. S., Ghiaasiaan, S. M., and Kirkconnell, C. S., 2008, "Anisotropic Steady-Flow Hydrodynamic Parameters of Microporous Media Applied to Pulse Tube and Stirling Cryocooler Regenerator," Cryogenics, **48**, pp. 112–121.
[7] Whitaker, S., 1973, "The Transport Equations for Multi-Phase Systems," Chem. Eng. Sci., **28**, pp. 139–147.
[8] Gray, W. G., and O'Neill, K., 1976, "On the General Equation for Flow in Porous Media and Their Reduction to Darcy's Law," Water Resour. Res., **12**, pp. 148–154.
[9] Kaviany, M., 1995, *Principles of Heat Transfer in Porous Media*, 2nd ed., Springer-Verlag, Berlin.
[10] Quintard, M., Kaviany, M., and Whitaker, S., 1997, "Two-Medium Treatment of Heat Transfer in Porous Media: Numerical Results for Effective Properties," Adv. Water Resour., **20**, pp. 77–94.
[11] Moyne, C., Didierjean, S., Amaral Souto, H. P., and da Silveira, O. T., 2000, "Thermal Dispersion in Porous Media: One Equation Model," Int. J. Heat Mass Transfer, **43**, pp. 3853–3867.
[12] Coulaud, O., Morel, P., and Caltagiorne, J. P., 1988, "Numerical Modeling of Nonlinear Effects in Laminar Flow Through a Porous Medium," J. Fluid Mech., **190**, pp. 393–407.
[13] Kuwahara, F., Nakayama, A., and Koyama, H., 1996, "A Numerical Study of Thermal Dispersion in Porous Media," ASME J. Heat Transfer, **118**, pp. 756–761.
[14] Kuwahara, F., Shirota, M., and Nakayama, A., 2001, "A Numerical Study of Interfacial Convective Heat Transfer Coefficient in Two-Energy Equation Model for Convection in Porous Media," Int. J. Heat Mass Transfer, **44**, pp. 1153–1159.
[15] Kuwahara, F., Yamane, T., and Nakayama, A., 2006, "Large Eddy Simulation of Turbulent Flow in Porous Media," Int. Commun. Heat Mass Transfer, **33**, pp. 411–418.
[16] Nakayama, A., Kuwahara, F., Umemoto, T., and Hayashi, T., 2002, "Heat and Fluid Flow Within an Anisotropic Porous Medium," ASME J. Heat Transfer, **124**(4), pp. 746–753.
[17] Nakayama, A., Kuwahara, F., and Kodama, Y., 2006, "An Equation for Thermal Dispersion Flux Transport and Its Mathematical Modeling for Heat Transfer and Fluid Flow in a Porous Medium," J. Fluid Mech., **563**, pp. 81–96.
[18] Nakayama, A., Kuwahara, F., and Sano, Y., 2007, "Concept of Equivalent Diameter for Heat and Fluid Flow in Porous Media," AIChE J., **53**, pp. 732–736.
[19] Vafai, K., and Tien, C. L., 1981, "Boundary and Inertia Effects on Flow and Heat Transfer in Porous Media," Int. J. Heat Mass Transfer, **24**, pp. 195–203.
[20] Vafai, K., and Amiri, A., 1998, "Non-Darcian Effects in Confined Forced Convective Flows," *Transport Phenomena in Porous Media*, D. B. Ingham and I. Pope, eds., Pergamon, New York.
[21] Hsu, C. T., and Cheng, P., 1990, "Thermal Dispersion in a Porous Medium," Int. J. Heat Mass Transfer, **33**, pp. 1587–1597.
[22] FLUENT Inc., 2006, "Fluent 6 User Manual.
[23] Weiss, J. M., and Smith, W. A., 1995, "Preconditioning Applied to Variable and Constant Density Flows," AIAA J., **33**, pp. 2050–2057.
[24] FLUENT Inc., 2006, "GAMBIT 2 User Manual.
[25] Kim, S.-M., 2008, "Numerical Investigation on Laminar Pulsating Flow Through Porous Media," MS thesis, Georgia Institute of Technology, Atlanta, GA.
[26] Benarji, N., Balaji, C., and Venkateshan, S. P., 2008, "Unsteady Fluid Flow and Heat Transfer Over a Bank of Flat Tubes," Heat Mass Transfer, **44**, pp. 445–461.
[27] Raju, K. S., and Narasimhan, A., 2007, "Porous Medium Interconnector Effects on the Thermohydraulics of Near-Compact Heat Exchangers Treated as Porous Media," ASME J. Heat Transfer, **129**, pp. 273–281.
[28] Sahiti, N., Lemouedda, A., Stojkovic, D., Durst, F., and Franz, E., 2006, "Performance Comparison of Pin Fin In-Duct Flow Arrays With Various Pin Cross-Sections," Appl. Therm. Eng., **26**, pp. 1176–1192.

Aerodynamic Analysis of a Vehicle Tanker

Ramon Miralbes Buil

Luis Castejon Herrer

Research Group in Vehicles and Road Safety (VEHIVIAL), CPS, University of Zaragoza, Zaragoza 50012, Spain

The aim of this article is the presentation of a series of aerodynamic improvements for semitrailer tankers, which reduce the aerodynamic resistance of these vehicles, and, consequently, result in a positive impact on fuel consumption, which is substantially reduced (up to 11%). To make the analysis the computational fluid dynamics (CFD) methodology, using FLUENT, has been used since it allows simulating some geometries and modifications of the geometry without making physical prototypes that considerably increase the time and the economical resources needed. Three improvements are studied: the aerodynamic front, the undercarriage skirt, and the final box adaptor. First they are studied in isolation, so that the independent contribution of each improvement can be appreciated, while helping in the selection of the most convenient one. With the aerodynamic front the drag coefficient has a reduction of 6.13%, with the underskirt 9.6%, and with the boat tail 7.72%. Finally, all the improvements are jointly examined, resulting in a decrease of up to 23% in aerodynamic drag coefficient. [DOI: 10.1115/1.3077135]

Keywords: aerodynamic, undercarriage skirts, tank, vehicle tanker, nozzle, boat-tails, drag, penetration, consumption, vehicle, articulated

1 Introduction

From its inception, aerodynamics has been a field linked to aerospatial engineering. Nonetheless, the first study in aerodynamics appeared in 1934 and was applied to an automobile, the Chrysler Airflow. Nowadays, factors such as the increase in the price of fuel, the dwindling of renewable energy sources, the greenhouse effect, etc., have made an impact on the automobile industry and encouraged the production of vehicles, which are less polluting and are more energy-efficient. In turn, this has led to modifications in vehicle-design criteria, as well as to the development and application of techniques suited to such purposes. Aerodynamics, which allows the optimization of vehicles by merely varying their external design, changing the superficial finish, and diminishing tolerance between component parts, is one such design strategy.

That is why in recent years the external appearance of vehicles has undergone great changes with the purpose of reducing both the transversal area and the aerodynamic penetration coefficient, replacing the straight lines of yesteryear with new and sinuous shapes and more stylized profiles [1]. These developments are the result of the application of strict efficiency and economic profitability criteria, since approximately half of the energy used by a vehicle is used to counteract the resistance of the atmosphere. This in itself would suffice to prove the importance of aerodynamics, which is the only way of overcoming this invisible obstacle. Over the past 30 years, the average penetration coefficient of automobiles has gone down by 40%, an improvement that has brought about a 19% reduction in fuel consumption. However, similarly significant developments in relation to the aerodynamics of larger sized trailers have not taken place, because the principal developments studied in the past few years were on trucks. These are essential for the future development of more environmentally-friendly vehicles; should improvements be carried out, they could entail a feasible 15% [2] reduction in fuel consumption.

Therefore, 20% improvements in a vehicle's aerodynamic penetration coefficient can lead to savings of up to 10% in annual expenditure, to savings of up to 12,000 l in fuel, and to the lowering of carbon dioxide emissions by almost 30 tons [3].

It should also be kept in mind that aerodynamic improvements not only influence consumption and the power required by vehicles; they also increase their stability and decrease the effects of aerodynamics on other vehicles traveling on the same road, as well as diminishing splashing and improving the vehicle's resistance to lateral winds, etc.

Therefore, an aerodynamic analysis of tankers was considered essential in order to verify how certain elements improve the aerodynamics of the whole and thus contribute to the vehicle's overall performance.

New aerodynamic elements applicable to vehicle tankers and which considerably reduce the vehicle's aerodynamic resistance were also developed.

2 Main Aerodynamic Improvements for Semitrailers

Before undertaking a detailed study of the aerodynamic improvements implemented, the vehicle's energy budget has to be calculated using Clark's equation [4], as follows:

$$P = \tfrac{1}{2}\rho \cdot C_x \cdot A_t \cdot V^3 + \mu \cdot M \cdot G \cdot V + M \cdot G \cdot V \cdot \sin\theta \qquad (1)$$

This equation is a simplified view of the energies required to move a vehicle, since neither the performance of the transmissions or the motor's heat losses are taken into account, which nonetheless are extremely useful data when it comes to assessing the contribution of each factor to the power required to set a vehicle in motion.

As may be appreciated, aerodynamic power depends on the cubing of speed, whereas the dependence of the other two equations is linear.

That is why aerodynamic improvements are truly effective at high speeds, whereas at low speeds they may even result in an increase in the vehicle's maximum allowed weight (PMA) (M), which could be counterproductive.

Therefore, aerodynamic improvements are specially recommended for vehicles that travel regularly at high speeds, whereas they are not recommendable for vehicles that perform distribution tasks within cities or generally circulate at low speeds.

Contributed by the Fluids Engineering Division of ASME for publication in the JOURNAL OF FLUIDS ENGINEERING. Manuscript received September 1, 2008; final manuscript received December 5, 2008; published online March 11, 2009. Assoc. Editor: Zvi Rusak.

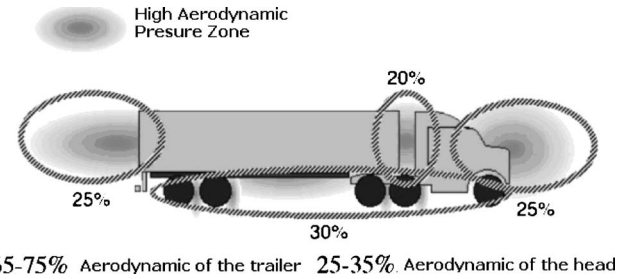

Fig. 1 Wind-averaged drag values for an articulated vehicle with a square box [4]

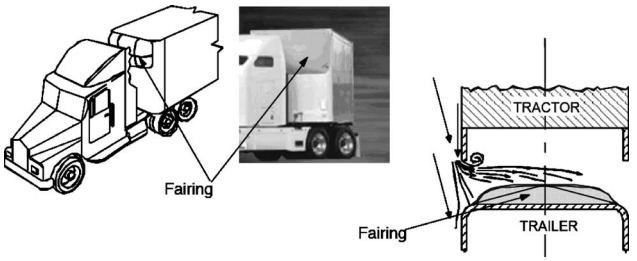

Fig. 3 Aerodynamic fairings

If we look closely at the previous equation we see that the main factors that can be modified are the vehicle's transversal area (A_t), the aerodynamic coefficient (C_x), and the tire friction coefficient (μ) with low consumption tires.

Regarding the vehicle's transversal area, we may notice that the width of an articulated vehicle designed for the transport of commodities is determined both by the width of the tractor and by its height. However, the use of tankers with a low level chassis diminishes the overall height and allows the use of tractors with a lower height or smaller superior spoilers.

As far as the aerodynamic resistance coefficient is concerned, several aerodynamic improvements will lower this coefficient. Among these, a distinction must be made between those which apply to the tractor and those which apply to the semitrailer, which is responsible for up to 70% of aerodynamic losses (see Fig. 1). These losses could be reduced by up to 40% by using the available technology and would equate to a 28% reduction in the aerodynamic resistance coefficient. Figure 1 shows the high pressure areas of an articulated vehicle associated with high aerodynamic losses.

If we manage to lower the effects of pressure on each of these areas, the overall aerodynamics of the vehicle will therefore improve considerably.

It should be pointed out that latter-day aerodynamic improvements are applied mainly to square box [5] vehicles and therefore have to be adapted for their use with tankers. Among these, we will be examining boat-tails, aerodynamic undercarriage skirts and aerodynamic fairings.

2.1 Boat-Tails . Boat-tails (see Fig. 2) prevent the detachment of the outer layer of the rear end of the box by preventing pressure gradients that would generate vorticity.

There are several possible boat-tail configurations. One is the use of rear plates (up to 4% aerodynamic improvement). Another is the application of round beam sections (up to 5%) [6] to the rear area of the box, although the use of one type of boat-tail or the other depends on the type of box, the maximum size of the vehicle, etc.

2.2 Aerodynamic Fairings. These aerodynamic elements are fixed on the upper front area of the semitrailer (see Fig. 3) and redirect the air flow that appears in that area toward the box, keeping it out of the king-pin cavity and thus involving an aerodynamic improvement of up to 3% [7].

2.3 Aerodynamic Undercarriage Skirt. This part prevents the entry of air in the lower part of the vehicle, both in the tractor area and the semitrailer area, decreasing air flow in these areas, which due to the wheels and several parts of the vehicle's lower area would otherwise generate a turbulent flow that would adversely affect the vehicle's aerodynamics. A decrease of up to 7% [8] can be achieved this way (see Fig. 4).

3 Methodology for Aerodynamic Calculation Using CFD

A commercial aerodynamic program was used for the aerodynamic calculation of the vehicle and its possible modifications. The following methodology was used for modeling, discretization, and vehicle calculation.

3.1 Computer Aided Design (CAD) Modeling. In order to proceed with the analysis, the first step is to perform CAD modeling of the vehicle's outer area and remove or simplify certain elements, such as the vehicle's rearview mirrors, turn signals, small external accessories, sleeves, and other auxiliary elements, as the modeling of these elements would involve an excessively complex and detailed finite element model [9,10].

In our particular case, a CAD model faithfully reflecting the external dimensions of both the vehicle and the tractor was designed, and therefore we chose to use the main dimensions of a tanker supplied by CryoEnergy S. A. (Tarrega, Spain) [11], to which a medium range tractor was added (see Figs. 5 and 6).

This cab was used as a basis, removing all the optional aerody-

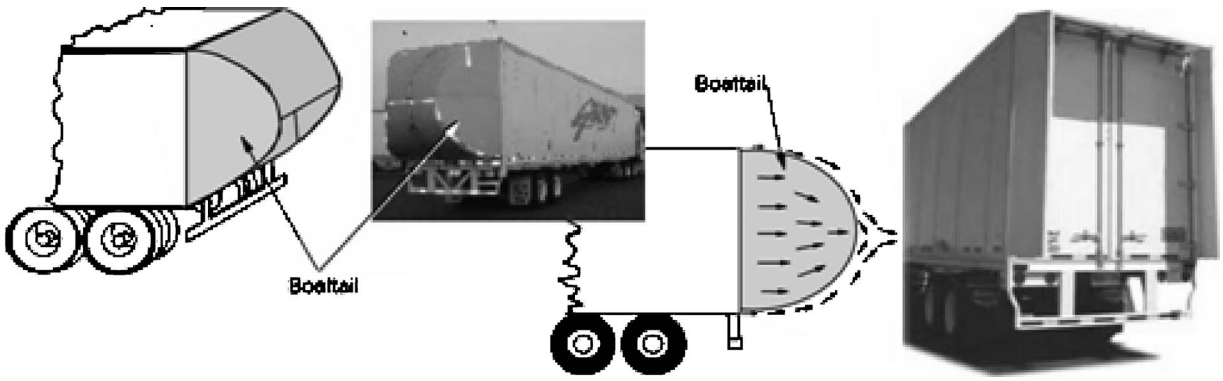

Fig. 2 Boat-tails

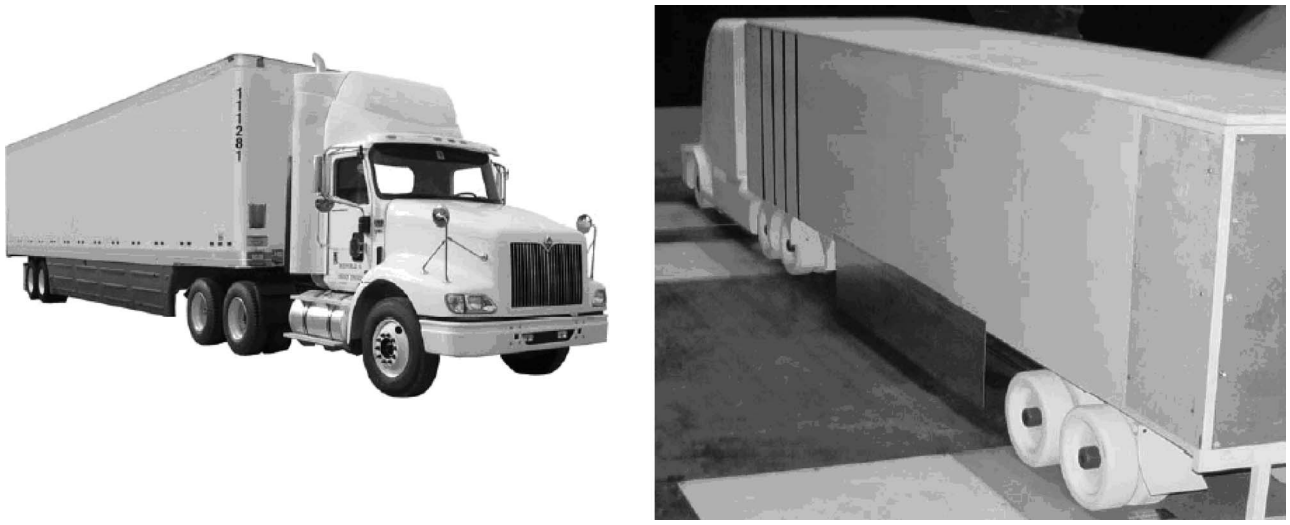

Fig. 4 Aerodynamic undercarriage skirt

namic accessories that may come with it: spoiler, lateral air flow streamliners, and bumper spoiler. These elements were not used, as we only intended to affect the semitrailer. The reason for not using them is that since these elements are cab accessories, not all cabs employ them, and also that, due to the fact that they have been studied and optimized in depth, these elements have many different configurations and shapes.

Fig. 5 Baseline equipment trailer

Fig. 6 Baseline equipment trailer

The air inlet of the vehicle's radiator was also left out of the modeling, because taking this factor into account would have required a very elaborate model of the vehicle, which would, in turn, have involved numerical complications that would have made calculation unfeasible. Besides, the contribution of this part to the global model is relatively small and is not under study here [9,10,12].

As far as the tanker is concerned, the turn signals, sleeves, and tubes of the lower area of the tanker, etc., were removed.

The several elements, which comprise the tanker's lower area, were not removed, since this is one of the areas under study, despite the fact that this entails an increase both in the complexity of the model and in the number of elements that comprise it.

In relation to the tire area, the wheel pitch and the empty spaces within it, along with its dimensions, were maintained in order to correctly model the contribution of these elements to the vehicle, since the tire area significantly affects the vehicle's overall aerodynamics and is one of the areas subject to study [9,10,12]. It may be worth pointing out that a symmetrical model was used to reduce the necessary computational cost. Consequently, only half the vehicle was modeled.

3.2 Discretization Through Volumetric Elements. In order to perform modeling using volumetric elements, the vehicle's CAD was taken as the starting point and introduced into a volume, which is to simulate the air on the outside of the vehicle. The following volume—in keeping with the recommendations of other authors [9,10,12] and those of the program—was considered for this purpose [12].

In theory, there should be a distance of 2000 mm in the air volume of a vehicle similar to the one selected between the front part of the vehicle and the air inlet, and a distance of 10,000 mm between the end of the vehicle and the air outlet in order to perfectly collect the slipstream generated by the vehicle. Regarding both lateral and superior distances, these should be at least 4000 mm in relation to the outermost tangent surface.

The dimensions of this volume are such that the air circulating in the areas furthest from the vehicle is not altered by the latter, which implies that the imposition of contour conditions on the outer area of the volume will not be altered by the vehicle, as this would involve a modification of the model's air flows and, consequently, an error in the results.

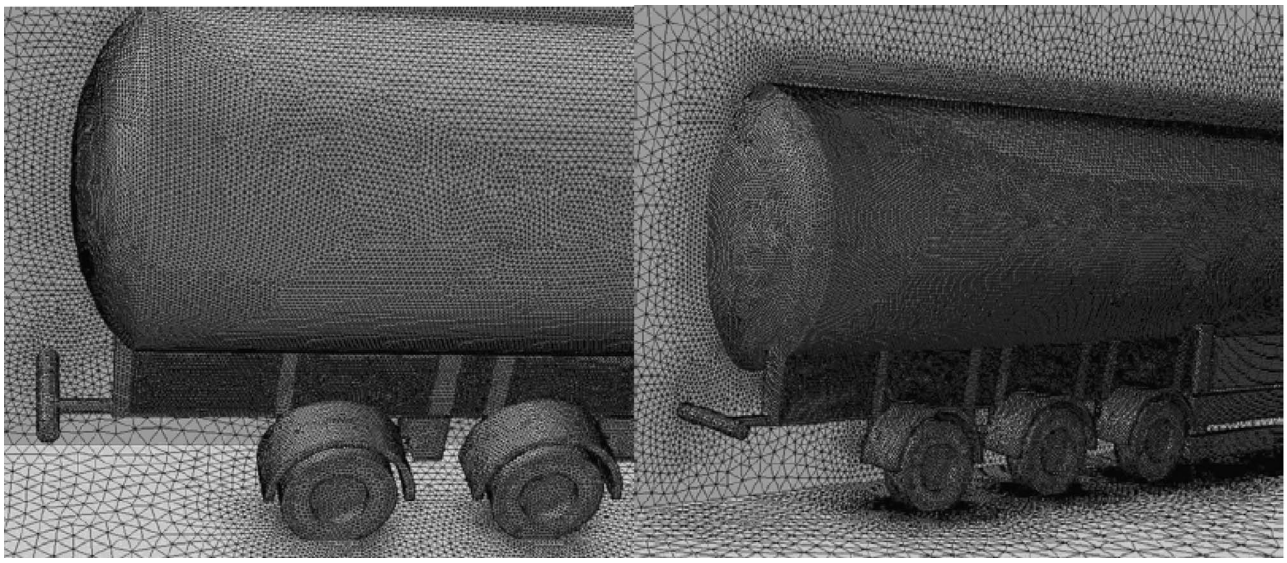

Fig. 7 Mesh of the baseline equipment trailer (rear zone)

The next step was to extract the vehicle's volume from the total volume, with which we could obtain a "negative image" of the vehicle with regards to how discretization will be carried out

To do so, a tetrahedral mesh with lineal Lagrange elements was chosen, because it allows moderately simple vehicle discretization and an optimum degree of approximation in relation to computational cost.

First of all, discretization of the outer surfaces was performed both on the inside and on the outside. The size of these surface elements depends on the area in which discretization is carried out [9,10,12], on its magnitude and on previous experience, although it was attempted to reduce the number of elements to the minimum, with the proviso that they be as equilateral as possible in order to ensure convergence and reduce time and calculation requirements. A more elaborate discretization was performed in those areas where greater speed gradients were expected, allowing for improved simulation of air flow in those areas: the wheel pitch, the front of the vehicle, the area between the cab, and the tank and the rear part of the vehicle, where detachment of the outer layer will occur.

After the discretization of the surfaces was performed, "boundary layers" [13] were imposed. This procedure allows us to perform fine meshing of the zones immediately surrounding the surfaces of the vehicle in order to faithfully model the vehicle's outer layer. To this end, an initial element size of 6 mm and a boundary layer of three elements with a mesh growth factor of 1.2 [9,10,12] was chosen. The reason for building such a mesh was to try to correctly approximate the outer layer, despite the fact that this entails a substantial increase in the number of elements and an increase in computational cost; however, this is justifiable and was necessary for the correct modeling of the outer layer of fluid.

Following this, discretization of the remaining air volume was carried out; in order to do so, meshing of the outer area with a larger size element (1000 mm) was performed, since attached flow will be preponderant in this area and there will be no flow alterations or speed gradients. In order to perform discretization, a size function was used, allowing control of the growth size of the elements from the vehicle to the outside area. To achieve this, a maximum element size of 1000 mm and a 1.2 growth factor—the maximum recommended by the program—was imposed. In this way, discretization with the most equilateral surfaces possible can be achieved (see Figs. 7 and 8).

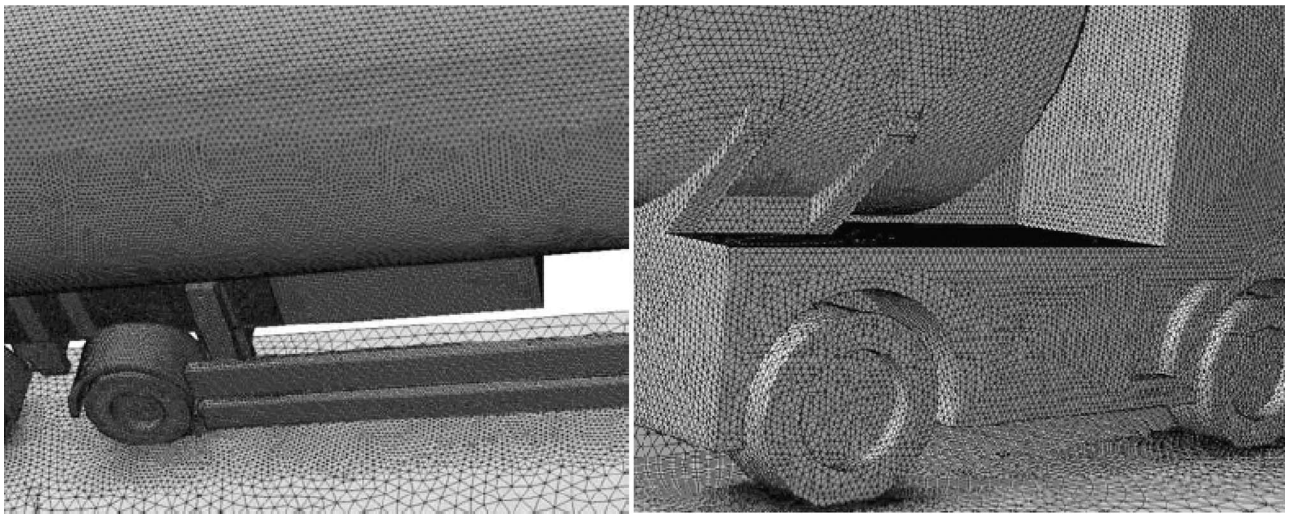

Fig. 8 Mesh of the baseline equipment trailer (middle zone and tractor)

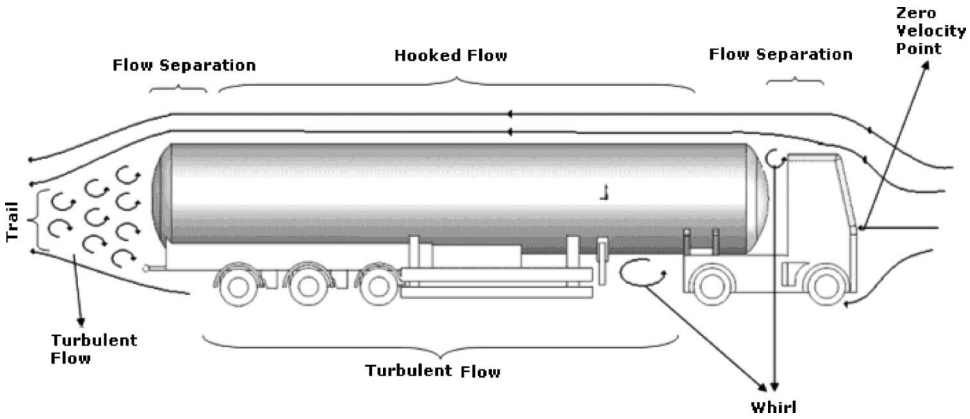

Fig. 9 Flow around a semitrailer tanker (side view)

3.3 Aerodynamic Calculation. In order to perform aerodynamic calculation, several tasks have to be carried out prior to the calculation proper:

3.3.1 Definition of Solution Options. A "segregated" solution model—recommended for this type of calculations—was chosen in order to lower computational requirements. This model uses a double precision calculation (recommended for aerodynamic calculation of vehicles) [14,15] for a stationary (steady) model based on node calculation and is recommended by the program in order to achieve better results with this type of calculation.

3.3.2 Definition of the Turbulence Model. A turbulence model based on k-ε type realizable Reynolds average Navier-Stokes (RANS) equations [14–16] and a wall treatment with nonequilibrated flow were chosen [17]. The choice of this turbulence model was mainly due to the fact that nowadays it is the most commonly used one for aerodynamic calculations and because it also offers an optimum degree of approximation in regard to computational requirements.

3.3.3 Definition of Contour Conditions. Since there are several areas, different contour conditions were considered for each of them. An air flow at a constant speed (30 m/s) in a tangential direction [7] with very low turbulence (0.1% turbulence intensity) was introduced for the entry boundary, which means that any flow that there may be will be laminar. Regarding the upper, lateral, and rear areas, these were simulated as being open to the outside, with a pressure of 1 atm and an air flow of 30 m/s in the relevant direction.

The ground was modeled as a smooth surface traveling at the same speed as the fluid (30 m/s) [18], and the wheels were considered smooth and rotational surfaces, coherent with the speed of the vehicle [17].

Symmetry was imposed on the interior wall and the vehicle's walls were considered fixed and smooth walls without friction. This was due to the fact that the contribution of friction between the fluid and the surface in relation to the global model represents less than 10% of the resistant contribution and that the implementation of this contribution would entail a substantial increase in computational cost and might even have lead to divergent results. Nonetheless, it would be useful to establish, very precisely and by means of experiments, the friction coefficient of each of the model's superficial finish types in order to establish their contribution to the aerodynamic resistance, which would not be substantially modified by variations in the vehicle's geometry, since the latter depends mainly on the choice of superficial finishes.

Thus, simulation of the movement of the vehicle is possible, but from the relative viewpoint of the tanker.

3.3.4 Selection of Options for Solving the Equations. A SIMPLE-C [13] type resolution algorithm was chosen to solve the pressure-speed fields, which is the appropriate resolution scheme for discretizations with elements not aligned with the flow [19]. In addition, standard discretization schemes were used for pressure solution and second order schemes were used for calculating momentum and turbulence. These are the parameters recommended by the program for this type of calculations.

It should be pointed out that in order to improve the model's convergence, first order equations were used for calculating momentums and turbulences during the first 300 iterations and that the second order scheme was implemented subsequently.

4 Adaptation of Aerodynamic Improvements to the Tankers

In this paper, only those aerodynamic improvements directly applicable to cryogenic tanks will be analyzed; and therefore, despite the fact that they improve the aerodynamics of the tank area, the improvements applied to the tractor will not be taken into account in this study.

Before proceeding with the analysis, it should be pointed out that aerodynamic resistance coefficients for latter-day articulated vehicles can be extracted from article 20, and that these can be used to verify the results obtained in the calculation of the original vehicle. Thus, the aerodynamic resistance coefficient of a vehicle with the characteristics of the one we are dealing with is roughly 0.69.

As a starting point for the analysis of this type of vehicles, the way in which air flow covers the outer surface of the vehicle must be understood qualitatively. In order to do so, we will set out from the previous experience existing regarding automobiles [20–22].

On the basis of this information it may be presumed that in a tanker-type articulated vehicle [23], there will be a flow of particles like the one shown in Fig. 9. Therefore, just like in a car, there will be an area at the front where particles will stagnate due to their collision with the frontal area, although since our frontal area is much larger and its aerodynamic shape is much less stylized than a car's, and also because this area is perpendicular to the flow, this area will be much larger. There will also be an area near the king-pin cavity in which the outer boundary will become detached due to the existence of the said cavity, whereas the particles entering the cavity will collide with its rear part, creating a turbulent zone and, presumably, low longitudinal speed and high vorticity.

Since the external geometry of the tank has no protuberances, projections, cavities, etc., it is likely that coupling will recur behind the cavity of the king-pin, and therefore, that there will be attached flow in this area.

In the vehicle's rear area, where the surface ends, flow separation will recur, presumably with low longitudinal speed, and a turbulent slipstream will be generated behind the vehicle.

Table 1 Total resistant forces and aerodynamic resistance coefficients of all the cases considered

	Without aerodynamic improvements and lower case		Without aerodynamic improvements and post case	
Zone	Total resistance force (N)	Aerodynamic Resistance Coefficient (C_d)	Total resistance force (N)	Aerodynamic Resistance Coefficient (C_d)
Head Tractor	1258,3000	0,3429	1291,2500	0,3436
First wheel-head	75,0700		69,2800	
Second wheel-head	49,1900		24,9700	
Trailer	986,4800	0,2755	1170,9000	0,3138
First wheel-trailer	20,0500		18,2200	
Second wheel-trailer	8,0900		7,8580	
Third wheel-trailer	7,9200		12,9700	
Total	2405,1000	0,6184	2595,4480	0,6574

	With lower case and boat tail		With lower case and undercarriage skirt		With lower case and fairing	
Zone	Total resistance force (N)	Aerodynamic Resistance Coefficient (C_d)	Total resistance force (N)	Aerodynamic Resistance Coefficient (C_d)	Total resistance force (N)	Aerodynamic Resistance Coefficient (C_d)
Head Tractor	1292,5500	0,3432	1316,0000	0,3475	1271,0000	0,3419
First wheel-head	54,6800		64,2200		72,4500	
Second wheel-head	36,6800		21,0000		35,1600	
Trailer	970,5000	0,2634	767,3000	0,2114	854,1000	0,2385
First wheel-trailer	17,7100		43,4700		12,9500	
Second wheel-trailer	8,5000		12,2600		626,3400	
Third wheel-trailer	9,8520		8,6200		9,2500	
Total	2390,4720	0,6066	2232,8700	0,5590	2881,2500	0,5804
Improvement (%)	7,7260		9,6082		6,1356	

	With lower case and all aerodynamical improvements		With post case and all aerodynamical improvements	
Zone	Total resistance force (N)	Aerodynamic Resistance Coefficient (C_d)	Total resistance force (N)	Aerodynamic Resistance Coefficient (C_d)
Head Tractor	1308,0500	0,3455	1324,0400	0,3532
First wheel-head	51,2200		62,4100	
Second wheel-head	33,5700		37,6100	
Trailer	622,0000	0,1753	514,4500	0,1524
First wheel-trailer	19,5700		20,0100	
Second wheel-trailer	9,0900		10,9300	
Third wheel-trailer	11,4900		9,1200	
Total	2054,9900	0,5207	1978,5700	0,5056
Improvement (%)	15,7891		23,0904	

The existence of turbulent flow in the lower part of the vehicle may be presumed due to the large amount of elements and projections in that area. Besides, the presence of the wheels and their turning will generate turbulence and additional flow detachment.

When we speak of null speed we assume a viewpoint relative to the vehicle.

Once the flow was theoretically established, the next step was a numerical verification of the hypotheses set forth; therefore, numerical calculation and postprocessing of the original configuration of the articulated vehicle was carried out.

Total forces and aerodynamic coefficients for all configurations are reflected in Table 1.

The global aerodynamic resistance coefficient is 0.618, which is within the established range for this type of vehicles [24]. This coefficient is somewhat high, because a tractor without aerodynamic elements—which involve considerable aerodynamic penalization—was used. This is also appreciable in relation to the contribution of each part of the articulated vehicle to the global resistance coefficient: 55.4% in the tractor and 44.6% in the body. It should also be pointed out that the body's contribution to the vehicle's average total drag is inferior to the 65–75% range indicated in Fig. 1. This is because this figure established the contribution for a square box semitrailer, the aerodynamic coefficient of which is usually 5% superior to that of a semitrailer tanker [18] and due to the use of a vehicle with aerodynamic improvements in the tractor.

Once the correctness of the aerodynamic resistance coefficient and the resistant forces of the vehicle have been established, the next step is to analyze the several areas, which make up the vehicle so as to verify in which areas flow detachment occurs and turbulent flow predominates. In order to do so, we analyzed pressure maps (high pressures indicate vorticity and turbulent flow), speed maps (low relative speeds indicate vorticity and turbulent flow), turbulence energy maps, and particle flow maps (draft lines were analyzed in order to perform this analysis, as well as an analysis of the flow of particles in motion, which was not included here due to its being a moving image).

It must be pointed out that in order to keep the article relatively short, only the more representative images of the vehicle were included.

As shown in Fig. 10 and predicted earlier, the low speed areas are the lower part of the vehicle, the king-pin cavity area and the slipstream of the tank; i.e., these are the areas with greater turbulence and higher pressures. This figure shows the longitudinal speed of the vehicle. It shows the wake in the rear part of the vehicle and indicates a high aerodynamical resistance. It also shows, in the bottom part of the vehicle past the tractor, a zone with low velocity and the same in the wheel zone of the tanker. This indicates high aerodynamical losses too. Analyzing Figs. 11 and 12 that show the k turbulence parameter and then the zones with high aerodynamical losses, these match with the zones previously mentioned and with Fig. 9, so these zones should be modified to improve the aerodynamics. These zones also have whirls that indicate turbulence (see Fig. 10 and 13) and cause aerodynamical losses, usually because the geometry of the vehicle is discontinuous, and the attached flow changes to a turbulence one. In Fig. 10 there is a zero velocity zone in the gap between the tractor and the trailer and it matches with a high losses zone (see Figs. 11 and 15).

We also notice in Figs. 10 and 13 a stagnation zone in the front area (that is one of the zones with high aerodynamical losses of the tractors), the detachment of the outer layer above the cab in the vehicle's rear part and the lower part of the tractor, as well as ⟨⟨coupling⟩⟩ of the flow in the upper part of the tank (all was predicted in Fig. 9).

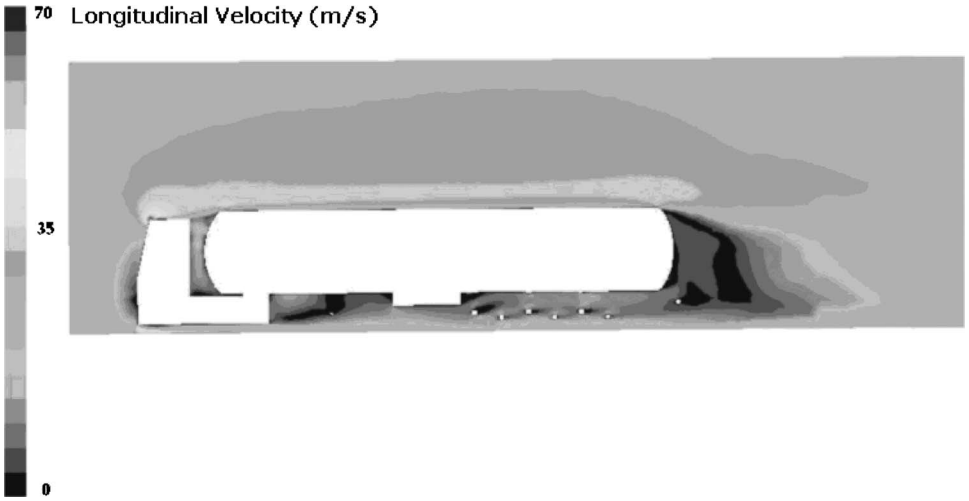

Fig. 10 Longitudinal speed of the original configuration at the vehicle's plane of symmetry

Moreover, we may appreciate high fluid speeds (which are completely normal) on the edges of the tractor (see Figs. 14 and 15) as a result of the latter's stagnation.

If we perform a cut, which is parallel to the plane of symmetry and near the lateral surface of the cab, we can appreciate the effect of the tires on the speed and the increase in turbulence due to this phenomenon (see Fig. 16) and an increase in the aerodynamical losses, and the effect of the change in geometry on the bottom part of the trailer near the tractor

If we perform a cut on a horizontal plane located 2 m above the road we can verify the flows and speeds shown in Fig. 5 and we can also obtain flows, turbulence, speed, etc.

A close look at Fig. 13 reveals that the flow of particles is very similar to the one proposed and that the areas where the k turbulence parameter is highly correlated with those areas in which high aerodynamic losses were predicted.

The analysis of the tire area, where turbulent flow predominates, as evidenced in Fig. 20, is also worth paying special attention to. A detachment of the outer layer in the areas near the wheels may also be appreciated, as well as in the lower part of the vehicle, the latter presumably due to the discontinuity between the tractor and the semitrailer.

Once the analysis was carried out, the conclusion was that the

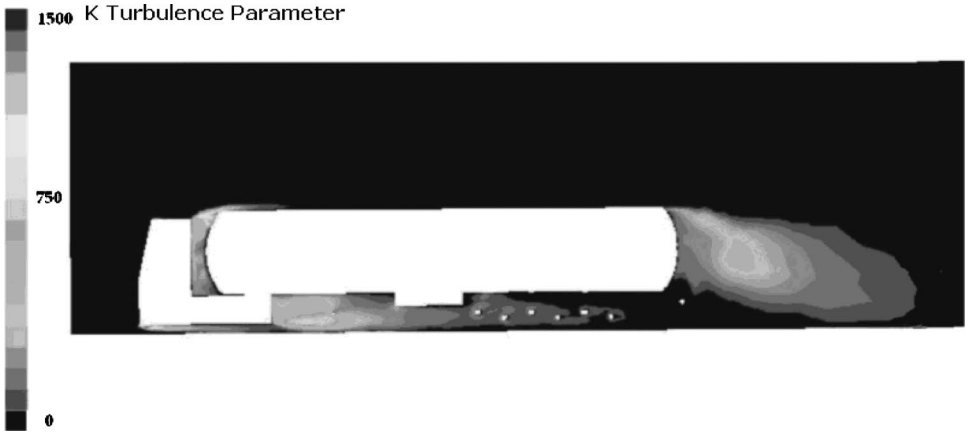

Fig. 11 k turbulence parameter of the configuration original at the vehicle's plane of symmetry

Fig. 12 k turbulence parameter on a horizontal plane 2 m above the road

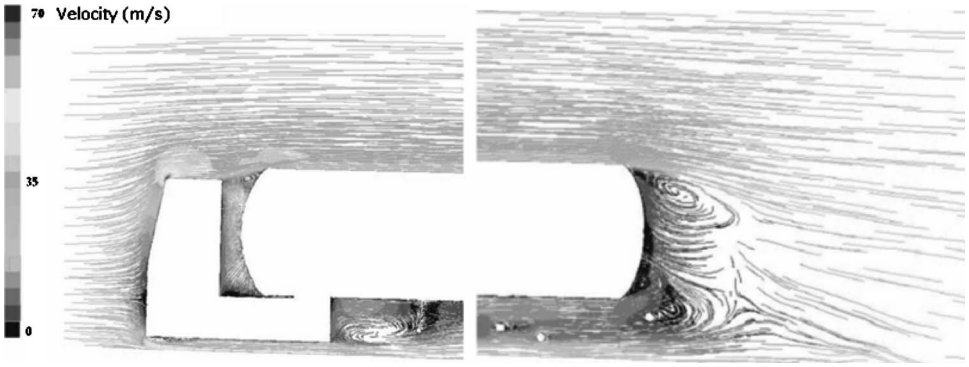

Fig. 13 Flow lines and associated speeds of the original configuration at the vehicle's plane of symmetry for the cab and rear areas

previously established flow hypotheses were correct, and consequently that modification of the king-pin cavities and the wheels would be necessary in order to reduce the vehicle's aerodynamic losses. Regarding the slipstream area of the vehicle, no initial modifications had to be undertaken, since the aerodynamic profile and the level of turbulence are correct and flow detachment cannot be avoided in that area; the configuration with the box in the rear will require modification, since it generates greater flow detachment and more turbulence, which ought to be prevented.

It is worth mentioning that depending on the positioning of the box (in the rear or the front part) there are two different tanker configurations. Each of them will be studied separately and certain aerodynamic improvements will have to be adapted for each configuration. Due to the shape of the tank itself, some of the aerodynamic improvements proposed for vehicles with a square box are inefficient for this type of semitrailer. The use of boat-tails, aerodynamic fairings, and rear vorticity generators, for example, would require adaptation. Due to the geometry, the use of vortex

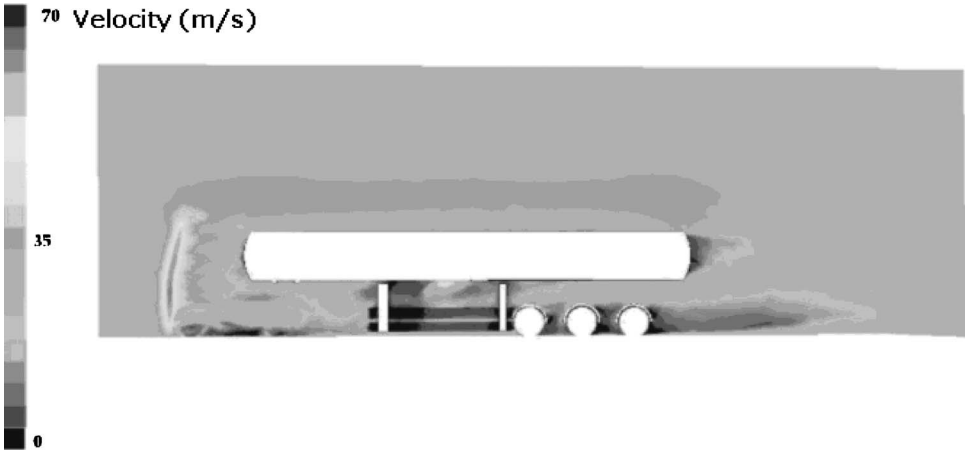

Fig. 14 Longitudinal speed of the original configuration at a plane parallel to the plane of symmetry and in the tire area

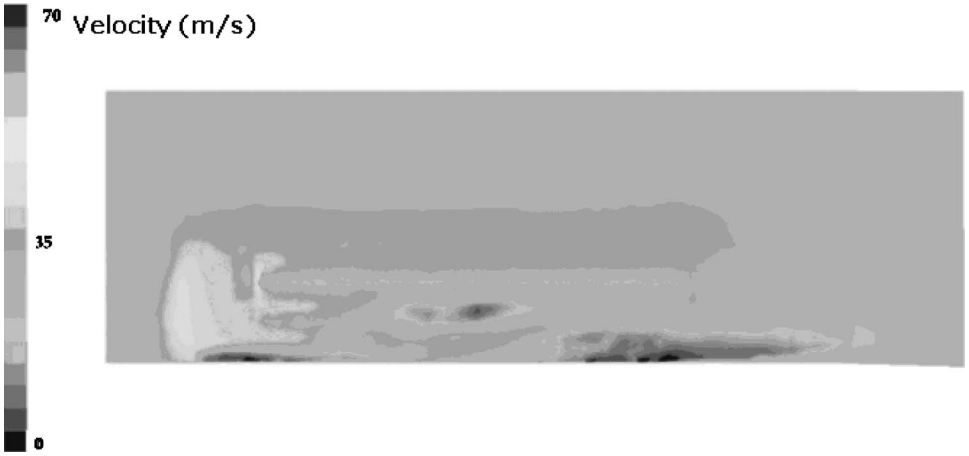

Fig. 15 Longitudinal speed of the original configuration at a plane parallel to the plane of symmetry tangential to the tank

Fig. 16 ***k*** **turbulence parameter on a horizontal plane in the tire area**

traps in the lower front part of our vehicle is also impossible, and therefore, this improvement cannot be implemented either.

The main aerodynamic elements subject to study will be undercarriage skirts. An aerodynamic modification based on the boattail will also be designed for the vehicle with a rear box configuration in order to prevent the detachment of the outer layer of this zone, which we will call aerodynamic ⟨⟨box adaptor⟩⟩; on the other hand, an aerodynamic improvement for the vehicle's front area—in order to prevent the generation of vorticity and the detachment of the outer layer of the king-pin cavity—will be designed on the basis of a modification of the aerodynamic fairings and the lateral air flow streamliners, but will be applied to the tank and will be named "aerodynamic front."

4.1 Undercarriage Skirts. At present, all newly built semitrailers have to implement lateral protection measures in compliance with EEC guideline 98/297. This directive regulates the use of lateral protectors. The use of these protective elements, in their horizontal spar configuration—the most widely used one nowadays—leads to aerodynamic penalization, since they favor detachment of the outer layer due to their discontinuities with the tank.

Furthermore, the cavities of the wheel area allow air to penetrate this area and therefore generate an aerodynamic penalization, which increases in proportion to the increase in the air flow running through that area; therefore, the use of aerodynamic undercarriage skirts will be implemented to reduce the air flow laterally penetrating the area.

Consequently, an aerodynamic improvement was suggested in order to decrease the aerodynamic penalization caused by these elements.

The aerodynamic improvement in question is based on the reduction of free edges and geometries capable of generating a detachment of the outer layer in the area between the tractor and the wheels of the vehicle, since in this area there are many elements that generate vorticity and aerodynamic losses.

To this end, we suggest a continuous surface going from the front area of the semitrailer to the rear area, comprising of three clearly differentiated areas, and additionally, made out of different materials.

(1) The area between the tractor and the parking holder (A): this area is to be made of plastic materials, since it will not be subjected to important mechanical stress. Its function is to avoid air penetrating the lower area of the tank from the lateral areas, mainly issuing from the tractor.
(2) The area between the parking holder and the wheels (B): this part was designed according to EEC directive 98/297 and allows the use of said area as a lateral protector in compliance with previous specifications.
3) The area of the semitrailer's wheels (C): this part covers both the cavities located above the vehicle's wheelguards and those between the semitrailer's wheels, as these cavities generate vorticity and aerodynamic losses.

We can see the aerodynamic improvements in Fig. 17.

When we analyze the results obtained we will see that *k* turbulence is reduced in the lower part of the vehicle (see Figs. 16 and 18). This indicates a decrease in turbulence in the area, and therefore a decrease in aerodynamic losses.

The trajectories of particles (Fig. 19) follow the direction of the flow and very small amounts of fluid penetrate the vehicle's lower area, as might have been expected, while the curved part in area A performs its task, preventing air flow in that area (Fig. 20). This indicates that the turbulence flow first has decreases and then aerodynamical losses. This is because the underskirt avoids abrupt geometry changes and then the whirls that are generated are lower (see Figs. 18 and 20 versus Fig. 11).

On the other hand, we may see that the final curved shape of area C of the undercarriage skirt redirects flow and reduces slipstream in that area (see Fig. 20).

Regarding the forces acting on the vehicle (see Table 1) and the aerodynamic resistance coefficient, we see that the vehicle's aerodynamic coefficient is 0.56, i.e., 9% less, which means that the aerodynamic benefit of this part is considerable and has no impact in terms of weight increase (approximately 77 kg)

4.2 The Aerodynamic Front. The king-pin area is a zone in which detachment of the outer layer and high vorticity occur, as shown in Fig. 11. Consequently, it is an area with high aerodynamic losses, and therefore we suggested an aerodynamic improvement in order to reduce the king-pin cavity and redirect the air in that area to prevent whirlwinds and detachments of the outer layer.

The aerodynamic front was designed so as not to interfere with the vehicle's maneuvers or with access to the area when it comes to connecting it to the tractor. With this in mind, geometry such as

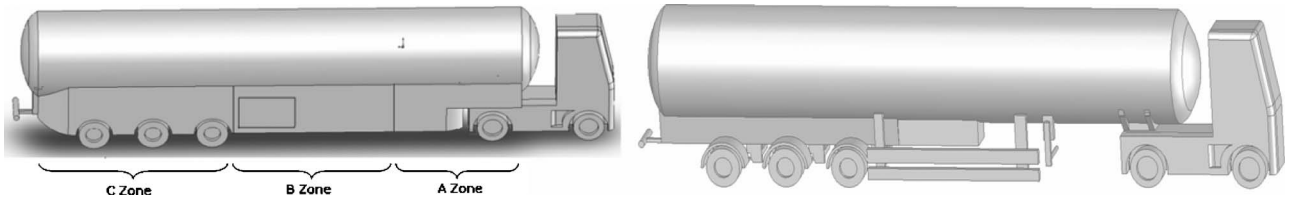

Fig. 17 Aerodynamic undercarriage skirt in a configuration with the box in the lower part versus linebase one

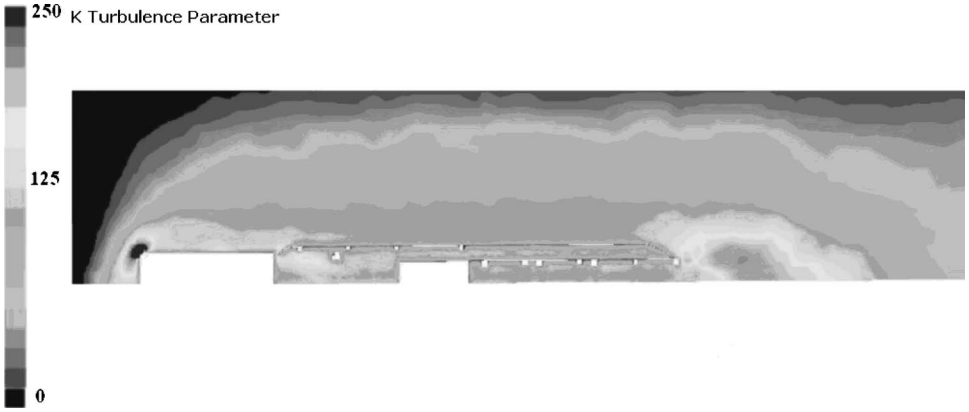

Fig. 18 *k* turbulence parameter in the aerodynamic undercarriage skirt area

the one which appears in Figs. 21 and 22 was suggested.

This geometry reduces the size of the king-pin cavity both in its lower and upper parts, and also performs the same function as the lateral air flow streamliners of the tractor, preventing air from penetrating the cavity and redirecting it to the outside area.

It is worth pointing out that the aerodynamic front can be made out of low density materials such as aluminum or plastic, as it is not an element subject to mechanical stress. Therefore, given an appropriate selection of materials and low thickness, the weight penalization for including these materials will be inferior to the aerodynamic improvement obtained. The approximate weight of the part when built in PVC with an approximate thickness of 3 mm will be 42.3 kg.

After analyzing the results obtained for this configuration, we appreciate a reduction in the *k* turbulence parameter of the aerodynamic front (Fig. 23 as opposed to Fig. 11) in relation to the initial parameter, which indicates a decrease in turbulence in the area and therefore an aerodynamic improvement, as expected. This is because the gap between the tractor and the trailer has

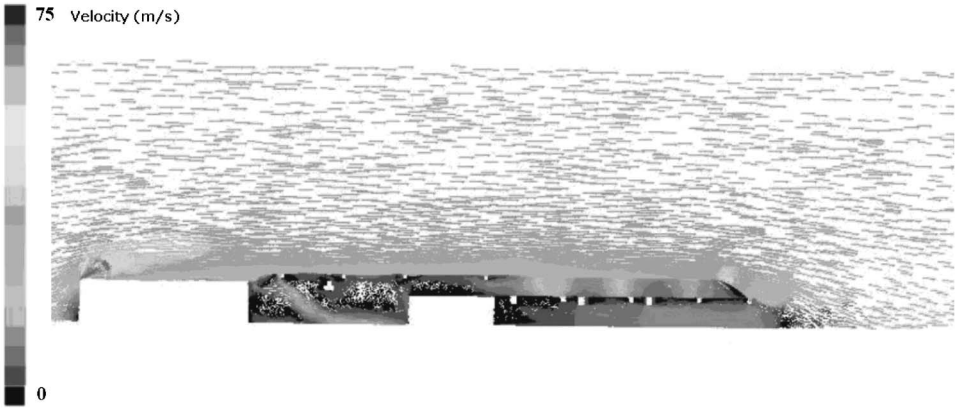

Fig. 19 Speed in the aerodynamic undercarriage skirt area

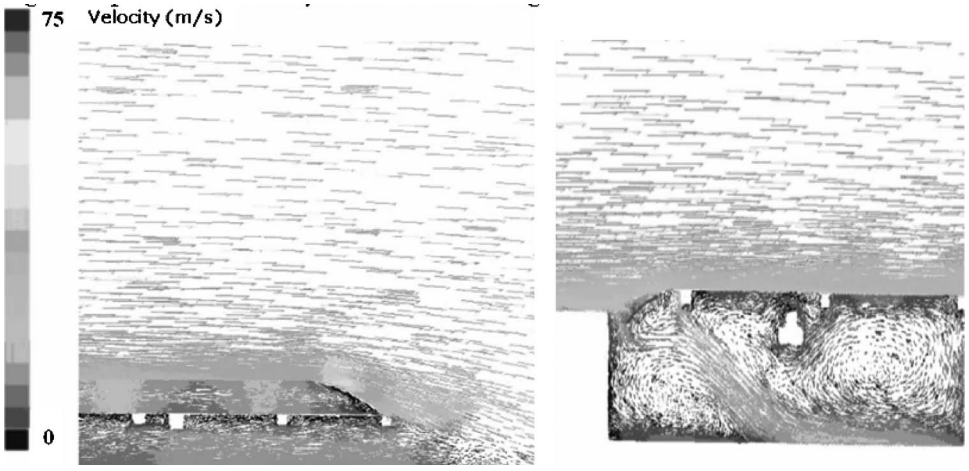

Fig. 20 Detail of areas A (right) and C (left) of the aerodynamic undercarriage skirt

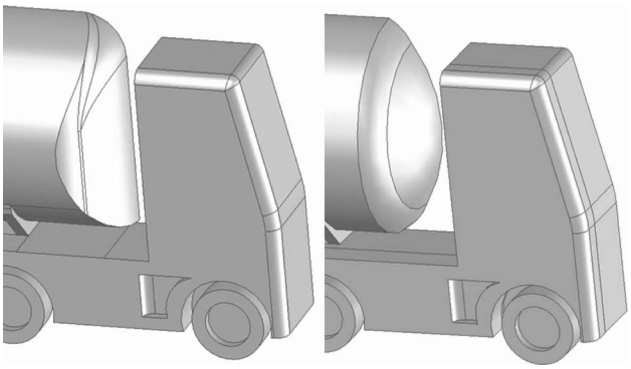

Fig. 21 Vehicle tanker with an aerodynamic front versus linebase one

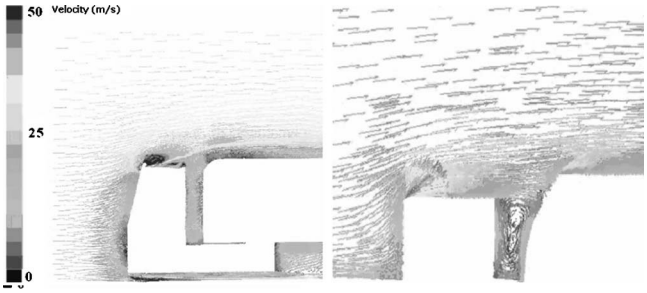

Fig. 24 Flow lines at the plane of symmetry and on a vertical plane 2 m above the ground in the king-pin cavity area for a vehicle with an aerodynamic front

been reduced and the new geometry reduces geometry changes.

Likewise, if we analyze both the path lines and the speed of the vehicle (Fig. 24 as opposed to Fig. 14), we appreciate a decrease in turbulent vortices in the king-pin cavity area because the geometry changes are lower.

In relation to the model's forces and aerodynamic coefficients, a 6.2% force reduction, besides a substantial improvement of the aerodynamic resistance coefficient, which now has a value of 0.58, (Table 1) may be pointed out.

4.3 The Aerodynamic Box Adaptor. The vehicle being analyzed has two different box configurations in which the elements for manipulating the load are placed and which allows loading and unloading operations. One configuration has the box in the rear part and the other one has the box in the lower part of the vehicle.

The disadvantage of the configuration with the box in the rear part of the vehicle is that it causes disturbances in air flow lines, increases vorticity, and leads to detachment of the outer layer, as can be appreciated in Figs. 25 and 26 that indicate zones with high aerodynamical losses. This is due to the fact that this configuration involves cavities between the box and the rear part of the tank, and thus the aerodynamic improvement of the tanker is due to the shape of its rear bottom part, which reduces the vorticity of the vehicle's slipstream as well as the detachment of the outer layer. In the following images we may appreciate the increase in vorticity due to the presence of the box and an increase in the slipstream generated behind the vehicle (see Fig. 27). We may also appreciate an increase in the k turbulence parameter in relation to the model with the box in the lower part (Fig. 11 as opposed to Fig. 25).

As might have been expected, this rear box configuration considerably worsens the aerodynamic coefficient, which reaches 0.657, i.e., 6.25% more.

The use of aerodynamic elements between the box and the rear part of the tank in order to allow for transition between these zones is suggested. To this end, curved shapes that prevent the

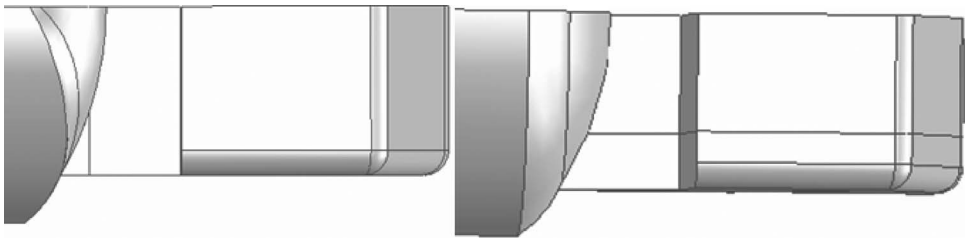

Fig. 22 Vehicle tanker with an aerodynamic front versus linebase one. Top view.

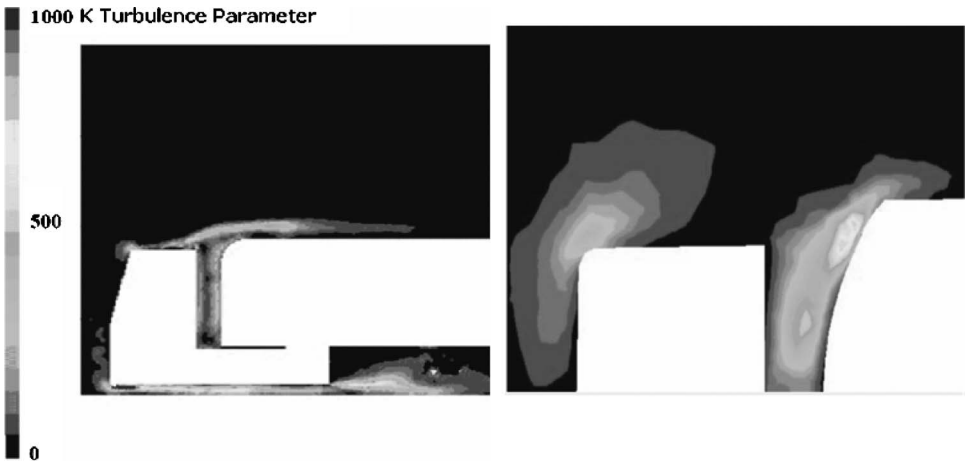

Fig. 23 k turbulence parameter on the plane of symmetry and on a vertical plane 2 m above the ground in the king-pin area for a vehicle with an aerodynamic front

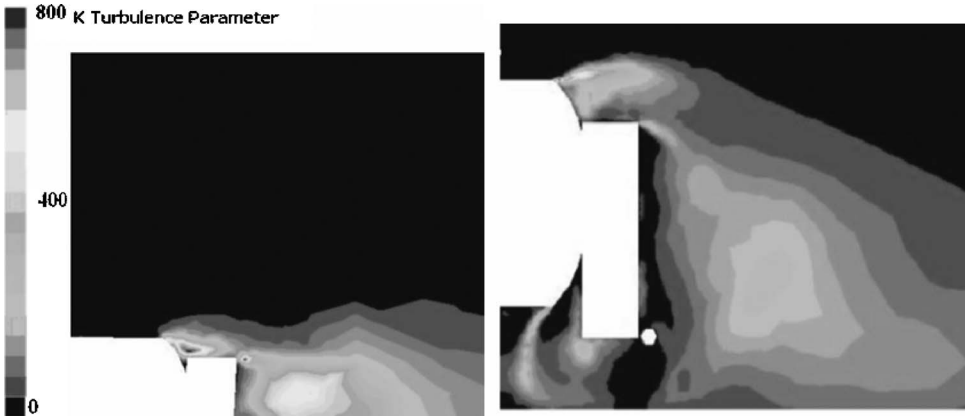

Fig. 25 ***k*** **turbulence parameter on a horizontal plane 2 m above the ground and at the plane of symmetry for a rear box configuration without improvements**

detachment of the outer layer of the said area and minimize overall aerodynamic losses were used.

Since these elements are not subject to significant mechanical stress, they can also be made out of plastic, which minimizes the total weight contribution (57 kg in 3 mm PVC)

As a result, the vehicle's slipstream (Figs. 25 and 26 as opposed to Fig. 29) is reduced.

If we pay attention to the movement of particles, we will notice that flow detachment is not as sharp in the vehicle's rear area (Fig. 28), and therefore an aerodynamic improvement might be ex-

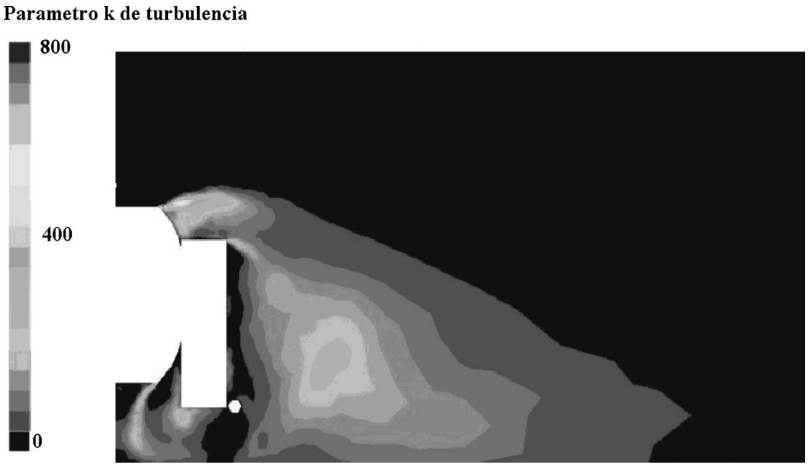

Fig. 26 ***k*** **turbulence parameter at the plane of symmetry for a rear box configuration without improvements**

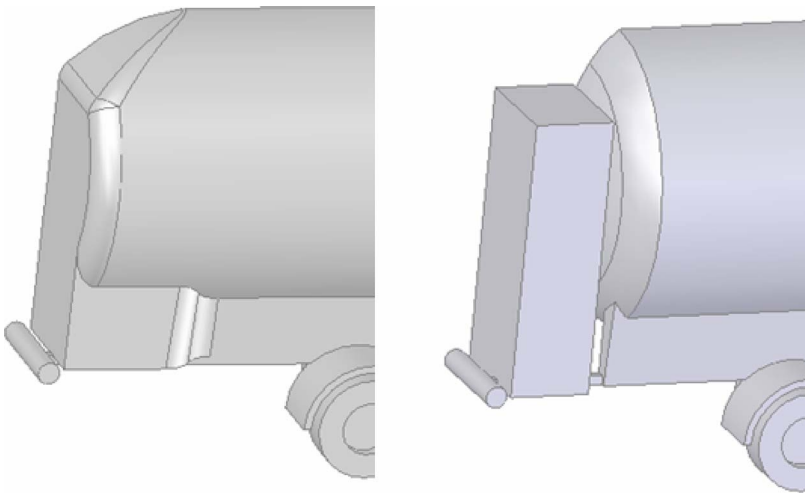

Fig. 27 Final box adaptor versus baseline one

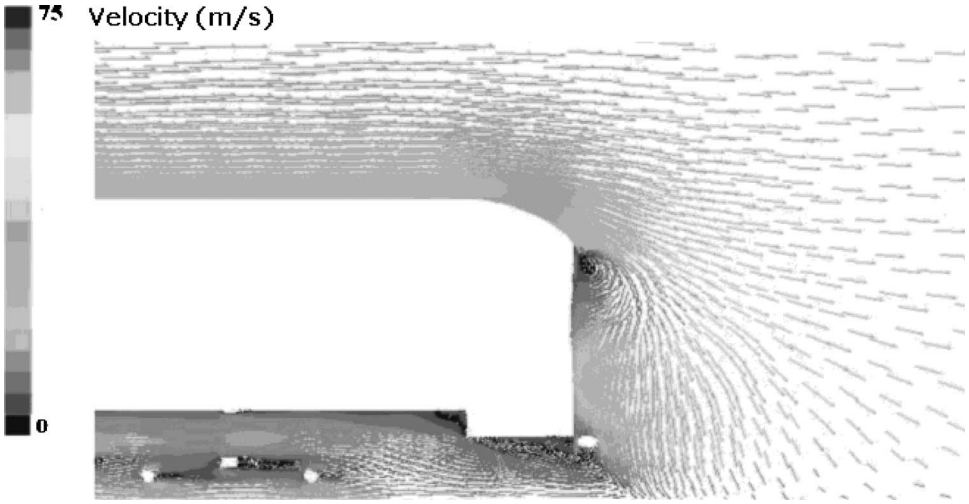

Fig. 28 Detail of the flow lines at the plane of symmetry in a vehicle with final box adaptor

pected in this area.

The *k* turbulence parameter decreases in the rear part of the vehicle (Fig. 26 as opposed to Fig. 29).

We can appreciate a 7.6% reduction in the forces and aerodynamic resistance coefficients (Table 1) and a 0.606 aerodynamic coefficient in relation to the rear box configuration. The lower part of the vehicle shows an aerodynamic improvement of 3% due to the fact that the rear part is more aerodynamic than the front, although this reduction does not compensate for the need to change the geometry of that area in the vehicle with lower box configuration (see Fig. 30).

4.4 Global Contribution of all the Aerodynamic Improvements Shown. To complete the analysis, an aerodynamic calculation of both box configurations including all the aerodynamic improvements at our disposal was carried out in order to verify the overall contribution of these improvements to the vehicle.

To this end, all previous aerodynamic improvements were adapted with the purpose of jointly integrating them with the vehicle and achieving a perfect union of the different parts in order to avoid detachment of the outer layer and make the vehicle even more aerodynamic.

Consequently, these were the geometries chosen.

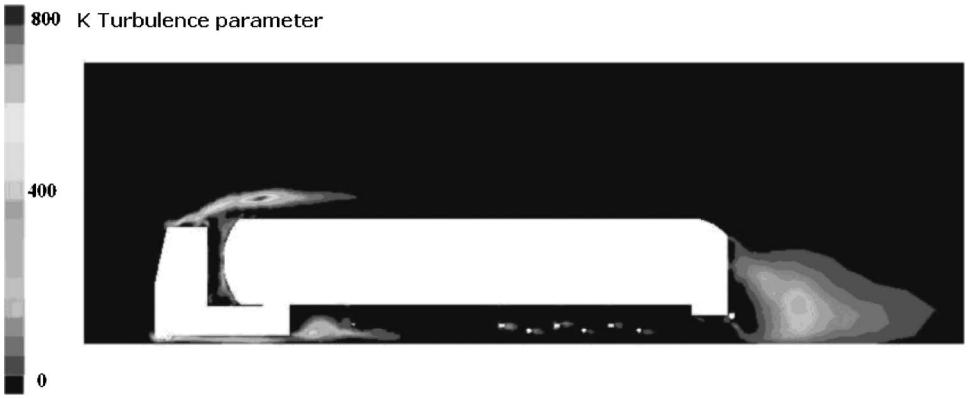

Fig. 29 *k* turbulence parameter at the plane of symmetry in a vehicle with final box adaptor

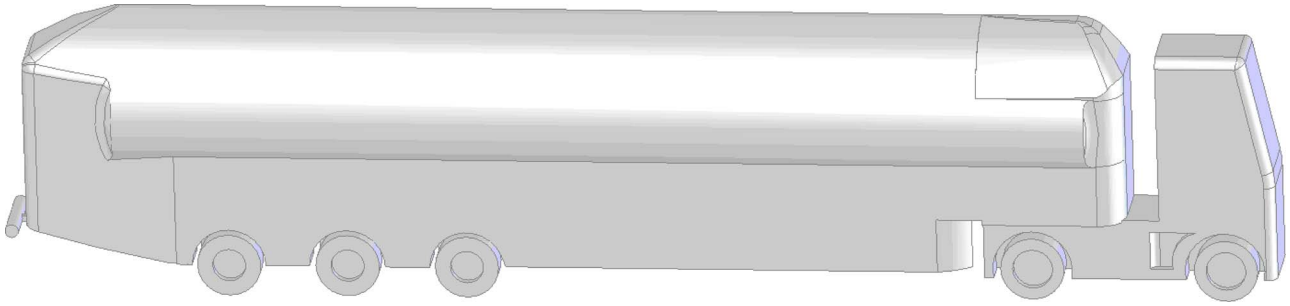

Fig. 30 Front area of a vehicle with all the aerodynamic improvements, regardless of box configuration and equipped with a rear box in the rear area

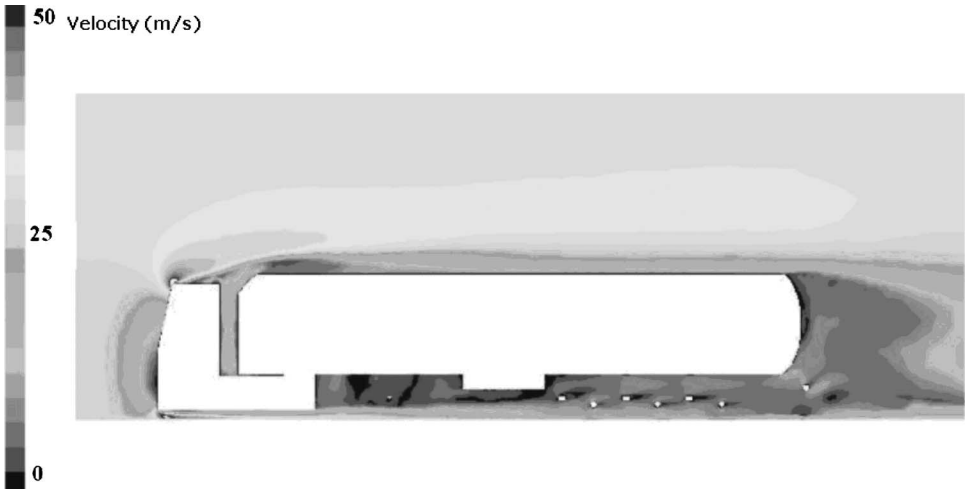

Fig. 31 Speed at the plane of symmetry in a vehicle with lower box configuration and all the improvements

If we examine the results obtained for the lower box configuration, we find a 0.52 aerodynamic coefficient, i.e., 15.85% less, due both to the contribution of the undercarriage skirt and that of the aerodynamic front, as well as to the joint integration of both elements. This can be appreciated in Figs. 31–33, in which we may notice the reduction of the k vorticity parameter in the undercarriage skirt area and the king-pin cavity. We also notice the movement of particles, which tends to produce less vortices and, consequently, to generate less turbulence. Thus the aerodynamic improvements are expected to prove effective (see Table 1).

The implementation of all the aerodynamic improvements for the rear box configuration yields a 0.505 aerodynamic coefficient, i.e., 23% less in relation to the original rear box configuration, as might have been expected (see Fig. 34). This aerodynamic coefficient is noticeably inferior to that of the vehicle with the lower box configuration including all the aerodynamic improvements, due to the fact that the configuration used for the rear box is more aerodynamic, although the improvement obtained amounted only to 3%.

As far as turbulence is concerned, and as a result of the aerodynamic improvements implemented in these areas, we notice a decrease in the value of the k turbulence parameter in the slipstream, the wheel area and the king-pin cavity (Fig. 33 versus Fig. 14).

We may also notice, in Fig. 35 versus Fig. 13, that there are less vortices in the flow lines and that flow is redirected.

Figures 33 and 36 (versus Fig. 13) shows that the turbulence in the bottom zone and in the wheel zone of the trailer has been reduced, because the underskirt decreases the geometry changes and redirects the air flow properly (see Figs. 32 and 35 versus Fig. 13).

5 Economical Analysis

All the improvements that have been used in the cryogenic tanker trailer can be used in any type of tanker trailer without the need to make any modification, so the analysis that has been done is for all types of tankers. The benefit of these improvements is clear regardless of the vehicle tanker, but the percentage can change depending on the geometry of the tanker. In this paper a standard tanker has been used.

To know if the improvements are viable it is essential to make an economic analysis of them in the US market, so we have used the NADA [21,22,25] database and the "Truck Inventory Use and Survey" [26]. They indicate that in 2003 there were, in USA, 85,174,800 trailers and out of them 34,056,134 were tanker trail-

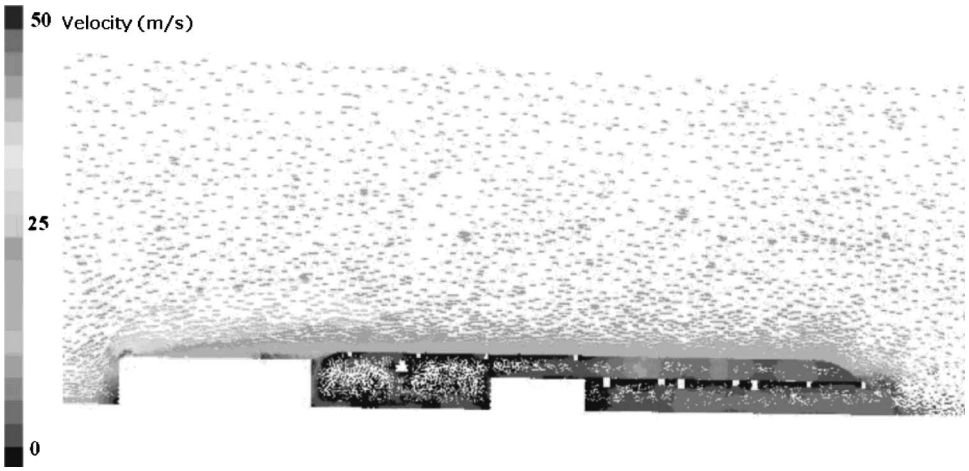

Fig. 32 Flow lines on a vertical plane 1 m above the ground in a vehicle with lower box configuration and all the improvements

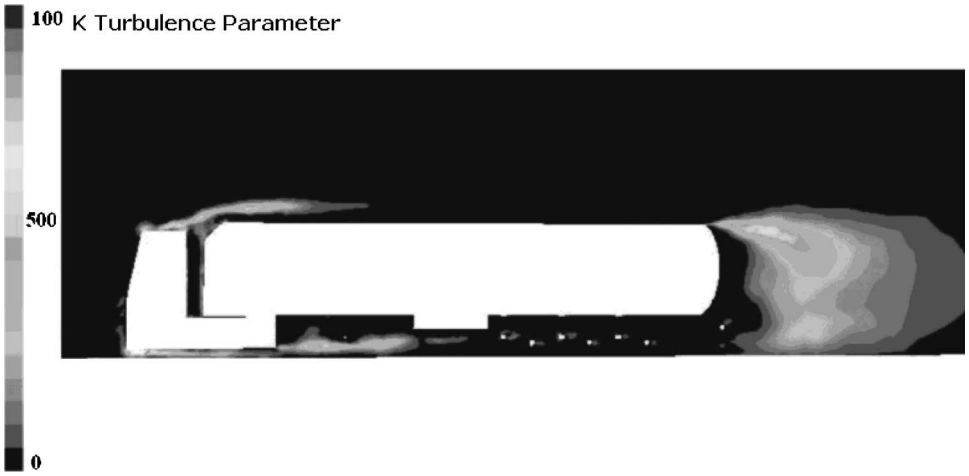

Fig. 33 ***k*** **turbulence parameter at the plane of symmetry in a vehicle with a lower box and the improvements**

ers. For the cost analysis a price of 2.1 $/gal (11/09/2008) has been used and a vehicle consumption of 16 gal/100 miles and 100.000 miles/year for a standard vehicle. This indicates an annual consumption of 16,000 gal and a cost of 33,600 $/year. As for the improvements, the repercussion of them on the consumer depends on some factors (average speed, driving style, orography, etc., but can vary from 10% for slow trailers to 50% for trailers that make railway routs. 40% has been used). The potential costs have been estimated (see Table 2).

The economic results show that with low cost (less than $1100)

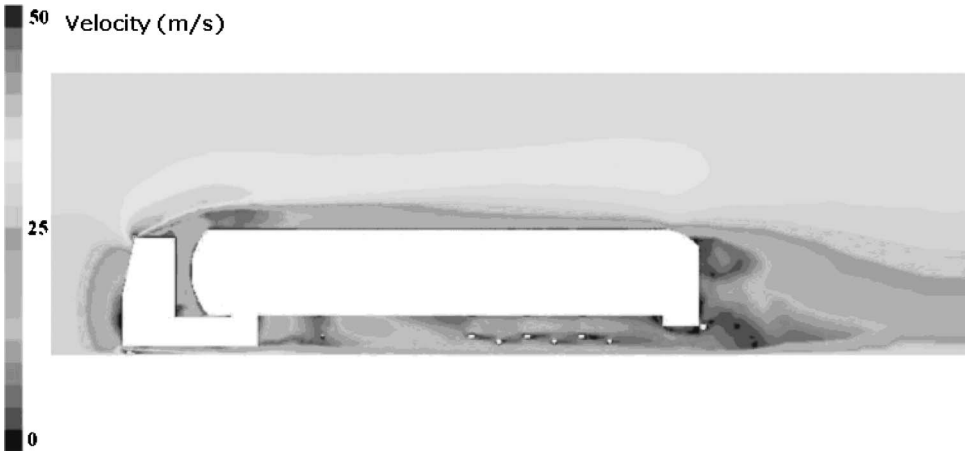

Fig. 34 Speed at the plane of symmetry in a vehicle with rear box configuration and all the improvements

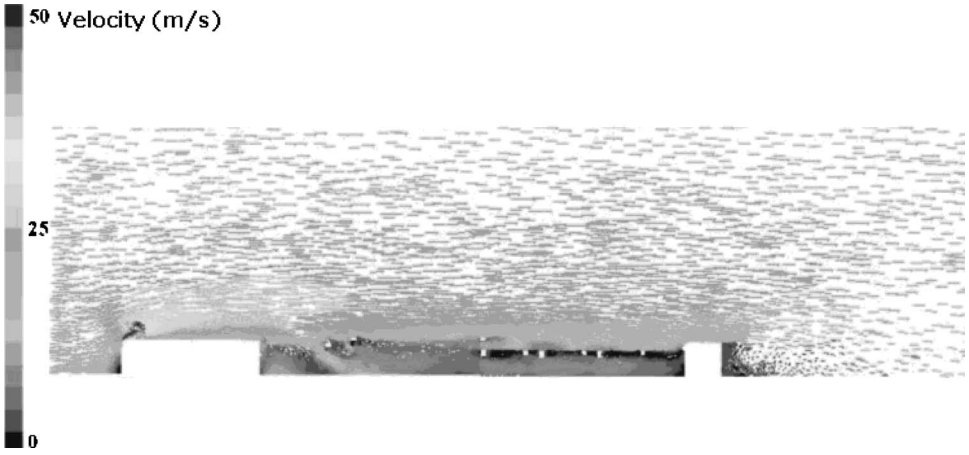

Fig. 35 Flow lines on a vertical plane 1 m above the ground in a vehicle with a rear box and all the improvements

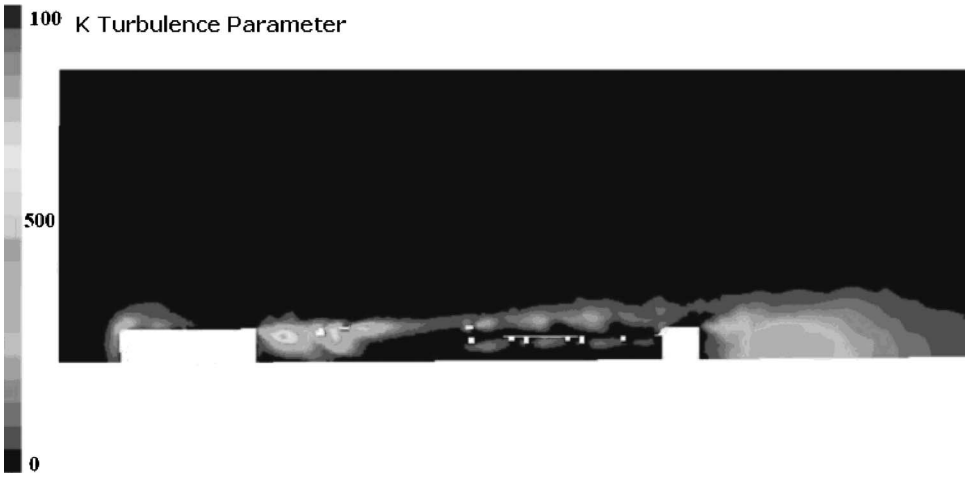

Fig. 36 ***k*** **turbulence parameter on a vertical plane 1 m above the ground in a vehicle with a rear box and improvements**

Table 2 Economical analysis of the improvements

	Undercarriadge skirt	Aerodynamic front	Box adaptor	All improvements (rear box)	All improvements (lower box)
Cost ($)	650	450	530	1540	1050
Saving ($/1000 miles)	12,902	8,198	10,376	32,175	20,268
Saving ($/year)	1290,24	819,84	1037,568	3217,536	2026,752
Miles to pay	50378,224	54888,759	51080,989	47862,712	51807,029
ROI (years)	0,504	0,549	0,511	0,479	0,518
Reduction CO^2 (Tm/year)	1,740	1,105	1,399	4,338	2,732
Increase of autonomy (miles/gal)	0,240	0,153	0,193	0,599	0,377

the fuel consumption is cut down and the annual saving can be $2100, so the return on investment (ROI) is approximately 0.5 years and the economic gain is clearly large. (all economic results are in Table 2). There are also environmental benefits with the CO_2 emissions being reduced by 2.73 Tm during a year.

6 Conclusions

Following a detailed analysis of the results obtained and the methodology implemented, the conclusion reached was that CFD programs are very useful tools for performing aerodynamic modifications in vehicles at a very low cost, and that they allow the achievement of satisfactory results in a short period of time.

There is a wide field of research and a number of improvements to be explored as far as aerodynamic improvements in articulated tanker-type semitrailers are concerned. This is due to the fact that latter-day vehicles have few or no aerodynamic improvements owing to the small amount of research carried out in this transport sector. Therefore, bearing in mind the results obtained and the future prospects of reducing fuel consumption in vehicles, this field of research would seem most promising.

It must be pointed out that the coefficient of aerodynamic resistance can be considerably lowered without modifying the dimensions of the elements subject to mechanical stress by adding external aerodynamic elements that do not entail substantial weight penalization, such as those included in this chapter. Thus the vehicles presently being used can implement these improvements to reduce fuel consumption and improve energy efficiency without having to resort to far-reaching modifications.

In relation to the aerodynamic improvements introduced, it is worth pointing out that the aerodynamic skirt entails the greatest aerodynamic gain of all, and involves a 9% improvement in the aerodynamic coefficient, by preventing the flow of air toward the lower part of the vehicle, where turbulence is predominant.

The contribution of the remaining aerodynamic improvements is also relevant, and their use is always advantageous (see Table 1), although the undercarriage skirt is preferable as an initial aerodynamic improvement. Should the others be implemented as well, they ought to be integrated with the use of the skirt. The integrated use of all these improvements can lead to an aerodynamic improvement of up to 23%, which would measure up to an improvement of up to 11% in fuel consumption. Although this comes close to the 15% expounded in Sec. 1, it does not include improvements in the tractor or those improvements due to modifications in the shape of the resistant elements, which may make up for that 4% difference.

Last but not the least relating to the economic aspect, the aerodynamical improvements have a ROI of 0.5 years and the economic benefit is clearly substantial.

References

[1] Morelli, A., 2000, "A New Aerodynamic Approach to Advanced Automobile Basic Shapes," SAE Technical Paper No. 2000-01-0491, p. 104.
[2] Wood, R. M., and Bauer, S. X. S., 2003, "Simple and Low Cost Aerodynamic Drag Reduction Devices for Tractor-Trailer Trucks," SAE Paper No. 2003-01-3377.
[3] Bachman, L. J., Erb, A., and Bynum, C. L., 2005, "Effect of Single Wide Tires and Trailer Aerodynamics on Fuel Economy and NO_x Emissions of Class 8 Line-Haul Tractor ," SAE Paper No. 05CV45.
[4] Rutledge, W. H., Polansky, G. F., and Clark, E.L., 1988, "Aerodynamic Design and Performance of a Bent-Axis Geometry Vehicle," J. Spacecr. Rockets, **25**(4), pp. 257–262.
[5] Wood, R. M., 2004, Advanced Aerodynamic Trailer Technology.
[6] 2007, FreightWing's web page, http://www.freightwing.com
[7] 2007, Nosecone's web page, http://www.nosecone.com
[8] Graham, S., and Bigatel, P., 2001, "Freight Wing Trailer Aerodynamics," Technical Report No. JA-132.
[9] Kleber, A., 2005, "Simulation of Air Flow Around an OPEL Astra Vehicle With Fluent," International Technical Development Center, Adam, Opel AG, Journal Articles by FLUENT Software users, www.fluent.com/solutions/articles/ja132.pdf

[10] Saiz, V., 2005, "Estudi i Simulació Aerodinàmica del Roadster FS1," MS thesis, Escola Tècnica d'Enginyers Industrials de Barcelona, Barcelona, Spain.
[11] ROS ROCA INDOX CryoEnergy, http://www.cryoenergy.net
[12] Canet, J. M., Bugeda, G., and Oñate, E., 1991, *Simulación Numérica de la Aerodinámica de Vehículos*, Centro Internacional de Métodos Numéricos en Ingeniería, Barcelona, Spain.
[13] 2004, FLUENT 6.2 Documentation, User's Guide, Fluent, Inc.
[14] Parneix, S., Durbin, P. A., and Behnia, M., 1998, "Computation of 3-D Turbulent Boundary Layer Using theV2 Model," Flow, Turbul. Combust., **60**, pp. 19–46.
[15] Menter, F. R., 1994, "Two-Equation Eddy-Viscosity Turbulence Models for Engineering Applications," AIAA J., **32**(8), pp. 1598–1605.
[16] Davidson, L., 2003, *An Introduction to Turbulence Models*, Chalmers University of Technology, Reston, VA.
[17] Durbin, P. A., 1991, "Near-Wall Turbulence Closure Modelling Without 'Damping Functions'," Theor. Comput. Fluid Dyn., **3**, pp. 1–13.
[18] Mercker, E., and Knape, H. W., 1989, "Ground Simulation With Moving Belt and Tangential Blowing for Full-Scale Automotive Testing in a Wind Tunnel," SAE Paper No. 890367.
[19] Skea, A. F., Bullen, P. R., and Qiao, J., 1998, "The Use of CFD to Predict the Air Flow Around a Rotating Wheel," MIRA, International Symposium on Automotives Technology and Automation, Düsseldorf, Germany.
[20] Wong, J. Y., 1993, *Theory of Ground Vehicles*, 2nd ed., Wiley, Ottawa, Canada.
[21] Carr, G. W., 1983, "Potential for Aerodynamic Drag Reduction in Car Design," Int. J. Veh. Des., pp. 51–52.
[22] Carr, G. W., 1983, "Potential for Aerodynamic Drag Reduction in Car Design," Int. J. Veh. Des., pp. 176–196.
[23] Heisler, H., 2002, *Advanced Vehicle Technology*, 2nd ed., Butterworth–Heinemann, Oxford, pp. 584–617.
[24] Comisión Nacional para el Ahorro de Energía de México (Mexico D.C., Mexico), 2007, www.conae.gob.mx
[25] National Automobile Dealers Association, http://www.nada.org/
[26] U.S. Census Bureau, "Truck Inventory and Use Survey," http://www.census.gov/svsd/www/tiusview.html

Dr. Ramon Miralbes Buil *obtained a degree in Industrial Engineering from Zaragoza University in 2005 (Spain), with specialization in Vehicle and Machinery Design. From this time on, he continued his Ph.D. studies in the area of New Materials for Road Transport in this university. In February 2008 he finished his Ph.D. studies with the thesis: "Flow-Termo-Mechanical Analysis of Cryogenic Tanker Vehicles" and is working on several research projects involving vehicle strength and rigidity performance simulation by the FEM. He also works as an Associate Professor in the area of Design and Graphic Expression at the University of Zaragoza.*

Dr. Luis Castejon Herrer *graduated with a degree in Mechanical Engineering (University of Zaragoza, Spain, 1992) and a Ph.D. in Mechanical Engineering (University of Zaragoza, Spain, 1998). Dr. Luis Castejon Herrer is a full Professor in Transportation Engineering at the University of Zaragoza. Since 1991, he has been involved in several projects in the areas of Vehicle Dynamics and New Materials for vehicles, buses, railways, and ground transportation. He has written over 120 papers in technical journals and international congresses and 9 books, published in Europe. He has been a researcher in the European BRITE-EURAM Project "MULTEX-COMP" and he has collaborated in other European projects such as "SEABUS" and "AFICOSS." He has participated in several R + D Spanish projects. He developed his Ph.D. thesis on the simulation of roll over of metallic and composite buses by means of FEM, obtaining the Doctoral Special Award of the University of Zaragoza.*

Free Surface Model Derived From the Analytical Solution of Stokes Flow in a Wedge

R. W. Hewson[1]
School of Mechanical Engineering,
University of Leeds,
Woodhouse Lane,
Leeds, LS2 9JT UK
e-mail: r.w.hewson@leeds.ac.uk

The formation of a thin liquid film onto a moving substrate is a commonly encountered industrial process, and one that is encountered in lubrication, oil extraction processes, and coating flows. The formation of such a film is analyzed via the analytical Stokes flow solution for the flow in a wedge bounded on one side by a free surface and on the other by a moving surface. The full solution is obtained by numerically integrating a set of ordinary differential equations from far downstream, in the region of the final film thickness. The results show excellent agreement with the results obtained by the Bretherton equation, the Ruschak equation, the Coyne and Elrod model, and a two-dimensional free surface finite element simulation of the problem. [DOI: 10.1115/1.3089540]

1 Introduction

The deposition of a thin liquid film is commonly encountered in a number of tribological and coating applications [1–3] and involves the deposition of the thin film onto a moving substrate as it sweeps from a fluid filled gap, as shown in Fig. 1. As such there have been a number of analyses of the problem, most notably that of Bretherton [4] (see also Ref. [5]) who, using a similar method of matched asymptotic expansion as Landau and Levich [6], determined the residual fluid deposited onto a moving substrate by,

$$\frac{h_0}{r} = 1.337\mathrm{Ca}^{2/3}, \quad \mathrm{Ca} \in (0, 10^{-2}) \tag{1}$$

where h_0 is the residual film thickness, r is the (constant) meniscus radius, and Ca is the capillary number given by $\mathrm{Ca}=\mu U/\sigma$ (μ is the fluid viscosity, U is the substrate speed, and σ is the interfacial surface tension).

Ruschak [7] used the finite element method (FEM) to obtain an empirical expression governing the residual film thickness to gap ratio for higher capillary numbers than those for which the Bretherton expression is valid.

$$\frac{h_0}{h_{\theta=\pi}} = 0.54\sqrt{\mathrm{Ca}}, \quad \mathrm{Ca} \in (10^{-2}, 10^{-1}) \tag{2}$$

where $h_{\theta=\pi}$ is the initial fluid filled gap. One limitation of Ruschak's equation is that although it predicts the residual film thickness accurately, the nonconstant meniscus radius means that Eq. (2) is not able to calculate the local pressure at the point of film formation, an important parameter, and one that is often used as a pressure boundary condition in a range of different coating and lubrication problems. This is noted by Thompson et al. [8] who compared the finite element method with the lubrication approximation for reservoir fed rigid roll coating.

Coyne and Elrod [9] derived a set of four ordinary differential equations (ODEs) to describe the process of film formation by solving the Navier–Stokes equations along the free surface. The model assumes a quadratic velocity profile to describe the flow perpendicular to the free surface. One limitation of the model is the stiffness of the set of equations around the free surface stagnation point (occurring at $3H$). Despite this, the method has been used by some investigators as a free surface boundary condition for lubrication [3] (via a function fitted to the data in Coyne and Elrod's paper [9]) as well as for coating problems [2,7].

The cavitation boundary condition can have a significant effect on the pressure profile within the lubricated geometry studied [10]. In addition to the film splitting model described here, there are a number of other models that can be applied to lubrication flows to describe the film splitting process, these include the Swift–Steiber condition [11] and the Prandtl–Hopkins condition [12,13] ($u=du/dx=0$) (as examined for the case of roll coating by Savage [14]).

Hewson et al. [15] solved the film forming problem as a boundary value problem (BVP) for shear thinning fluids obeying both the power law and the Ellis fluid models. The results for the Newtonian fluids (power index $n=1$) compared well with those of the Coyne and Elrod model and the Bretherton and Ruschak equations within their ranges of applicability. The model described here is an attempt to provide a solution to the film forming problem, in a similar way to that of Coyne and Elrod (i.e., the numerical solution of ODEs) using equations that are computationally more stable, in doing so the film forming process has been described for a range of capillary numbers and contact angles. The primary difference between the model presented here and that of Coyne and Elrod is that the flow described here is based on the solution of Stokes flow in a wedge type geometry rather than as a quadratic velocity profile perpendicular to the free surface (as is consistent with the lubrication approximation).

2 Model Formulation

The problem is solved using an analysis similar to that of the long wave approximation but with the local flow solution based on the Stokes solution for the flow in a wedge shaped geometry. For such an assumption to be strictly valid, the free surface radius of curvature must be greater than the residual film thickness [16]—in addition to the work of Snoeijer the analysis here uses a similar method to that of Cox [17,18]. This is valid in the region where the free surface is close to the moving substrate—i.e., in the region where viscous forces are greatest [4]. In undertaking the analysis the variation in film thickness in the region where the free surface is close to the moving substrate is taken into account in determining the free surface profile.

The solution of Stokes flow in a wedgelike geometry with one free surface, one moving surface, and a net flux is formulated in polar coordinates and solved in terms of the stream function ψ, as follows:

[1]Corresponding author.

Contributed by the Fluids Engineering Division of ASME for publication in the JOURNAL OF FLUIDS ENGINEERING. Manuscript received July 24, 2008; final manuscript received January 15, 2009; published online March 11, 2009. Assoc. Editor: Malcolm J. Andrews.

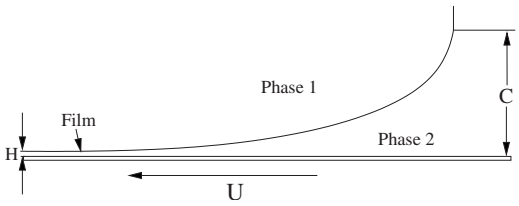

Fig. 1 Illustration of the fluid film forming process

$$\nabla^4 \psi = 0 \tag{3}$$

where $u_r = 1/r\,\partial\psi/\partial\theta$ and $u_\theta = -\partial\psi/\partial r$ are the velocity components in the radial and normal directions, respectively. The problem geometry and local coordinate system employed is shown in Fig. 2. All lengths (x, r) have been made nondimensional by dividing by the residual film thickness (H), by making the velocities nondimensional by dividing by the substrate velocity the flow rate (q) within the fluid domain is equal to one, and the capillary number defined earlier is recovered. The solution of Eq. (3) for the flow in a wedge requires the following boundary conditions to be applied:

$$\psi = 0 \quad \text{at} \quad \theta = 0 \tag{4}$$

$$\psi = -1 \quad \text{at} \quad \theta = \alpha \tag{5}$$

$$\frac{1}{r}\frac{\partial \psi}{\partial \theta} = -1 \quad \text{at} \quad \theta = \alpha \tag{6}$$

$$\frac{1}{r^2}\frac{\partial^2 \psi}{\partial \theta^2} = 0 \quad \text{at} \quad \theta = 0 \tag{7}$$

In order to solve Eq. (3) subject to the boundary conditions (4)–(7), two simpler solutions were sought, with the final solution being the sum of these solutions. The first of these is for the flow in a wedge with a free surface and a stationary surface with a net flux. For this problem the following solution is obtained:

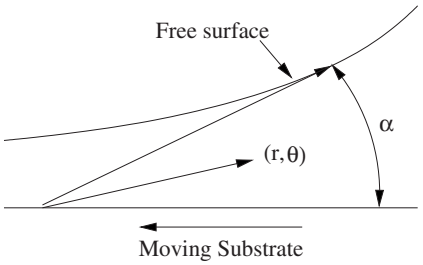

Fig. 2 Definition of the local coordinate system (r, θ), the local tangent to the free surface $\theta = 0$, and the moving substrate $\theta = \alpha$

$$\psi_1 = -\frac{2\theta\cos^2\alpha - \theta - \sin\theta\cos\theta}{2\alpha\cos^2\alpha - \alpha - \sin\alpha\cos\alpha} \tag{8}$$

For the case of a free surface, a moving surface, and zero net flux, the following equation is obtained:

$$\psi_2 = r\frac{(\theta\cos\theta\sin\alpha - \alpha\cos\alpha\sin\theta)}{\alpha - \sin\alpha\cos\alpha} \tag{9}$$

For more information of the solution of viscous flow in a wedge the reader is referred to the work of Moffatt [19] or the more recent derivation of Paggi and Carpinteri [20]. The general solution of Eq. (3) subject to boundary conditions (4)–(7) is the sum $\psi = \psi_1 + \psi_2$—due to the linear nature of the stream function equation and the corresponding addition of the boundary conditions. The sum of the two stream functions is shown graphically in Fig. 3. From the solution of the stream function ψ, the pressure gradient along the free surface can be obtained (at the free surface $\theta = 0$).

$$\frac{\partial p}{\partial r} = \frac{-2r\cos^3\alpha - 4r\alpha\sin\alpha\cos^2\alpha + (2r - 4\sin\alpha)\cos\alpha - 4\alpha + 2\alpha r\sin\alpha}{r^3(-2\alpha\cos^3\alpha\sin\alpha + 2\alpha^2\cos^2\alpha - \alpha^2 + \cos^2\alpha - \cos^4\alpha)} \tag{10}$$

By applying this pressure gradient equation and those describing the meniscus curvature and surface tension ($p = \kappa/\mathrm{Ca}$, where κ is the meniscus curvature $\kappa = d\alpha/ds$ at the free surface), the free surface profile can be obtained and the problem defined as a set of

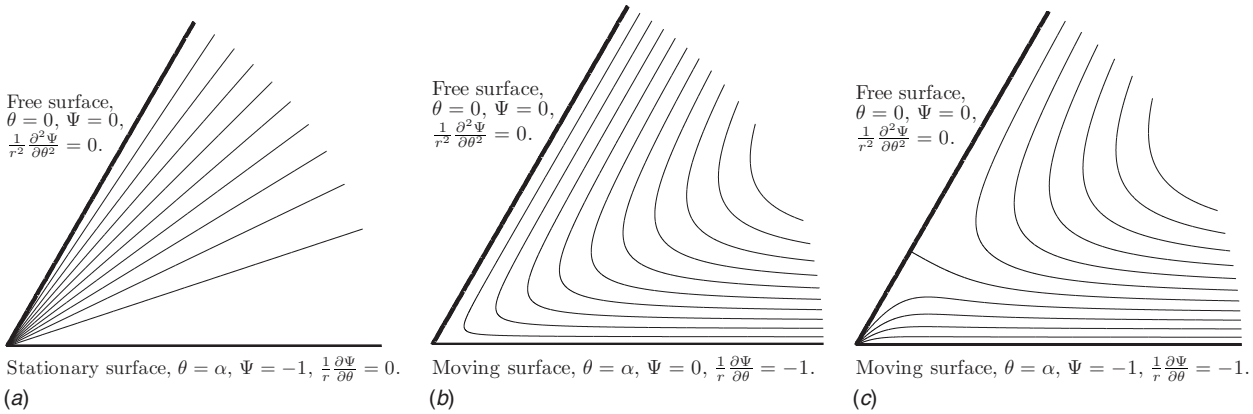

Fig. 3 Graphical representation of the addition of ψ_1 and ψ_2: note the free surface stagnation point predicted by the addition of the two stream functions ψ_1 and ψ_2

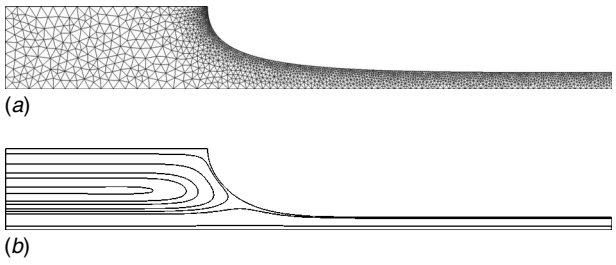

Fig. 4 COMSOL MULTIPHYSICS finite element implementation of the free surface problem

four first order ODEs (with respect to distance along the free surface s), one of which is Eq. (10) ($\partial p/\partial r = dp/ds$), the other three are as follows:

$$\frac{d\alpha}{ds} = -Cap \tag{11}$$

$$\frac{dh}{ds} = \sin(\alpha) \tag{12}$$

$$\frac{dx}{ds} = \cos(\alpha) \tag{13}$$

where h is the film thickness perpendicular to the substrate, and x is the distance along the substrate from the initial condition. Equation (13) is not required in order to close the problem but provides information on the distance downstream from the origin, allowing the meniscus shape to be determined. In addition to the four ODEs the identity $r = h/\sin\alpha$ is also used. The set of four ODEs were solved using MATLAB's general ODE solver *ode45* and were integrated from downstream, in the final film region to an angle of $\alpha = 90$ deg (however different limits of α can be used if required—as determined by the contact angle). It should also be noted that it is possible to solve the set of equations as a BVP with the option of using a further equation ($dq/ds = 0$) describing the flux if this is to be solved for. For this approach the reader is referred to Ref. [15]. The initial conditions used are characteristic of the final film thickness with a perturbation applied to the free surface angle ($\alpha = 10^{-5}$ rad). These initial conditions allow stable perturbation independent solutions to be obtained. The model detailed here has the advantage over the widely used analysis of Coyne and Elrod [9], in that the instability in obtaining their solution is not present in this analysis. As the solution is obtained

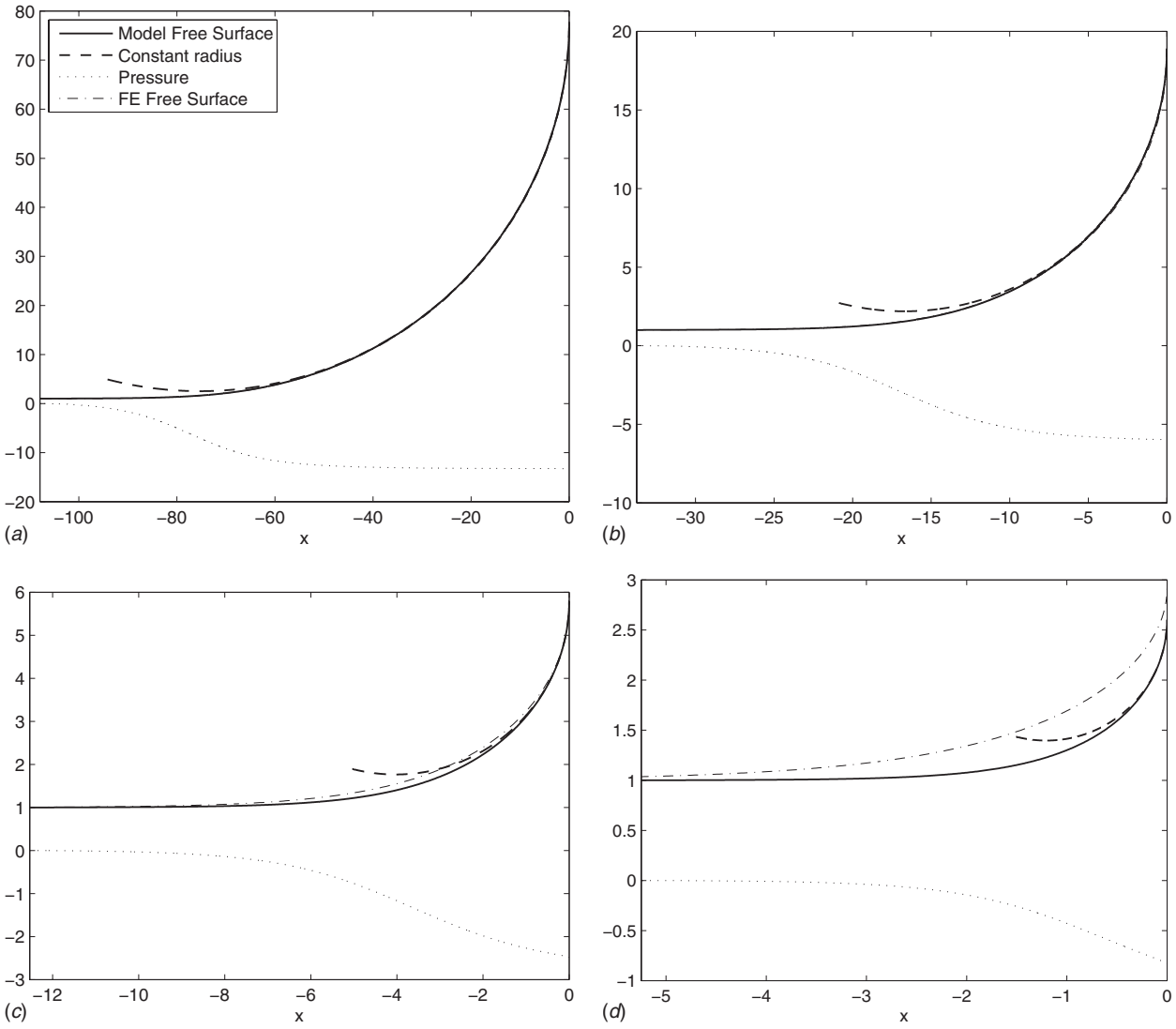

Fig. 5 Free surface meniscus shape, pressure distribution and constant radius at $\theta = 90$ deg, as obtained by the analytical model (Eqs. (10)–(13))

using numerical integration rather than by solving the problem as a BVP as in the analysis of Hewson et al., the model is memory and time efficient and allows the model to be applied to a wide range of coating type flows.

2.1 FEM. The FEM was used to compare with the model results. The simulation was undertaken in COMSOL MULTIPHYSICS using the arbitrary Lagrangian Eulerian (ALE) method. The fluid was modeled as Stokes flow with the free surface curvature obtained by calculating the rate of change with distance along the free surface of the angle the free surface makes with the moving substrate (an implementation that can be achieved in COMSOL by defining the free surface angle as an additional variable along the boundary). The simulation used to obtain the results had 27,733DOF and solution times were of the order of 10 min; the mesh and an example solution are shown in Fig. 4. The velocity inlet boundary condition on the left hand side of the domain is quadratic, consistent with the lubrication approximation. The flow rate across this boundary was varied until the angle the free surface made with the symmetry boundary condition (along the top of the domain) was 90 deg. The main results extracted from the FEM simulations where the final film thickness and the free surface profile. To facilitate the analysis the final film thickness was solved for with the gap $h_{\theta=\pi}$ kept fixed, this is accounted for in Sec. 3 were the results have been appropriately scaled.

3 Results and Discussion

Figure 5 shows the free surface profile for a range of different capillary numbers; also plotted is a constant radius based on the curvature at $\theta=90$ deg. It is interesting to note that as the capillary number decreases then as would be expected, the meniscus shape follows the constant radius more closely and that the greater the viscous forces, the greater the proportion of the meniscus that is not constant in radius. For capillary numbers of Ca=0.001 and Ca=0.01, the finite element and model results are almost identical (the finite element results line is obscured by the free surface line obtained from the model). For a capillary number of Ca=0.1 there is still good agreement between the model and the finite element results, with the model capturing the divergence from the constant radius reasonably well. However, for a capillary number of Ca =1 the results diverge significantly.

Perhaps the results of greatest interest are those of the final film thickness and the meniscus curvature—which allows the local pressure to be determined and can be applied as a boundary condition in a range of different lubrication analyses. Here a comparison is made with the results of the Bretherton equation, Ruschak's equation, and the numerical results of Coyne and Elrod as well as the FEM.

Figure 6(*a*) shows how the residual film thickness varies with capillary number. It can be seen that these results are in excellent agreement with one another. Comparing the radius of curvature to film thickness ratio at $\alpha=90$ deg (Fig. 6(*b*)) shows general agreement for capillary numbers below Ca=0.1 (if a constant meniscus radius is assumed for Ruschak's model a constant radius of curvature of unity would result due to the choice of scaling employed). It can be seen that both the model described here and that of Coyne and Elrod both represent the free surface curvature for low capillary numbers reasonably well. The model described here more closely follows the finite element results for capillary numbers below Ca$\approx$0.1 however the Coyne and Elrod model is more accurate as the capillary number increases further.

The reducing accuracy of the model for higher capillary numbers is consistent with the observation that the analysis is valid for the location where the free surface radius of curvature is large relative to the film thickness. This is in agreement with the analysis of Bretherton [4], however unlike the analysis of Bretherton the divergence from a constant radius is accounted for, alluding to the possibility that the analysis may be able to predict the film profile at higher capillary numbers—something already shown by examining the free surface profile data.

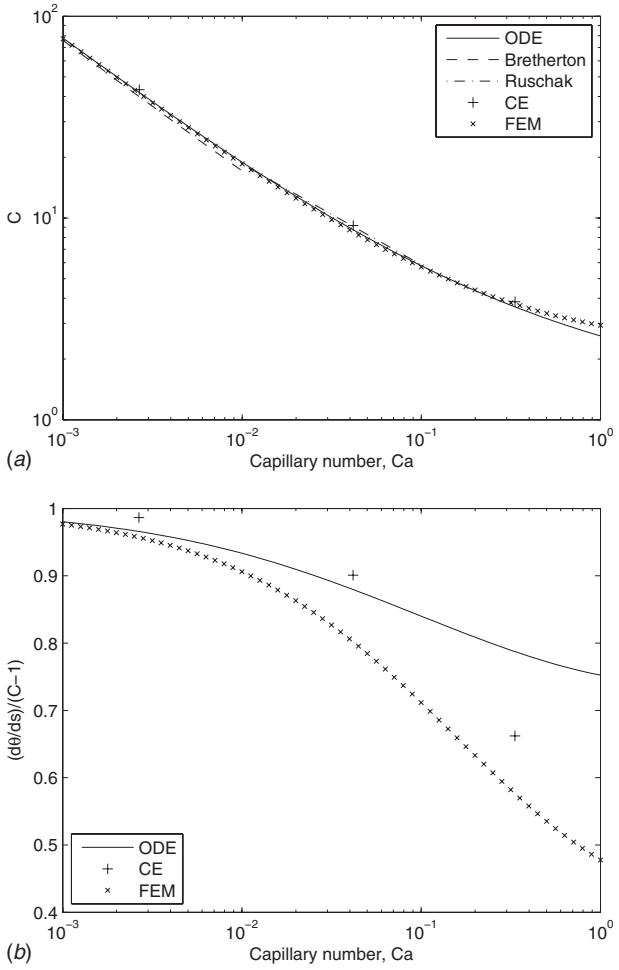

Fig. 6 Results of the model, compared with Bretherton equation, Ruschak equation, and Coyne and Elrod (CE) results; for (*a*) gap, $h_{\theta=0}$ (at $\theta=90$ deg) and (*b*) scaled meniscus radius of curvature $d\theta/ds/(h_{\theta=\pi}-1)$

4 Conclusions

The model detailed here provides an accurate and reasonably efficient means of calculating the free surface shape of a fluid film drawn from a gap. The method is more stable than that developed by Coyne and Elrod and allows greater capillary numbers to be investigated than the simpler relationships developed by Bretherton and Ruschak. It should be noted that there is some additional computational cost associated with the solution, when compared with the elegant solution of Bretherton so a compromise between computational cost and accuracy at moderately high capillary numbers must be borne in mind when deciding on the free surface model to adopt. However the model outlined here provides an extension to higher capillary numbers compared with the Bretherton equation, with the results showing that a capillary number of Ca=0.1 is a realistic upper limit for the model.

Acknowledgment

It is a pleasure to acknowledge Yeaw Chu Lee for his interesting discussions on Stokes flow.

References

[1] Greener, J., and Middleman, S., 1979, "Theoretical and Experimental Studies

of the Fluid Dynamics of a Two-Roll Coater," Ind. Eng. Chem. Fundam., **18**(1), pp. 35–41.
[2] Benkreira, H., Edwards, M. F., and Wilkinson, W. L., 1982, "Ribbing Instability in the Roll Coating of Newtonian Fluids," Plastics and Rubber Processing and Applications, **2**, pp. 137–144.
[3] Priest, M., Dowson, D., and Taylor, C. M., 2000, "Theoretical Modelling of Cavitation in Piston Ring Lubrication," Proc. Inst. Mech. Eng., Part C: J. Mech. Eng. Sci., **214**(3), pp. 435–447.
[4] Bretherton, F., 1961, "The Motion of Long Bubbles in Tubes," J. Fluid Mech., **10**, pp. 166–168.
[5] Park, C. W., and Homsy, G. M., 1984, "Two-Phase Displacement in Hele Shaw Cells: Theory," J. Fluid Mech., **139**, pp. 291–308.
[6] Landau, L., and Levich, B., 1942, "Dragging of a Liquid by a Moving Plate," Acta Physicochim. URSS, **17**, pp. 42–54.
[7] Ruschak, K. J., 1982, "Boundary-Conditions at a Liquid Air Interface in Lubrication Flows," J. Fluid Mech., **119**, pp. 107–120.
[8] Thompson, H. M., Kapur, N., Gaskell, P. H., Summers, J. L., and Abbott, S. J., 2001, "A Theoretical and Experimental Investigation of Reservoir-Fed, Rigid-Roll Coating," Chem. Eng. Sci., **56**(15), pp. 4627–4641.
[9] Coyne, J. C., and Elrod, H. G., 1970, "Conditions for the Rupture of a Lubricating Film. Part 1: Theoretical Model," ASME J. Lubr. Technol., **92**, pp. 451–456.
[10] Cameron, A., 1979, *Basic Lubrication Theory*, Longman, Greens, New York.
[11] Swift, H. W., 1932, "The Stability of Lubricating Films in Journal Bearings," Proc. Inst. of Civ. Eng. (UK), **233**, pp. 267–288.
[12] Prandtl, L., 1928, "Motion of Fluids With Very Little Viscosity," Technical Memorandum of the National Advisory Committee, NACA.
[13] Hopkins, M. R., 1957, "Viscous Flow Between Rotating Cylinders and a Sheet Moving Between Them," Br. J. Appl. Phys., **8**, pp. 442–444.
[14] Savage, M. D., 1982, "Mathematical-Models for Coating Processes," J. Fluid Mech., **117**, pp. 443–455.
[15] Hewson, R. W., Kapur, N., and Gaskell, P. H., 2005, "Film Formation Model of Shear Thinning Power Law Fluids Using Lubrication Analysis," European Coating Symposium, Bradford, West Yorkshire.
[16] Snoeijer, J. H., 2006, "Free-Surface Flows With Large Slopes: Beyond Lubrication Theory," Phys. Fluids, **18**(2), pp. 021701.
[17] Cox, R. G., 1986, "The Dynamics of the Spreading of Liquids on a Solid-Surface. Part 1. Viscous-Flow," J. Fluid Mech., **168**, pp. 169–194.
[18] Boender, W., Chesters, A. K., and Vanderzanden, A. J. J., 1991, "An Approximate Analytical Solution of the Hydrodynamic Problem Associated With an Advancing Liquid Gas Contact Line," Int. J. Multiphase Flow, **17**(5), pp. 661–676.
[19] Moffatt, H. K., 1964, "Viscous and Resistive Eddies Near a Sharp Corner," J. Fluid Mech., **18**(1), pp. 1–18.
[20] Paggi, M., and Carpinteri, A., 2008, "On the Stress Singularities at Multimaterial Interfaces and Related Analogies With Fluid Dynamics and Diffusion," Appl. Mech. Rev., **61**(2), pp. 020801.

Numerical and Experimental Investigations of Steam Condensation in LP Part of a Large Power Turbine

Włodzimierz Wróblewski
e-mail: wlodzimierz.wroblewski@polsl.pl

Sławomir Dykas

Institute of Power Engineering and Turbomachinery,
Silesian University of Technology,
Gliwice, Poland

Andrzej Gardzilewicz
Institute of Fluid-Flow Machinery,
Polish Academy of Science,
Gdansk, Poland
e-mail: gar@imp.gda.pl

Michal Kolovratnik
Czech Technical University in Prague (CTU),
Prague, Czech Republic
e-mail: kolovrat@fsid.cvut.cz

This paper presents the experimental investigations of steam flow with condensation in the blading system of the low-pressure (LP) part of a 360 MW turbine. To this end, special probes were used, which provided flow visualization opportunities including localization of the front of condensation, determining distributions of pressure, temperature, velocity, and flow angle in the inter-row gaps, measurements of water droplet concentration and sizes. The measurements have proved that the condensation process in the LP turbine might be of heterogeneous nature, depending on the concentration of chemical impurities in steam. The measurement results constituted the basis for computational fluid dynamics (CFD) flow calculations, which were performed using the time-dependent 3D Reynolds averaged Navier–Stokes equations coupled with two-equation turbulence model (k-ω SST) and additional conservation equations for the liquid phase. The set of governing equations has been closed by a "local" real gas equation of state. The condensation phenomena were modeled on the basis of the classical nucleation theory. The heterogeneous condensation model on the insoluble and soluble impurities was implemented into presented CFD code. The system of governing equations was solved by means of a finite volume method on a multiblock structured grid. The obtained numerical results and experimental data were compared and discussed. [DOI: 10.1115/1.3089544]

1 Introduction

The flow of steam through the blades of a low-pressure (LP) turbine results in condensation that unfavorably influences efficiency of power generation. The homogeneous condensation in steam flow occurs when there are no foreign nuclei. In real conditions, for steam power cycle, the steam always contains some impurities of both insoluble and soluble characters. Therefore, in real turbine, the wetness appears as a result of a mixed homogeneous/heterogeneous condensation or pure heterogeneous condensation, everything depends on the quantity of foreign nuclei.

The lack of experimental data for the steam flow with heterogeneous condensation and new data for the flow with pure homogeneous condensation limit the progress in numerical modeling of the wet steam flows. It is very difficult to reproduce the real conditions in large output turbine in experiment; it refers to the flow conditions and steam quality, the number, and the sort of the impurities. The impurities may change the mechanism of the liquid phase generation and may intensify the corrosion and erosion processes. Many operational experiences in the power plants (e.g., Refs. [1,2]) and author's own observations confirm that facts.

In the feedwater cycle of power plant, different sources of impurities may be identified: mechanical, chemical, or electrochemical ones. Particles that exist in steam are soluble and insoluble compounds (salts and alkalis). For the parameter range occurring in water-steam cycle, these impurities can be divided into groups with and without phase change. In the first group, sodium chloride (NaCl) is the most important one, taking into consideration condensation process, which dissolves just above the saturation line of pure steam. As regards condensation on soluble particles, it is necessary to take into account the size change of the particles and the solution concentration in the droplets. The condensation model requires knowledge of many physical and chemical properties of the salt solution in steam. It is often very hard to find enough information in the references, as well as from the feedwater analysis in the power plant.

Two processes have to be considered during steam expansion in the turbine: homogeneous and heterogeneous condensations. Steam impurities, necessary to initiate heterogeneous condensation, occur in the form of suspension of particles, which are insoluble or soluble in water. The chemical and physical properties of a suspension influence the size of the droplets nucleated on the particles and the nucleation process.

It is possible to model various types of condensation processes, i.e., homogeneous and heterogeneous ones (on soluble and insoluble particles). The necessary step in the nonequilibrium wet steam flow modeling is the validation of the numerical models against the experimental results. The development of numerical methods for wet steam flow calculations has to allow for real gas properties, which, in fact, is the fundamental one for correct calculations of the condensation process. The correct calculation of the steam flow for low pressures close to the saturation line and for high pressures needs to implement the real gas equation of state into numerical algorithm. The relation between thermal parameters of state is nonlinear within these ranges and does not follow the ideal equation of state. Moreover, in the case of wet steam, a two-phase flow model has to be considered.

The developed steam condensing flow models have been validated against experimental data for simple 2D test cases. Usually, they are the Laval nozzles in which 1D flow form dominates. All available experimental investigations relate to the homogeneous condensation, whereas in real turbine the heterogeneous condensation is predominant. Therefore, validation of the numerical algorithm for modeling the flow in real turbine stages by means of such test cases is not easy; it has been discussed in Refs. [3,4].

The comparison of the numerical modeling and measurements

Contributed by the Fluids Engineering Division of ASME for publication in the JOURNAL OF FLUIDS ENGINEERING. Manuscript received October 30, 2007; final manuscript received October 6, 2008; published online March 9, 2009. Assoc. Editor: Chunill Hah.

of the flow in real turbine of the large output is not often published. The crucial value of such verification comes down to the assessment of flow conditions for real LP steam turbine stages by means of the CFD code.

This paper presents the results of experimental and numerical investigations of 3D flows through the last two stages of the LP part of a 360 MW turbine. The problems of condensation in a LP steam turbine has been presented and discussed also, e.g., by Hesler et al. [5], Bakhtar and Heaton [6], and Petr et al. [7].

Measurements of thermodynamic parameters, the size, and concentration of water droplets together with CFD results have been described below. The presented work was performed by research teams of the Institute of Fluid-Flow Machinery from Gdansk (PL), the Czech Technical University (CTU) of Prague, and the Silesian University of Technology (PL) within the framework of the Research Project No. 3T10B04726 sponsored by the State Committee for Scientific Research in Poland.

2 Physical and Mathematical Model

2.1 Governing Equations. All results presented in this paper were obtained by means of the in-house CFD code. The code is based on the time-dependent 3D Reynolds averaged Navier–Stokes (RANS) equations formulated for the vapor/water mixture, which are coupled with a two-equation turbulence model (k-ω SST model), and with additional mass conservation equations for the liquid phase: two for homogeneous condensation,

$$\frac{\partial(\rho y_{\mathrm{hom}})}{\partial t}+\frac{\partial(\rho y_{\mathrm{hom}}u)}{\partial x}+\frac{\partial(\rho y_{\mathrm{hom}}v)}{\partial y}+\frac{\partial(\rho y_{\mathrm{hom}}w)}{\partial z}=\frac{4}{3}\pi\rho_l\left(r^{*3}J_{\mathrm{hom}}+3\rho n_{\mathrm{hom}}r_{\mathrm{hom}}^2\frac{dr_{\mathrm{hom}}}{dt}\right)$$

$$\frac{\partial(\rho n_{\mathrm{hom}})}{\partial t}+\frac{\partial(\rho n_{\mathrm{hom}}u)}{\partial x}+\frac{\partial(\rho n_{\mathrm{hom}}v)}{\partial y}+\frac{\partial(\rho n_{\mathrm{hom}}w)}{\partial z}=J_{\mathrm{hom}} \tag{1}$$

and one for heterogeneous condensation:

$$\frac{\partial(\rho y_{\mathrm{het}})}{\partial t}+\frac{\partial(\rho y_{\mathrm{het}}u)}{\partial x}+\frac{\partial(\rho y_{\mathrm{het}}v)}{\partial y}+\frac{\partial(\rho y_{\mathrm{het}}w)}{\partial z}=4\pi\rho_l\rho n_{\mathrm{het}}r_{\mathrm{het}}^2\frac{dr_{\mathrm{het}}}{dt} \tag{2}$$

The droplet radius r_{het} in the heterogeneous condensation is calculated from the relation

$$r_{\mathrm{het}}=\left(r_p^3+\frac{3}{4\pi}\frac{y_{\mathrm{het}}}{\rho_l n_{\mathrm{het}}}\right)^{1/3} \tag{3}$$

where r_p is the radius of the particle on which the droplet is growing.

For the two-phase nonequilibrium flow, it has been assumed that the volume occupied by droplets is negligibly small. The interaction between droplets is not taken into account in the model. The heat exchange between the liquid phase and the solid boundary, and the velocity slip between vapor and the liquid phase are neglected. The nonslip assumption is much less significant than the effects of the thermal nonequilibrium [8]. The conservation equations are formulated for the two-phase mixture with the specific parameters calculated with the following relations:

$$h=h_v(1-y)+h_1y$$

$$s=s_v(1-y)+s_1y \tag{4}$$

$$\rho=\rho_v/(1-y)$$

The value of the nonequilibrium wetness fraction y is calculated as the sum of the homogeneous and heterogeneous wetness obtained from the conservation equations for the liquid phase (1) and (2).

2.2 Equation of State. For wet steam flow calculations, the set of ten governing equations has to be closed by a real gas equation of state (EOS). The formulation of the real gas EOS is compound even in case when simplified model has been used. The idea of applied real gas EOS consisted in creation of equation of state with as simple mathematical form as possible, but simultaneously very accurate. The simple mathematical form can be very accurate, but only within the small parameters range.

The mathematical form of used real gas EOS is similar to the virial equation of state with one virial coefficient.

$$\frac{p\nu}{RT}=Z(T,\nu)=A(T)+\frac{B(T)}{\nu} \tag{5}$$

where $A(T)$ and $B(T)$ are defined as

$$A(T)=a_0+a_1T+a_2T^2$$

$$B(T)=b_0+b_1T+b_2T^2$$

The coefficients $a_i,b_i(i=0,\ldots,2)$ of the polynomials $A(T)$ and $B(T)$ are the functions of temperature only, and they can be found from an approximation of thermodynamic properties of steam calculated using IAPWS-IF'97 [9]. It is easily to notice that this equation is represented by a relatively uncomplicated approximate surface.

The equation of state (5) is called the "local" real gas equation of state because, due to the simple mathematical form, it can be applied locally within the limited parameter range only.

Expressions for the specific enthalpy, specific entropy, and other properties such as specific heat capacities and speed of sound can be determined from the standard thermodynamic relations.

The concept of the local real gas equation of state can be applied to determine the thermodynamic properties of any real gas, in the case when the simple mathematical form is needed.

2.3 Nucleation and Droplet Growth Model. The homogeneous condensation phenomenon is modeled on the ground of the classical nucleation theory of Volmer, Frenkel [10], and Zeldovich and continuous droplet growth model of Gyarmathy [11].

The nucleation rate, i.e., number of supercritical droplets produced per unit mass of vapor per unit time, is calculated from the relation derived by the assumption of thermodynamic equilibrium between critical droplets and vapor. Additionally, the nonisothermal correction factor C proposed by Kantrowitz [12] has been used because the isothermal model assumption does not apply to the vapor:

$$J_{\mathrm{hom}}=C\left(\frac{2\sigma}{\pi}\right)^{1/2}m_v^{-3/2}\frac{\rho_v^2}{\rho_l}\exp\left(-\beta\frac{4\pi r^{*2}\sigma}{3kT_v}\right) \tag{6}$$

where coefficient C is calculated from the relation

$$C=\left[1+2\frac{\gamma-1}{\gamma+1}\frac{h_v-h_l}{RT_v}\left(\frac{h_v-h_l}{RT_v}-\frac{1}{2}\right)\right]^{-1}$$

and m_v is the mass of a water molecule and β is the correction factor (in the calculations assumed=1).

The radius of critical clusters r^* for the applied real gas EOS (5) has a form that differs from the known relation for ideal gas:

$$r^*=\frac{2\sigma}{\rho_l(f(p_v)-f(p_s))-(p_v-p_s)} \tag{7}$$

where

$$f(p)=\frac{b}{2}\ln p+c-\frac{b}{2}\ln\left(\frac{1+\frac{c}{b}}{1-\frac{c}{b}}\right)$$

$$b=A(T)RT$$

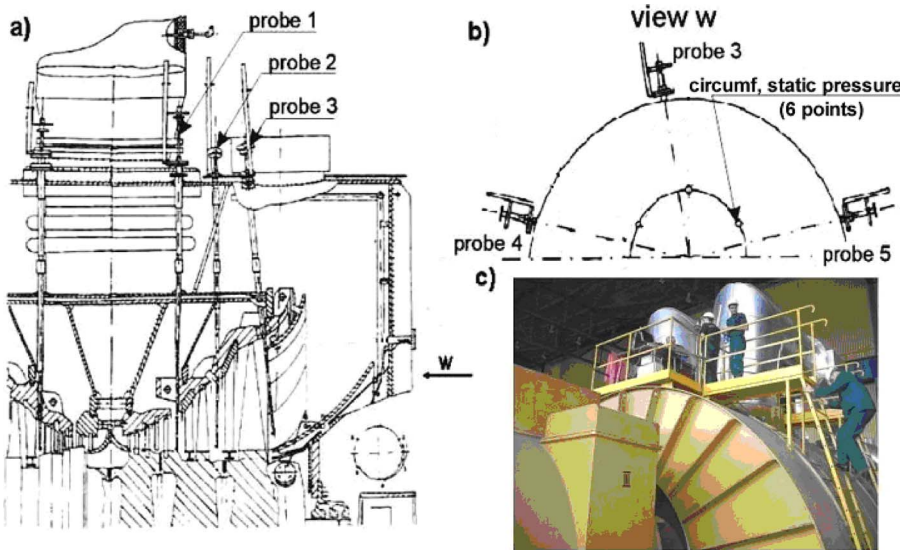

Fig. 1 Location of probes in the blade system of a 360 MW turbine LP part of Belchatow Power Plant: meridional section (*a*), cross section (*b*), and photo of measurement stand (*c*)

$$c = [(A(T)RT)^2 + 4pB(T)RT]^{1/2}$$

Equation (7) has an ideal gas form since $A \to 1$ and $B \to 0^-$.

The further behavior of the critical droplets can be described by suitable droplet growth law. The size of the droplets for the vapor under low pressure is much smaller than mean free path of the vapor molecules. Therefore, the growth of the droplets should be governed by considering molecular and macroscopic transport processes (Hertz–Knudsen model). Difficulties to choose the condensation and accommodation coefficients make the application of the Hertz–Knudsen model very difficult to calculate. This problem can be avoided by using Gyarmathy's droplet growth model, which takes into account diffusion of vapor molecules through the surrounding vapor, as well as heat and mass transfer, and the influence of the capillarity:

$$\frac{dr}{dt} = \frac{1}{\rho_l} \frac{\lambda_v}{(1 + 3.18\ \mathrm{Kn})} \cdot \frac{r - r^*}{r^2} \frac{T_s - T_v}{h_v - h_l} \tag{8}$$

In the case of heterogeneous condensation model, the nucleation process is neglected. The droplet growth on the particle impurities, which are assumed to be spherical with the given initial mean radius and concentration, is modeled according to the same droplet growth law (8).

The model of heterogeneous condensation on soluble particles is based on the work of Gorbunov and Hamilton [13]. In the model, the influence of the NaCl salt is taken into account.

Knowledge of specific physical and chemical parameters of the salt solution in steam is necessary for process definition. This information is usually inaccessible due to the lack of experimental research in this field. Physical model includes supplementary parameters, such as molality of salt solution M_l and the activity of water a_w:

$$M_l = \frac{1000 n_s}{n_w M_{ww}} \tag{9}$$

$$a_w = 1 - \sum_{i=1}^{3} a_i M_l^i, \quad M_l < M_{l\,\max}$$

$$a_w = 1 - \sum_{i=1}^{3} a_i M_{l\,\max,}^i \quad M_l > M_{l\,\max} \tag{10}$$

where M_{ww} is the molar mass of water and for NaCl is $M_{l\,\max} = 6.109$ mol/kg. The coefficients are $a_1 = 3.2975479 \times 10^{-2}$ kg/mol, $a_2 = 2.081262 \times 10^{-4}$ kg^2/mol^2, and $a_3 = 1.85425 \times 10^{-4}$ kg^3/mol^3. The activity of water is used to specify the saturated pressure for the aqueous solution necessary in Eqs. (7) and (8).

The surface tension for a water solution of soluble particles is calculated from the relation according to Gorbunov and Hamilton [13]:

$$\sigma = \sigma_o(T) + BM_l \tag{11}$$

where the value of surface tension σ_0 is for $M_l = 0$ mol/kg (pure steam). Constant B depends on the solution (for NaCl it equals 1.62×10^{-3} N kg/(m mol).

3 Numerical Method

The numerical calculations were carried out using the in-house CFD code (TRACOFLOW). The system of governing equations was solved on a multiblock structured grid with the use of the finite volume method integrated in time with the explicit Runge–Kutta method. In time integration, the fractional step method was used to split the equations into an adiabatic and a diabatic part in order to apply different time steps for the flow and condensation calculations. The Monotone Upstream-centered Schemes for Conservation Laws (MUSCL) technique was implemented to get a third order accuracy in space. For modeling the stator-rotor interaction, a mixed-out technique was used. A detailed description of the numerical method can be found in Refs. [14,15], where the validation of the CFD code against laboratory tests has been presented.

4 Experimental Investigations in the LP Turbine

4.1 Thermal and Flow Measurements. The instrumentation installed at the 18 K360 turbine and used for thermal and flow measurements is shown in Fig. 1.

Figure 1 shows the location of special measuring probes in the spaces between the last stage rows. These probes allowed (a) measuring pressure and temperature distributions, and evaluating velocity magnitudes and angles; (b) visualizing the flow and localizing the beginning of condensation; and (c) taking samples of

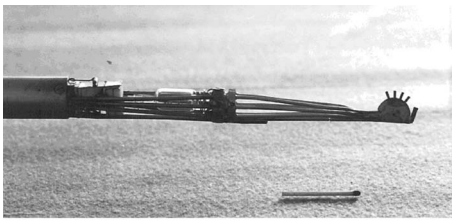

(*a*)

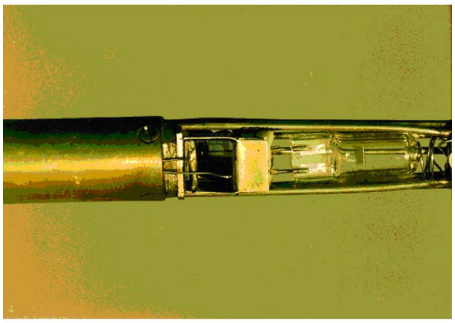

(*b*)

Fig. 2 Plate probe for thermal and flow measurements (*a*) including the optical system (*b*)

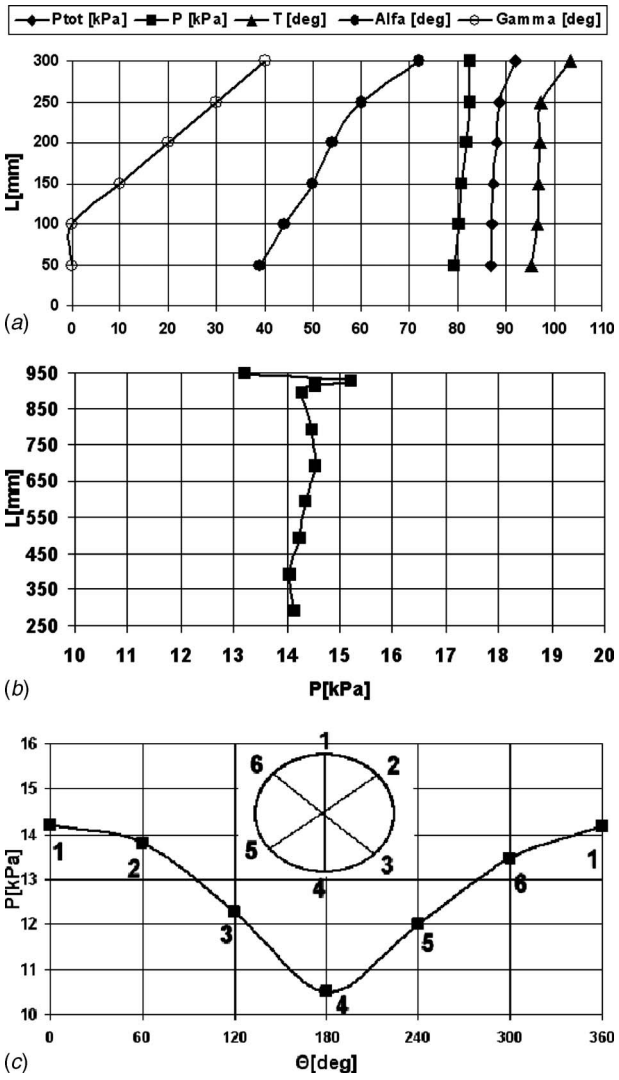

Fig. 3 Measurement radial parameters at the inlet fourth stage (*a*) and behind the last stage (*b*). Circumferential static pressure at the root stage behind the turbine (*c*).

early condensate for chemical analyses.

The probes can be mounted during nonstop operation into special seats prepared during an overhaul of the turbine. The measuring probe, presented in Fig. 2, can be classified as a disk probe. This type is not sensitive to water films that form on it [16]. The probe tip consists of four (five) Pitot tubes inclined toward the flow at four various pitch angles (every 20 deg from −20 up to +40 (60)). It allows us to determine the streamline angles in meridional plane. It is also possible to measure the total pressure, which is taken as the highest value of all four readings. Two holes have been made on the side surface of disk to determine the yaw angle. The holes are also used to determine the static pressure. The whole tip of probe (the head and the tubes) is lined inside and covered outside with Teflon to avoid watering of the probe and to assure effective blowthrough and extraction of deposited water. Smooth regular flowthrough is assured at joints of tubes of different diameters. Owing to this, the probe disk was miniaturized to a diameter of less 20 mm. The diameter of the probe tubes is less than 1 mm. In order to perform the blowthrough of the probe, a cutoff valve has been installed, which links all tubes with atmosphere. When the blowthrough is switched off and the measurement starts, the complete leak tightness is secured. It is vital that the probe is placed properly with respect to the flow. Therefore, turbine geometry is studied and the probe is aligned carefully prior to the measurement. Visualization is based on a special telescope. The probe is equipped with an optical system adjusted for microphotography purposes, see Fig. 2.

1000 W halogen lighting is a part of the system to enable the flow visualization. TV camera or an Olympus system can be utilized here. A special wiper cleans the prismatic eyepiece if watered. Before each measurement, the measuring probes were calibrated at the laboratory rigs. This, along with the stabilization of the genset operating parameters, provided a high accuracy of the measurements, in which temperature was assessed with an uncertainty equal to ±0.5 K, and pressure—with that equal to ±0.5%. The uncertainty in evaluating flow inclination angles was equal to ±2 deg in the circumferential plane and ±10 deg in the meridional plane. The measuring procedure was described in detail by Gardzilewicz and Marcinkowski [17].

The investigations were done for two characteristic loads of 300 MW and 360 MW.

During thermal and flow measurements, sections between the three last stages were radially traversed (probes 1–3), as shown in Fig. 1. These measurements were completed by measurements in circumferential direction behind last stage (probes 4 and 5).

The unsymmetrical flow behind the turbine checked additionally by static pressure measurements at six points of circumference distributed each 60 deg.

A complete set of the measured results can be found in Ref. [18].

Selected results of these measurements, which were a database for numerical calculations, are shown in Fig. 3 (concerned power of 360 MW). They include all measurement parameters at the inlet to the fourth stage and distribution of static pressure along the radial and circumferential directions behind last stage. Other necessary data from the complete set are presented in the next paragraph in order to compare them with calculation results.

It is noteworthy that the thermal measurements made it possible to determine the course of the expansion line in the wet steam area. Average enthalpy values required for this purpose were obtained from additional heat balance calculations and mass flow rate known from experiment [17]. The shape of the expansion line for one of the reported experimental case (made with the liquid phase measurements −360 MW, case 2) is shown in Fig. 4. In this figure, an area is marked in which the condensation begins. This

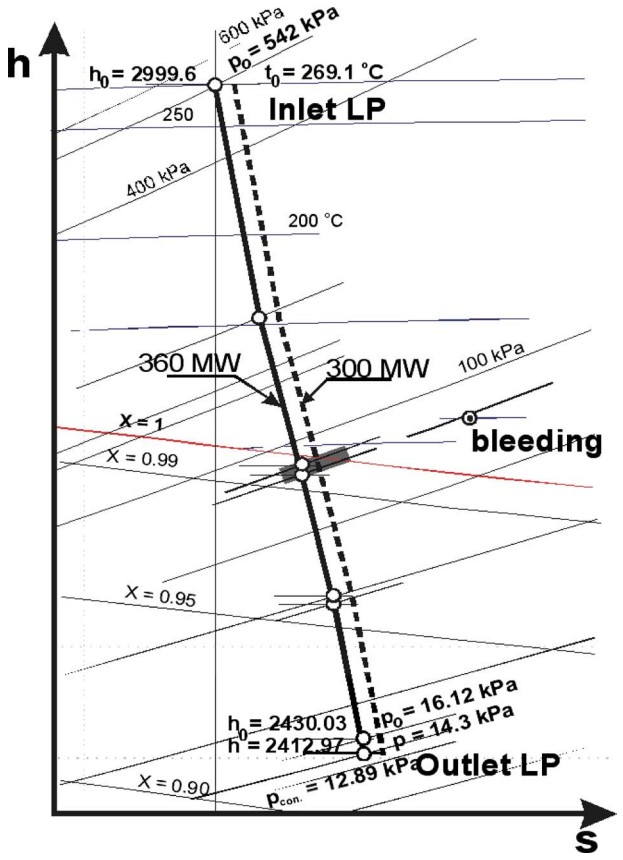

Fig. 4 Expansion lines in LP part of a 360 MW turbine

area, detected by the optical system of the probe, is situated behind the third stage, below the saturation line, which could possibly be explained by the heterogeneous nature of the steam condensation process at the presence of other chemical compounds. The presence of chemical inclusions was confirmed by pH conductivity tests and chemical analyses of the first condensate and condenser water samples. This is presented in Table 1. Noteworthy are high numbers of Na and Cl ions, which, according to investigations by Steltz et al. [19] and Svoboda et al. [20], accelerate the condensation process.

Table 1 Calculated mass flow rates $\dot{m}$ (kg s^{-1}) (case 1)

Adiabatic	Homogeneous condensation	Homo-/heterogeneous condensation	Heterogeneous condensation
103.5	102.2	102.1	101.8

4.2 Measurement of Liquid Phase Characteristics. Measuring the liquid-phase structure in the LP part was a special part of 360 MW turbine tests. The optical measurements require a special measuring device. Therefore, the CTU team was invited, who has long-time experience with this problem. Measurements of the droplet size distribution and steam wetness were carried out by an extinction probe, developed at CTU [7]. The probe measures the multispectral extinction of light, i.e., attenuation (I/I_o), caused by the light scattering on droplets, at the series of light wavelengths.

The universal measuring system with an extinction probe was used for measuring the multispectral light extinction. The probe measures the transmittance $(I/Io)_i$, caused by the light scattering on droplets, of the light beam transmitted through the wet steam at the series of light wavelengths $\lambda_i (i=1,\ldots)$. The layout of the measuring system is shown in Fig. 5(*a*), while the measuring head of the extinction probe with the 25 mm diameter is presented in Fig. 5(*b*).

The distribution function $F(D)$ of the droplet sizes, together with the wetness fraction y, is then found by means of computer analysis (using Mie's theory of light scattering on droplets) of the measured transmittance data I/I_o. In principal, the problem leads to the solution of the system of the first kind Fredholm integral equations.

The structure of fine droplets at the measurement site was evaluated from the measurement data I/I_o by means of the CTU inversion method using the well-known exponential law:

$$\frac{1}{l}\ln\left(\frac{I_o}{I}\right)_i = \frac{\pi}{4}\int_{D_{\min}}^{D_{\max}} E(\pi D/\lambda_i, m)F(D)D^2 dD \qquad (12)$$

where i means the discrete wavelength.

The Sauter mean droplet diameter and volume concentration of droplets could be evaluated then from Eqs. (13) and (14), respectively.

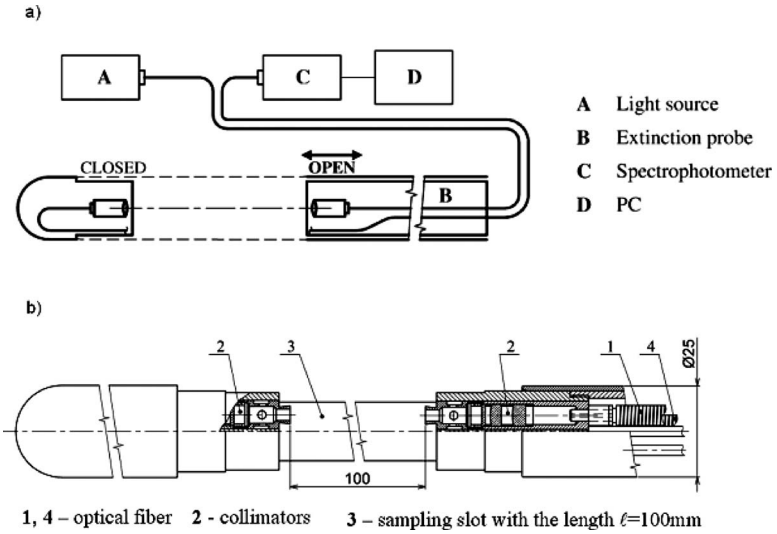

Fig. 5 Measuring system of CTU extinction probe (*a*) and head of extinction probe (*b*)

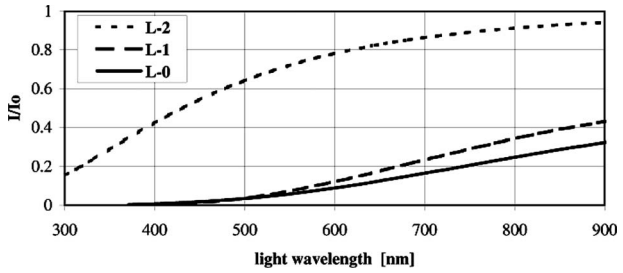

Fig. 6 Variation in transmittance measured at the blade midspan behind the L-0, L-1, and L-2 stages

$$D_{32} = \frac{\int_{D_{\min}}^{D_{\max}} F(D)D^3 dD}{\int_{D_{\min}}^{D_{\max}} F(D)D^2 dD} \tag{13}$$

$$n = \int_{D_{\min}}^{D_{\max}} F(D)dD \tag{14}$$

For measured values of static pressure p at the measuring levels, the corresponding steam wetness was determined according to the equation

$$y = \frac{1}{1 + \left(\frac{\pi}{6} \frac{\rho_l}{\rho_v} \int_{D_{\min}}^{D_{\max}} F(D)D^3 dD \right)^{-1}} \tag{15}$$

where ρ_v and ρ_l are assumed as saturation parameters.

Measuring the multispectral extinction was carried out at the exit of the last three stages of the LP part of the steam turbine always in several traverse positions along the blade height. Let us denote the fifth (the last), fourth, and the third stages of turbine by L-0, L-1, and L-2, respectively.

The measuring slot of the probe was oriented according to the outlet yaw angles measured by IF-FM Gdansk and checked using $(I/I_o)_{\min}$ of the optical extinction probe.

The primary result of the extinction measurements in the turbine is the dependence of the transmittance I/I_o on the light wavelength λ for each measuring position. Figure 6 shows an example of the measured variation $I/I_o = f(\lambda)$ at the blade midspan behind the L-0, L-1, and L-2 stages.

As it can be seen from Fig. 6 (L-2) under nominal operating conditions of the turbine, it is probable that nucleation might start at the L-2 stage. It is to be emphasized that the liquid phase at L-2 was observed at the blade midspan only. In addition, the occurrence of the liquid phase was not observed in repeated measurements. It confirms that the onset of the nucleation process can move along the LP flow path in accordance with the possible operation variation in the turbine inlet steam parameters. Behind the L-1 and L-0 stages, liquid phase was observed in all measuring points along the blade height.

According to Eqs. (12)–(15), the liquid phase parameters are calculated. The Sauter mean diameter D_{32} of droplets was evaluated according to Eq. (13) from measured transmittance data. For evaluation of the corresponding steam wetness, according to Eq. (15), the values of static pressure measured by the IF-FM Gdansk were used. The obtained variation in steam wetness (fine droplets only) along the blade height with traverse coordinate is also shown in Fig. 12. The uncertainty in estimation of the steam wetness and diameter D_{32} values is about 10%.

5 Numerical Results

The presented experimental data were the basis for the CFD calculations and the validation tests. A numerical analysis was performed for the geometry of the last two stages of the five-stage LP cylinder of a 360 MW steam turbine (3000 rpm). The analyzed last two stages operate in the conditions under saturation line.

Two different measurements were performed in the power plant for the loads 300 MW (case 1) and 360 MW (case 2). In case 1, only flow parameters were measured. In case 2, the liquid phase parameters were included in the experimental study.

5.1 Test Case 1: Without Liquid Phase Measurements. The measurements in this case were made without a liquid phase probe, and only thermal and flow parameters could be compared. The turbine operated with a lower load and high condenser back pressure. Boundary conditions at the inlet were taken from the measurements and were assumed as constant along the blade length. The total temperature was $t_0 = 103\,^{\circ}\mathrm{C}$, and the total pressure $p_0 = 87$ kPa. The flow angles were assumed as the linear distribution in the radial direction: angle α changed from 62.4 deg to 80.4 deg, and β from -6 deg to 36 deg. This distribution was taken as a linear approximation of the measurement values to eliminate high changes between the measured values especially in the tip region.

Calculations were performed using the adiabatic and diabatic flow models. In the diabatic flow model, the liquid phase occurs due to the condensation process. The case called "adiabatic" flow model takes only into account gas phase, and steam under saturation line is assumed as the supercooled steam. This is a nonphysical flow model (without phase change) and steam parameters are determined by local real gas equation of state. The solution obtained from adiabatic flow model is used as initial condition for diabatic flow model calculations.

Due to the lack of information regarding the steam quality, the type of the condensation process was unknown. Theoretically, three types of flows are available: with pure homogeneous condensation when the steam is clean, with homoheterogeneous condensation for small quantity of steam, and finally with heterogeneous one when the condensation on the impurities is predominant. In all cases, the radius of impurities was $r_p = 10^{-8}$ m and the concentrations at the inlet were $n_{\mathrm{het}} = 10^{13}$ kg^{-1} and $n_{\mathrm{het}} = 10^{16}$ kg^{-1}. Impurities regarded as insoluble were taken into considerations in all calculations. There were simplifications in the geometry of the flow path. The bleed between stages was not taken into account and the tip clearances were neglected.

The calculated static pressure and flow angle distributions along the blade were compared with measurements in Fig. 7. The static pressure in the gap between stages calculated for condensation models is higher than in the experiment, but the discrepancy is not significant. The flow angle distribution obtained using the heterogeneous condensation model is similar to the experimental results. The flow angles calculated with the homogeneous and heterohomogeneous models are in this case about 10 deg higher. At the outlet, the static pressure distributions in all cases are similar but in outlet swirl angle only for the diabatic one are relatively close to the experimental data. In the measurements at the outlet, the high influence of the leakage flow at the tip is visible and this is the reason of discrepancies in this region. It should be admitted that the static pressure as the boundary condition at the outlet was assumed for calculations in the cross section located downstream from the measurement plane. It was necessary due to the too short distance between the trailing edge and the probe, not acceptable for the calculations.

The wetness fraction plots in the midspan for different condensation models are presented in Fig. 8. In this figure, the condensation onset can be easily recognized.

In the case of pure heterogeneous condensation, the liquid phase in the steam flow occurs earlier—in the end part of the

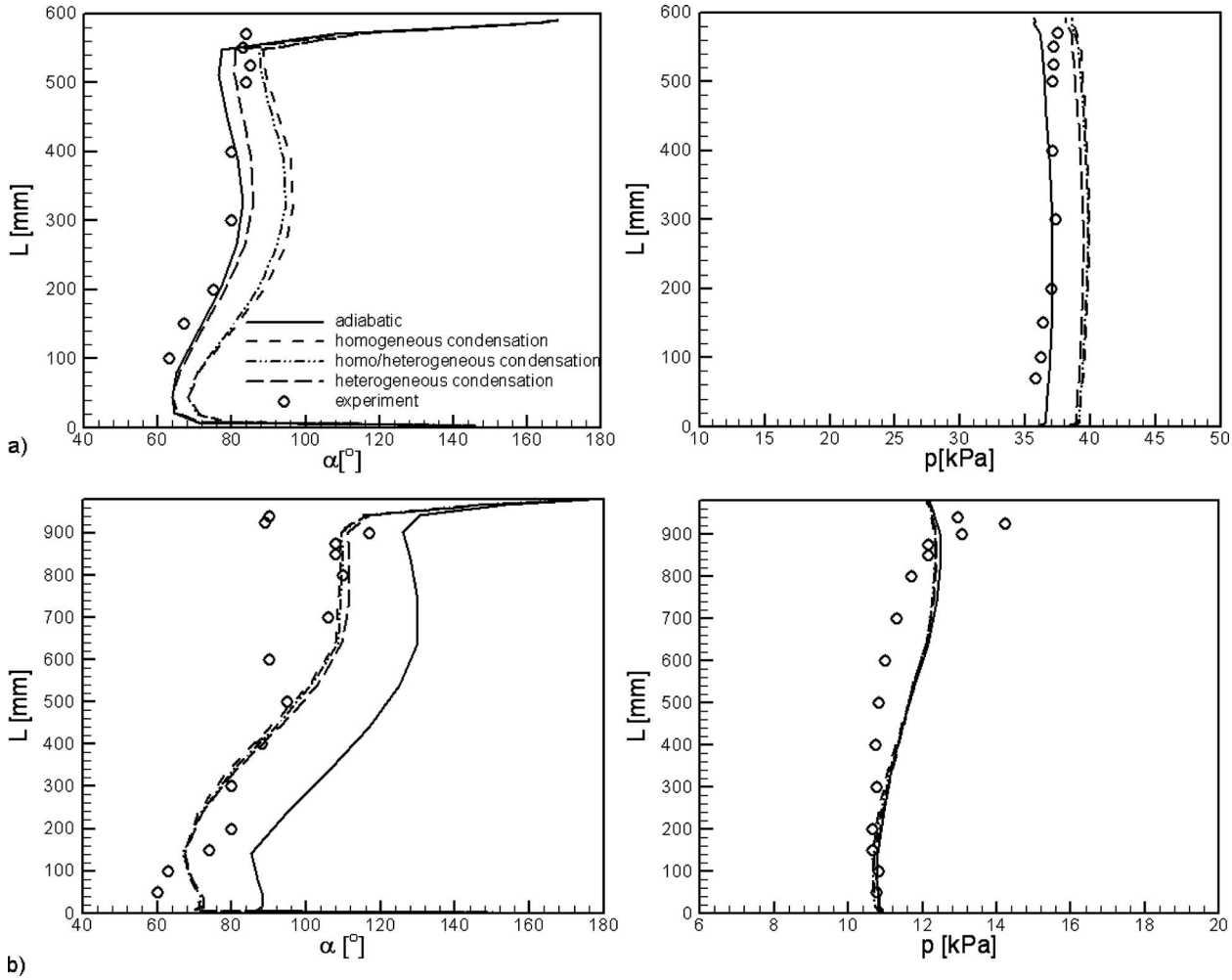

Fig. 7 Static pressure and flow angle distributions: (*a*) between the last two stages and (*b*) at the outlet

stator of penultimate stage (Fig. 8). The liquid phase appears not as rapid as in the homogeneous case. It is the reason that the thermodynamic losses are smaller. Figure 9 presents the radial distribution of circumferentially averaged wetness fraction between the stages and at the outlet. At the outlet, the wetness fraction is smaller for the homogeneous case but between the stages the values of wetness fraction are similar for homogeneous and mixed homo-/heterogeneous condensation models.

The mass flow rates were calculated in all cases and gathered in Table 1. The results obtained using the condensation models are similar and less than in the adiabatic flow model and also are less about 5% than the value estimated from the measurement data at the inlet to the penultimate stage.

This test case proves that the assumption of impurities gives better results. The fact that the condensation starts earlier in the turbine than in the case with homogeneous model only was confirmed visually during the experiments. This tendency was observed in calculations only for pure heterogeneous condensation (Figs. 8 and 9).

5.2 Test Case 2: With Liquid Phase Measurements. The boundary conditions at the inlet and outlet for TRACOFLOW CFD code were determined from the measurements for a 360 MW load, assuming that the inlet steam was superheated. For these calculations, the presence of the chemically soluble impurities was assumed. Based on the chemical analyses of the condensate samples in the condenser (Table 2), the NaCl salt concentration was assumed to be close to 2 ppb (parts per billion). It corresponds to particle concentration $n_{het}=2\times10^{14}$ kg^{-1}, and particle radius of 2 nm when clusters with 100 molecules are assumed. The similar structure of the clusters was also considered in Ref. [21]. The static outlet pressure of $p_{out}=14.3$ kPa was assumed at the midspan, as the circumferentially averaged value. The outlet conditions were assumed in the plane located downstream from the measurement plane.

Similar to the previous case, the rotor tip clearance was not modeled. The liquid phase separation in the stages was not modeled as well.

The computational domains for RANS calculations were discretized by means of the structural multiblock grid (eight blocks for each blade row). The total number of grid nodes was above 600,000. The Reynolds number calculated with the use of the total parameters at the inlet, the inlet speed of sound, and blade chord was $\mathrm{Re}=1.7\times10^{6}$.

The spanwise distributions of parameters were calculated on the basis of circumferentially mass averaged quantities at the inlet, in the gap between stages and at the outlet. For assumed concentration of salt impurities, the heterogeneous condensation was predominant in the flow. The calculated mass flow rate was 102 kg/s, that is, about 3% less than that calculated from measured data at the turbine outlet. The main cause of this discrepancy could be the circumferential outlet pressure variation, which was not taken into account in the steady-state calculations.

The distributions of the absolute angle and static pressure between the stages and at the stage outlet are presented in Fig. 10.

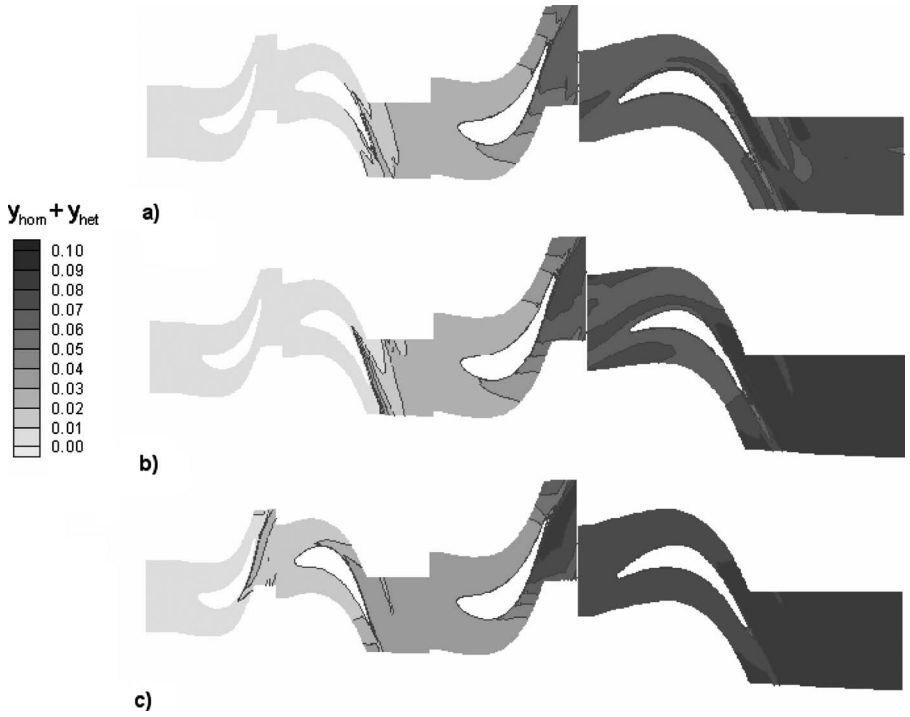

Fig. 8 Wetness fraction at the midspan section: (*a*) homogeneous, (*b*) homoheterogeneous, and (*c*) heterogeneous condensations

The numerical results are compared with the experimental data.

The calculated flow angles at the outlet coincide relatively well with the measurement data (Fig. 10(*b*)). The comparison of calculated parameters with experiment between the stages is shown in Fig. 10(*a*). The absolute outlet angle is within the range between 60 deg and 90 deg without taking into account endwall boundary layers. The maximum discrepancy between the calculated and measured values is twice as big as the measurement error. The calculated distribution of static pressure is consistent with the experiment.

To show the wet steam formation, the blade-to-blade cross sections of stages at the midspan are presented in Fig. 11. For the assumed soluble impurities in the steam, the condensation process shows homo- and heterogeneous patterns, but the second one is

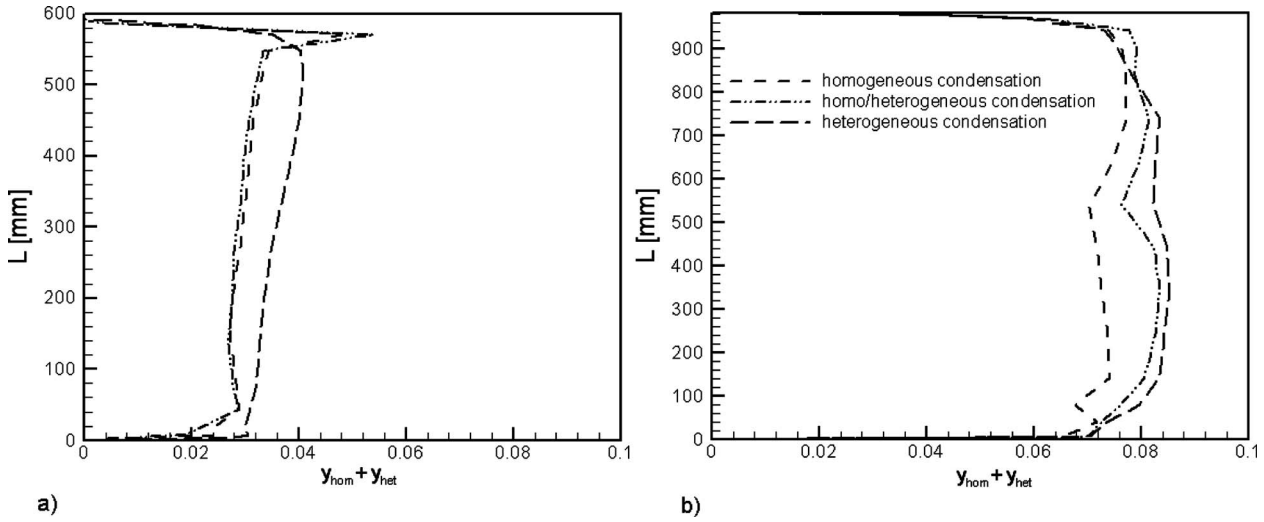

Fig. 9 Wetness fraction distributions: (*a*) between the last two stages and (*b*) at the outlet

Table 2 Results of chemical analyses of condensate samples

Notation	pH	Na^+	K^+	NH_4^+	Cl^-	SO_4^-	SiO_2	Fe
Unit	-	μg/kg	μg/kg	μg/kg	μg/kg	μg/kg	μg/kg	μg/kg
Condensate behind the LP part	8–8.4	2–3	<5	-	<2	1–2	2–3	7–8
First condensate	6.8–6.9	180	40	60	130	90	900	1200

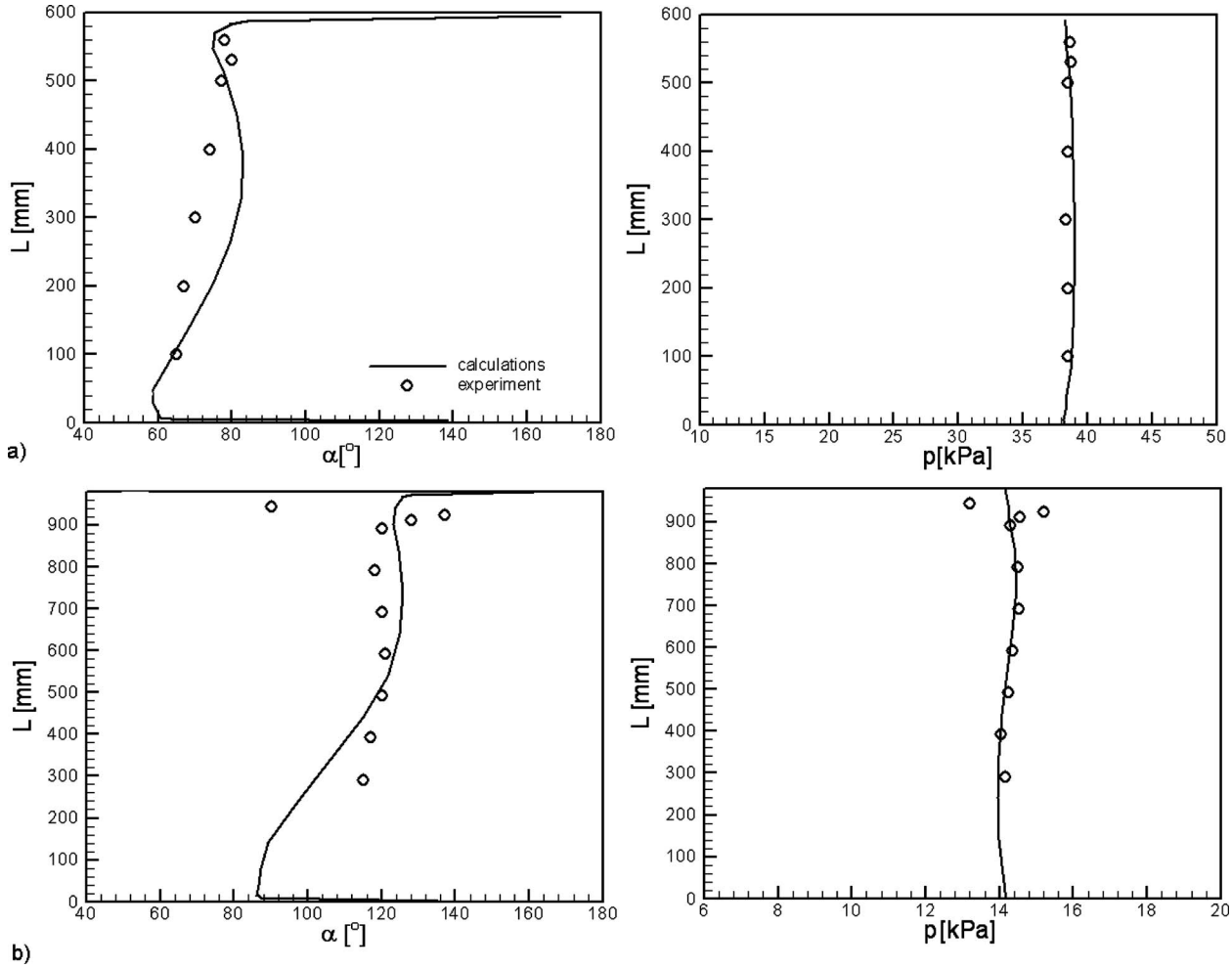

Fig. 10 Flow angle and static pressure distribution: (*a*) between the last two stages and (*b*) at the outlet

predominant. The liquid phase generated in the flow forms in 65–70% on the salt particles. The beginning of the condensation process is in the stator row of the first calculated stage (Fig. 12(*a*)). The proper conditions for the homogeneous condensation

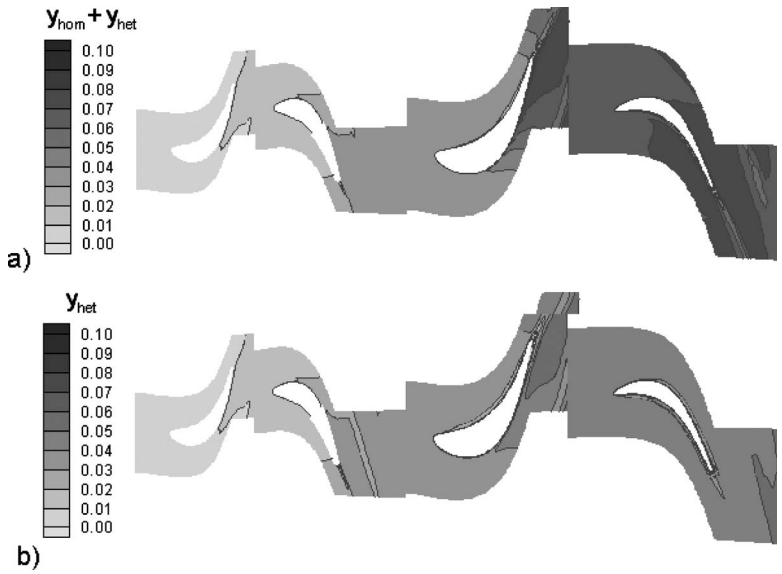

Fig. 11 Wetness fraction contours at midspan section: global wetness fraction contours (homogeneous and heterogeneous) (*a*) and wetness fraction contours generated only due to the heterogeneous condensation (*b*)

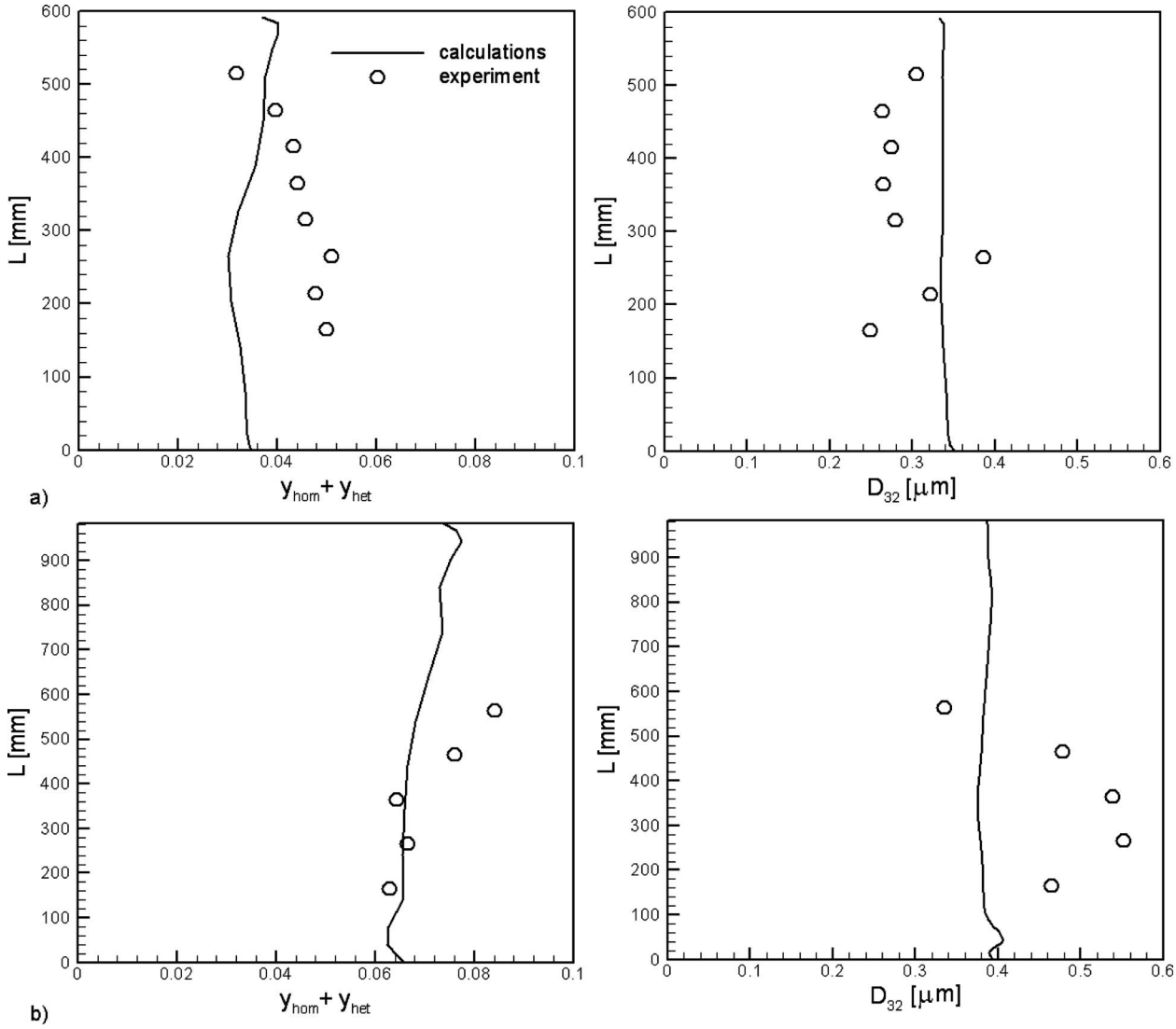

Fig. 12 Wetness fraction and mean droplet Sauter diameter: (*a*) between the last two stages and (*b*) at the outlet

are in the rotor row of the first stage as can be deduced from the wetness contours in Figs. 11(*a*) and 11(*b*). The contours are shown for the global wetness fraction obtained due to the homogeneous and heterogeneous condensation processes and for the wetness fraction generated only on the soluble particles.

The spanwise distributions of the wetness fractions and droplet radii in the gap between stages and at the stage outlet are shown together with experimental data in Fig. 12. The relatively good agreement in the wetness fraction distributions is observed below the midsection at the outlet. The calculated wetness fraction between the stages is about 30% smaller than that estimated from the experimental data. This difference is high in the midpart of the blade and decreases in the tip sections. The discrepancies at the outlet are smaller than those between the stages. This can be explained by fact that at the outlet the equilibrium in the wet steam was achieved. The simplifications in condensation models and the accuracy of the real-scale measurements bear on the discrepancies in the flow parameters between the calculations and experiment.

In Fig. 12, the spanwise distributions of the Sauter mean diameters are presented. From calculations, the volume averaged diameter is obtained; therefore, the Sauter diameter was calculated on the basis of droplet size spectrum known from experiment.

The calculated droplet radii show a more even distribution and are confined within the same range in the both sections.

6 Conclusions

The reported investigation of steam flow through the LP part of a 360 MW turbine suggests that the heterogeneous condensation might be a dominating process for the considered concentration of impurities (NaCl). This could be the reason why supercooling is not observed in the turbine, and the condensation starts practically close to the saturation line. The optical extinction test reveals that the water droplets recorded in the turbine flow can be as large as 300–500 nm in diameter. The comparison of the flow field parameters obtained by means of TRACOFLOW in-house CFD code and from experimental data shows relatively good correspondence and confirms proper modeling of the real gas properties and condensation processes in the steam flowing through the stages.

The applied CFD tool has been before thoroughly validated against laboratory experiments. It has been possible to validate the mathematical model under conditions present in the real turbine as well.

It should be emphasized that it was the first step in the comprehensive analysis of the condensation phenomena using numerical and experimental research made for the working steam turbine of large output.

Acknowledgment

The authors would like to thank the Polish Ministry of Science and Information Technology for the financial support of the Research Project No. PB 1431/T10/2004/26 and the management of the Belchatow Power Plant for the consent for onsite measurements.

Nomenclature

a_w = activity of water in solution
D = droplet diameter, m
D_{32} = Sauter mean droplet diameter, m
E = Mie extinction function
F = distribution function of diameter D, m^{-3}
h = specific enthalpy, J kg^{-1}
I_o = incident light intensity (no droplets)
I = light intensity
J = nucleation rate, m^{-3} s^{-1}
k = Boltzmann constant, J K^{-1}
l = light path length in wet steam, m
L = blade height, m
m = relative refraction index, mass, kg
$\dot{m}$ = mass flow rate, kg s^{-1}
M_l = molality, mol kg^{-1}
M_w = molal mass, kg $kmol^{-1}$
n = number of droplets, kg^{-1}
p = pressure, Pa
R = individual gas constant, J kg^{-1} K^{-1}
r = radius, m
r^* = critical radius, m
s = specific entropy, J kg^{-1} K^{-1}
T = temperature, K
u,v,w = velocity components in Cartesian coordinates, m s^{-1}
y = wetness fraction, kg kg^{-1}
Z = compressibility coefficient
x,y,z = Cartesian coordinates, m
α = inclination angle, deg
θ = circumferential angle, deg
λ = wavelength of light, m, thermal conductivity, W m^{-1} K^{-1}
ρ = density, density of the mixture, kg m^{-3}
γ = isentropic exponent
ν = specific volume, m^3 kg^{-1}
σ = surface tension, N m^{-1}

Subscripts

0 = total parameter
hom = homogeneous
het = heterogeneous
v = vapor phase
l = liquid phase
s = saturation value
w = water

References

[1] Keller, H., 1974, "Erosionkorrosion an Nassdampfturbinen," VGB Kraftwerktechnik, **54**, pp. 292–295.
[2] Jonas, O., 1985, "Steam Turbine Corrosion," Mat. Perf., **24**(2), pp. 9–18.
[3] Bakhtar, F., White, A. J., and Mashmoushy, H., 2005, "Theoretical Treatments of Two-Dimensional, Two-Phase Flows of Steam and Comparison With Cascade Measurements," Proc. Inst. Mech. Eng., Part C: J. Mech. Eng. Sci., **219**, pp. 1335–1355.
[4] Wróblewski, W., Dykas, S., and Gepert-Niedobecka, A., 2007, "Condensing Steam Flow Computations—Validation Problems," Seventh European Conference on Turbomachinery, Conference Proceedings, Athens, K. D. Papailiou, F. Martelli, and M. Manna, eds., pp. 841–848.
[5] Hesler, S., Shuster, L., and McCloskey, T., 1998, "Optical Probe of Measurement of Steam Wetness Friction in LP Turbine," *IPJC II*, ASME, New York, PWR-Vol. 33.
[6] Bakhtar, F., and Heaton, A. V., 2005, "Effects of Wake Chopping on Droplet Sizes in Steam Turbines," J. Mech. Eng. Sci., **219**(C12), pp. 1357–1367.
[7] Petr, V., Kolovratník, M., and Hanzal, V., 2003, "Instrumentation and Tests on Droplet Nucleation in LP Steam Turbines," Power Plant Chemistry, **5**(7), pp. 389–395.
[8] White, A. J., Young, J. B., and Walters, P. T., 1996, "Experimental Validation of Condensing Flow Theory for a Stationary Cascade of Steam Turbine Blade," Philos. Trans. R. Soc. London, Ser. A, **354**, pp. 59–88.
[9] Wagner, W., Cooper, J. R., Dittmann, A., Kijima, J., Kretzschmarr, H.-J., Kruse, A., Mareš, R., Oguchi, K., Sato, H., Stöcker, I., Šifner, O., Takaishi, Y., Tanishita, I., Trübenbach, J., and Willkommen, Th., 2000, "The IAPWS Industrial Formulation 1997 for the Thermodynamic Properties of Water and Steam," Trans. ASME: J. Eng. Gas Turbines Power, **122**(1), pp. 150–181.
[10] Frenkel, J., 1946, *Kinetic Theory of Liquids*, Oxford University Press, New York.
[11] Gyarmathy, G., 1960, "Grundlagen einer Theorie der Nassdampfturbine," Ph.D. thesis, ETH, Zürich.
[12] Kantrowitz, A., 1951, "Nucleation in Very Rapid Vapor Expansions," J. Chem. Phys., **19**, pp. 1097–1100.
[13] Gorbunov, B., and Hamilton, R., 1997, "Water Nucleation on Aerosol Particles Containing Both Soluble and Insoluble Substances," J. Aerosol Sci., **28**(2), pp. 239–248.
[14] Dykas, S., 2001, "Numerical Calculation of the Steam Condensing Flow," Task Quarterly, Scientific Bulletin of Academic Computer Centre in Gdansk, **5**(4), pp. 495–519.
[15] Wróblewski, W., Dykas, S., and Gepert, A., 2006, "Modeling of Steam Flow With Heterogeneous Condensation," *Monografia 95*, Wydawnictwo Politechniki Śląskiej, Gliwice, in Polish.
[16] Lagun, V. P., Simoyu, L. L., and Frumin, Yu. Z., 1975, "Full-Scale Tests of the Exhaust Hoods of a High-Capacity Steam Turbine," Teploenergetika (Moscow, Russ. Fed.), **22**(2), pp. 31–35.
[17] Gardzilewicz, A., and Marcinkowski, S., 1995, "Diagnosis of LP Steam Turbine Prospects of Measuring Techniques," Proceedings of the ASME Joint Power Generation Conference, Vol. 3, pp. 349–358.
[18] Gardzilewicz, A., Marcinkowski, S., Karwacki, J., and Kurant, B., 2006, "Results of Measurements of Condensing Steam Flow in LP Part of Turbine 18 K in Belchatow Power Plant," IF-FM Report Nos. 5681 and 6157.
[19] Steltz, W., Lindsay, P., and Lee, W., 1983, "The Verification of Concentrated Impurities in Low Pressure Steam Turbine," ASME Winter Meeting, WA.
[20] Svododa, R., Phlug, H.-D., and Warnecke, T., 2003,"Investigation into the Composition of the Early Condensate in Steam Turbines," Power Plant Chemistry GmbH, Neulusshei.
[21] Petr, V., and Kolovratnik, M., 2001, "Heterogeneous Effects in the Droplet Nucleation Process in LP Steam Turbines," Proceedings of the Fourth European Conference on Turbomachinery, Florence, Italy, pp. 783–792.

The Effects of Inlet Geometry and Gas-Liquid Mixing on Two-Phase Flow in Microchannels

M. Kawaji[1]
Department of Chemical Engineering and Applied Chemistry,
University of Toronto,
200 College Street,
Toronto, ON, M5S 3E5, Canada

K. Mori
Department of Mechanical Engineering,
Osaka Electro-Communication University,
18-8 Hatsu-cho,
Neyagawa, Osaka, Japan 572-8530

D. Bolintineanu
Department of Chemical Engineering and Applied Chemistry,
University of Toronto,
200 College Street,
Toronto, ON, M5S 3E5, Canada

The effects of gas-liquid inlet geometry and mixing method on adiabatic gas-liquid two-phase flow in a microchannel of 100 μm diameter have been investigated using a T-junction inlet with the same internal diameter as the microchannel. Two-phase flow patterns, void fraction, and friction pressure drop data obtained with the T-junction inlet were found to be significantly different from those obtained previously with a reducer inlet. For the T-junction inlet, the two-phase flow patterns in the microchannel were predominantly intermittent flows with short gas and liquid plugs/slugs flowing with nearly equal velocities. The void fraction data then conformed nearly to that of a homogeneous flow model, and the two-phase friction multiplier data could be described by the Lockhart–Martinelli correlation applicable to larger channels. However, when a reducer inlet was used previously and the diameter of the inlet section was much larger than that of the microchannel, an intermittent flow of long gas slugs separated by long liquid slugs became prevalent and the void fraction decreased to values far below the homogeneous void fraction. The differences in the two-phase flow characteristics between a T-junction inlet and reducer inlet were attributed to the differences in the gas bubble/slug generation mechanisms. [DOI: 10.1115/1.3089543]

1 Introduction

Few two-phase flow studies are yet available in the literature that involved a microchannel diameter of 100 μm or less as noted in recent reviews by Serizawa [1] and Thome [2]. The available results for microchannels have shown certain differences from those for conventional channels: bubbly and droplet flows may not always occur in microchannels, the void fraction data in microchannels may deviate from the Armand correlation [3] and the two-phase friction pressure drop in microchannels could be predicted by conventional models.

The available results also indicate that the adiabatic two-phase flow characteristics in the same microchannel such as flow patterns, void fraction, and friction pressure drop can vary significantly depending on the microchannel inlet configuration and the gas-liquid mixing method, unlike in minichannels and conventional channels.

Stanley et al. [4] investigated two-phase pressure drop and heat transfer in the square and rectangular aluminum channels of hydraulic diameters D_h ranging from 56 μm to 256 μm. They mixed water with argon, helium, or nitrogen gas upstream of the microchannel and injected the two-phase mixture from a $\frac{1}{4}$ in. tube into the microchannel test section, so the inlet was a reducer with sudden reduction in diameter from $\frac{1}{4}$ in. to 56–256 μm. They reported that the conventional semi-empirical correlations for two-phase pressure drop overpredicted their microchannel data substantially.

Air-water two-phase flow experiments were conducted in 25 μm and 100 μm circular microchannels connected to a reducer-type inlet by Serizawa and co-workers [5,6]. Five flow patterns were observed: dispersed bubbly flow, gas slug flow, liquid-ring flow, liquid lump flow, and liquid droplet flow. The occurrence of liquid-ring flow and liquid lump flow clearly indicated that there are differences in the flow patterns between microchannels of $D \leq 100$ μm and minichannels of $D \geq 1$ mm.

Kawaji and co-workers [7,8] investigated the two-phase flow of nitrogen gas and water through horizontal circular microchannels of 50–250 μm diameter. The gas and liquid were mixed in a reducer inlet where the diameter changed from 750 μm down to the microchannel diameter. They reported significant differences in the flow pattern maps and void fraction data from those previously described for minichannels with diameters above ~1 mm. In particular, they reported the existence of flow patterns unique to microchannels (liquid-ring flow and serpentinelike gas core flow). Furthermore, the time-average void fraction data deviated from Armand's correlation [3], which is normally applicable to minichannels with diameters ~1 mm. This was in contrast with the void fraction data of Serizawa et al. [6] for a 20 μm circular microchannel, which could be well described by Armand's type correlation.

Chung et al. [9] later found that the two-phase flow characteristics in a 96 μm square channel and a 100 μm circular channel connected to the same reducer inlet used by Kawahara et al. [7] were quite similar and independent of the channel cross section for a mixture of nitrogen gas and water. Furthermore, Kawahara et al. [10] found only a moderate effect of fluid properties such as liquid viscosity and surface tension on the two-phase flow characteristics in a microchannel.

Besides the reducer-type inlet, several different inlet designs and gas-liquid mixing methods have been used to inject a two-phase mixture into a microchannel. A simple T-junction has also been popular particularly for microfluidic applications as used by Thorsen et al. [11], Okushima et al. [12], Günther et al. [13], Xu et al. [14], Garstecki et al. [15], and Ide et al. [16], among others. In many cases, the T-junction diameter was the same as or close to the microchannel diameter, and its use was intended to produce monodisperse microbubbles. On the other hand, a much larger (1/8 in.) diameter T-junction was used by Xiong and Chung [17] upstream of a rectangular microchannel. The gas was injected into the liquid stream through a 200 μm diameter needle, which was inserted from the branch of the T-junction so that the needle tip would be positioned in the middle of the T-junction.

[1]Corresponding author.

Contributed by the Fluids Engineering Division of ASME for publication in the JOURNAL OF FLUIDS ENGINEERING. Manuscript received October 8, 2007, final manuscript received January 19, 2009; published online March 11, 2009. Assoc. Editor: Theodore Heindel. Paper presented at the Third International Conference on Microchannels and Minichannels (ICMM2005), Toronto, ON, Canada, June 13–15, 2005.

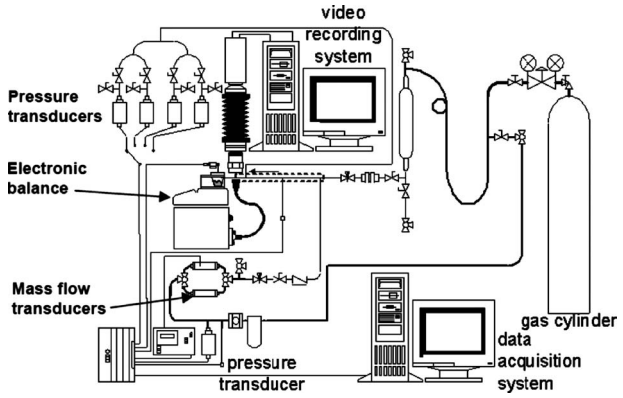

Fig. 1 Experimental apparatus

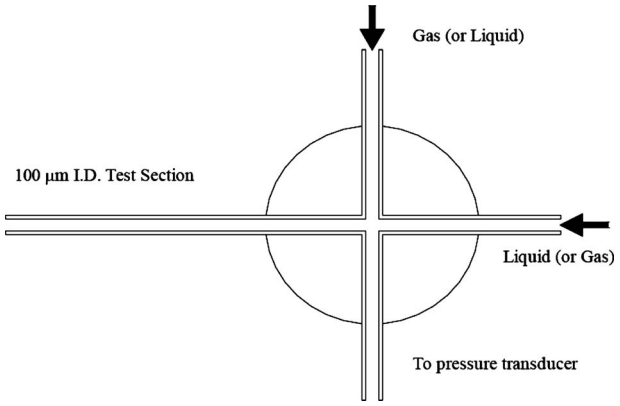

Fig. 2 Gas-liquid mixing at the microchannel inlet

In recent experiments, Yue et al. [18] used a Y-junction connected to square microchannels with 200 μm and 400 μm hydraulic diameters to absorb CO_2 gas into a water stream. Another inlet geometry used in the past involved a flow focusing method in a cross junction by Gañán-Calvo and Gordillo [19], Cubaud and Ho [20], and Garstecki et al. [21], where the gas flowed straight through the main line into the microchannel and liquid was injected from the sides through two branches at equal flow rates. This way, the gas stream could be pinched off to generate discrete small gas bubbles, short plugs, or long slugs depending on the gas and liquid injection rates. Another variation of the T-junction inlet was used by Waelchli and von Rohr [22], who injected gas and liquid streams from the opposite ends of the main channel. The two phases mixed at the T-junction where several 50 μm diameter round pins were placed to serve as a static mixer, and then the mixture flowed into the branch line connected to a microchannel.

As reviewed above, different types of inlet and gas-liquid mixing methods have been used in adiabatic two-phase flow experiments in microchannels, but no systematic comparisons of the two-phase flow characteristics have been carried out. Some of the results in the literature have shown significant differences, but the diameters of the microchannels were not the same, so the effects of the inlet geometry and mixing method cannot be readily isolated from those of the microchannel diameter. Hence, the objective of this work was to investigate the effect of the inlet geometry using the same microchannel of $\sim$100 μm diameter and identify the key reasons for differences in the two-phase flow characteristics observed in the microchannel. The same experimental apparatus and approach used by Kawahara et al. [7] and Chung and Kawaji [8] have been used again with the same microchannel but different inlet designs and gas-liquid mixing configurations.

Since there is no phase change heat transfer involved in this work, the results are not directly applicable to heat exchangers. Most relevant applications would be in microreactors in which gas and liquid streams are contacted in a microchannel to effect gas absorption with or without a chemical reaction. In the design of such microreactors, the gas-liquid inlet and mixing method can be chosen from a T-junction, Y-junction, co-axial reducer, cross junction, and others. Thus, it would be useful to understand better how the two-phase flow characteristics are affected by the inlet geometry and gas-liquid mixing method.

2 Experimental Apparatus and Data Analysis

Details of the present experiments are explained briefly. The reader can refer to Kawahara et al. [7] and Chung and Kawaji [8] for additional information not given here. Figure 1 illustrates the experimental apparatus used. De-ionized water was driven through the horizontal microchannel by a pneumatic-type pump after being mixed with nitrogen gas from a pressurized cylinder.

For the microchannel inlet, a Valco Nanovolume® four-way cross connector with an inner bore diameter of 100 μm was used to directly connect the microchannel test section to the gas and liquid injection lines as shown in Fig. 2. The fourth line was connected to a pressure transducer to measure the test section inlet pressure, so the inlet was effectively a T-junction. To study the effect of gas-liquid injection schemes for the T-junction inlet, two configurations were tested.

(1) Configuration 1 (ConFig 1): liquid injected into the main channel and gas injected into the branch
(2) Configuration 2 (ConFig 2): gas injected into the main channel and liquid injected into the branch.

In both configurations, mixing of the gas and liquid phases took place inside the 100 μm diameter junction immediately before the microchannel test section. Thus, there was no change in the tubing diameter between the gas-liquid mixing section and the microchannel test section.

Figure 3 illustrates the reducer inlet used previously by Kawahara et al. [7] and Chung and Kawaji [8] to mix the gas and liquid phases upstream of a microchannel. Liquid was injected through a 500 μm ID tube, while gas was injected through a 200 μm annular gap. The two streams mixed by flowing collectively into a 500 μm ID tube that was connected to a 250 μm ID T-junction for pressure measurement just upstream of the microchannel test section. The two-phase mixture thus flowed through 750 μm and 500 μm diameter tube sections before entering the 250 μm diameter T-junction and finally into the 100 μm diameter test section.

A circular microchannel (fused silica capillary tubing with standard polyimide coating from Polymicro Technologies, Phoenix, AZ) with an inner diameter of 100 μm used by Kawahara et al. [7] was again used in the present experiments. The total length of the test section from the gas-liquid mixing point to the exit of the microchannel was 65 mm. A sufficiently large length-to-diameter ratio (L/D=650) was used to diminish the entrance and exit ef-

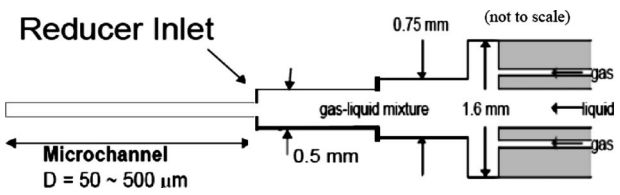

Fig. 3 Reducer inlet and mixer used by Kawahara et al. [7] and Chung and Kawaji [8]

Table 1 Measurement uncertainties

Parameters	Uncertainty range
Mass flow rate of liquid, m_L	$\pm 0.1\%$ to $\pm 1\%$
Mass flow rate of gas, m_G	$\pm 1\%$ to $\pm 10\%$
Superficial liquid velocity, j_L	$\pm 2.1\%$ to $\pm 3\%$
Superficial gas velocity, j_G	$\pm 3\%$ to $\pm 12\%$
Void fraction, ε	$\pm$ 0.05
Total two-phase pressure gradient, $(\Delta P/\Delta Z)$	$\pm 1\%$ to $\pm 4\%$
Two-phase frictional pressure gradient, $(\Delta P_f/\Delta Z)_{\mathrm{TP}}$	$\pm 2\%$ to $\pm 7\%$
Two-phase friction multiplier, ϕ_L^2	$\pm 2\%$ to $\pm 7\%$

fects. The window for flow visualization was located as far back as possible (46.1 mm from the gas-liquid mixing point) on the microchannel to achieve a well-developed flow.

Three pressure transducers (PX303 series from Omega Engineering (Stamford, CT)) covering different ranges (3450 ± 8.6 kPa, 690 ± 1.7 kPa, and 210 ± 0.52 kPa) were used to measure the pressure drop between the microchannel inlet and outlet. The liquid was discharged freely from the test section, so that the pressure was atmospheric and temperature ambient at the microchannel outlet.

The liquid flow rate was determined by using a load cell (50.97 ± 0.255 g, model ELJ-0.5N from Entran Devices (Fairfield, NJ)) to weigh the discharged liquid collected over time. The gas flow rate was measured using three mass flow meters (model 179A-23012 from MKS Instruments (Andover, MA), and models 8172-0411 and 8172-0451 from Matheson Gas Products (Montgomeryville, PA)) to encompass a wide range of conditions (1 ± 0.01 sccm, 10 ± 0.1 sccm, and 50 ± 0.5 sccm). The analog signals for all of the pressure, temperature, and mass flow rate readings were sampled at 10 Hz by a 16-bit data acquisition system (model NI 6035E from National Instruments (Austin, TX)).

Background illumination to see the flow patterns was generated by a cold lamp (model DCR III from Schott-Fostec (Auburn, NY)) located behind the test section. The view field was magnified by attaching a 20× microscope objective lens (model 378-802-2 from Mitsutoyo America Corporation (Aurora, IL)) to the video camera. A monochrome CCD camera (model TM-1040 from Pulnix America (Sunnyvale, CA)) with a resolution of $1024(\mathrm{H}) \times 1024(\mathrm{V})$ pixels, a maximum frame rate of 30 fps, and a shutter speed of 1/16,000 s was used for image capturing. The problem of optical distortion was dealt with earlier by Kawahara et al. [7]. They elected to not correct for optical distortion so that the images of the gas-liquid interfacial structure near the channel wall could be enlarged and better examined. Likewise, optical distortion is not addressed here for the same reason.

The previous experiments covered a range of $0.01 \leq j_L \leq 5.77$ m/s for the superficial liquid velocity and $0.02 \leq j_{G,\mathrm{avg}} \leq 73$ m/s for the average superficial gas velocity. The new experiments covered slightly smaller ranges: $0.027 \leq j_L \leq 2.05$ m/s and $0.1 \leq j_{G,\mathrm{avg}} \leq 50$ m/s. The values of dimensionless parameters calculated for the previous experiments are the Bond number ($0.000083 \leq \mathrm{Bo} \leq 0.0095$), the superficial Weber number for liquid ($0.00057 \leq \mathrm{We}_{LS} \leq 116$) and gas ($0.0000020 \leq \mathrm{We}_{GS} \leq 12$), the superficial Reynolds number for liquid ($2 \leq \mathrm{Re}_{LS} \leq 2300$) and gas ($0.4 \leq \mathrm{Re}_{GS} \leq 751$), and the capillary number ($0.00013 \leq \mathrm{Ca}_L \leq 0.070$). These values indicate the relative magnitudes of the forces involved (inertia > surface tension > viscous force > gravity).

2.1 Measurement Uncertainties and Data Analyses. The measurement uncertainties estimated for the present experiments are summarized in Table 1. A propagation of error analysis [23] was performed to estimate the uncertainties in the derived quantities such as superficial velocities, void fraction, and pressure gradients.

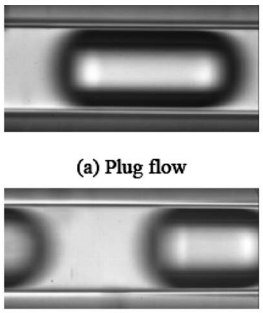

(a) Plug flow

(b) Plug flow with two gas plugs separated by a short liquid slug

(c) Slug flow with a ring-shaped liquid film around a gas core

(d) Semi-annular flow (short liquid slugs existed between long gas slugs)

Fig. 4 Two-phase flow patterns observed in a microchannel with a micro-T-junction inlet

Initially, experiments were conducted with de-ionized water to calculate the single-phase friction factor from the frictional pressure drop. The computed friction factor was compared with the conventional value for laminar flow in a pipe. The two-phase frictional pressure drop was calculated by subtracting estimates of the pressure drop due to inlet contraction and flow acceleration from the total pressure drop measured in the horizontal channel. To estimate the pressure drop attributed to the acceleration of the flow, the void fraction at the inlet and outlet of the test section was estimated based on the homogeneous flow model.

3 Results and Discussion

The experimental results on the two-phase flow patterns, void fraction, and two-phase friction pressure drop obtained with a T-junction inlet will be presented and compared with those reported previously by Kawahara et al. [7] for a reducer inlet to determine the effects of inlet geometry and gas-liquid mixing method.

3.1 Two-Phase Flow Patterns. The two-phase flow patterns obtained in the present experiments are found to be quite different from those observed in our previous work. Typical examples of the flow patterns seen in the present experiments for both Configurations 1 and 2 are shown in Fig. 4. Short gas bubbles or plugs such as those shown in Figs. 4(*a*) and 4(*b*) were seldom observed in the previous experiments using a series of reducer sections between the gas-liquid mixer and the microchannel test section. Instead, slug flows with a long gas core shown in Fig. 4(*c*) and surrounded by a thin, thick, or wavy liquid film were predominant. Thus, the flow patterns observed in the present experiments were classified differently from the previous experiments and according to the following definitions.

(1) Bubbly flow: the presence of spherical bubbles whose diameters are less than the diameter of the microchannel
(2) Plug flow: the presence of gas plugs that are shorter than the width of the viewing window (~250 μm) and are separated by liquid bridges

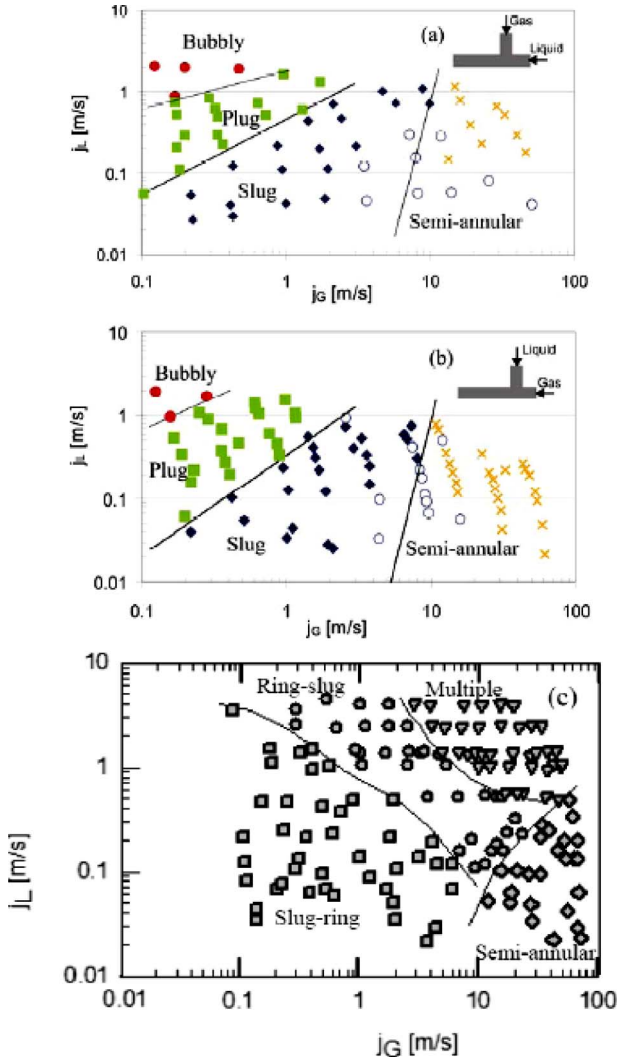

Fig. 5 Two-phase flow pattern maps for a micro-T-junction inlet (*a*) ConFig. 1 and (*b*) ConFig. 2, and (*c*) a reducer inlet used by Kawahara et al. [7] (an open circle indicates the occasional appearance of a ring-film flow pattern)

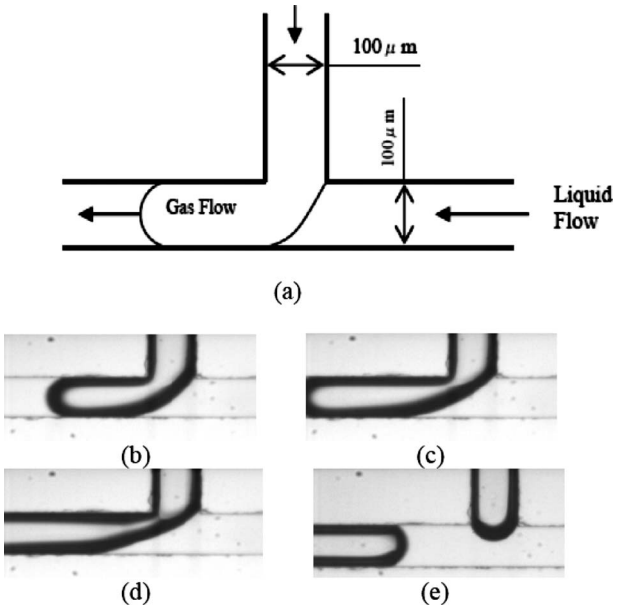

Fig. 6 Sequence of images showing gas plug generation at a micro-T-junction (from Ref. [24])

(3) Slug flow: the presence of gas slugs that are longer than the viewing window
(4) Semi-annular flow: long gas core surrounded by a liquid film and interrupted by infrequent liquid slugs
(5) Ring flow: 10% or more of the images for a given run have a ring-shaped liquid film surrounding the gas core

The two-phase flow pattern maps were then constructed based on the above definitions for the two T-junction inlet configurations as shown in Fig. 5. At low superficial gas velocities $j_G < 1$ m/s, bubbly flow, plug flow, and slug flow patterns appeared at progressively lower liquid flow rates. At moderate to high superficial gas velocities $j_G > 2$ m/s, slug and semi-annular flow patterns were observed. An open circle (○) in Figs. 5(*a*) and 5(*b*) indicates the occasional appearance of a ring-film flow pattern.

The difference in the gas and liquid injection configurations for the micro-T-junction inlet had only a small effect on the flow pattern map as clear from a comparison of Fig. 5(*a*) and 5(*b*). However, these results for the micro-T-junction inlet were significantly different from the map previously obtained for a reducer inlet case by Kawahara et al. [7] and shown in Fig. 5(*c*). When the inlet section consisted of a series of reducer sections from 750 μm to 100 μm (Fig. 2), the predominant flow pattern observed was a slug flow with a long gas core surrounded by a thin, thick or ring-shaped film. Depending on the frequency of the appearance of different liquid film shapes, the flow patterns were defined as slug-ring, ring-slug, and multiple flows (Fig. 5(*c*)).

Although a semi-annular flow pattern was observed in both micro-T-junction and reducer inlet experiments, a strong difference existed between them in the appearance of short gas bubbles and plugs. This is due to the fact that small gas bubbles are readily created at the T-junction inlet as reported in previous studies. The mechanism of small gas bubble generation at the micro-T-junction can be readily illustrated as shown in Fig. 6. Such a mechanism had been previously investigated for the ConFig. 1 case (liquid injected into the main channel while gas is injected into the branch, Fig. 6(*a*)) by Shibata et al. [24]. Short gas plugs were observed to be generated as a result of interfacial instability or pinch-off at the corner of the T-junction as shown in Figs. 6(*b*)–6(*e*).

Although no flow visualization was conducted for ConFig. 2, a similar interfacial instability or pinching off of a gas bubble or plug at the micro-T-junction can be conjectured. Thus, regardless of which phase is injected into the main channel or the branch, the use of a T-junction to mix and inject the gas-liquid mixture into a microchannel can result in two-phase flow patterns that are very different from those observed in the reducer inlet case. The larger inlet cross section ($D = 750$ μm) for the reducer inlet used by Kawahara et al. [7] would allow larger gas bubbles to form upstream of the microchannel test section. When these gas bubbles flow into the microchannel with a much smaller diameter ($D = 100$ μm), the gas slug length would increase by more than 50 times, as illustrated in Fig. 7. Thus, for example, if the diameter of the gas bubble formed in the inlet section were 2 mm, then it would form a 100 mm long gas slug in the microchannel. This can explain why Kawahara et al. [7] obtained mostly long gas core flows with a reducer inlet rather than short gas plug flows.

The present flow pattern results obtained with a T-junction inlet are now compared with the previous results obtained with other types of inlet as shown in Fig. 8. Only the bubbly-to-plug (or slug) and slug-to-annular (or semi-annular) flow pattern transition boundaries are indicated. Although the transition boundaries are represented by thin lines, the flow patterns did not change as sharply as suggested by those lines. Nevertheless, the present

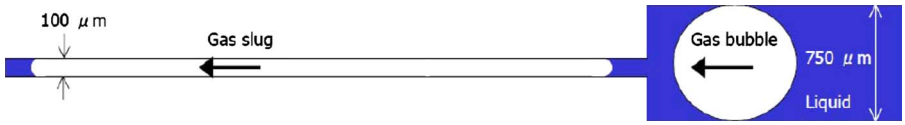

Fig. 7 Formation of a long gas slug from a bubble in a reducer inlet (not to scale)

T-junction inlet results are in general agreement with previous studies for both bubbly-to-slug and slug-to-annular flow transition boundaries.

It is noted in Fig. 8 that unlike the reducer inlet results obtained by Kawahara et al. [7], the flow pattern transition boundaries obtained by Serizawa et al. [6] are in agreement with the T-junction inlet results. This may be attributed to the small diameter of the gas injection nozzle (D=40 μm) used within the 300 μm diameter reducer inlet section, which was connected to a 25 μm diameter microchannel. The size of the gas bubbles generated could have been much smaller than the internal diameter of the reducer due to the small size of the gas injection nozzle and the effect of co-axially flowing liquid, so the phenomenon illustrated in Fig. 7 may not have occurred in the experiments of Serizawa et al. [6].

3.2 Void Fraction. The differences in the two-phase flow patterns obtained in microchannels with a T-junction inlet and reducer inlet can also cause large differences in the void fraction as discussed below. To estimate the void fraction in the 100 μm microchannel, about 300 video images were analyzed for each run. The instantaneous void fraction was estimated for plug flow images such as those shown in Fig. 4 by measuring the length of a gas bubble or plug and calculating the volume by assuming a cylindrical shape with semispherical caps. The instantaneous void fraction was then computed as the ratio of the gas volume to the total channel volume within the viewing window. The images were assigned a void fraction of zero when they showed only the liquid flowing alone in the entire view window or a void fraction of unity when they showed a continuous gas core with a thin-smooth liquid film or ring-shaped liquid film. The time-averaged void fraction was then obtained by averaging the instantaneous void fraction values from about 300 images. The effect of optical distortion on the above-mentioned method of measuring the void fraction, particularly for long gas core flows with ring-shaped films and thick liquid films, was previously addressed by Kawahara et al. [7].

The time-averaged void fraction (ε) data for the T-junction inlet are plotted against the volumetric quality $\beta(=(J_G/J_G+J_L))$ in Figs. 9 and 10 for Configurations 1 and 2, respectively. The homogeneous flow model ($\varepsilon=\beta$) and the Armand correlation [3] for narrow channels recommended by Ali et al. [25] are also shown in the figures, respectively. Ali et al. [25] recommended using a correlation of the form ($\varepsilon=0.8\beta$) originally developed by Armand [3] for narrow rectangular channels with $D_H \sim 1$ mm.

Both Configurations 1 and 2 data show a linear relationship between the void fraction and volumetric quality, consistent with the homogeneous flow model and Armand's correlation, but unlike the nonlinear relationship obtained by Kawahara et al. [7] for the reducer inlet case and given by

$$\varepsilon = \frac{0.03\beta^{0.5}}{1 - 0.97\beta^{0.5}} \tag{1}$$

Equation (1) indicates the void fraction to increase slowly with increasing volumetric quality and then exponentially after $\beta \cong 0.8$. This trend implies a strong departure from homogeneous flow and indicates a large velocity slip between the liquid and gas phases.

Thus, as the inlet geometry was changed from a reducer to T-junction, the two-phase flow patterns in the microchannel changed and this also strongly affected the time-average void fraction. For example, a plug flow pattern with alternating passages of

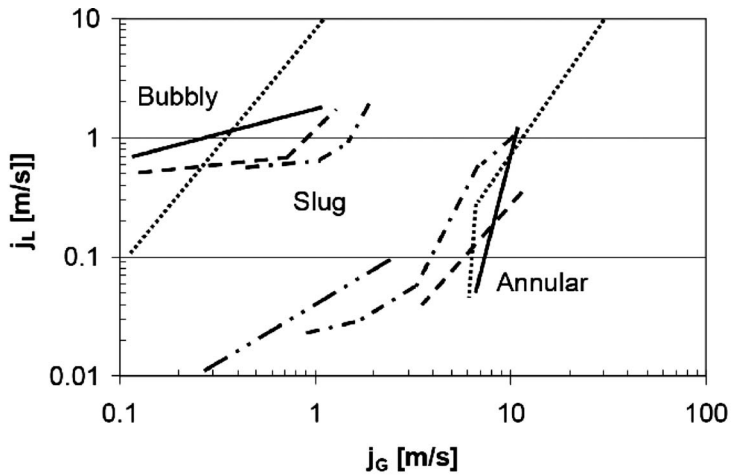

Line	*Authors*	*Inlet Type*	*Microchannel Shape*	*Hydraulic Diameter (μm)*
———	Present	T-junction	Circular	100
·····	Serizawa et al. [6]	Reducer	Circular	25
— · —	Cubaud and Ho [20]	Cross	Rectangular	200
— · · —	Waelchli and von Rohr [22]	T-junction	Rectangular	187
– – –	Yue et al. [18]	Y-junction	Rectangular	200

Fig. 8 Comparison of flow pattern transition boundaries

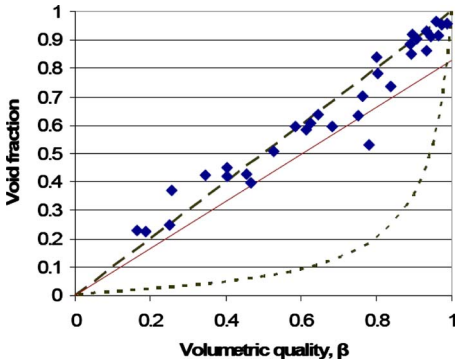

Fig. 9 Void fraction data for Configuration 1 of the T-junction inlet; (– – –) homogeneous model ($\varepsilon=\beta$), (——) Armand correlation ($\varepsilon=0.833\beta$), and (----) Eq. (1))

short gas and liquid plugs as shown in Fig. 4 would lead to a slip ratio close to unity, which is representative of a homogeneous flow. Since such a plug flow pattern was not observed in the reducer inlet case, the void fraction deviated strongly from the homogeneous flow model in the experiments of Kawahara et al. [7]. The present data show that the inlet geometry and the method of gas-liquid mixing can drastically change the time-average void fraction for the same microchannel at given superficial gas and liquid velocities.

3.3 Friction Pressure Drop. The two-phase friction pressure drop was evaluated from the measured total pressure drop by subtracting the acceleration pressure drop. The data were correlated using the Lockhart–Martinelli correlation [26], which was developed based on a separated flow assumption. This correlation uses a two-phase friction multiplier ϕ_L^2 defined as follows:

$$\left(\frac{\Delta P_f}{\Delta Z}\right)_{\mathrm{TP}} = \phi_L^2\left(\frac{\Delta P_f}{\Delta Z}\right)_L \tag{2}$$

where $(\Delta P_f/\Delta Z)_L$ is the frictional pressure drop when liquid is assumed to flow alone in the channel.

The two-phase friction multiplier has been correlated in terms of the Lockhart–Martinelli parameter X given by

$$X^2 = \frac{(\Delta P_f/\Delta Z)_L}{(\Delta P_f/\Delta Z)_G} \tag{3}$$

where $(\Delta P_f/\Delta Z)_G$ is the frictional pressure drop when the gas is assumed to flow alone in the channel. A widely used correlation to calculate the friction multiplier is that proposed by Chisholm and Laird [27].

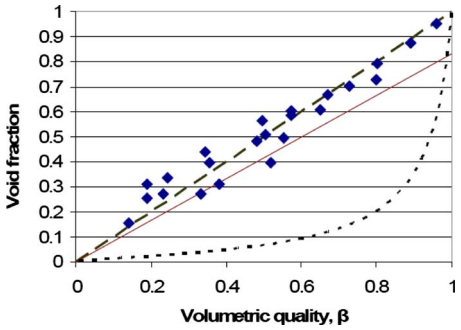

Fig. 10 Void fraction data for Configuration 2 of the T-junction inlet; (– – –) homogeneous model ($\varepsilon=\beta$), (——) Armand correlation ($\varepsilon=0.833\beta$), (----) (Eq. (1))

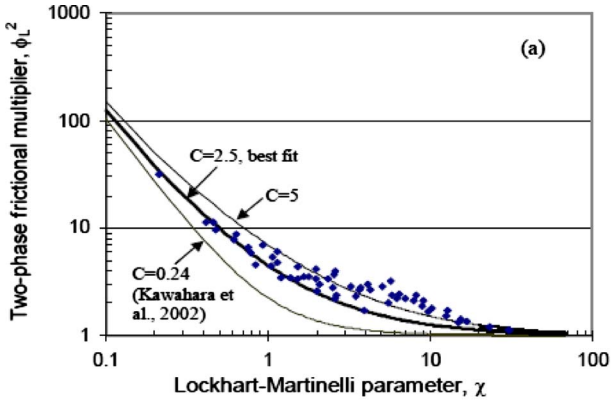

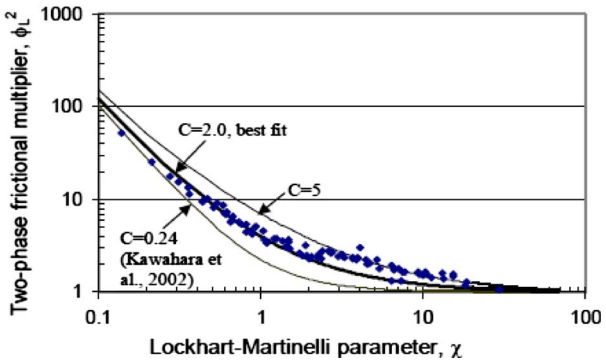

Fig. 11 Two-phase friction multiplier data for (*a*) ConFig. 1 and (*b*) ConFig. 2 of the T-Junction Inlet

$$\phi_L^2 = 1 + \frac{C}{X} + \frac{1}{X^2} \tag{4}$$

where the coefficient C is a constant ranging in value from 5 to 20 for larger channels, depending on whether the liquid and gas flows are laminar or turbulent. In conventional channels and minichannels, a strong mass velocity effect has been observed in the two-phase friction multiplier data [25], because the flow can change from laminar to turbulent as the total mass velocity is increased. The C-value in Eq. (4) is also known to decrease as the channel's hydraulic diameter is reduced [28,29].

The two-phase friction multiplier data obtained with a T-junction inlet in the present experiments are compared with the Lockhart–Martinelli correlation in Fig. 11. Also shown are the curves given by Eq. (4) with $C=5$ and the best fit values of $C=2.0$ and 2.5 for the present experiments, as well as $C=0.24$ for the reducer inlet experiments obtained by Kawahara et al. [7]. Overall, the Lockhart–Martinelli model with properly chosen values of C can be used to predict the two-phase friction multiplier data reasonably well for the T-junction inlet experiments. Switching the gas and liquid injection lines in the T-junction (Configurations 1 and 2) is seen to have only a minor effect.

The data from the T-junction inlet experiments for both Configurations 1 and 2 can be represented by different C-value curves depending on the range of the Lockhart–Martinelli parameter ($C=2.0$ or 2.5 for $X<2$, and $C=5$ for $X>3$). These C-values are more than ten times greater than the value of $C(=0.24)$, obtained for the reducer inlet by Kawahara et al. [7]. Although not shown here, only small deviations from the $C=0.24$ curve were seen for the reducer inlet data for comparable ranges of gas and liquid flow rates tested [7]. This is likely to be due to a greater variety of flow patterns observed in the T-junction inlet experiments described earlier. Thus, as in the void fraction data, the two-phase friction

pressure drop could be significantly different between the T-junction and the reducer inlet cases indicating the strong effect of the inlet geometry.

4 Conclusion

The effects of inlet geometry and gas-liquid injection method on adiabatic two-phase flow in a 100 μm microchannel have been investigated experimentally. Nitrogen gas and water were injected into a micro-T-junction with the same diameter as the microchannel connected downstream. The two-phase flow patterns observed have been found to differ strongly from those obtained in a previous study using a reducer inlet and a 750 μm diameter mixing section. For the micro-T-junction inlet, plug and slug flows with alternating short gas plugs and liquid slugs were observed, which were rarely observed in the reducer inlet case.

Due to the obvious differences in the flow patterns observed, the void fraction data for the micro-T-junction inlet case agreed with the homogeneous flow model, unlike the data obtained with a reducer inlet with a 750 μm diameter mixing section. The two-phase friction multiplier data could be well correlated in terms of the Lockhart–Martinelli parameter but the value of the constant C in Chisholm's correlation was much larger than the value obtained for the reducer inlet case.

Since the time-average void fraction (and consequently interfacial area) and friction pressure drop would strongly affect the performance of microchannel devices such as microreactors for direct contacting of gas and liquid streams, the dimensions and type of a gas-liquid mixer to be used at the microchannel inlet would have to be carefully considered in the design process.

Acknowledgment

This work was supported by a Discovery research grant from the Natural Sciences and Engineering Research Council of Canada. K. Mori would like to thank Osaka Electro-Communication University for a research leave grant, which allowed a one-year stay at the University of Toronto.

Nomenclature

Bo = Bond number
C = coefficient in Eq. (4)
Ca = capillary number
D = tube inner diameter (m)
g = gravitational acceleration (m/s^2)
j = superficial velocity (m/s)
L = length (m)
m = mass flow rate (kg/s)
P = pressure (Pa)
Re = Reynolds number
u = axial velocity (m/s)
We = Weber number
X = Lockhart–Martinelli parameter
Z = flow direction coordinate (m)

Greek Symbols

β = volumetric quality
ε = void fraction
ΔP = pressure drop
μ = dynamic viscosity (Pa s)
ϕ_L^2 = two-phase friction multiplier
ρ = density (kg/m^3)
σ = surface tension (N/m)

Subscripts

f = friction
G = gas phase
L = liquid phase
M = mixing section
S = superficial
TP = two-phase

References

[1] Serizawa, A., 2006, "Gas-Liquid Two-phase Flow in Microchannels," *Multiphase Flow Handbook*, C. T. Crowe, ed., CRC Press, Boca Raton, FL.
[2] Thome, J. R., 2006, "State-of-the-Art Overview of Boiling and Two-Phase Flows in Microchannels," Heat Transfer Eng., **27**(9), pp. 4–19.
[3] Armand, A. A., 1946, "The Resistance during the Movement of a Two-phase System in Horizontal Pipes," Izv. Vses. Teplotekh. Inst. (AERE-Lib/Trans. 828), **1**, pp. 16–23.
[4] Stanley, R. S., Barron, R. F., and Ameel, T. A., 1997, "Two-Phase Flow in Microchannels," *Micro-Electro-Mechanical Systems (MEMS)*, ASME, DSC-Vol. 62/HTD-Vol. 354, New York, pp. 143–152.
[5] Serizawa, A., and Feng, Z. P., 2001, "Two-Phase Flow in Micro-Channels," Proceedings of the Fourth International Conference on Multiphase Flow, New Orleans, LA, May 27–Jun. 1.
[6] Serizawa, A., Feng, Z., and Kawara, Z., 2002, "Two-Phase Flow in Microchannels," Exp. Therm. Fluid Sci., **26**(6–7), pp. 703–714.
[7] Kawahara, A., Chung, P. M.-Y., and Kawaji, M., 2002, "Investigation of Two-Phase Flow Pattern, Void Fraction and Pressure Drop in a Microchannel," Int. J. Multiphase Flow, **28**(9), pp. 1411–1435.
[8] Chung, P. M. Y., and Kawaji, M., 2004, "The Effect of Channel Diameter on Adiabatic Two-Phase Flow Characteristics in Microchannels," Int. J. Multiphase Flow, **30**(7–8), pp. 735–761.
[9] Chung, P. M.-Y., Kawaji, M., Kawahara, A., and Shibata, Y., 2004, "Two-Phase Flow Through Square and Circular Microchannels—Effect of Channel Geometry," ASME J. Fluids Eng., **126**(4), pp. 546–552.
[10] Kawahara, A., Kawaji, M., Chung, P. M.-Y., Sadatomi, M., and Okayama, K., 2005, "Effects of Channel Diameter and Liquid Property on Void Fraction in Adiabatic Two-Phase Flow Through Microchannels," Heat Transfer Eng., **26**(3), pp. 13–19.
[11] Thorsen, T., Roberts, R. W., Arnold, F. H., and Quake, S. R., 2001, "Dynamic Pattern Formation in a Vesicle-Generating Microfluidic Device," Phys. Rev. Lett., **86**, pp. 4163–4166.
[12] Okushima, S., Nishisako, T., Torii, T., and Higuchi, T., 2004, "Controlled Production of Monodisperse Double Emulsions by Two-Step Droplet Breakup in Microfluidic Devices," Langmuir, **20**, pp. 9905–9908.
[13] Günther, A., Khan, S. A., Thalmann, M., Trachsel, F., and Jensen, K. F., 2004, "Transport and Reaction in Microscale Segmented Gas—Liquid Flow," Lab Chip, **4**, pp. 278–286.
[14] Xu, J. H., Li, S. W., Wang, Y. J., and Luo, G. S., 2006, "Controllable Gas-Liquid Two Phase Flow Patterns and Monodispersive Microbubbles in a Microfluidic T-Junction Device," Appl. Phys. Lett., **88**, pp. 133506.
[15] Garstecki, P., Fuerstman, M. J., Stone, H. A., and Whitesides, G. M., 2006, "Formation of Droplets and Bubbles in a Microfluidic T-Junction—Scaling and Mechanism of Break-Up," Lab Chip, **6**, pp. 437–446.
[16] Ide, H., Kimura, R., and Kawaji, M., 2007, "Optical Measurement of Void Fraction and Bubble Size Distributions in a Microchannel," Heat Transfer Eng., **28**(8), pp. 713–719.
[17] Xiong, R., and Chung, J. N., 2007, "An Experimental Study of the Size Effect on Adiabatic Gas-Liquid Two-phase Flow Patterns and Void Fraction in Microchannels," Phys. Fluids, **19**, p. 033301.
[18] Yue, J., Chen, G. W., and Yuan, Q., 2004, "Pressure Drops of Single and Two-Phase Flows Through T-Type Microchannel Mixers," Chem. Eng. J., **102**, pp. 11–24.
[19] Gañán-Calvo, A. M., and Gordillo, J. M., 2001, "Perfectly Monodisperse Microbubbling by Capillary Flow Focusing," Phys. Rev. Lett., **87**, p. 274501.
[20] Cubaud, T., and Ho, C. M., 2004, "Transport of Bubbles in Square Microchannels," Phys. Fluids, **16**, pp. 4575–4585.
[21] Garstecki, P., Stone, H. A., and Whitesides, G. M., 2005, "Mechanism for Flow-Rate Controlled Breakup in Confined Geometries: A Route to Monodisperse Emulsions," Phys. Rev. Lett., **94**, p. 164501.
[22] Waelchli, S., and von Rohr, P. R., 2006, "Two-Phase Flow Characteristics in Gas—Liquid Microreactors," Int. J. Multiph. Flow, **32**(7), pp. 791–806.
[23] Kline, S. J., and McClintock, F. A., 1953, "Describing Uncertainties in Single Sample Experiments," Mech. Eng. (Am. Soc. Mech. Eng.), **75**, pp. 3–8.
[24] Shibata, Y., Ikeda, K., Hanri, T., Chung, P. M. Y., and Kawaji, M., 2003, "Study on Two-Phase Flow Through a T-Junction," Proceedings of the Fourth ASME-JSME Joint Fluids Engineering Conference, Honolulu, Hawaii, Jul. 6–11, Paper No. FDSM2003-45385.
[25] Ali, M. I., Sadatomi, M., and Kawaji, M., 1993, "Two-Phase Flow in Narrow Channels Between Two Flat Plates," Can. J. Chem. Eng., **71**(5), pp. 657–666.
[26] Lockhart, R. W., and Martinelli, R. C., 1949, "Proposed Correlation of Data for Isothermal Two-Phase, Two-Component Flow in Pipes," Chem. Eng. Prog., **45**(1), pp. 39–48.
[27] Chisholm, D., and Laird, A. D. K., 1958, "Two-Phase Flow in Rough Tubes," Trans. ASME, **80**(2), pp. 276–286.
[28] Mishima, K., and Hibiki, T., 1996, "Some Characteristics of Air-Water Two-Phase Flow in Small Diameter Vertical Tubes," Int. J. Multiphase Flow, **22**(4), pp. 703–712.
[29] Kawaji, M., 1999, "Fluid Mechanics Aspects of Two-phase Flow," *Handbook of Phase Change: Boiling and Condensation*, Taylor & Francis, London, Chap. 9, pp. 205–259.

A Principle to Generate Flow for Thermal Convective Base Sensors

Thien X. Dinh
e-mail: thien@cfd.ritsumei.ac.jp

Yoshifumi Ogami

Department of Mechanical Engineering,
Ritsumeikan University,
1-1-1 Nojihigashi,
Kusatsu, Shiga 525-8577, Japan

This paper presents a thin millimeter-scaled device that can generate a closed flow within itself with a velocity of the order of a few m/s. The device comprises a piezoelectric pump with a PZT membrane, housing chamber, and a closed network channel connected to the housing chamber through a specific throat. We investigate the device by computational fluid dynamics. This device is used to produce several free jet flows depending on the structure of the network channel. In this study, four jet flows comprising two perpendicular pairs of flows are demonstrated. If the PZT membrane vibrates within a suitable range, the self-similarity of the axial velocity (along the jet direction) to the cross distances scaled by the half-widths of the jet is observed for a certain range of axial distance. Each jet flow can bend almost freely in three dimensions. The two remaining flow components are small as compared to the axial component. The device potentially has wide applications in flow-based sensors. [DOI: 10.1115/1.3089538]

Keywords: microfluidics, micropumps, piezoelectrics, numerical simulation, free jet flows

1 Introduction

Microfluidics is a concept that is used to manipulate flow in devices whose dimensions range from millimeters to micrometers. Microfluidics has attracted attention for several reasons in recent years. The first reason is the development of microelectromechanical systems (MEMS), which simplifies the fabrication of miniaturized devices. The second reason is the numbers of fields that are related to microfluidics, such as convection-based sensors, analytical chemistry, and "lab-on-a-chip."

The flow is usually a vital aspect in the functioning of microfluidic devices. For example, biological samples must be moved through the components of miniature assay systems [1,2] and a coolant must be forced through microheat exchangers [3]. Another great application of flow in microfluidics is the Coriolis effect-based sensors (e.g., gyroscope) in which jet flow is required. The flow in this type of sensors is usually generated by a self-contained valveless micropump. The advantage of self-contained valveless micropump Coriolis effect-based sensors is the absence of moving parts, with exception of the diaphragm. Therefore, it reduces the risk of damage or fragility as an incoherent of mechanical sensors. Furthermore, the convective sensors with valveless pump have quick respond performance. One of the greatest difficulties of the Coriolis effect-based sensors is forming jet flow, which can freely vibrate in space. In the recent applications for gyroscopes [4–6], only one jet flow was created. This makes the measurement ability of the gyroscopes limited in two components of angular rate. In two later works, MEMS technique was applied to fabricate the devices. The jet flow can bend "freely" on one plane. Therefore, they are single axis sensors. The former gyroscope is dual axes sensing because the jet can move in three-dimensional space. However, it is not compatible with MEMS process, except for the fabrication of hotwires. In these works, the flow properties have not been discussed in detail.

In this paper, we present a piezoelectrically actuated microfluidic device that can create a closed flow with four jet flows. The structure of the device is compatible to planar layer-by-layer geometry that is feasibly produced by lithography-based microfabrication techniques. The working principle and some primitive results are presented. All velocity components are examined. However, the axial component is mostly studied, since it is the most important flow characteristic.

2 The Device and Working Principle

The sealed device comprises the pump chamber, the housing chamber, and a network channel on a substrate. The pump chamber and the network channel are connected through a housing chamber and the throats (Fig. 1). The network channel includes the drive-channel and the main chamber in which the jet flow is created. One end of the main chamber is connected to the outermost channel through the nozzle, and the other end directly matches the back-channels. The depth and length of the main chamber are 1.5 mm and 3 mm, respectively. The main nozzle, whose width and depth are 0.3 mm and 0.5 mm, respectively, is located at a distance of 4 mm from the center of the housing chamber. The widths of the other channels are typically 0.5 mm, and their depths are the same as that of the main chamber. On the top surface of the pump chamber, a thin piezoelectric layer is bonded to vibrate this surface. The device is cylindrical and has a diameter and depth of 10 mm and 2 mm, respectively.

The working principle of the device relies on the behavior of the flow through the throat, as shown in Figs. 2(*a*) and 2(*b*). The length and thickness of the arrows qualitatively represent the flow rates and their directions in the designated channel. In the pump phase, the fluid in the housing chamber can be easily pushed straight into the drive-channel than into the back-channels, which are perpendicular to the flow. In the suction phase, because of the geometry of the throat, the back flow from the drive-channel slows down and becomes comparable to those from the back-channels. Therefore, the former flow is interrupted by the two latter perpendicular flows. Additionally, the back flow from the drive-channel experiences the diffuser-nozzle effect, wherein the resistance of the nozzle is higher than that of the diffuser. Due to this effect at the throat, a jet flow is created in the main chamber through the nozzle (Fig. 1).

Contributed by the Fluids Engineering Division of ASME for publication in the JOURNAL OF FLUIDS ENGINEERING. Manuscript received June 25, 2008; final manuscript received January 14, 2009; published online March 11, 2009. Assoc. Editor: James A. Liburdy. Paper presented at the 2007 ASME International Mechanical Engineering Congress (IMECF2007), Seattle, WA, November 10–16, 2007.

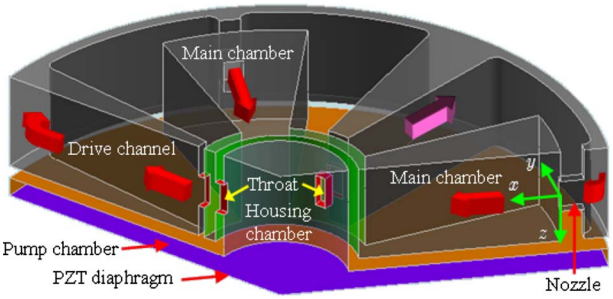

Fig. 1 Structure design of the device

3 The Governing Equations and Numerical Setup

The flow is generated by the vibration of a PZT diaphragm in a sealed packed device. Therefore, the fluid inside the device is compressed or extended due to the oscillation of the diaphragm. To cover these effects, the governing equations of the motion of a compressible Newtonian fluid are used as follows:

$$\frac{\partial \rho}{\partial t} + \nabla \cdot \rho \boldsymbol{u} = 0 \tag{1}$$

$$\frac{\partial \rho \boldsymbol{u}}{\partial t} + (\boldsymbol{u} \cdot \nabla)\rho \boldsymbol{u} = -\nabla p + \nabla \cdot (\mu \nabla \boldsymbol{u}) \tag{2}$$

Here, $\boldsymbol{u}$ and p denote the velocity vector and pressure of the flow field; μ and ρ are the dynamic viscosity and density of the fluid, respectively. Since the working fluid is air, the relation between pressure and density can follow the state equation of an ideal gas, $p=\rho R_a T/M_w$, where R_a is the universal gas constant, M_w is the molecular weight, and T is temperature. To close the governing equations, the solution of temperature is needed by solving the energy equation

$$\frac{\partial \rho c_p T}{\partial t} + (\boldsymbol{u} \cdot \nabla)\rho c_p T = \nabla \cdot (\lambda \nabla T) \tag{3}$$

In Eq. (3), λ and c_p are the thermal conductivity and specific heat coefficient of the fluid, respectively.

In our simulation, the change of temperature is insignificant (i.e., 0.5 K); thus the density varies mainly with the change of pressure due to the deformation of the PZT diaphragm.

Because of the symmetry flow feature, only one-eighth of the device is simulated. The computational domain is discretized into a structural mesh grid system by using GAMBIT, a commercial software developed by ANSYS, Inc. The mesh grids are clustered for regions where a high velocity gradient exists, i.e., near the walls, throat, and main nozzle. Then, FLUENT 6.3 (ANSYS, Inc.) is employed to obtain approximate values for the flow variables in this grid system. A second-order accuracy scheme is used for the convection and diffusion terms of each governing equation. The discretization equations are advanced with time by a second-order time stepping method. The semi-implicit method for pressure-linked equation (SIMPLE) scheme is used as the velocity-pressure coupling algorithm. The general version of the algebraic multigrid method (AMG) is used to solve the Poisson equation. The simulations were performed on RedHat 7.3 OS on a Pentium III CPU with 4 Gbyte memory.

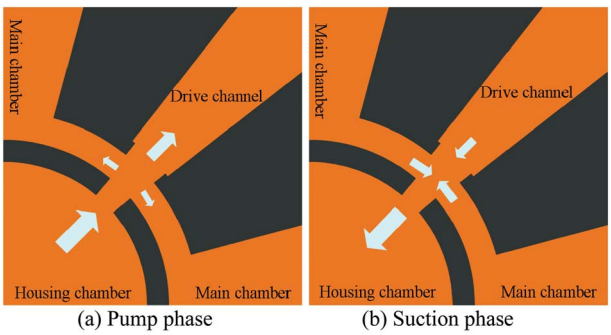

Fig. 2 Working principle of the device

Usually, the PZT diaphragm is excited by an alternating circuit with frequency f. Therefore, the time step should be determined according to this frequency by the following expression:

$$\Delta t = \frac{1}{fN} \tag{4}$$

where N is an arbitrary integer. For the exact reproduction of the flow behavior in 1 cycle of the PZT diaphragm oscillation, N is selected to be greater than 20.

The grid sensitivity or simulation accuracy was assessed in advance by several additional simulations on a refined double mesh. The solution for the mass flow rate in the jet nozzle is compared for the cases of "coarse" and "fine" meshes. If the solutions for the coarse and fine grids differ by less than 1%, the coarse grid system is selected for the simulation. A mesh with 300,000 grid points is sufficient to accurately simulate the flow.

The reference fluid properties, i.e., ideal air, are as follows: temperature=298 K, molecular weight M_w=28.96 g/mol, viscosity $\mu=1.789\times10^{-5}$ Pa s, thermal conductivity $\lambda=2.42\times10^{-3}$ w/m K, and specific heat c_p=1006.43 J/kg K. The estimated Knudsen number, $\mathrm{Kn}=\lambda_F/L$, where $\lambda_F\sim100$ nm is the mean free path of the air and is less than 10^{-3}. Hence, the continuum hypothesis and nonslip condition at the walls are applicable.

The PZT diaphragm is assigned as the inlet surface condition for the simulation model of the device. Assuming uniform force distribution on the membrane, which is mounted at its perimeter, the displacement at a distance r from the center of the membrane is given by [7]

$$\delta(r,t) = \Theta(t)\left[1-\left(\frac{r}{R}\right)^2\right]^2 \tag{5}$$

where the displacement of the membrane center $\Theta(t)$ is a function of time depending on the applied electric power and R denotes the radius of the membrane. Since the applied power varies sinusoidally with time at frequency f, we obtain

$$\Theta(t) = \Theta_0 \sin(2\pi f t) \tag{6}$$

Because Θ_0 (of the order of tens of microns) is small as compared to the depth of the pump chamber ($\sim$300 μm), it is not necessary to use the deformation mesh in the simulation. The local rate of deformation of the diaphragm is converted to local velocity applied on the inlet surface by taking derivative of Eq. (5) respective with time as

$$v(r,t) = 2\pi f \Theta_0\left[1-\left(\frac{r}{R}\right)^2\right]\cos(2\pi f t) \tag{7}$$

A commercial PZT membrane usually comprises $LiNbO_3$ with a natural frequency of 7 MHz. Therefore, in the present simulation, the frequency is selected as 7 MHz. This implies that the membrane functions at its resonance frequency.

4 Results and Discussion

In order to facilitate the discussion, a Cartesian coordinate system is designated with the origin located at the center of the nozzle outlet. The x-, y-, and z-axes correspond to the axial, horizontal, and vertical directions, respectively, as shown in Fig. 1. The corresponding velocity components along the x-, y-, and z-directions are denoted as u, v, and w.

Figures 3(a) and 3(b) shows the instantaneous vector velocity field at the throat for the discharge and suction phases, respec-

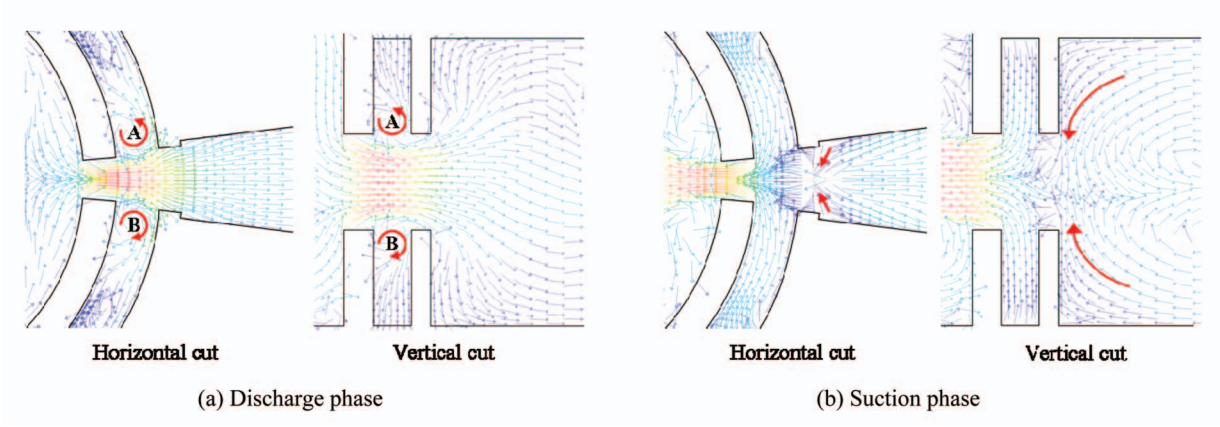

Fig. 3 Flow behavior at the throat in the discharge phase (*a*) and suction phase (*b*)

tively. The vectors are plotted with constant length for simplification. The magnitude of the vector velocity is represented by the color bar. The highest and lowest values are represented by red and blue, respectively. The working principle of the device is clearly observed. In the discharge phase, there is a ring-shaped circulatory flow (its cross sections are indicated by characters A and B in the front and side views, as shown in Fig. 3(*a*)) around the throat. It intercepts the flow from the throat to the back-channels. The flow from the housing chamber goes straight to the drive-channel. In the suction phase, the flows from the back-channels are comparable to that from the drive-channel at the throat. Then, the former slows down the fluid from the drive-channel to the housing chamber. Moreover, the secondary flow from the wall of the drive-channel (indicated by the arrows in Fig. 3(*b*)) also contributes to slowing down the flow from this channel to the housing chamber. Consequently, only a small portion of the flow in the drive-channel, which was created in the pump phase, is sucked back into the housing chamber. The other major portion still flows in the drive-channel. We can observe this effect by the division of the vector velocity field into opposite directions at the throat, as shown in Fig. 3(*b*).

Figure 4 shows the variation in the spatial-average axial velocity at the nozzle outlet, U_J, against the dimensionless time $t \times f$. We observe that the flow attains the steady state after 4 cycles of vibration of the membrane. It is also observed that U_J completes 1 cycle during the dimensionless time $t \times f = 1$. In other words, the flow in the main chamber oscillates at the same frequency as the PZT membrane. It should be noted that the PZT vibrates at a very high frequency. Therefore, it is expected that the flow is almost in the steady state for the application's time scales.

Hereafter, the characteristics of one jet flow are considered, and all the mentioned quantities are the time averaged values. In our present simulation, the time averaged values are computed in the period of $20 \leq t \times f \leq 60$. This ensures that the flow in the main chamber has reached steady state, and that time is long enough for taking averaged values.

The measured profile of the axial velocity $u(x, y=0, z)$ along the z-direction at different axial locations, x, is plotted in the left-hand side of Fig. 5 for the case of $\Theta_0 = 15$ μm. Similarly, the right-hand side of Fig. 5 plots the profiles of the axial velocity $u(x, y, z=0)$ against the y-distance from the axis of the jet flow for the same working conditions. From Fig. 5, it is evident that the peaks of the profile decrease with an increase in the axial distance from the nozzle, x. This implies that the jet decays with an increase in the axial distance from its source. The tails of these profiles have negative values. This shows that there is a circulatory flow in the main chamber.

Often, a central characteristic of free jet flows is self-similarity. Therefore, roughly, the self-similar property of a jet flow can be used to measure its freedom in space, which is an important feature in Coriolis effect-based applications. As shown in Fig. 5, there is a secondary flow from the near wall of the main chamber to the jet flow. Therefore, we seek the self-similar property of the axial flow as a turbulent jet instead of a laminar jet.

In terms of the axial velocity field $u(x, y, z)$, the centerline velocity is

$$u_c(x) = u(x, 0, 0) \tag{8}$$

The jet's half-width along the y- and z-directions, $y_{1/2}(x)$ and

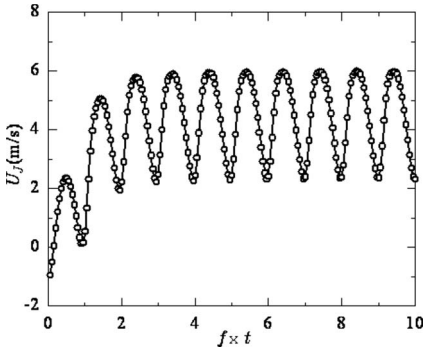

Fig. 4 Variation in the spatial-average axial velocity at the outlet of the nozzle against time. The maximum amplitude of the PZT membrane is 10 μm

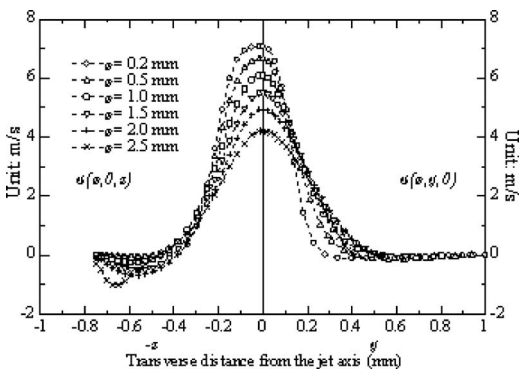

Fig. 5 Profiles of $u(x, 0, z)$ and $u(x, y, 0)$ against z and y, respectively, for $\Theta_0 = 15$ μm

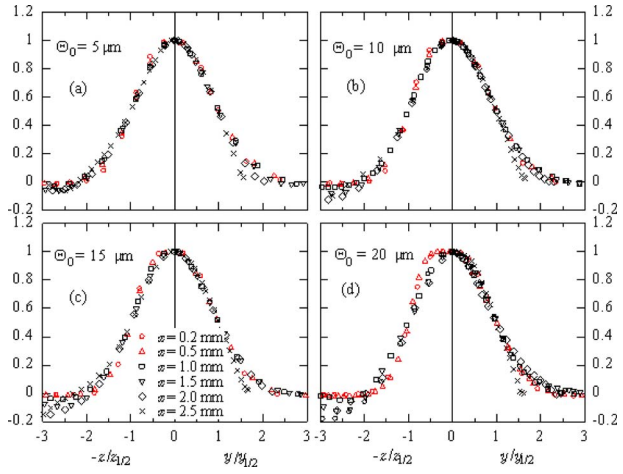

Fig. 6 Axial velocity of the jet against cross-distance for different amplitude vibrations of the membrane and different axial distance, *x*. The left-hand side of each figure shows a plot of $u(x,0,z)/u_c(x)$ against $z/z_{1/2}(x)$ and the right-hand side shows the variation in $u(x,y,0)/u_c(x)$ against $y/y_{1/2}(x)$.

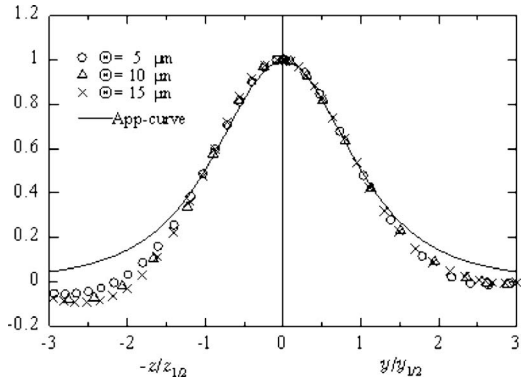

Fig. 7 Axial velocity of the jet against cross-distance for different amplitude vibrations of the membrane at $x=1.5$ mm. The left-hand side of each figure shows a plot of $u(x,0,z)/u_c(x)$ against $z/z_{1/2}(x)$ and the right-hand side shows the variation in $u(x,y,0)/u_c(x)$ against $y/y_{1/2}(x)$. The approximate curve is plotted by Eq. (10).

$z_{1/2}(x)$, respectively, are defined as the transverse distance from the jet axis to the location where the mean axial velocity is half of the centerline value $u(x,0,0)$ as [8]

$$u(x,y_{1/2}(x),0) = 1/2u_c(x)$$
$$u(x,0,z_{1/2}(x)) = 1/2u_c(x) \tag{9}$$

Figures 6(*a*)–6(*c*) show the plots of the profiles $u(x,0,z)/u_c(x)$ against $z/z_{1/2}(x)$ on the left-hand side and those of $u(x,y,0)/u_c(x)$ against $y/y_{1/2}(x)$ on the right-hand side for $\Theta_0=5$, 10, and 15 μm, respectively. It is interesting to note that the profiles on both sides of Figs. 6(*a*)–6(*c*) collapse into a single curve for a range of x. The tails of the profiles are slightly deviated. The important conclusion is that the axial velocity profile exhibits the self-similar property. It is found that the secondary flow and back-channel flows affect the profiles of $u(x,0,z)/u_c(x)$ against $z/z_{1/2}(x)$, as shown in the left-hand side of Figs. 6(*a*)–6(*c*). This is clearly observed for the case when $\Theta_0=15$ μm (left-hand side of Fig. 6(*c*)). Therefore, the profiles of $u(x,0,z)/u_c(x)$ against $z/z_{1/2}(x)$ near the back-channels ($x>2$ mm) or nozzle ($x<0.5$ mm) are no longer self-similar. It is observed that for $\Theta_0=5-15$ μm, the profiles of $u(x,0,z)/u_c(x)$ against $z/z_{1/2}(x)$ are adequately self-similar when x ranges from 0.5 mm to 2 mm. In contrast, only the effect of the back-channel flows affects the profiles of $u(x,y,0)/u_c(x)$ against $y/y_{1/2}(x)$, which breaks the self-similarity of these profiles for $x>2$ mm (right-hand side of Figs. 6(*a*)–6(*c*)). The self-similar region for the profiles of $u(x,y,0)/u_c(x)$ against $y/y_{1/2}(x)$ is 0.2 mm$<x<2$ mm (shown in right-hand side of Figs. 6(*a*)–6(*c*)). Furthermore, it is observed from Figs. 6(*a*)–6(*c*) that self-similarity is assured within twice the jet's half-width region (i.e., $y/y_{1/2}(x)\leq 2$ and $z/z_{1/2}(x)\leq 2$). In the region of 0.5 mm$<x<2$ mm, the profiles of $u(x,y,0)/u_c(x)$ against $y/y_{1/2}(x)$ and those of $u(x,0,z)/u_c(x)$ against $z/z_{1/2}(x)$ are symmetrical to each other. In other words, the flow is similar to an axisymmetric flow. From these discussions, the jet flow is expected to be free in three dimensions in the range of 0.5 mm $<x<2$ mm.

It should be noted that the self-similar profiles of the axial velocity correspond to the cross-distance scaled by the jet's half-width. This implies that the jet flow created in the main chamber is more similar to a turbulent jet flow than to a laminar jet flow. Theoretically, the profiles of the axial velocity of a laminar jet flow are self-similar to the momentum width (i.e., $\sim[J/u_c^2(x)]^{1/2}$, where J denotes the surface integral of the momentum of the jet at its outlet).

Figure 6(*d*) plots the axial velocity profiles in the same manner as Figs. 6(*a*)–6(*c*), with the exception that $\Theta_0=20$ μm. This shows that the self-similar profiles are no longer observed for the entire range of axial distance. This is because the effects of the secondary and back-channel flows expand throughout the main chamber. These effects destroy the free property of the jet. Therefore, the flows cannot be self-similar. It is noteworthy that self-similarity in the main chamber requires a specific condition for the amplitude of vibration of the PZT membrane and occurs for a certain range of distance from the nozzle. In Coriolis effect-based sensor applications, a flow that is less affected by the wall of the channel is preferable. Therefore, the recommended Θ_0 in our present studied device should be around 10 μm. A general conclusion here is that amplitude of the vibration of the PZT membrane is an important factor for studying the device sensitivity.

Figure 7 plots the axial velocity profiles at $x=1.5$ mm (middle of the self-similar region) in the same manner as Fig. 6 for the cases of $\Theta_0=5$, 10, and 15 μm. They also collapse onto a single curve. In other words, the self-similar profile is not affected by the jet's velocity. The solid lines represent the approximate curves obtained by the following equation [8]:

$$f(\xi) = (1+S\xi^2)^{-2} \tag{10}$$

where S is computed by the nonlinear least squares method and its value is 0.411 for both sides of Fig. 7. ξ is a dimensionless variable representing $y/y_{1/2}(x)$ or $z/z_{1/2}(x)$. Figure 7 shows that in the range of $y/y_{1/2}(x)\leq 1.25$ and $z/z_{1/2}(x)\leq 1.25$, the velocity distribution can be evaluated by Eq. (10).

In order to complete the description of the axial velocity, the axial variations in the center axial velocity $u_c(x)$ and the jet's half-widths $y_{1/2}(x)$ and $z_{1/2}(x)$ must be determined in the self-similar region (i.e., 0.5 mm$<x<2$ mm).

For practical applications, the center axial velocity $u_c(x)$ should be relatively measured with the center velocity of the diaphragm, i.e., $2\pi\Theta_0 f$. It is found that $u_c(x)/2\pi\Theta_0 f$ varies linearly with the axial distance in the self-similar region, as plotted in Fig. 8. A lower amplitude vibration of the membrane generates a higher slope coefficient (absolute value) because the flow magnitude decreases more rapidly for decreasing Θ_0.

A feature of the current design (compatible with MEMS photolithography fabrication on a silicon wafer) is that the ratios of the main chamber depth to the nozzle depth and that of the main chamber width to the nozzle width are different. This results in the

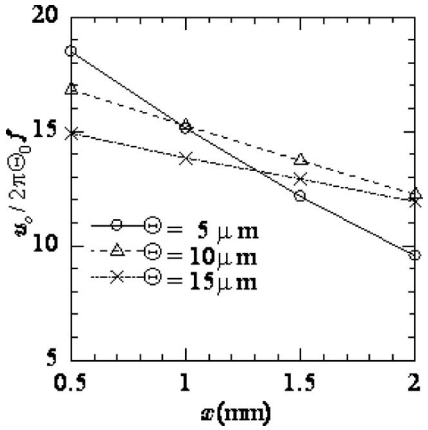

Fig. 8 Variation in the center velocity against axial distance in the self-similar region

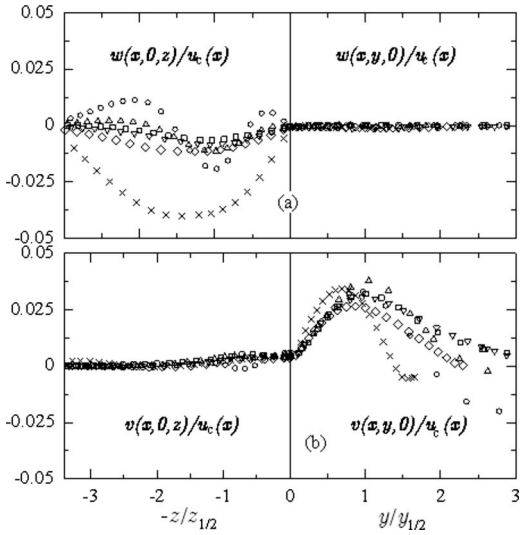

Fig. 10 Variation of cross-stream velocity components with radial distance in the self-similar region. The left-hand side of each figure shows plots of v or $w(x,0,z)/u_c(x)$ against $z/z_{1/2}(x)$ and the right-hand side shows the variation of v or $w(x,y,0)/u_c(x)$ against $y/y_{1/2}(x)$.

difference between $y_{1/2}(x)$ and $z_{1/2}(x)$, as shown in Fig. 9. The half-widths of the flow in the depth, $z_{1/2}(x)$, appear to remain unchanged with axial distance, x, and their values are approximately 0.2. Figure 9 also shows that the jet spreads along the y-direction. The spread is approximately linear with a rate, $dy_{1/2}/dx$, of around 0.45–0.5.

The other flow components, $v(x,y,z)$ and $w(x,y,z)$, along the y- and z-directions, respectively, are also examined in the self-similar region (i.e., 0.5 mm$<x<$2 mm). Similar to the examination of the axial flow, $v(x,y,z)/u_c(x)$ and $w(x,y,z)/u_c(x)$ are plotted as functions of $y/y_{1/2}(x)$ and $z/z_{1/2}(x)$, respectively, as shown in Fig. 10. The self-similar properties are not observed in these cross section velocity components. The cross profiles, $v(x,y,z)/u_c(x)$ against $z/z_{1/2}(x)$ and $w(x,y,z)/u_c(x)$ against $y/y_{1/2}(x)$, approach zero. Physically, a circulatory flow is created in the bracelet shape in the main chamber encompassing the jet flow, as shown in Fig. 11, which plots the mean velocity vector on the horizontal and vertical planes. This also explains why the tails of the axial velocity profiles against $y/y_{1/2}(x)$ or $z/z_{1/2}(x)$ are not self-similar. It is observed in Fig. 10 that $v(x,y,z)$ and $w(x,y,z)$ are of the same order of magnitude and are very small—less than $u_c(x)$ by a factor of 25—as shown in Fig. 10. This implies that a passive scalar (e.g., temperature) is mainly transported by axial flow.

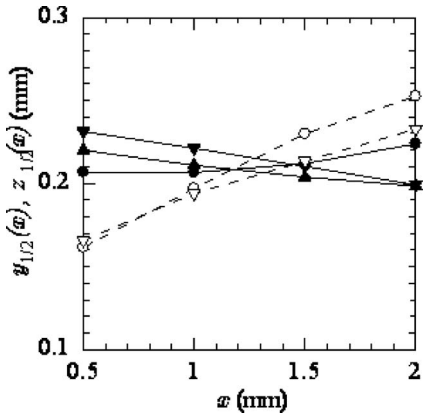

Fig. 9 Variation of half-widths against axial distance in the self-similar region. Black symbols $z_{1/2}(x)$, white symbols $y_{1/2}(x)$, circle Θ_0=5 μm, upward-facing triangle Θ_0=10 μm, and downward-facing triangle Θ_0=15 μm.

5 Conclusions

A simple device that is compatible with planar layer-by-layer geometries and can create several jet flows within is proposed and numerically studied by computational fluid dynamics. In this study, four jet flows are independently formed. The principle of the device is presented.

The axial velocity component is self-similar with a cross-stream nondimensionlized by the half-widths of the jet flow if the amplitude of vibration of the PZT membrane lies in a suitable range. This implies that the spread of the jet flow along two perpendicular directions is similar to a turbulent free jet flow. The self-similar region covers almost the entire main chamber, except in areas very close to the nozzle or the back-channels.

In the self-similar region, the jet flow is expected to vibrate freely in three dimensions.

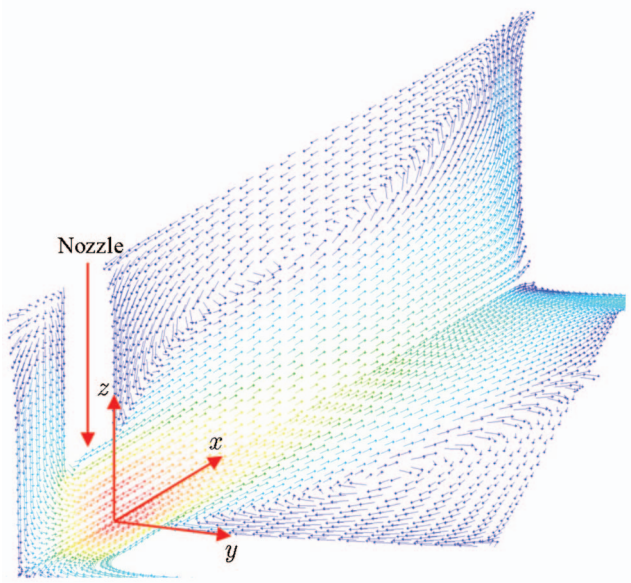

Fig. 11 Time averaged velocity fields on two perpendicular planes containing the axis of the jet flow in the main chamber

The two remaining components of the flow are small as compared to the axial component.

Furthermore, the characteristics of the centerline axial velocity, as well as the half-widths of the jet, should be addressed in a general way. The device has been investigated only for one specific dimension. Since the geometry, throat, and nozzle may contribute significantly in optimizing the operation of the device, these factors should be carefully considered in the future.

References

[1] Woolley, A. T., Hadley, D., Landre, P., deMello, A. J., Mathies, R. A., and Northrup, M. A., 1996, "Functional Integration of PCR Amplification and Capillary Electrophoresis in a Microfabricated DNA Analysis Device," Anal. Chem., **68**, pp. 4081–4087.

[2] Taylor, M. T., Nguyen, P., Ching, J., and Petersen, K. E., 2003, "Simulation of Microfluidic Pumping in a Genomic DNA Blood-Processing Cassette," J. Micromech. Microeng., **13**, pp. 201–208.

[3] Zhang, L., Koo, J. M., Jiang, L., Asheghi, M., Goodson, K. E., Santiago, J. G., and Kenny, T. W., 2002, "Measurements and Modeling of Two-Phase Flow in Microchannels With Nearly Constant Heat Flux Boundary Conditions," J. Microelectromech. Syst., **11**, pp. 12–19.

[4] Dau, V. T., Dao, V. D., Shiozawa, T., Kumagai, H., and Sugiyama, S., 2005, "A Dual Axis Gas Gyroscope Utilizing Low Doped Silicon Thermistor," 18th IEEE MEMS, pp. 626–629.

[5] Zhou, J., Yan, G., Zhu, Y., Xiao, Z., and Fan, J., 2005, "Design and Fabrication of a Microfluidic Angular Rate Sensor," 18th IEEE International Conference on Micro Electro Mechanical Systems (MEMS), pp. 363–366.

[6] Saito, K., Komatsu, G., and Kato, K., 2001, "An Analysis of Fluid Behavior on Gas Angular Rate Sensor," JSME Int. J., Ser. C, **67**, pp. 135–140.

[7] Bassi, A., Gennar, F., and Symonds, P. S., 2003, "Anomalous Elastic-Plastic Respond to Short Pulse Loading of Circular Plates," Int. J. Impact Eng., **28**, pp. 65–91.

[8] Pope, S. B., 2000, *Turbulent Flows*, Cambridge University, Cambridge.

Pressurized Flow in a Mesostructured Silica Modified by Silane Groups

Venkata K. Punyamurtula

Aijie Han

Yu Qiao[1]
e-mail: yqiao@ucsd.edu

Department of Structural Engineering,
University of California, San Diego,
La Jolla, CA 92093-0085

By applying a quasihydrostatic pressure, water or electrolyte solution can be compressed into a surface treated MSU-H mesoporous silica. Based on the pressure-volume curves, thermodynamic and kinetic characteristics of the pressurized flow are analyzed. For pure water based system, continuum theory explains the testing data quite well but fails to capture the rate effect. For electrolyte solution based system, the classic interface theory breaks down, probably due to the unique ion behaviors in the nanoenvironment. [DOI: 10.1115/1.3089542]

1 Introduction

Liquid behavior in nanoenvironment has been an important research topic for more than a decade [1,2], which shed much light on fundamental mechanisms governing solid-liquid interactions at small length and time scales. The studies in this area have been immensely useful to developing better techniques for drug delivery, micro-/nanotransportation, micro-/nanofabrication, biosensing, etc.

Over the years, energy dissipation associated with nanofluidic behaviors has drawn considerable attention [3,4]. The initial idea was based on the assumption that, as a liquid flows in nanopores and the internal friction takes place across the large pore surface, the energy dissipation capacity can be ultrahigh. Such a system may have great applicability in advanced dampers, bumpers, and armors. For instance, in an experiment performed by Li [5], bending moments were applied on a hydrophilic nanoporous silica block soaked by water. As water flowed from compressive parts to tensile parts, there was a detectable damping effect. However, the energy dissipation efficiency was lower than the expected level.

Recently, an improved concept has been investigated by a few research teams [6–11], including the authors of this paper, who replaced the hydrophilic nanoporous solids by hydrophobic ones. Due to the capillary effect, as a hydrophobic nanoporous material is immersed in water, the nanopores remain empty. Once a high pressure is applied on the liquid phase, pressure induced infiltration (PII) would occur, accompanied by conversion of a significant amount of external work to excess solid-liquid interfacial energy. In a number of nanoporous systems, the excess solid-liquid interfacial energy cannot be converted back to the hydrostatic pressure as the external loading is removed; that is, the sorption isotherm curves are hysteretic, which results in ultrahigh energy dissipation efficiency larger than a few J/g, much better than many conventional protective materials [12]. A similar design concept can be extended to nonpolar liquids using lyophobic nanoporous materials, which has led to an even higher energy density [13,14]. In these investigations, it has been noticed that increasing degree of hydrophobicity, decreasing pore size, and adding electrolytes can be of beneficial effects to improving system performance.

2 Experimental Procedure

In the current study, we investigated a MSU-H type nanoporous silica that was commonly used as adsorbent and catalyst support. It was of a hexagonal framework, small pore size, and relative large specific pore volume, ideal for energy absorption applications. The network material was obtained from Sigma-Aldrich (St. Louis, MO) (CAT No. 643637). The as-received material was in powder form. The particle size was 20–80 μm. According to a gas absorption analysis using a Tristar-3000 analyzer, the average pore size was 7.1 nm, the specific pore volume was 0.9 cm^3/g, and the specific pore surface area was 510 m^2/g. Figure 1 shows the Barrett–Joyner–Halenda (BJH) analysis result of nanopore volume distribution. Its pore surface was hydrophilic, and therefore could not be directly used for PII testing. In order to modify the pore surface structure, the silica particles were first dried at 100°C in a vacuum oven for 24 h and then refluxed in a silane agent solution in a hot mantle. The solution was prepared by injecting 1 part of chlorotrimethylsilane into 40 parts of dry toluene. Prior to the refluxing, the mixture had been gently stirred at room temperature for 10 min. The refluxing time ranged from 3 h to 24 h. During this process, the chlorotrimethylsilane molecules diffused into the nanopores and formed hydrophobic $O-Si(CH_3)_3$ groups at nanopore walls, changing the surface wettability [15]. The treated sample was vacuum filtered, washed with dry toluene, and dried at 100°C for 24 h in vacuum.

Figure 2 depicts the PII experimental setup, which consisted of 0.2 g of surface treated silica particles immersed in 7 g of liquid, a steel cylinder, and a piston. A compressive load was applied on the liquid phase through the piston by an Instron machine, forcing the piston into the cylinder at a constant rate. The liquid phase was either de-ionized water or saturated aqueous solution of sodium chloride. The compression rate, V, was 1–20 mm/min. The quasihydrostatic pressure in the liquid, p, was calculated as P/A_0, with P being the axial load and $A_0=286$ mm^2 being the cross-sectional area of the cylinder. The piston displacement, δ_p, was also measured, based on which the liquid volume change was calculated as $\Delta V_0=\delta_p \cdot A_0$. As the pressure exceeded 30–40 MPa, the piston was moved out of the cylinder at the same rate. Figures 3 and 4 show the typical sorption isotherm curves. The resolutions of load and displacement measurements were 250 N and 20 μm, respectively.

3 Results and Discussion

Without the surface treatment, the silica is hydrophilic and thus the nanoporous particles can be infiltrated by water. Under this condition, as shown by the dashed curve in Fig. 3, no infiltration can be observed in the PII experiment. With the surface treatment, as shown by the solid curves, infiltration plateaus are formed. The infiltration plateau is defined as the middle portion of the loading part of sorption isotherm where the slope is much smaller than that of the linear compression sections. The surface treated nanoporous silica particles are initially filled by entrapped air. As the pressure is sufficiently high (4.5 MPa and 8.1 MPa for silicas surface treated for 3 h and 24 h, respectively), liquid starts to enter the largest nanopores. As a result, the system volume decreases rapidly. As the pressure rises, smaller nanopores are involved in the PII process, during which the entrapped gas molecules are dissolved by the confined liquid. Note that the interactions among gas and liquid molecules in a nanopore can be fundamentally different from that in a bulk phase, as demonstrated by the molecular dynamics simulation in Ref. [16]. As the nanopore wall confines the molecular motion, there must be a sufficiently large "gap" between the gas molecule and the solid surface; otherwise,

[1]Corresponding author.

Contributed by the Fluids Engineering Division of ASME for publication in the JOURNAL OF FLUIDS ENGINEERING. Manuscript received February 23, 2007; final manuscript received March 11, 2008; published online March 6, 2009. Assoc. Editor: Ali Beskok.

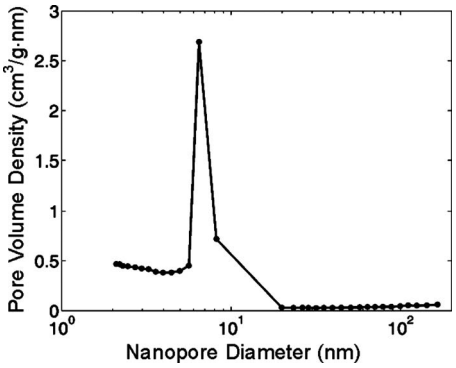

Fig. 1 The BJH analysis result of the nanopore volume distribution

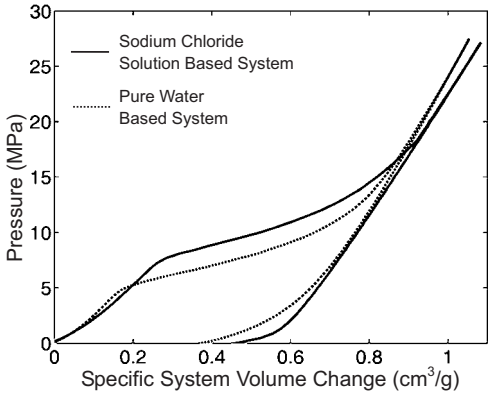

Fig. 4 The effect of addition of sodium chloride. The silica is surface treated for 3 h.

the liquid molecules would be blocked. When the pressure is lowered, since gas phase nucleation may be energetically unfavorable, the confined liquid does not come out of the nanopores [17]; that is, a decrease in solid-liquid interfacial energy associated with the expansion of a nanobubble can be lower than the energy required for "evaporating" molecules from liquid phase to vapor phase, which causes a significant hysteresis in sorption isotherm. The enclosed area of the loading-unloading cycle indicates the dissipated energy (Table 1).

According to Fig. 3, the infiltration volume of the silica surface treated for 3 h, which can be measured by the width of infiltration

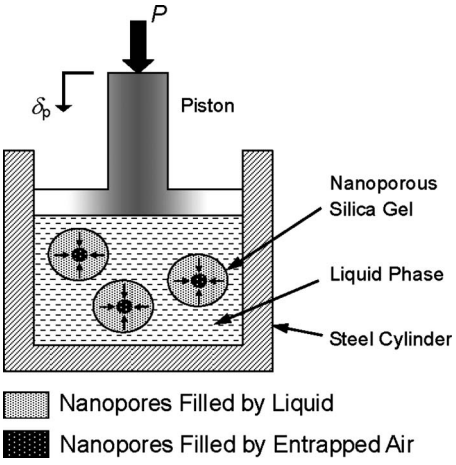

Fig. 2 A schematic of the testing system

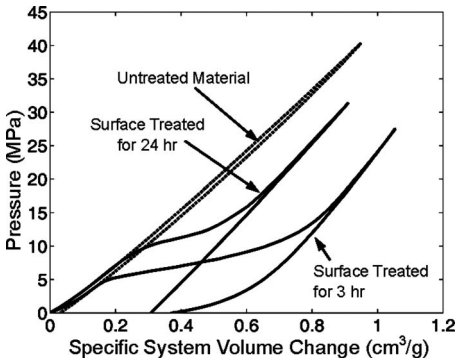

Fig. 3 Typical sorption isotherm curves of pure water based system. The specific system volume change is defined as the system volume change normalized by the mass of the nanoporous silica.

plateau, is about 0.7 cm^3/g, smaller than the BJH measurement result of nanopore volume of untreated silica. Note that the molecular size of $O-Cl(CH_3)_3$ is around 0.26 nm. As the nanopore surface is covered by a surface group layer, the effective pore size should be reduced from 7.1 nm to 6.6 nm, and the effective pore volume would decrease by about 15%, from 0.9 cm^3/g to 0.76 cm^3/g, quite close to the infiltration volume. The effective solid-liquid interfacial tension, according to the classic Young's equation, can be calculated as $\Delta\gamma = p_{in} \cdot r/2 = 13$ mJ/m^2, with p_{in} being taken as 7.9 MPa and $r = 3.3$ nm.

As the surface treatment time, t_r, is increased to 24 h, the infiltration pressure largely rises to 12.4 MPa, while the infiltration volume decreases considerably from 0.7 cm^3/g to 0.4 cm^3/g, even though the nanoporous structure does not change. This phenomenon may be attributed to the formation of dense layers of silane groups at nanopore surfaces. When the surface coverage is saturated, in a prolonged surface treatment process, chlorotrimethylsilane molecules would continue to diffuse into the nanopores. Consequently, the pore volume decreases. The reduction in accessible pore volume from 0.7 cm^3/g to 0.4 cm^3/g is equivalent to a change in effective nanopore radius from 3.3 nm to 2.5 nm. With the same solid-liquid interfacial tension of 13 mJ/m^2, the infiltration pressure would increase from 7.9 MPa to 10.5 MPa, which is quite close to the values shown in Fig. 3. That is, the large variation in infiltration pressure and volume associated with the increase in treatment time are caused by the decrease in empty nanopore space.

If the liquid motion in nanopores could be described by a circular Poiseuille flow, as the infiltrating liquid molecules move along the pore wall, an additional pressure must be applied to overcome the viscosity effect. For a zero-order approximation, the pressure increase can be assessed as $dp = 32\mu \cdot v \cdot dz/D^2$ [18], where $\mu = 10^{-3}$ Pa s is the liquid viscosity, v is the inflow rate, dz is the pore depth, and $D = 6.6$ nm is the effective pore diameter for the silica sample that is treated for 3 h. In the current study, the cross-sectional area of the testing cylinder, A_0, is 286 mm^2, and therefore it takes about 30 s to fill the nanopores. The average silica particle size is about 50 μm. Thus, the inflow rate, v, is

Table 1 Energy absorption capacity of surface treated MSU-H silica (J/g)

		Surface treatment time (h)		
Experimental condition		3	12	24
	In pure water	5.1	5.6	3.1
$v = 1$ mm/min	In saturated NaCl solution	6.8	7.0	3.6
$v = 20$ mm/min	(in pure water)	5.2	5.6	3.2

around 1 μm/s, and the characteristic value of dz is about 10 μm. Consequently, when the piston speed changes from 1 mm/min to 20 mm/min, the sorption isotherm curve should shift along the pressure axis by a few MPa, which was not observed in the PII experiment. When the loading rate varied in this range, the infiltration plateaus were nearly identical. Clearly, in the confining nanoenvironment, the no-slip boundary condition is no longer valid, and the definition of liquid viscosity breaks down, which explains why the internal-friction-based energy dissipation mechanism did not have the expected energy density [5].

As sodium chloride is added in the liquid phase, as shown in Fig. 4, while the infiltration volume does not vary, the infiltration pressure becomes much higher. The p_{in} increase is about 2.2 MPa, which corresponds to a large variation in effective solid-liquid interfacial tension of about 8.6 mJ/m^2, 66% of that of pure water. Note that the surface tension of saturated sodium chloride solution is larger than that of pure water by less than 10% [19]. The large increase in the effective interface tension should be related to the confinement effect of pore walls on ion distribution. In a nanopore, normal to the pore surface, there is no enough space for the formation of a double layer. The bulk phase may not exist. Therefore, the effective ion concentration is higher than that at a large solid surface; that is, the ion structure is affected by the opposite nanopore surface, causing a "squeezing" effect, which can lead to a higher liquid composition sensitivity. The details of the fundamental mechanisms are still under investigation.

4 Conclusion

To summarize, through a pressure induced infiltration experiment on a surface treated MSU-H nanoporous silica, the liquid motion in nanopores are examined. For the system under investigation, the classic capillary theory can be employed to relate the infiltration pressure to the nanopore size. However, the continuum theory does not explain the low sensitivity of sorption isotherm to loading rate. It also fails to capture the large variation in infiltration pressure caused by addition of sodium chloride.

Acknowledgment

This work was supported by the Army Research Office under Grant No. W911NF-05-1-0288, for which the authors are grateful to Dr. D.M. Stepp.

References

[1] Sansom, M. S. P., and Biggin, P. C., 2001, "Biophysics: Water at the Nanoscale," Nature (London), **414**, pp. 156–158.

[2] Majumder, M., Chopra, N., Andrews, R., and Hinds, B. J., 2005, "Experimental Observation of Enhanced Liquid Flow Through Aligned Carbon Nanotube Membranes," Nature (London), **438**, pp. 44–46.

[3] Borman, V. D., Grekhov, A. M., and Troyan, V. I., 2000, "Investigation of the Percolation Transition in a Nonwetting Liquid-Nanoporous Medium System," J. Exp. Theor. Phys., **91**, pp. 170–181.

[4] Fadeev, A. Y., and Eroshenko, V. A., 1997, "Study of Penetration of Water Into Hydrophobized Porous Silicas," J. Colloid Interface Sci., **187**, pp. 275–282.

[5] Li, J. C. M., 2000, "Damping of Water Infiltrated Nanoporous Glass," J. Alloys Compd., **310**, pp. 24–29.

[6] Martin, T., Lefevre, B., Brunel, D., Galarneau, A., Di Renzo, F., Fajula, F., Gobin, P. F., Quinson, J. F., and Vigier, G., 2002, "Dissipative Water Intrusion in Hydrophobic MCM-41 Type Materials," Chem. Commun. (Cambridge), **2002**, pp. 24–25.

[7] Borman, V. D., Belogorlov, A. A., Grekhov, A. M., Lisichkin, G. V., Tronin, V. N., and Troyan, V. I., 2005, "The Percolation Transition in Filling a Nanoporous Body by a Nonwetting Liquid," J. Exp. Theor. Phys., **100**, pp. 385–397.

[8] Surani, F. B., Kong, X., and Qiao, Y., 2005, "Two-Staged Sorption Isotherm of a Nanoporous Energy Absorption System," Appl. Phys. Lett., **87**, p. 251906.

[9] Surani, F. B., Kong, X., Panchal, D. B., and Qiao, Y., 2005, "Energy Absorption of a Nanoporous System Subjected to Dynamic Loadings," Appl. Phys. Lett., **87**, p. 163111.

[10] Kong, X., and Qiao, Y., 2005, "Improvement of Recoverability of a Nanoporous Energy Absorption System by Using Chemical Admixture," Appl. Phys. Lett., **86**, p. 151919.

[11] Kong, X., Surani, F. B., and Qiao, Y., 2005, "Effects of Addition of Ethanol on the Infiltration Pressure of a Mesoporous Silica," J. Mater. Res., **20**, pp. 1042–1045.

[12] Lu, G., and Yu, T., 2003, *Energy Absorption of Structures and Materials*, CRC, Boca Raton, FL.

[13] Punyamurtula, V. K., and Qiao, Y., 2007, "Hysteresis of Sorption Isotherm of a Multiwall Carbon Nanotube in Paraxylene," Mater. Res. Innovations, **11**, pp. 37–39.

[14] Punyamurtula, V. K., Han, A., and Qiao, Y., 2007, Damping Properties of Nanoporous Carbon-Cyclohexane Mixtures," Adv. Eng. Mater., **9**, pp. 209–211.

[15] Lim, M. H., and Stein, A., 1999, "Comparative Studies of Grafting and Direct Syntheses of Inorganic-Organic Hybrid Mesoporous Materials," Chem. Mater., **11**, pp. 3285–3295.

[16] Qiao, Y., Cao, G., and Chen, X., 2007, "Effects of Gas Molecules on Nanofluidic Behaviors," J. Am. Chem. Soc., **129**, pp. 2355–2359.

[17] Han, A., Kong, X., and Qiao, Y., 2006, "Pressure Induced Infiltration in Nanopores," J. Appl. Phys., **100**, p. 014308.

[18] Fay, J. A., 1994, *Introduction to Fluid Mechanics*, MIT, Cambridge, MA.

[19] Hartland, S., 2004, *Surface and Interface Tension*, CRC, Boca Raton, FL.